Design, Analysis and Optimization of Novel Photo Electrochemical Hydrogen Production Systems

By

Musharaf Rabbani

A Thesis Submitted as Partial Fulfillment
of the Requirements for the degree of Doctor of Philosophy
in
Mechanical Engineering

Faculty of Engineering and Applied Science
University of Ontario Institute of Technology

Oshawa, Ontario, Canada, 2013

Abstract

Hydrogen is a green-energy carrier with a high heat of combustion. If obtained from renewable sources, it could be the ultimate and environmentally benign solution for the future energy requirements. This thesis presents the candidate's research on the photochemical hydrogen production cycle, motivations and objectives, literature survey, thermodynamic modeling, exergoeconomic modeling, electrochemical modeling, statistical modeling and preliminary results of the photochemical research. The process selected for the present study is known as the "chloralkali process". The main objective of this research is, in this regard, to develop a hybrid system that produces hydrogen by photo chemically splitting water and neutralizing the by-products (i.e. hydroxyl ions) into a useful industrial process. To be more specific, the objective of this present study is to develop a system that combines photochemical hydrogen production with electrochemical chlorine and sodium hydroxide production in a photo electrochemical chloralkali process. Initially, a series of experiments are performed by using an electric power supply. These initial experiments are followed by photo electrochemical experiments, experiments with salt water, experiments without hole scavenger material and solarium experiment.

The results of electrochemical experiments show that the concentration of brine in the anolyte compartment and the concentration of electrolyte in the catholyte compartment do not affect the rate of chlorine and hydrogen production. The applied voltage, reactor temperature, and current density have a significant effect on the rate of hydrogen production. The optimal brine concentration is 225 g/L and the optimal electrolyte concentration is 25g/450ml. The increasing temperature reduces the solubility, thus increasing the rate of hydrogen production. Also, increasing the electrode surface area in contact with the working fluid increases the rate of hydrogen production.

During the photo electrochemical experiments, three different process parameters are studied, namely light intensity, catalyst concentration, and applied voltage. Using statistical models and experimental data, correlations for the production rate of products are developed. Energy and exergy efficiencies are calculated to assess the performance. An optimization study

for photo electrochemical experiments is performed in order to find the optimal catalyst concentration. Using the optimal catalyst concentration from the photo electrochemical experiment results, experiments with salt water in catholyte are performed. The results show that salt concentration does not have any significant effect on the rate of hydrogen production. During the photo electrochemical experiments, it is observed that applied voltage has a significant effect on the rate of photochemical hydrogen production. This fact is further explored by performing experiments without hole scavenger material. The results show the continuous production of hydrogen. Ultimately, this means that a solid electrode can replace the hole scavenger material.

Energy, exergy, and exergoeconomic models for a heliostat based hybrid system are developed. A radiation model is coupled with a thermodynamic model in order to predict the rate of hydrogen, chlorine, and sodium hydroxide production for a given light intensity at a particular time. The parameters of the radiation model are set to simulate two varied weather conditions-namely a clear sky and a turbid sky environmental setting. Toronto is assumed to be a place where photo electrochemical chloralkali plant is located. The result shows that the maximum intensity occurs at noon time with the surface angle of 22^{o} in an environment with a clear sky. The cost of hydrogen is calculated from the exergoeconomic model. The average annual cost for the hydrogen based on this model is calculated to be 0.7$/kg for a clear sky environment and 1.3$/kg for a turbid sky environment.

To find the minimum required potential, the electrochemical model is developed. The parametric study of different processing parameters shows that the brine concentration and electrolyte concentration do not have significant effect on required cell potential. Current density, temperature, and distance between electrodes, however, have a significant effect on cell potential. The results of the electrochemical model are consistent with the electrochemical experimental results.

Acknowledgements

I would like to express my sincere gratitude to my supervisor Dr. Ibrahim Dincer and my co-supervisor Dr. Greg. F. Naterer, for giving me the great opportunity to work on this interesting project at UOIT. I also appreciate their unwavering guidance, steady encouragement and moral support throughout my PhD study.

I am also thankful to my parents and siblings for their constant encouragement and support throughout my Doctoral Degree.

I would also like to thank my colleagues at CERL, especially Dr. Zhaolin Wang, Mr. Edward Secnik and Mr. Gord Koehne for their kind attention and help in building the experimental setup used throughout my research endeavours

I would like to extend my gratitude to Ms. Cerene Belli for proof reading and editing my thesis.

Furthermore, the financial support provided by the Phoenix Canada Oil Company Ltd. and the Natural Sciences and Engineering Research Council of Canada (NSERC) is gratefully acknowledged.

Table of Contents

List of Figures

List of Tables

Nomenclature

A	Anode; Area (m^2)
$\dot{C}$	Cost rate ($/s)
$\dot{D}$	Diffuse irradiance (W/m^2)
E	Open circuit voltage (V); Eccentricity correction factor
$\dot{Ex}$	Exergy rate (kW)
ex	Specific exergy (kJ/kg)
F	Faraday constant (sA/mol); Scattering fraction
$\dot{G}$	Gibbs free energy rate (kW)
g	Specific gibbs free energy (kJ/kg)
$\dot{H}$	Enthalpy rate (kW)
h	Specific enthalpy (kJ/kg)
I	Current (A); Irradiance (W/m^2); Thickness (mm)
i	Current density (A/m^2)
K	Electrical conductivity ($ohm^{-1}m^{-1}$)
L	Distance (m)
m	Mass (kg)
$\dot{m}$	Mass flow rate (kg/s)
M	Molar mass (kg/kmol)

Mo Molality (kmol/1,000kg water)

N Number of levels; Day number in the year

n No. of moles (kmol)

P Pressure (kPa)

$\dot{Q}$ Heat transfer rate (kW)

R Universal gas constant (kJ/kmol-K)

$\dot{S}$ Entropy rate (kW)

s Specific entropy (kJ/kg-K)

t Time (s)

T Temperature (^{o}C)

$\dot{U}$ Internal energy (kJ)

u Specific internal energy (kJ/kg)

v Specific volume, m^3/kg

V Visibility (km); voltage (V)

W Water vapour thickness (cm)

X Mass fraction

$\dot{Z}$ Equipment cost rate ($/s)

Subscript and superscript

a Aerosols; Air mass at actual pressure

b Beam

c	Forward scattering of total scattering
d	Diffuse
dew	Dew point
n	Normal
sc	Solar constant (1367, W/m^2)
sol	Solution
m-	Broadband
r	Rayleigh; air mass standard at local pressure
g	Generation
Reactor	Reactor
Ho	Heliostat
PV	Photovoltaic
ch	Chemical
oz	Vertical ozone layer
o	Standard; reference state
Ro	Rayleigh optical
is	Horizontal
xd	Destruction
′	Actual conditions

Greek Symbols

α	Solar altitude (degrees)
Δ	Change
σ	Membrane thickness
σ	Stefan-Boltzmann constant (5.67×10^{-8} W m^{-2} K^{-4})
Ω	Morality (kmol/m^3)
λ	Wavelength (μm)
η	Efficiency
ϕ	Tilt angle
θ	Angle of incidence; the angle between normal to the surface and the sun–earth line (degrees)
θ_z	Zenith angle (degrees)
ρ_a	Albedo of the cloudless sky (dimensionless)
ρ_c	Albedo of cloud (dimensionless)
ρ_g	Albedo of ground (dimensionless)
β_1, β_2	Angstrom turbidity-parameters (dimensionless)
ρ	Density (kg/m^3)
	Day angle (in radians)
δ	Declination, north positive (degrees)
δ_c	Declination of characteristics days, north positive (degrees)

τ	Scattering transmittances (dimensionless)
τ_{aa}	Transmittance of direct radiation due to aerosol absorptance (dimensionless)
τ_{as}	Transmittance of direct radiation due to aerosol scattering (dimensionless)
T	Temperature (^{o}C)
γ	Activity Coefficient
ω	Hour angle, solar noon being zero and the morning is positive (degrees)
ω_1	Hour angle at the middle of an hour (degrees)
ω_o	Single-scattering albedo (dimensionless)
ω_s	Sunset-hour angle for a horizontal surface (degrees)
χ	Reflectivity of the ground
φ	Function
ζ	Tilt angle of a surface measured from the horizontal (degrees)
ψ	Latitude

Acronyms

AEM	Anion exchange membrane
ANOVA	Analysis of Variance
bpy -	2,2-bipyridine
bpm	2,2'-bipyrimidine
CEM	Cation exchange membrane
CERL	Clean energy research laboratory

Cl_2	Chlorine
DMA	Dimethylanyline
dpp	2,3'-bis(2.pyridyl)pyrazine
DMF	Dimethylformamide
DOE	Design of experiments -factorial design, Department of energy
df	Degrees of Freedom
HHV	Higher heating value
LHV	Lower heating value
NaOH	Sodium hydroxide
Phen	1,10-phenanthroline
RSM	Response surface methodology
SS	Sum of squares
tpy	2,2',6',2''-terpyridine

Chapter 1

Introduction

1.1 Hydrogen as an Energy Carrier

Due to the rapid industrial and population growth, the energy demand of the world is increasing day by day. The reserves of the conventional energy sources (i.e. oil, natural gas and coal) are also depleting at the same pace. The emission of carbon dioxide and other toxic gasses have also raised ecological concerns. Nuclear power plant disasters in Japan after a major tsunami have raised questions about the safety and the security of nuclear energy. In order to address all of those challenges and to ensure the sustainability of an energy supply source, different options are under consideration by different governments. Germany has planned to shut off each of its 22 nuclear power plants by 2022 and obtain all of the required energy from hydro and other renewable sources. The US Department of Energy (DOE) has proposed a transition plan from an oil-based economy to a hydrogen-based economy by 2040. Canada is heavily investing in renewable sources of energy and is currently offering different incentives to those who are partially or fully meeting their energy demands with the use of renewable energy sources, (specifically solar energy).

Technology evolution has been boosted up by the introduction of energy systems in our society. Energy is the basic component for most business and social productivity today. The use of traditional fuels and higher energy content has brought about vast developments in the world. This revolution of industrial development started in the 18^{th} and 19^{th} century when the fuel evolution changed from wood to coal and from coal to petroleum products in 20^{th} century.

Sustainable development is a process of developing land, cities, businesses, communities, etc. that "meet(s) the needs of the present without compromising the ability of future generations to meet their own needs." The report continues: When a kilogram of gasoline is burned, it makes 3.2 kilograms of carbon dioxide and 1.0 kg of water. The extraction and combustion of fossil fuels is a major threat to the environment because of land damage, smog, acid rain and changes in the composition of the atmosphere. Environmental damage and atmospheric changes may soon alter the weather and climate patterns of the earth resulting in grave problems of all its inhabitants. Hydrocarbons have extraordinary value as the source of chemicals used to produce goods and other essentials for living beings [1, 2].

According to the Biogenic Theory, energy dense fossil fuels such as coal, petroleum, shale oil, tar sands, and natural gas were formed under high temperatures and pressure from biological residue over millions of years. In our present era, hydrocarbons are not sustainable. This is due to the fact that the majority of our societies use fossil fuels. It is important to consider the fact that vast amounts of solar energy are stored in various forms of nature such as petroleum, shale oil, coal, tar sands and natural gas. The commercial oil drilling industry in Pennsylvania produced an average of 15-20 barrels per day in 1859. This average was the supply of petroleum equal to approximately 1.8 trillion barrels. However, the production today yields approximately 0.9 billion barrels of petroleum, while the demand of petroleum is approximately 105 million barrels per day. With the continued increase in population figures, it is estimated to be 10 billion by 2050. Upon acquiring the oil, the energy input for new oil extraction continues to increase. In some cases, the energy required to obtain a barrel of represents 50% of the energy inherent in the oil itself. The overall natural gas spare is assessed to be about 1.4×10^{14} m^3 with production of an estimated 2.4×10^{12} m^3 annually. Upon comparison, however, the lifetimes continue to shorten considerably [1, 3]. The coal saved is assessed at 9.1×10^{11} tons and per year consumption is estimated to be 5×10^{9} tons. While it is estimated that the world has enough 'harvestable free' coal for energy use for approximately 250 years, natural gas for 60 years, nuclear fuel for another 200 years, the proverbial "devil" appears to be in the details upon consideration of rate of use of our economically recoverable reserves [1].

There is a disadvantage linked with hydrocarbon fuels that even their most reliable devotee has to admit, and that is environmental pollution [1, 4]. In 1896 Arrhenius [5] put forth the concern that carbon dioxide from fossil fuel burning could raise the infrared opacity of the atmosphere enough to warm earth [6]. Carbon dioxide is a greenhouse gas trapping long wavelength radiation (heat) emitted by earth. Hence, more CO_2 in the atmosphere and the temperature increases, less CO_2 and the temperature decreases. Earth's baseline temperature, and that which we are comfortable with, appears to be finely balanced. Tilt the earth a small amount in one direction and it is 90°F in Pennsylvania, tilt the earth in a similarly modest amount in the other direction, and it is 10°F in Pennsylvania (twenty years ago the balance was approximately 75°F to -10°F, but things are quite warmer here now). Approximately 6 billion tons of carbon dioxide are produced every year by human activity, 80% of which is the result of the burning of fossil fuels. Coal produces 430 grams of carbon dioxide/kWh, while natural gas produces 190 g of CO_2/kWh. Current CO_2 levels are easily measured and future levels accurately predicted by simple arithmetic: burning so many tons of coal releases so many tons of CO_2. At the beginning of the Industrial Revolution in the 18th Century, the atmospheric carbon dioxide level was 270 ppm(a value that had held steadily for millions of years). This value increased to 370 ppm within the 20th Century, reaching 383 ppm in 2007 [1]. Climate models suggest that levels of 550 ppm would lead to a magnitude of warming equal to that of the cooling seen in the last ice age. So rather than an ice age, it appears we may soon have a 'steam age.' Like the ice age, one can suggest that humans will survive; however, one can also anticipate some substantial and unpleasant disruptions.

From 1990 to 2004, the world's CO_2 emissions increased by 24.4% [1, 7]. If anything approaching the current situation continues (≈ 1 billion gasoline powered vehicles), we will easily and soon surpass 550 ppm - bringing rates well into the upper 600 ppm levels [1, 5]. The cost of the environmental and health related damages caused by burning fossil fuels is commonly ignored, as it is a non-specific person that suffers.

As supply now exceeds demand, large-energy users are able to readily meet energy requirements by means of importation. In the United States today, approximately 66% of the oil consumed is imported; 66% of this consumption is spent on transportation. of this 66%, a

substantial amount is used to enable cars and light trucks. The Government of the United States has deemed freely available Middle Eastern oil to be of the utmost importance in terms of energy consumption, and backs this up with a vast (and expensive) military presence across the Middle East [8- 9]. Two key points to keep in mind are: (1) nations always have, are currently, and will continue to fight wars over needed resources, and (2) societies will not happily go back to the life style of the pre-industrialized world.

The world's most authoritative body of climate scientists conclude that 55.85% reductions in greenhouse gas emissions are necessary to stabilize atmospheric concentrations [1, 9]. To eliminate anthropogenic CO_2 emissions, we require non-carbon-emitting energy sources. It is imperative to find a suitable and sustainable energy alternative to the present energy-supply system. We propose that hydrogen appears to be a promising and useful candidate to replace hydrocarbon fuels. Also noteworthy is the fact that the sun gives energy levels of 3×10^{24} joules/ year to the Earth, which is 10,000 times greater than our present global energy consumption rate. Furthermore, the world is blessed with a vast abundance of desert lands (19.2×10^6 km^2) [10] that, one imagines, would be ideally suited for capturing solar energy in a sustainable fashion for the use of society.

In 1780, water gas was produced for the first time. Water gas consisted of a mixture of 50% hydrogen, 40% CO plus CO_2, and nitrogen. Following the existence of water gas, came the existence of town gas during the early 1800's to the mid-1900's. Town gas consisted of a mixture of 50% hydrogen, 30% methane, 6% CO, and traces of other gases. The use of these hydrogen-rich gases ceased to be used in the 1960s when natural gas became abundant. On a side note, Konstantin Tsiolkovsky first proposed hydrogen-fuelled rocket propulsion for space flights in the late 1890s [1].

In 1990, the world's first solar-powered hydrogen production plant became operational at Solar-Wasserstoff-Bayern, a research and testing facility in southern Germany. In 1994, Daimler Benz demonstrated the performance if its first NECA I (New Electric CAR) fuel cell vehicle at a press conference in Ulm, Germany. In 1999, Europe's first hydrogen-fuelling stations were opened in the German cities of Hamburg and Munich [1].

There are different sources of renewable energy which include solar, wind, tidal energy etc. If not required, the energy from these renewable energy resources cannot be stored directly. Among various other options, hydrogen emerged as an ideal energy-source candidate because of its ability to store and distributes energy resources. Hydrogen performs clean combustion with zero environmental impact. The output of the hydrogen combustion is water.

Among various methods of solar energy conversion, much attention is given to photocatalytic water splitting because of its potential significance in directly obtaining "green" hydrogen (H_2) from water. If successfully developed with economic viability, this could be a major technology discovery that could solve both energy and environmental problems together in the future. Conversion of solar energy into chemical energy, through light-driven water splitting, generates an environmentally benign hydrogen gas. This carbon-free fuel has a high energy output, relative to its molecular weight. The by-product of water splitting can either be neutralized into oxygen or chlorine and caustic in a chloralkali process.

Solar energy is used by plants, which then becomes either utilized by animals as biomass, or degrades to produce hydrocarbon reserves. The rate at which the world is using fossil fuels today makes it essential to look at alternative means to harness solar energy. Among other various methods of utilizing solar energy, we can harness solar energy without the use of plants. The global energy demand combined with climatic changes makes it essential to harvest solar energy. Successfully harvesting this energy source can include either the conversion of the light energy into thermal energy (in thermal conversion schemes), or via electrical energy by using solar cells or fuels through light (in chemical energy conversion schemes).

In the future, water might replace fossil fuels as the primary resource of hydrogen. Hydrogen is distributed via national networks of both hydrogen-transport pipelines and fuelling stations. Hydrogen energy and fuel cell power are clean, abundant, reliable and affordable. These factors contribute to a source becoming an integral part of all sectors of the world economy.

Hydrogen is known as an energy carrier and not an energy source. It is not readily available in nature, however, energy from an energy source can be used to produce it. A solar

cell can produce modest amounts of electricity, even when it is cloudy, by the conversion of the diffuse light to power. The calculations show that an area of 100×100 miles square would yield an energy supply level equivalent to that of 1.019×10^{20} Joules per year (in 1999) – the amount used annually in the entire United States [1]. The energy received by 48 contiguous states of USA is 1.766×10^{23} Joules per year (assuming 8.38 Joules/cm^2/min) [1]. The supply of energy from the Sun to the Earth is gigantic: 3×10^{24} joules a year, (approximately 10,000 times greater than the global population currently consumes). Covering 0.1% of the Earth's surface with solar cells (with an efficiency of 10%) would satisfy our present energy requirements [1-9]. This remains an enormous challenge, made even greater by the fact that we lack a serious effort to achieve it. Since our energy is now predominately provided by fossil fuels, we note that fabrication of solar cells comes with a CO_2 emission price tag. For a silicon solar cell, it appears that three years of (non-carbon emitting) power generation are required to compensate for the CO_2 emitted during fabrication [10].

Hydrogen is an ideal energy carrier because: (1) it can be produced from and converted into electricity at relatively high efficiencies; (2) its raw material for production is water; (3) it is a renewable fuel; (4) it can be stored in gaseous, liquid or metal hydride form; (5) it can be transported over large distances through pipelines or via tankers; (6) it can be converted into other forms of energy in more ways and more efficiently than any other fuel; (7) it is environmentally compatible in that its production, storage, transportation, and end use do not produce pollutants, greenhouse gases, or any other harmful effects on the environment (except in some cases the production of nitrous oxides). Unfortunately, hydrogen currently suffers from high production costs.

Hydrogen is the most abundant element in the universe. Representing 90% of the universe by weight, it is the third most abundant element in our planet. Hydrogen is the lightest element with a density of 0.08988 g/liter at STP. Hydrogen is colorless, odourless, tasteless, and non-toxic under normal conditions. Liquid hydrogen has a density of 0.07 g/cc compared to 0.75 g/cc for that of gasoline. Hydrogen production via biomass pyrolysis involves heating the biomass rapidly to high temperatures in the absence of oxygen. Depending upon the organic

nature of the biomass, products like hydrogen, methane, carbon monoxide, carbon dioxide, tar, oils, carbon, and other solid, liquid, and gaseous products are produced as a result of pyrolysis.

$$\text{Biomass} + \text{thermal energy} + \text{steam} \rightarrow H_2 + CO + CO_2 + CH_4 + \text{hydrocarbons} + \text{ash}$$

Transportation systems based on the use of petroleum fuels are presently the lifeblood of the modern world. The status quo, however, will not last for more than a few years. A permanent solution is to form a stable and environmentally-friendly transportation sector based on renewable sources of hydrogen and/or electricity. The energy needed to ignite hydrogen at stoichiometric air/fuel ratio is almost one order of magnitude less than that needed for gasoline, (0.017 mJ for hydrogen vs. 0.24 mJ for gasoline). It has a wide flammability range (4% to 75% for hydrogen vs. 1.4% to 7.4% for gasoline), and the engine can work in wide a range of H_2 fuel/air ratios from stoichiometric to very lean mixtures [1, 5]. It has a high auto-ignition temperature (576°C), allowing the use of high-compression ratios. The low density of hydrogen, however, makes the volumetric energy density of the air/fuel mixture low. The stoichiometric air to hydrogen ratio by volume is 2.4:1; therefore, in stoichiometric conditions, hydrogen will occupy 29.6% of the cylinder volume whereas gasoline will occupy only about 2% [1].

Other promising types of fuel cells utilizing hydrogen are proton exchange membrane fuel cells (PEMFC), phosphoric acid fuel cells (PAFC), molten carbonate fuel cells (MCFC), and solid oxide fuel cells (SOFC). The PEM fuel cells use a proton conducting solid polymer membrane as an electrolyte. The operating temperature ranges from 60°C to 120°C, with an efficiency of 40–50%. The PAFC uses liquid phosphoric acid as the proton conducting electrolyte, (usually held in a silicon carbide matrix). The operating temperature ranges from 150°C to 210°C.

The burning of hydrogen (within pure oxygen) produces only water. If, however, hydrogen is burned in air, oxides of nitrogen (NO_x) can be formed. This is known to be the cause of urban smog and acid rain. In comparison to the burning of fossil fuels, the amount of these oxides generated by burning hydrogen are essentially nil. The atmospheric hydrogen concentration is about 4 ppm. Hydrogen added to the air, by its use as a fuel, will enter without making any measurable change in the long-term concentration.

Due to its low energy per unit volume, hydrogen is generally stored as a compressed gas or liquid for practical applications. Hydrogen becomes liquid at 20K; a volume of liquid hydrogen weighs only 10% as much as the same volume of gasoline. Obviously, handling problems can be severe at 20K. In order to serve as a practical fuel for transportation, hydrogen must be highly compressed to minimize the fuel storage volume. Typical hydrogen storage pressures are 2000 to 5000 psi. Existing hydrogen generation technologies typically produce hydrogen gas at atmospheric pressure to 375 psi. Two alternatives to pressurized gaseous hydrogen storage are available: liquefied hydrogen and metal hydrides. Liquefying hydrogen, however, calls for expensive, elaborate equipment to cool the gas to –253°C; all of these factors take energy. Metal hydrides are expensive, heavy, and have a limited lifespan, showing decay in energy storage capacity after repeated cycling. Further research is needed on approaches for hydrogen storage using the reversible formation of safely transportable chemical compounds.

The risks associated with hydrogen usage are of the same order of magnitude as gasoline or natural gas; all risks can be addressed in order to use the source safely once a proper understanding of their properties is achieved. Safety precautions for use of hydrogen in the home and in industrial applications are similar to those required for natural gas. The safety advantages of hydrogen include its great speed of dissipation, low flame luminosity, lack of toxic gas production on combustion, and total lack of toxicity. Hydrogen is somewhat harder to ignite with heat than is natural gas, but is more easily ignited with electric sparks. The safety advantages of H_2 are partially offset by the wide combustion mixture range of hydrogen (4 to 75 vol %) compared to natural gas (5 to 15 vol %). Hydrogen is considered to be a dangerous gas due to its wide flammability range and low ignition energy.

1.2 Motivation

Hydrogen is mostly used as a chemical rather than as a fuel. For the purpose of effective renewable energy, hydrogen has been considered as a very good fuel source as well as a potential energy carrier for a future energy supply. Renewable sources contribute about 5% of the total hydrogen production. Various ways of producing hydrogen from solar technologies include: thermochemical, photo-electrochemical, and photocatalytic hydrogen production. Biomass

products such as plants, micro-algae, and organic waste are also some of the other contributors to the production of hydrogen [12]. Electrolysis of water is a standard commercial technology for producing hydrogen. Some other technologies used to produce hydrogen include gasification, pyrolysis, and fermentation. These processes lend to the possibility of producing hydrogen from energy crops and biomass materials (those from forest residue and municipal sewage). Photo-electrochemical water splitting and photobiology are both long-term options for producing the required hydrogen from water, using solar energy. These technologies are still in the developmental phase [13].

Solar hydrogen production is one of the most promising and "green" solutions to today's crucial energy, environmental, and sustainability problems. The potential of photochemical and catalytic hydrogen production systems is extensive; however, the viability of these techniques at scaled up production rates is unclear. Along with hydrogen, researchers are also examining OH^- as part of hydrogen production cycles. For a sustainable hydrogen production cycle, these OH^- ions should be neutralized.

1.3 Scope and Objectives of Research

There are currently different methods of producing hydrogen. However, most of methods are not fully sustainable in long term. For example, Steam Methane Reforming (SMR) is an efficient method to produce hydrogen. However, this process is not sustainable for some key reasons: i) government penalties on the use of carbon emissions, ii) limited sources of methane, iii) high energy requirements and iv) high cost. Electrolysis of water is another method of producing hydrogen, although due to the high cost of electricity and the fact that production of electricity requires using fossils it also makes it an expensive process to adopt. On the other hand renewable energies carry an immense potential to address the world's energy needs. The problem with these renewable energies is that the energy from these renewable sources cannot be stored directly. Hydrogen production from renewable's can be a single step or multi step process. For example, hydrogen production via PV electrolysis is a multi step process. It involves i) the generation of electricity using PV panels with an efficiency of around 10% to 12% ii) using the generated electrical power with electrolysis efficiency of around 70% to produce hydrogen. Thus solar to

hydrogen efficiency is around 7%. Photochemical hydrogen production is appearing as an optimal option for producing hydrogen from solar radiation, which is a single step process. Due to the direct conversion of water into hydrogen and hydroxyls under sunlight, the photochemical hydrogen production process has a fairly high efficiency compared to the options discussed above. However, photocatalysts work in a specific wavelength range and do not use the entire solar spectrum. Due to this, even after having a number of advantages, photochemical hydrogen production is not economical. Also for continuous hydrogen production, photochemical hydrogen must be connected with another process where the by-product of water reduction process (OH^- ions) must be neutralized. In order to make this process economically viable, a complete engineering system is required.

The objectives of this present study are to perform experimental studies and modeling with the emphasis on engineering challenges involved in the photochemical hydrogen production and neutralization of OH^- ions (in a electrochemical chloralkali process). ZnS is used as a photo-catalyst. Na_2S is used as an electron donor material. The objectives achieved during the research are listed below.

1) The hydrogen production yield decreases over time in a process of photochemical hydrogen production, due to the phenomenon of increasing concentration of OH^- ions in the solution. All existing chloralkali process reactors cannot be coupled with a photochemical H_2 production reactor. In the electrolysis of brine, sodium ions pass through a cation exchange membrane and form NaOH. In cases of photochemical H_2 production, however, if one allows sodium ions to pass through the cation exchange membrane and enter the photochemical hydrogen production chamber the photochemical catalyst might be destroyed due to the corrosive nature of sodium. Even if the catalyst is not destroyed, one will still need to add another process to extract NaOH. This process, however, may not be a cost effective option for industry use.

In order to address the above mentioned problem, a new type of reactor design is designed that neutralizes OH^- effectively and does not mix NaOH with the catalyst and electron donor/ hole scavenger material. The details of the new reactor are given in chapter 4. The

designed reactor is close to the present reactor design. Therefore, all of the existing membrane reactors can easily modified to this newly proposed configuration.

2) Ion exchange membranes are used for selective ion passage from one media to another. Many of the commercially available membranes are used only for water applications. These membranes are not stable in highly alkaline and harsh chemical environments. There are some Nano filtration membranes that are stable in highly alkaline and harsh chemical environments. These are not, however, ion selective due to the fact that these membranes only stop a particular media based on molecular weight. For this reason, a particular ion exchange (both anion and cation exchange) membrane are required that can withstand highly alkaline and harsh chemical environments while allowing OH^- ions (from the hydrogen production unit) and Na^+ (from the brine unit) to pass through them.

3) Initially, experiments are performed by means of electrolysis in order to investigate and optimize different cell parameters. Based on the literature review, the following six different parameters are initially investigated for the newly designed reactor in the electrolysis experiments.

i. Concentration of electrolyte in the anolyte compartment;
ii. Concentration of brine;
iii. Cell voltage;
iv. Brine temperature;
v. Anode area in contact with electrolytic water;
vi. Cathode material;

These parameters are divided into two groups: i) numerical parameters ii) categorical parameters. The first five are treated as numerical parameters and the cathode material is treated as a categorical parameter. The effect of each parameter on the chloralkali process products are studied using a statistical method of analysis of variance (ANOVA). The details are given in Chapter 6.

Based on the experiments, optimization of the above mentioned parameters is performed using Stat-ease®. The purpose of the optimization is to find the optimal operating parameters

which maximize the rate of hydrogen, chlorine, and NaOH production. Stat-ease® uses a method developed by Derringer and Suich for optimization.

4) The optimized results of the electrolysis experiments are then used to investigate the following parameters in a photo reactor using deionized water.

i. Light Intensity;
ii. Catalyst concentration;
iii. Applied voltage;

All of the above listed parameters are treated as numerical parameters. In the end, optimization is performed to find the optimal catalyst concentration. The details are given in Chapter 6.

5) The optimized photo catalyst concentration is then used to study the effect of salt water on the rate of hydrogen production. The following three parameters are varied according to the factorial design of the experiments.

i. Concentration of salt;
ii. Light Intensity;
iii. Applied voltage;

All of the above listed parameters are treated as numerical parameters. The details are presented in Chapter 6.

6) Photo catalyst (i.e. ZnS in present study) uses only a portion of the solar spectrum (4% in case of ZnS). From an efficiency point of view, it is important to harness the unused portion of the solar spectrum. This harnessed energy can be used to produce additional hydrogen through electrolysis and also to eliminate the external power required to neutralize hydroxyl ions. Conditions conducive to harnessing the unused portion of the solar spectrum have been simulated using the optimized parameters from both the electrolysis and photo electrochemical parameters. The details are discussed in Chapters 5 and 6.

7) Based on the performed experiments, a statistical model is developed using an analysis of variance (ANOVA). This model yields the statistical significance of the individual parameters and their mutual effect on the production rate. Based on this method, the researchers study the interaction between different cell parameters and their mutual effect on the rate of chloralkali products. The details are discussed in Chapter 2. Following the experiments, predictive correlations are developed and utilized for modeling purposes. The main objective is to derive expressions for the rate of production of the chloralkali products (i.e. H_2, Cl_2 and NaOH) as a function of input parameters. Further details will be discussed in subsequent sections.

8) Based on the first and second laws of thermodynamics, the energy and the exergy models for the new reactor are developed. Quantitative energy and exergy analyses are performed to evaluate the thermodynamic performance of the water splitting system for hydrogen production. Energy and exergy models for the continuous reactor are also developed. Different parameters including light intensity, mass flow of brine, brine concentration and reactor temperature are also studied for the development of a continuous reactor. The total energy demand remains almost constant, the electrical energy usage decreases, while the thermal energy increases with increasing temperature. The reduction in electrical energy is advantageous from the perspective of the second law of thermodynamics because electricity has a higher energy quality than thermal energy. Thermodynamic performance is evaluated with the exergy analysis, which is based on the second law, (allowing process inefficiencies to be better identified). The effective techniques for the analysis and design of energy systems are often combined with thermodynamics and economic disciplines to achieve optimum designs. The details are discussed in Section 5.1.

9) Along with hydrogen, chlorine and sodium hydroxide are also useful products. Sodium hydroxide and chlorine also have many industrial applications. Chlorine and sodium hydroxide are not fuels; therefore, they cannot be used in standard energy and exergy efficiency definitions of fuels. For this reason, an exergoeconomic analysis is performed. Exergoeconomic includes the effects of all useful products, regardless of their energy content. In the present study, there is only one equation for exergoeconomic analysis and three unknowns. Therefore, the market price for the chlorine and sodium hydroxide will be used. The details are discussed in section 5.3.

10) In order to find the voltage drop across different cell compartments, an electrochemical model is developed. This includes decomposition voltage and the potential drop across the electrodes, membranes, and solutions. The details are discussed in Section 5.4.

11) Light intensity is an important parameter and, in fact, the key parameter in our study. The solar radiation model is used to predict the light intensity at the city of Toronto for two different weather conditions. The radiation model is coupled with thermodynamic model to predict the rate and cost of hydrogen production. The details are presented in Section 5.5.

12) The conceptual design of the photo electrochemical chloralkali process integration with the water treatment plant is also studied. Water passes from the anion and cation exchange bed in order to remove anionic and cationic impurities. Anion and cation exchange beds use anion and cation exchange resins, respectively. These resins become exhausted after a certain time frame and need to be refreshed or replaced. Chloralkali products can be used to refresh the exhausted resins. The details are discussed in Section 6.9.

1.4 Thesis Outline

This thesis is organized into seven chapters.

Chapter 2 presents the related background extending the introduction to solar hydrogen production and related photo-chemical and electrochemical hydrogen production processes, different chloralkali processes etc.

Chapter 3 provides a detailed literature review on the existing technologies of photo-chemical hydrogen production, electrochemical hydrogen production, chloralkali processes, and related details with regard to their achievements and future prospects.

Chapter 4 describes the system description of experimental and theoretical analysis accomplishments of this thesis. It contains all the introductory information that is taken into account during this research.

Chapter 5 contains the thermodynamic model for a batch and a large scale continuous reactor, exergoeconomic modeling, radiation modeling, and electrochemical modeling of a photo electrochemical chloralkali reactor.

Chapter 6 explains the results of the experimental and theoretical analysis of the system with corresponding discussions.

Chapter 7 summarizes the conclusions and some recommendations for future work.

Chapter 2

Background

2.1 Introduction

In this chapter, a detail background about electrolysis, photo electrolysis, photochemical hydrogen production and different types of chloralkali processes are presented.

2.2 Photo chemical hydrogen production

Photochemical hydrogen production is a light-driven process. For water reduction process purposes, an electron is required which breaks the water into hydrogen and hydroxyl ions.

$$H_2O + e^- \rightarrow \frac{1}{2}H_2 + OH^- \quad (2.1)$$

In the case of electrolysis, these electrons are supplied by electricity (usually obtained from burning fossils fuels). In the case of photo-chemical processes, an electron donor material or hole scavenger (for example DMA, Na_2S) donates electrons and acts as a sacrificial agent (i.e. depletes over time). It does, therefore need to be replaced once it is completely utilized. There are different types of photo catalysts that require different electron donor materials or hole scavenger material, depending upon the nature of Photo catalyst. These photo catalysts can broadly be divided into two major categories:

i. Heterogeneous photo catalyst
ii. Homogenous photo catalyst

The heterogeneous photo catalyst consists of solid phase particles that interact with liquid water in a photo-hydrogen production system. These catalysts can be used as a solid electrode or

in powder form. The heterogeneous photo catalyst is usually a semi-conductor device with a valance and conduction band. When a photon of light (having energy equal or larger than the band gap between the valance band and conduction band), the electron from the conduction band jumps into the conduction band and forms a hole in the valance band. The electron in the conduction band, along with the H_2O molecule, forms hydrogen and hydroxyl ions.

$$h\nu + SMD \rightarrow e^- + SMD^+ \tag{2.2}$$

$$H_2O + e^- \rightarrow \frac{1}{2}H_2 + OH^- \tag{2.3}$$

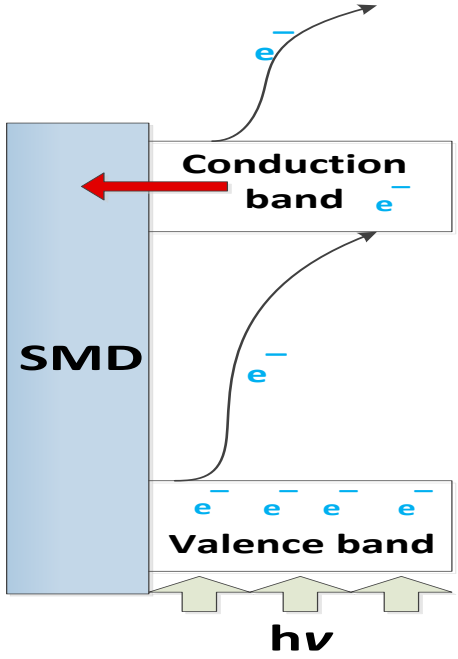

Figure 2.1: Heterogeneous photo catalyst.

Some of the well-known heterogeneous catalysts are zinc sulfide (ZnS), cadmium sulfide (CdS), titanium oxide (TiO_2) etc. It is desirable to use a catalyst with minimal energy gap. Some of the heterogeneous photo catalysts are not stable in water and undergo photo- corrosion, thus requiring a reducing agent (i.e. require hole scavengers). For example, ZnS and CdS are unstable in an aqueous solution. If, however reducing agents like sodium sulfide (Na_2S), sodium sulphate (Na_2SO_3) etc. (which act as a hole scavengers) are used, the photo catalyst is efficiently stabilized with no photo corrosion. These reducing agents are consumed over the specified

period of time and need to be replaced. Electric power supply can also be used to supply electrons via a solid electrode. Heterogeneous photo catalysts (especially in the form of powder) usually form an opaque, aqueous solution disabling light from passing through the hydrogen production chamber. Heterogeneous catalysts usually have high quantum efficiency and long life spans. For example, it has been reported in literature that ZnS have a quantum efficiency of over 90% and effectiveness even after 36 hours [14].

Homogenous catalysts are usually supramolecular structures in which small units or building blocks (each performing a specific task), combine together. There are three basic building blocks of a supramolecular structure as follows:

i. Light absorber
ii. Electron relay
iii. Electron collection center

Light absorbing units absorb light and accept electrons from an electron donor material. The accepted electron is then transferred to the electron relay, which transfers these electrons to the electron collection center. Water is introduced at the electron collection center and is oxidized to hydrogen and hydroxyl ions.

$$h\nu + ED \rightarrow e^- + ED^+ \tag{2.3}$$

$$H_2O + e^- \rightarrow \frac{1}{2}H_2 + OH^- \tag{2.4}$$

Homogenous photo catalysts usually allow the light to pass through there aqueous solution. An example of a homogenous catalyst is a brewer catalyst. Figure 2.2 shows a typical homogenous photo catalyst structure.

Electrolysis is a way of separating bonded elements or compounds by having an electric current move through them. Water electrolysis, for example, breaks up H_2O to hydrogen and oxygen. It is important to select the appropriate electrolysis, which will theoretically contain free ions that can act as an electrically conductive medium.

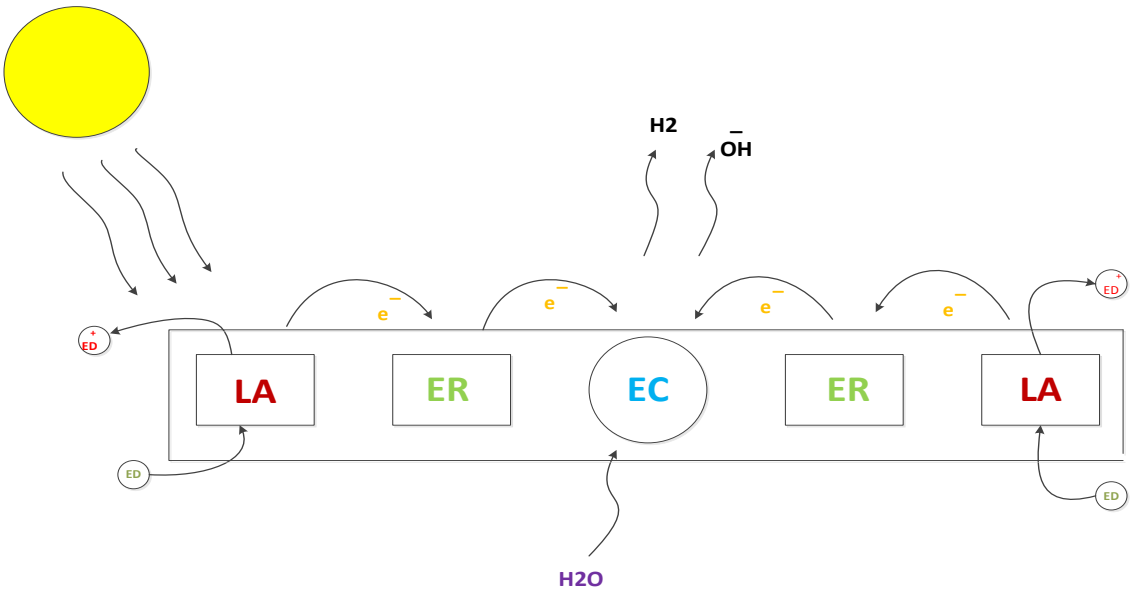

Figure 2.2: Structure of homogenous photo catalyst.

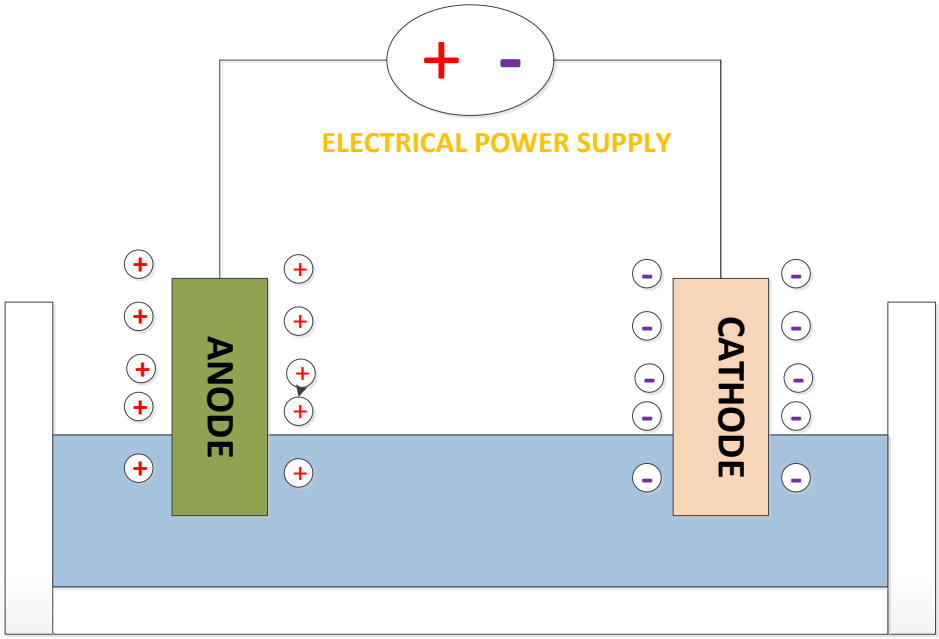

Figure 2.3: Electrolysis cell.

Electrolytes can break up into cations (positive ions +) and anions (negative ions -), which can carry the current. An electrolysis cell contains two electrodes namely cathode and anode. During the electrolysis of water, reduction and oxidation reactions occur at the same time which forms hydrogen gas at the cathode and oxygen gas at the anode part. The main problem

for producing hydrogen is that the fact that electricity is needed for this process (which is mainly generated from burning fossil fuels).

2.3 Harnessing the Unused Portion of the Solar Spectrum

Photo catalysts use only a portion of the solar spectrum for hydrogen production. Zinc sulfide, for example, only works in the UV region of the solar spectrum. The UV region is only 4% of the total solar spectrum. This means that 96% of the solar spectrum is not utilized.

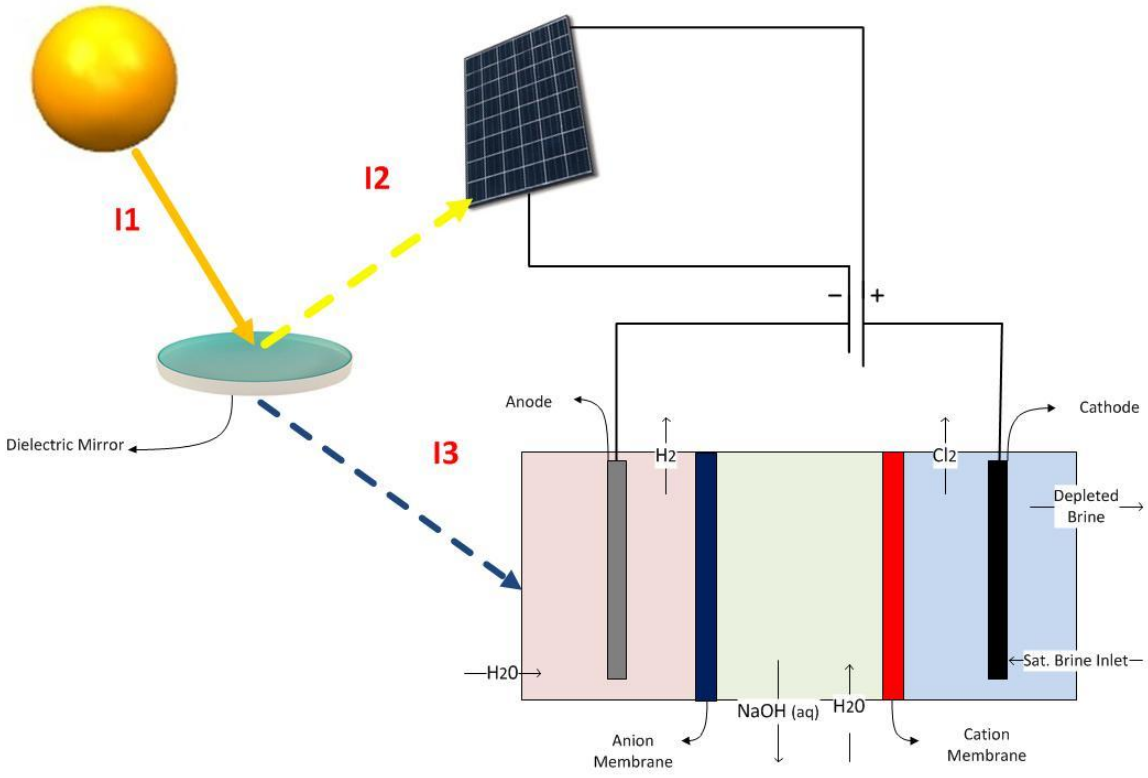

Figure 2.4: Conceptual design illustrating the unused portion of solar spectrum being harnessed and its utilization in the chloralkali process.

This, as a result, decreases the efficiency of the overall process and increases production cost. Similarly, cadmium sulfide works at the wavelength 510 nm to 520nm, using only 13% of the total spectrum. As a result, 87% of the input radiation is still not utilized. It is important,

therefore, to harness the unused portion of the solar spectrum in order to utilize all of the available light energy efficiently. Based on the nature of the catalyst, a procedure should be adopted.

A generalized way to harness the unused portion of the solar spectrum is by means of using dielectric mirrors. A dielectric mirror splits the incoming solar radiation into two different parts. It transmits one part of the solar spectrum and reflects the other. There are different varieties of dielectric mirrors available in the market which transmit certain portions of the wavelengths and reflect the remaining portion. Figure 2.4 shows the schematic of the dielectric mirror used in the photo electrochemical chloralkali process. The total solar radiation is represented in Figure 2.5 (from 280nm to 4000nm). The portion of the total radiation used to produce hydrogen by means of photochemical process is represented blue in Figure 2.5.

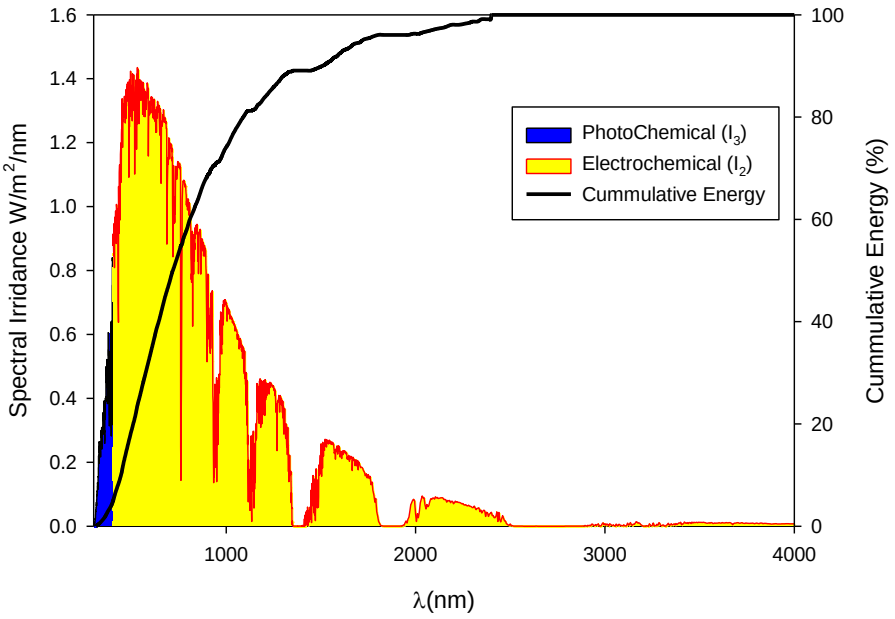

Figure 2.5: Solar spectrum for the photo electrochemical chloralkali process with ZnS as a photo catalyst.

Figure 2.5 represents the unused portion of the solar spectrum in yellow color and the fact that it is reflected by a dielectric mirror and collected by a PV array. A PV array produces

electricity that produces additional hydrogen by means of electrolysis. It will also produce chlorine and sodium hydroxide as a useful by-product. The electricity produced from the unused portion of the solar spectrum also supplies electrons for the photochemical process. As a result, one can get rid of the electron donor material or hole scavenger. In other words, recovering the unused portion can help to remove all of the consumables from the system, increasing both efficiency (i.e. production rate for a given input energy) and cost effectiveness. Figure 2.5 shows the solar spectrum for the photo electrochemical chloralkali process with ZnS as a photo catalyst.

2.4 Chloralkali Process

The chloralkali process (CAP) is an important industrial process that uses electricity and brine for the production of valuable industrial chemicals. The chemicals produced include chlorine, hydrogen and sodium hydroxide (also known as caustic soda). The term chloralkali refers to two chemicals (chlorine and an alkali), which are produced simultaneously after the electrolysis of an aqueous sodium chloride solution (i.e. saltwater).

The half-cell reduction reaction is

$$2H_2O + 2e^- \rightarrow H_2(g) + 2OH^- \quad (2.5)$$

At the cathode side, the water is reduced to hydrogen gas, and releases hydroxide ions in the solution.

The half-cell oxidation reaction is

$$Cl^- \rightarrow Cl_2 + 2e^- \quad (2.6)$$

At the anode location, saturated brine is passed through the chamber of the cell where chloride ions are oxidised to chlorine.

The overall reaction is

$$2NaCl + 2H_2O \rightarrow 2NaOH + Cl_2 + H_2 \quad (2.7)$$

Sodium ions (Na^+) react with the hydroxide ions OH^- to produce sodium hydroxide (NaOH).

2.4.1 Current Technologies in the Market

The chloralkali process is currently carried out in industry by using one of three different methods

i. Mercury cell
ii. Diaphragm cell
iii. Membrane cell

In each of these three methods, an aqueous sodium chloride solution is electrolysed to convert the chloride ions into chlorine gas. As a result of these methods, chlorine is produced at the anode (positive electrode), along with hydrogen, which is produced at the cathode (negative electrode). There are hundreds of companies in the world that produce and/or use Cl_2, H_2 and NaOH as a result of using the above mentioned technologies (62% diaphragm cell, 10% mercury cell, 24% membrane cell, 4% other technologies). Figure 2.6 shows the market share of the individual technology.

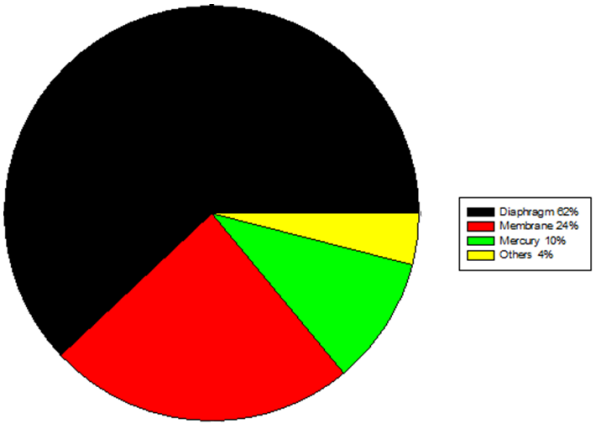

Figure 2.6: Market share of chloralkali technologies [Data from 15].

2.4.2 Mercury Cell

After the electrolysis, chlorine is generated at the anode.

$$Cl^- \rightarrow \frac{1}{2}Cl_2 + e^- \qquad (2.8)$$

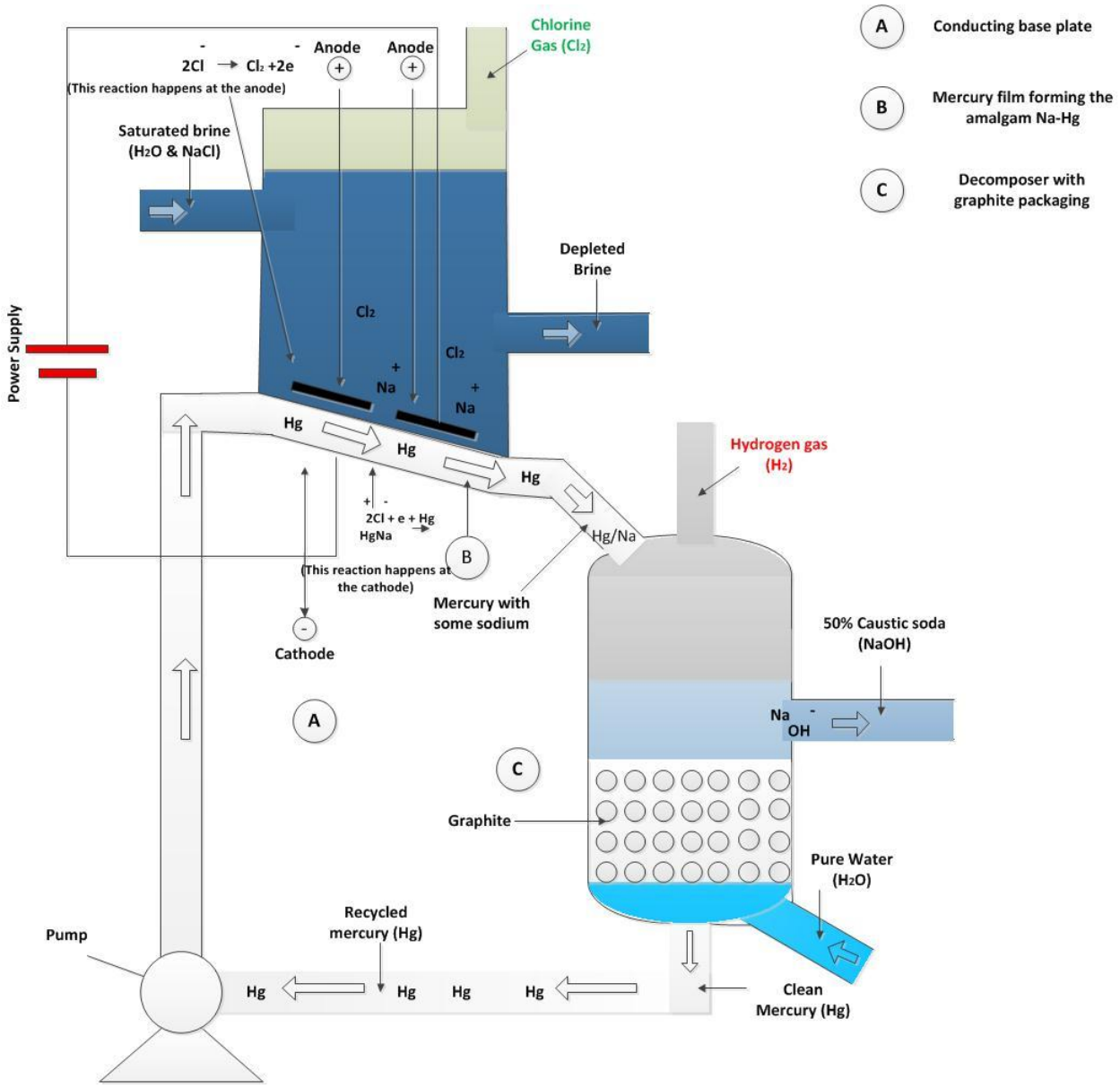

Figure 2.7: Mercury cell schematic [Modified from Ref. 15].

A sodium and mercury based solution, known as amalgam, is formed at the cathode.

$$Na^+ + e^- \rightarrow Na/Hg \tag{2.9}$$

The reaction of Na/Hg with water results in production of caustic soda.

$$Na/Hg + H_2O \rightarrow NaOH + \frac{1}{2}H_2O \tag{2.10}$$

This process is also known as the “Castner-Kellner Process” [16]. To elaborate, Figure 2.7 shows the schematic of a mercury cell. These cells have both steel bottoms and sides, which are coated with rubber. Also present, are end boxes for the brine (aqueous sodium chloride) and the mercury feed. Exit streams on the cell are equipped with a flexible rubber coated steel cover. Adjustable metal anodes hang from the top of the cell, and the mercury (cathode cell) flows on the inclined bottom.

The saturated brine solution floats on top of a thin layer of mercury (cathode). The electrolysis process creates chlorine at the anode and sodium at the cathode. The chlorine is then removed from the anode, cooled, dried, and compressed. On the other end of the cell, sodium combines with mercury to form sodium-mercury amalgam. The amalgam is further reacted with water in a separate reactor called the “decomposer” to produce hydrogen gas and a sodium hydroxide (caustic soda) solution. Sodium hydroxide and hydrogen are then separately cooled and the mercury is removed before proceeding to the storage, sales, or other processes [17]. It should be noted that both the hydrogen and chlorine gases are formed in separate steps. Due to the high cost of mercury and the potential effects that it can have on the environment, (proven by recent discoveries of high mercury concentration levels in fish populations) this technology has been phased-out.

2.4.3 Diaphragm Cell

The diaphragm cell structure includes a rectangular box with metal anodes that are supported from the bottom with copper-based plates. These copper-based plates carry a positive current. Figure 2.8 shows the schematic of a diaphragm cell. The cathodes are metal screens connected from one end to the other end of the rectangular tank. Asbestos is first dispersed as slurry in a bath, and then vacuum deposited onto the cathodes. This process forms a diaphragm.

The purpose of a permeable asbestos-based diaphragm is to prevent the caustic soda from reacting with the chlorine. Brine is then added into the anode side, which then flows into the cathode side. Chloride ions are oxidized at the anode to produce chlorine. Water then splits into both the hydroxyl ions and the hydrogen on the cathode side. The chlorine is then purified by the processes of liquefaction and evaporation [18]. The diaphragm prevents the reaction of the

caustic soda with chlorine. The concentration level of the sodium hydroxide that is formed is low.

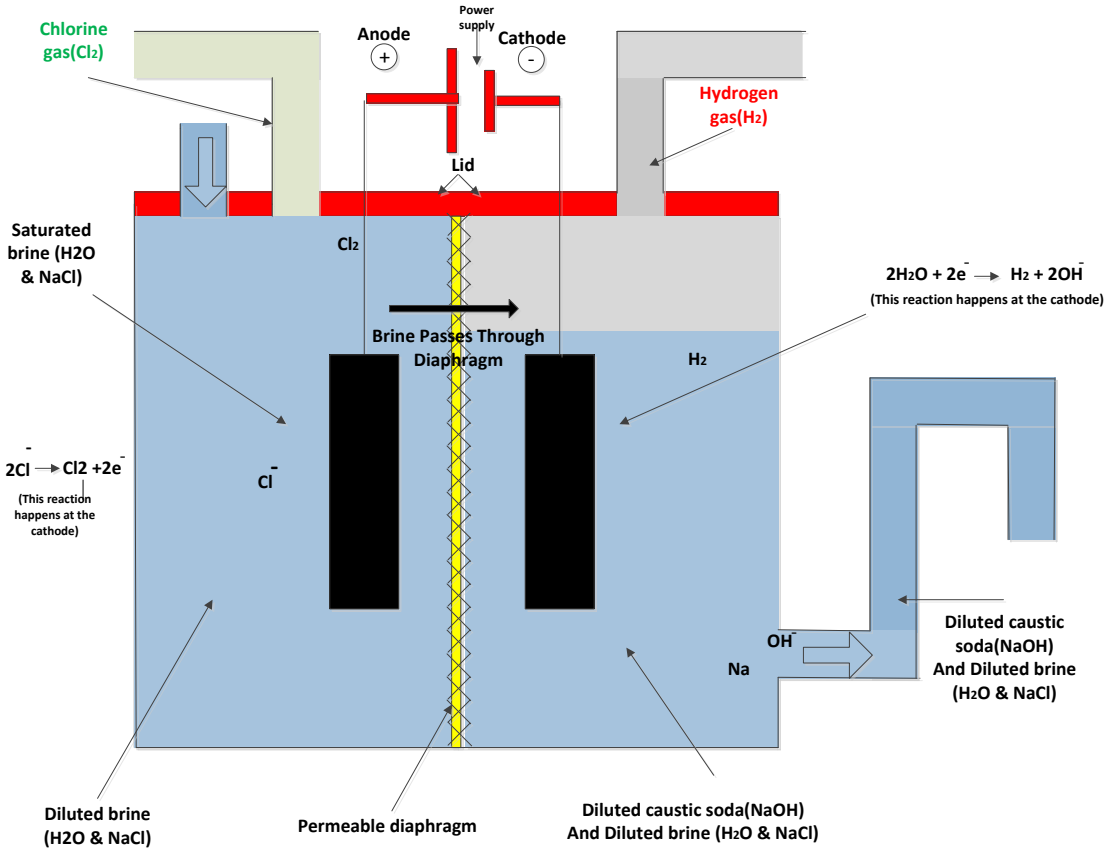

Figure 2.8: Schematic of diaphragm cell [Modified from Ref. 15].

2.4.4 Membrane Cell

The structure of this cell includes an ion-exchange membrane that separates the anode and the cathode. The separator is usually a bi-layer membrane made up of different materials, for example, the perfluorocarboxylic and perfluorosulfonic acid-based films that are sandwiched between the cathode and anode [19]. Saturated brine is then added to the anode side (the anolyte). DC voltage is supplied. Sodium chloride splits into both sodium and chloride ions. Sodium ions are passed through to the cathode side (catholyte) where they form a sodium hydroxide solution. As a result, the chloride ions are oxidised into chlorine gas at the anode. This

gas is then purified and stored. Hydrogen gas and hydroxide ions are formed at the cathode. Figure 2.9 shows the schematic of a diaphragm cell.

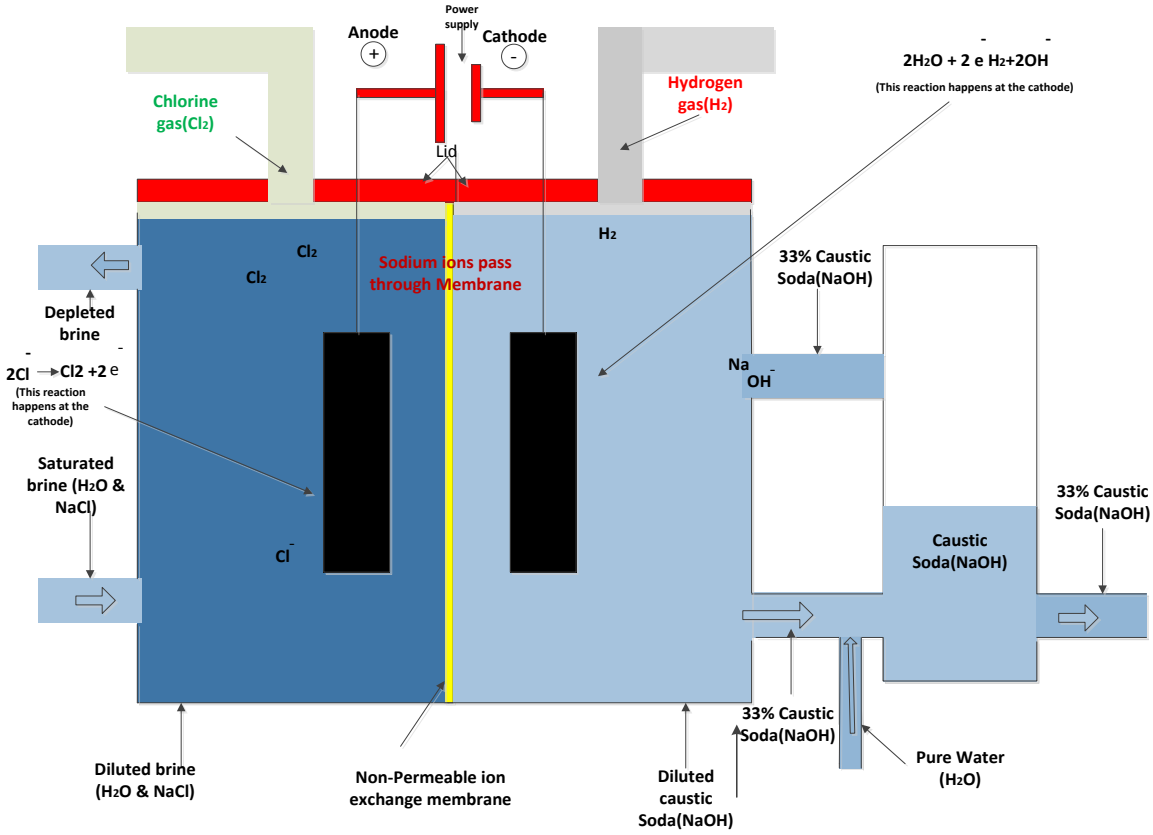

Figure 2.9: Membrane cell schematic [Modified from Ref. 15].

2.4.5 Industrial Uses of Chloralkali Products

There are currently hundreds of industries around the world using chloralkali processes. These industries produce and use approximately 140 billion pounds of chlorine (Cl_2) and sodium hydroxide (NaOH) annually. Chlorine is currently the fourth most highly produced chemical in the USA. Chlorine has a variety of industrial applications, as illustrated in Figure 2.10. Hydrogen is a clean- energy carrier with a high-heat of combustion (-286 kJ/mol). Figure 2.11 shows the various uses of hydrogen.

Sodium Hydroxide (NaOH) is a strong base and has a number of applications in chemical industries. Industrial uses of NaOH are shown in Figure 2.12.

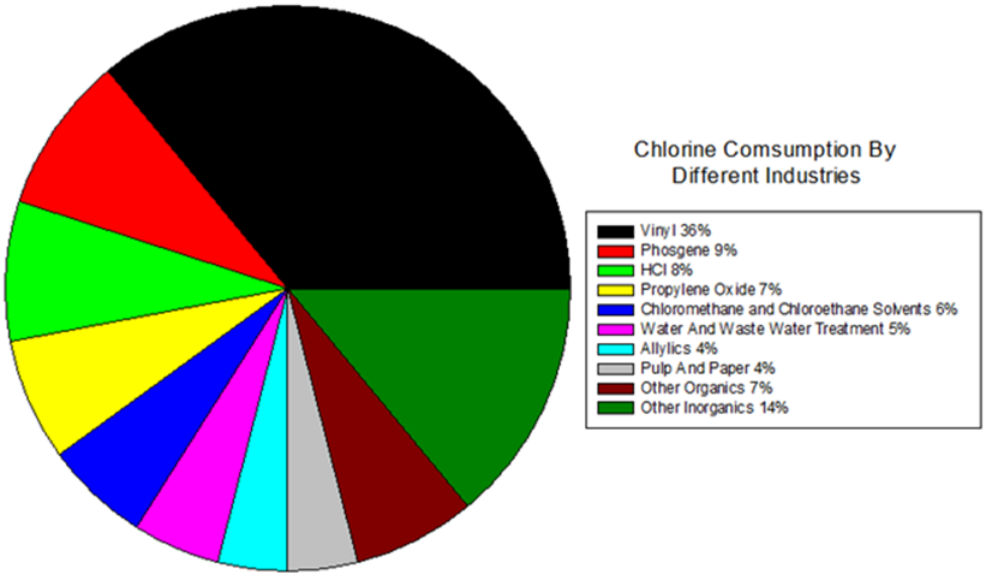

Figure 2.10: Chlorine consumption by different industries [Data from 15].

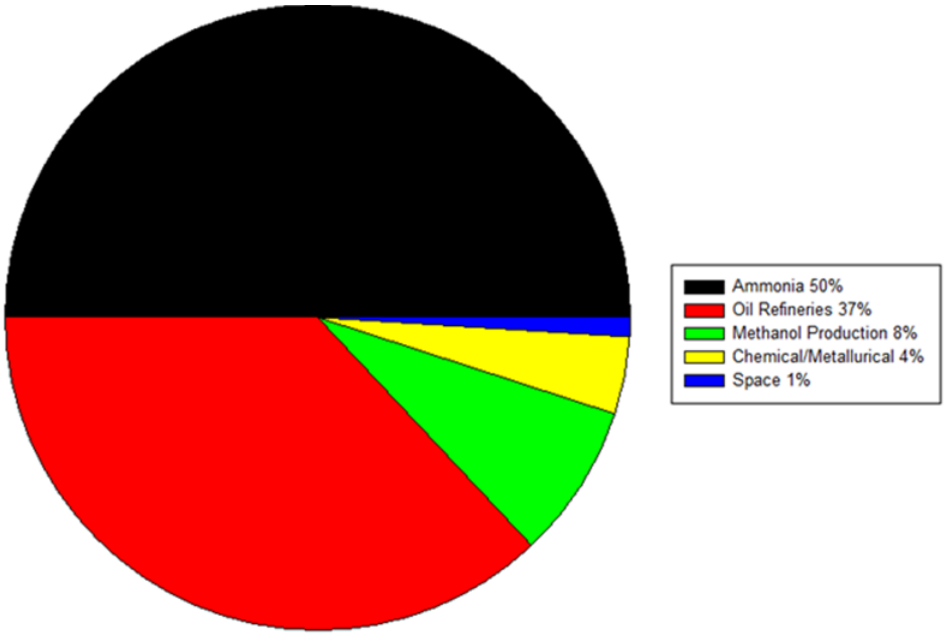

Figure 2.11: Uses of hydrogen gas [Data from 15].

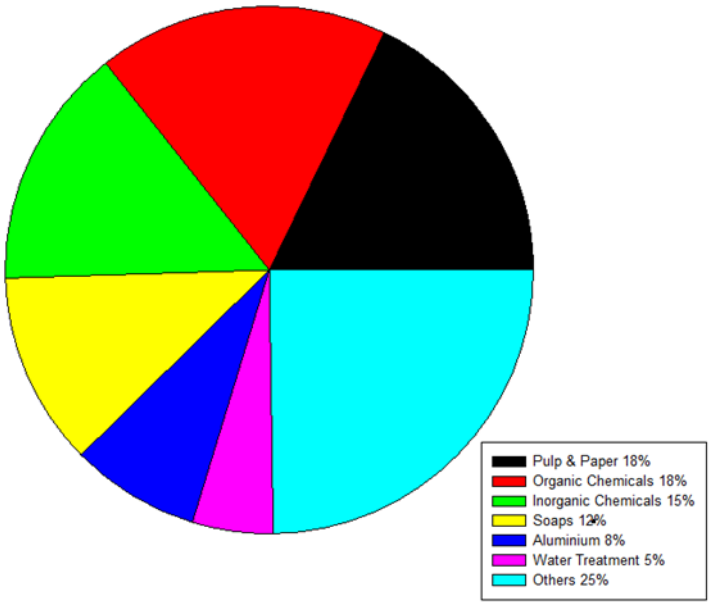

Figure 2.12: Uses of sodium hydroxide [Data from 15].

2.4.6 Comparison of Energy Costs of Three Common Methods

Table 2.1 provides a comparison between the different chloralkali technologies based on energy consumption. Compared to mercury and diaphragm cell, membrane cell technology requires least amount of energy input. Also, it does not require any mercury in processing and hence it is also safe and environmentally friendly. It provides maximum purity of hydrogen, chlorine and sodium hydroxide.

Figure 2.13 shows the cell voltage versus current density for different chloralkali technologies. The trends are linear for all technologies. The required cell voltage increases with increase in current density. Membrane cell requires the less voltage compared to diaphragm and mercy cell. This also results in higher efficiency in case of membrane cell. Further details about the energy requirement will be discussed in subsequent sections.

Table 2.1: Comparison of energy requirements for different chloralkali technologies.

	Mercury cell	**Diaphragm cell**	**Membrane cell**
Cell voltage, V	-4.4	-3.45	-2.95
Current density, A	1.0	0.2	0.4
Current efficiency for Cl_2, %	97	96	98.5
Energy consumption, kWh, per ton of NaOH a) Electrolysis only b) Electrolysis plus evaporation to 50% NaOH	 3150 3150	 2550 3260	 2400 2520
Purity Cl_2, %	99.2	98	99.3
Purity H_2, %	99.9	99.9	99.2
O_2 in Cl_2	0.1	1.2	0.3
Cl^- in 50% NaOH, %	0.003	1.1.20	0.005
Sodium hydroxide concentration prior to evaporation, %	50	12	35
Mercury pollution considerations	Yes	No	No
Requirement for brine purification	Some	More stringent	Very extensive
Production rate per single cell, tons NaOH per year	5000	1000	100
Land area for plant of 10^5 tons NaOH per year, m^2	3000	5300	2700

Data from [15].

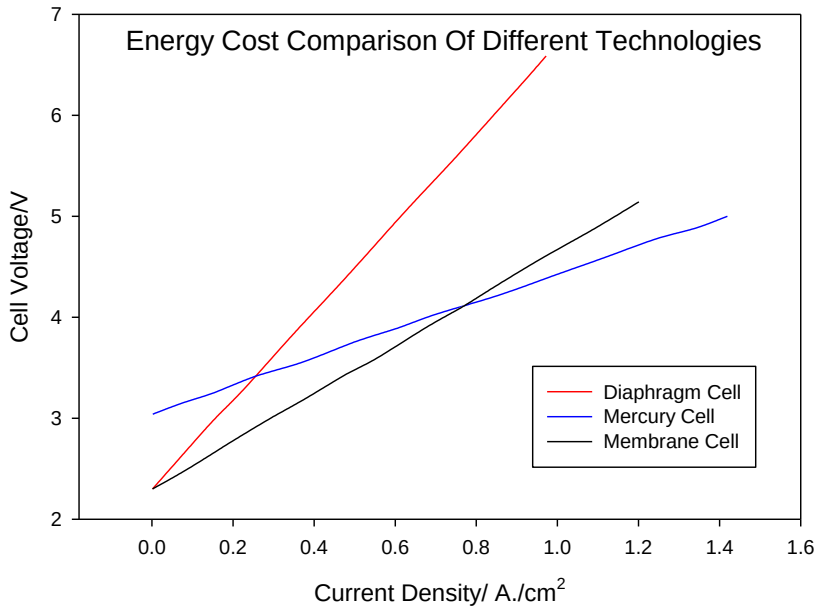

Figure 2.13: Cell voltage versus current density plots for 3 types of chloralkali cells [Data from 15].

2.5 Analysis of Variance (ANOVA)

ANOVA represents an analysis of the variations that are present in an experiment. This analysis establishes the hypothesis that the variation in an experiment is not greater than that of normal variation levels, in terms of individual characteristics and errors in measurements [20]. The null hypothesis in ANOVA is such that the means of the groups are equal. The normal-model based ANOVA assumes the independence, normality and homogeneity of the variances of the residuals. ANOVA is a statistical method used to find the statistical significance of the appropriate factors [21]. The ANOVA method consists of four main components.

2.5.1 Sum of Squares (SS)

The total sum of squares of the model is defined as the sum of the squared deviation from the mean based on the effect of an individual term(s), or the interaction between two terms. The sum of the squared deviation that is not explained by the model is also part of the definition [21.22].

$$SS_{Total} = SS_{Model\ terms} + SS_{Residual} \quad (2.11)$$

where $SS_{Residual}$ has two components [23.24],

$$SS_{Residual} = SS_{LOF} + SS_{Pure\ Error} \quad (2.12)$$

Here, SS_{LOF} is the portion of the residual $SS_{Residual}$ which is the result of the model, not fitting the data. It consists of the weighted sum of squared deviations between the mean responses at each factor level, along with the corresponding fitted value. The pure error sum of squares ($SS_{Pure\ Error}$) is a measure of the effect produced by the error associated with repeatability. It also consists of the corrected sum of squares of the repeated observations at each level of input combined with over-all levels of input.

2.5.2 Degrees of Freedom (df)

Degrees of freedom in ANOVA are defined as the minimum number of values required to specify all data points in the sample. N data points require N numbers of degrees of freedom. If the mean of the data is known and there are N data points, then the df is N-1 [20].

The total df for a given model is defined as

$$df_{total} = df_{Model\ Terms} + df_{Residual} \quad (2.13)$$

where each model term has one df and df for the residual, is defined as

$$df_{Residual} = df_{LOF} + df_{Pure\ Error} \quad (2.14)$$

In this case, df_{LOF} differs from the model. Linear models for scattered data have a high df, while quadratic (or cubic models) have less df for the same scattered data. This difference occurs because of an increase in the number of points captured by estimated model regression.

2.5.3 Mean Square Value

This is the ratio of the sum of squares to the degrees of freedom. Mathematically it can be expressed as [21]

$$MM = SS/df \tag{2.15}$$

As with SS and df, it is also calculated for both the error and model term.

2.5.4 F-Value

The F Value for model terms is a test for comparing the variance related to that term with the residual variance. More specifically, it is the ratio between the mean square value for the term and the mean square value for error [25].

$$F_{Term} = \frac{MM_{term}}{MM_{residual}} = \frac{\frac{SS_{term}}{df_{term}}}{\frac{SS_{residual}}{df_{residual}}} \tag{2.16}$$

For a larger F-value, the term is more effective in the model. The F value for LOF (lack of fit), however, should be small; otherwise a large error may become associated with the model term.

2.5.5 p-Value

This factor can be defined as the probability value for the term that is associated with the F value for this term. More specifically, encompasses the probability of having an F Value of this determined size based on the condition that the term did not have an effect on the response. In general, based on a 95% confidence level, a term that has a probability value less than 0.05 would be considered a significant effect. The model term, with probability value greater than 0.10, is generally regarded as not significant [26.27].

2.6 Regression Analysis

Factors involved in the calculation of ANOVA terms can either be quantitative or qualitative [23]. Quantitative factors are also referred to as “categorical factors”, (e.g., different electrodes in the photochemical hydrogen-production process). Qualitative factors are referred to as numerical factors, (e.g., voltage, brine concentration, and electrolyte concentration, brine temperature, etc.), that are present while using certain electrodes. Regression is an empirical equation in which output parameters are calculated in terms of input parameters. Empirical model equations have constants associated with them which can be determined by given output data. The general

approach to calculating these constants (determined from empirical equations) is known as a regression calculation.

In regression calculations, the "least squares" method is used to calculate the coefficients of the terms [24]. If the calculated regression captures all points, then the residual (error) is 1. If calculated regression is not able to capture all points between the input and output, then the residual value will be less than one and an error is then associated with it.

A three-input, linear model can be modeled as

$$y = a_0 + a_1x_1 + a_2x_2 + a_3x_3 \tag{2.17}$$

where y represents the output and x_1, x_2, x_3 represents input. A more complicated linear model which includes the interactions between two terms and the interaction between all three terms is given as follow

$$y = a_0 + a_1x_1 + a_2x_2 + a_3x_3 + a_4x_1x_2 + a_5x_2x_3 + a_6x_3x_1 + a_7x_1x_2x_3 \tag{2.18}$$

Similarly, quadratic and cubic model regressions can also be calculated. Calculations of quadratic and cubic terms will also include square and cubic input terms.

A cubic regression can be calculated as

$$y = a_0 + a_1x_1 + a_2x_2 + a_3x_3 + a_4x_1x_2 + a_5x_2x_3 + a_6x_3x_1 + a_7x_1x_2x_3 + a_9x_2^2 + a_{10}x_3^2 + a_{11}x_1^2x_2 + a_{12}x_2^2x_3 + a_{13}x_3^2x_1 + a_{14}x_1^2x_1 + a_{15}x_2^2x_1 + a_{16}x_3^2x_2 + a_{17}x_1^3 + a_{18}x_2^3 + a_{19}x_3^3 \tag{2.19}$$

In general, by adding more terms, one can improve the lack of fit (residual). As a result, however, the process is more complex.

2.7 Response Surface Methodology (RSM)

The Response surface methodology is treated as a useful method by which interactions between two input variables (and their mutual effects on the output), can be determined. The results are presented in terms of contours graphs, whereby two inputs will be placed on the X and Y axes.

The output is positioned on the Z-axis [28-29]. Contour lines connect the points with the same output value. For this case, more than two input interactions and the response surface can be found between different inputs, by fixing the remaining inputs. Consider the three input variable (x_1, x_2, x_3) process mentioned above. The response surface can be plotted for three different combinations of inputs. These combinations include $(x_1, x_2, y), (x_1, x_3, y)$ and(x_2, x_3, y). While plotting a response surface between(x_1, x_2), the other input x_3 acts as a constant [82].

2.8 Design of Experiments - Factorial Design (DOE)

Multi-variables occur in most experimental processes. For example, in the electrolysis of brine, one may study voltage, brine concentration, and electrolyte concentration, brine temperature, etc. Factorial design includes variations of these variables at different levels [28]. The number of experiments in factorial design depends upon the level of each variable.

By using factorial design, one is able to:

i. Vary individual input parameter(s) with different combinations of other input parameters.
ii. Apply ANOVA on a factorial design, in order to find the effect of individual input parameter(s) on an output. Use a similar approach to find the interaction between two input parameters and their mutual effect on the output response.
iii. Determine optimum conditions for controllable input, by keeping in view the uncontrollable inputs.

Thus, in short, the DOE is used to optimize the process for a best possible output.

2.9 Optimization

Optimizing a process is an important task, in order to attain the best possible performance (in the most economical way). There are different methods and techniques for optimizing different types of problems. The focus of present study is to perform optimization using a commercially available tool known as “Design Expert”. Design Expert uses an optimization method developed by Derringer and Suich. The objective function in this method is known as the “desirability factor”. The desirability factor ranges from zero to one for any given response. A value of one

represents the ideal case. A value of zero indicates that one or more responses fall outside desirable limits. The cumulative desirability factor is based on the function of desirability values of an individual response, along with the weight assigned to each response. It can be written as

$$D = (d_1^{X1} * d_2^{X2} * d_3^{X3} \dots\dots\dots\dots d_N^{Xn})^{\frac{1}{\Sigma Xn}} = \left(\prod_{i=1}^{N} d_i^{Xi}\right)^{\frac{1}{\Sigma XN}} \quad (2.20)$$

where "d" represents the desirability value for a response and "X" represents the importance given to the desirability value of response d. If equal importance is given to all the responses, than the desirability factor can be written as

$$D = (d_1 d_2 d_3 \dots\dots\dots\dots d_N)^{\frac{1}{N}} = \left(\prod_{i=1}^{N} d_i\right)^{\frac{1}{N}} \quad (2.21)$$

where "N" represents the total number of responses used in optimization. Optimization, itself, is generally performed in order to reach one of two different goals: i) maximize the output and ii) minimize the output.

For the first objective: If the goal is to maximize the output, than the desirability function for the response can be written as

$d_i = 0$ if response ≤ low value

$d_i = \left(\frac{Y_i - Y_L}{Y_H - Y_L}\right)^{w_i}$ $0 \le d_i \le 1$ as response varies from low to high

$d_i = 1$ if response ≥ high value

It should be noted that d_i represents the desirability for the i_{th} response, Y_i represents the response value, Y_L represents the lowest response value, Y_H represents the highest response value and w_i represents the weight function. If $w_i = 1$, than d_i will vary in a linear fashion between 0 and 1. Weights greater than 1 (In stat-ease®, maximum weight is 10), give more emphasis to the goal. Weights less than 1 (In stat-ease®, minimum weight is 0.1), give less emphasis to the goal.

For the second objective: If the goal is to minimize the output, than the desirability function for the response can be written as

$d_i = 0$ if response ≥ high value

$d_i = \left(\frac{Y_i - Y_L}{Y_H - Y_L}\right)^{w_i}$ $0 \geq d_i \geq 1$ as response varies from low to high

$d_i = 1$ if response ≤ low value

In summary, the design expert approach combines the individual desirability's of each response into a single number and then searches for the greatest overall desirability.

Chapter 3

Literature Review

3.1 Introduction

This chapter focuses on literature review about hydrogen production by means of PV electrolysis, photo catalytic hydrogen production and different chloralkali processes.

3.2 PV-Electrolysis Systems for Hydrogen Production

In electrolysis systems generated for hydrogen production, a PV solar cell is used to generate electricity. This electricity is then sent to a commercial-type water electrolyzer**.** Alternatively, a semiconductor PV cell can be immersed in an aqueous solution**.** In terms of commercial use, single-crystal Si solar cells generally have efficiency between 12-16%. On the other hand, water electrolysis units generally have approximately 85% electrical to hydrogen efficiency. In addition to these Figures, combined PV/electrolyzer systems (with commercially available components), have approximately 10% efficiency levels [30]. The system shown in Figure 3.1 is a system that reduces the costs and design difficulties which are often related to separate construction and direct connection of solar and electromechanical cells. In this system, electrodes are made up of single or multiple semiconductor p-n junctions that are irradiated while they are within the cell. This equipment can be built with an appropriate encapsulation of the semiconductors, which provides protection from the aqueous environment. The fact that hydrogen generation through PV-electrolysis units is very costly means that a maximum-power output (with changing solar insulation and temperature) should be maintained [31]. As a result,

commercial systems would have an integration of PV arrays with maximum-power point tracking devices (which is illustrated in Figure 3.2). This condition is described with average power conversion efficiency as a function of the partial load [31, 32].

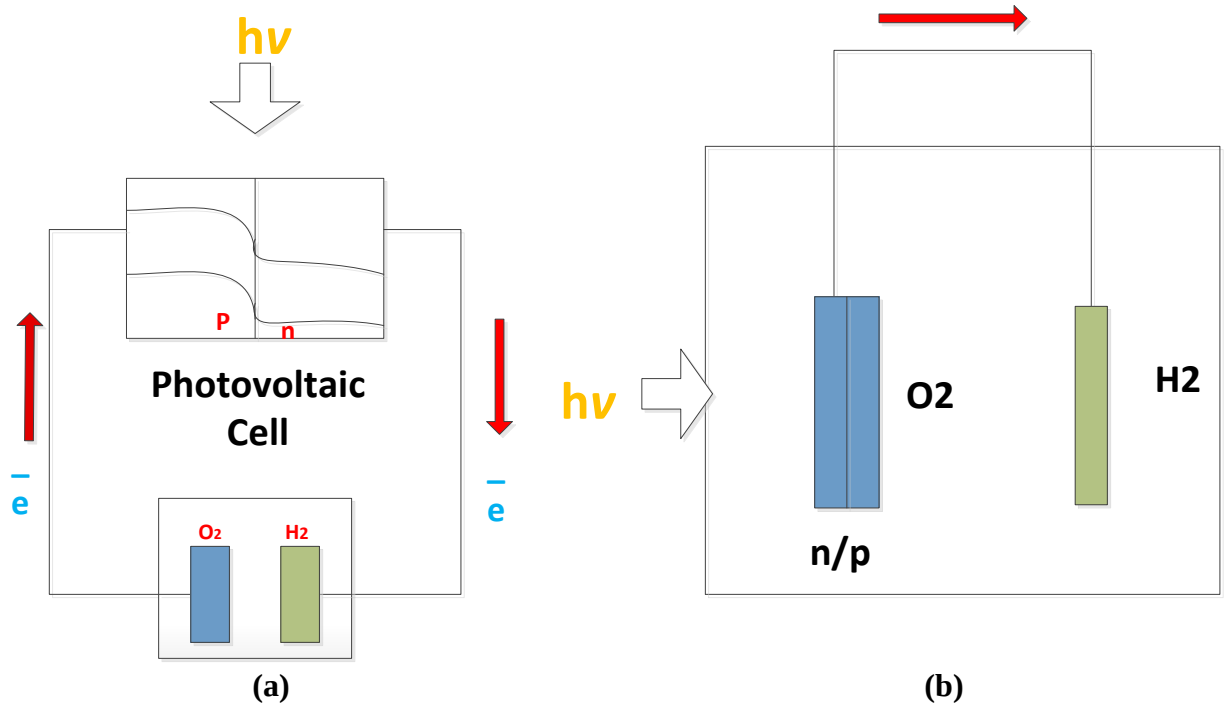

Figure 3.1: Schematic diagram for PV-electrolysis system for solar water splitting a) Electricity produced from PV cell running water electrolysis. b) PV assisted cell with semiconductor p/n junction as one electrode is dipped (Modified from [1]).

To generate solar hydrogen production, some countries such as Germany, Saudi Arabia, Brazil, Spain, Egypt, India, and Switzerland have selected PV-electrolysis systems. For example, a photovoltaic-electrolysis hydrogen production plant, near Riyadh, is owned by a German and Saudi Arabian cooperative [31-33]. In this plant, alkaline water-splitting is used with a mixture of water and potassium hydroxide. At the start up, conversion efficiency is found to be 13 -15% as related to the ambient temperature. Hydrogen that is produced through means of electrolysis consists of small amounts of oxygen, nitrogen and carbon dioxide (i.e. due to the impurities in water). This is especially true in instances whereby KOH vapours are present in the system [34, 35].

Ohmari et al. [36] have used RF magnetron sputtered p-type c-Si/n-type a-Si:H thin film solar cell for PV water electrolysis. Results show that this system would produce 3% of the conversion efficiency from solar to hydrogen states. Similarly, Currao et al. [37] have used an amorphous silicon solar cell with a combining photo -electrochemical cell to produce water photo-electrolyses. In that circumstance, AgCl photoanode and Pt cathode are used. In this aforementioned design, light goes to the AgCl photoanode and amorphous silicon solar cell, creating photo-electrochemical water splitting.

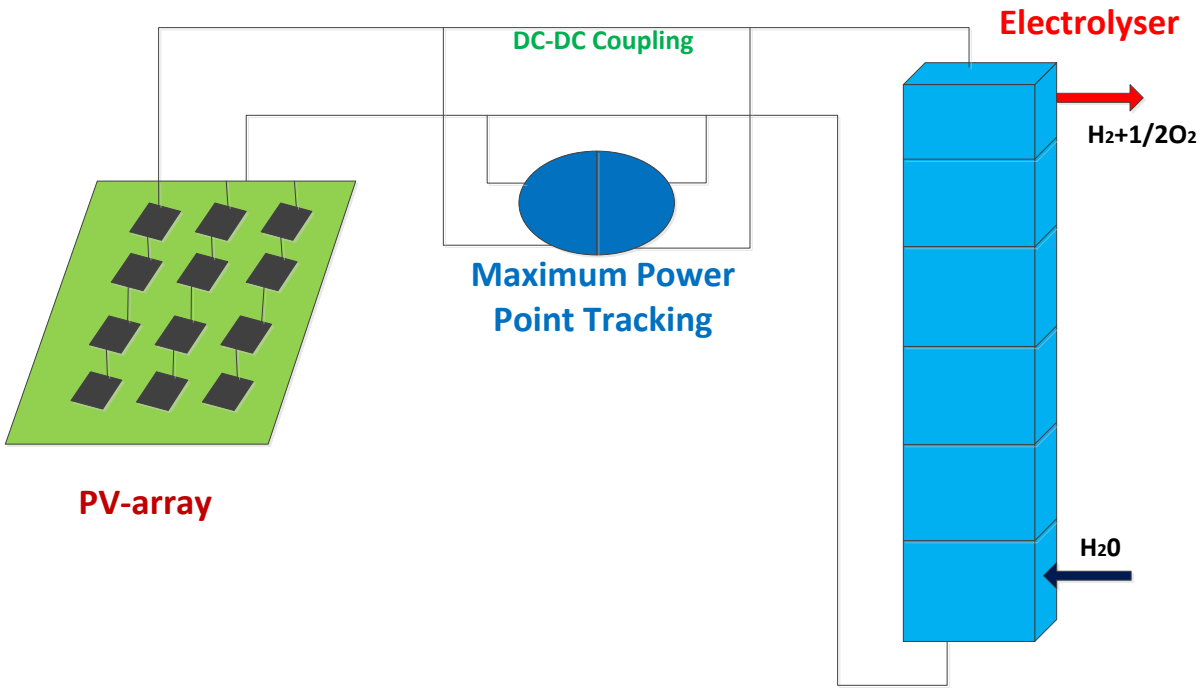

Figure 3.2: Schematic Diagram of PV-electrolysis system pilot plant (Modified from [1, 4, 6])

3.3 Multi-junction PV Cells for Hydrogen Production

Kocha et al. [38] have proposed a PV tandem cell which consists of GAINP2 homo junction grown epitaxially through a GaAs homo junction. This junction is connected through a transparent GaAs tunnel diode. This tandem cell is equal to two solar cells connected in a series. The $GAINP_2$ p/n junction and band gap of 1.83 eV absorb the visible light, while the GaAs p/n junction and bandgap of 1.42 eV absorb in the near-infrared region. After redesigning the front surface by using a Pt colloid, photo corrosion is prevented. Photo-electrochemical water

decomposition was ultimately achieved in 1M H_2SO_4. Stoichiometry of hydrogen and oxygen from the lighted surface was recorded to be 2.8:1. After eight hours had elapsed, oxygen had stopped reacting. In this particular case, the efficiency is recorded to be 4.10% for water splitting.

Khaselev and Turner [39] have proposed a newly designed direct water-splitting system, which is shown in Figure 3.3. The integrated monolithic photovoltaic-photo electrochemical device includes 4.0 μm thick top layers that are connected in series through a tunnel junction. This junction connects to a GaAs p/n junction bottom cell of a GaAs Surface. This system is different than a standard solid state tandem cell (in which case a PEC schottky – type junction is replaced with p/n junction). Electrons move toward the illuminated surface, while holes move toward the ohmic contact. In order to provide higher efficiency and better functioning of the device, the GaAs solar cell has to provide enough voltage. Thus, a mismatch between the band edges of the $GaInP_2$ and the water redox reaction will be sustained. Additionally, voltage should be provided in order to prevent voltage loss from causing from H_2 and O_2 reactions. Ultimately, total photo voltage output has to carry the thermodynamics of water splitting, polarization losses of anodic and cathodic processes, and the potential current-resistance drop in the bulk of the electrolyte. At the semiconductor electrode, two reasons have been noted for hydrogen production; one is low overvoltage loss for the H_2 evolution reaction, while the other reason is a result of the semiconductor surface being catholically protected [38, 39].

The efficiencies discussed with several monolithic, multi-junction integrated PV/electrolysis arrangements can be observed in Table 3.1. With a tandem arrangement, the efficiency rate from solar to hydrogen conversion is observed to be 16%. The efficiency rate of triple junction conversion is found to be 7.8%. [40]. In terms of the low-current density conditions of the a-Si system, the efficiency rate is observed to be 86%. Litch et al. [41] have proposed a new design that is essentially a multi-junction photo electrolysis cell water-splitting system that provides a 18.3% level of efficiency. Bipolar type semiconductors produce an open circuit voltage of 1.30V and maximum of 1.57V.

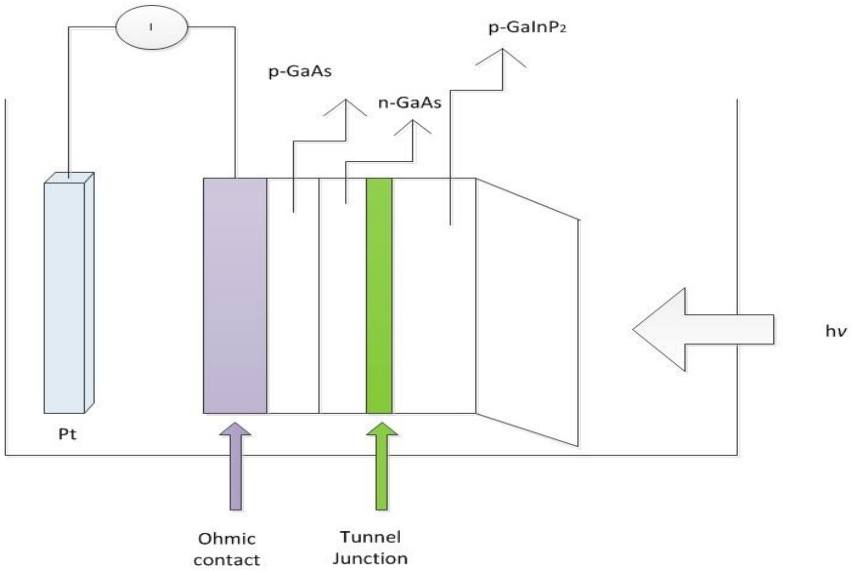

Figure 3.3: Schematic diagram for a Photo electrochemical-PV device (Modified from [1]).

The predicted dual-band gap photo electrolysis efficiency levels for solar water-splitting can range from 16% [14] to 10-18% [43]. Based on the findings of Licht et al. [41 - 44], however, predicted efficiency levels are lower than the actual water-splitting efficiency level. This condition is caused by two factors. The first factor is caused by underestimating the experimental optical energy conversion that is achieved by contemporary devices. The other factor is the caused by the underestimation of the achievable redox conversion of water to oxygen and hydrogen. Table 1 shows that optical-energy conversion values efficiency levels are higher than 20%. Additionally, all cells that are discussed in Table 1 show an open circuit photo potential that is greater than the minimum potential required to be able to split water. The predicted maximum efficiency levels of the photo electrolysis values are given in Table 3.1 as well. This approach has been provided by observing photo-efficiency values of several dual bandgap sensitizers. Selecting multiple band gaps with a combined maximum power point voltage that is tuned to the electrolysis potential of water is still problematic [45, 46].

Table 3.1: Predicted and measured photo electrolysis efficiencies.

Photovoltaics	**Light Level**	**η photo (measured)**	**η photoelectrolysis Predicted maximum**	**η photoelectrolysis Experimental**
GaInP/GaAs	1 Sun	30.3%	27.29%	-
GaInP/GaAs	180 Sun	30.2%	27.29%	-
GaAs/Si	350Sun	29.6%	27.28%	-
InP/GaInAs	50 Sun	31.8%	29-30%	-
GaInP2/GaAs;p,n/p	11 Sun	-	-	12.4%
GaInP2/GaAs; n/p, n/p	1 Sun	28.5%	-	16.5%
p-in a-Si (triple junction)	1 Sun	9.0%	-	7.8%
AlGaAs/Si	1 Sun	21.2%	19-20%	18.3%
p-i-n a-Si (triple junction)1	1 Sun	-	-	2.5%
n-i-p a-Si (triple junction)	1 Sun	-	-	5.6%
CdTe:CIGS2	1 Sun	16.5%; 18.4%	-	6.77%

one-chip PV device dipped into electrolyte. Data from ref [1]

Under 100 mW/cm^2 of light intensity, 3% of solar to hydrogen conversion efficiency is observed for a single chip photovoltaic water electrolysis device [47]. The p-i-n a-Si solar cell was collected at the bottom side of SnO_2 by plasma CVD. Co-Mo and Fe-Ni-O electrodes were arranged. After these electrodes were ready, they were held to the solar cell with conducting Ag paste and then dipped into the KOH solution for testing. A robust photo- electrochemical device through a triple junction n-i-p a-Si:H solar cell is covered with a fluorine doped tin oxide layer. This design is introduced by Kelly and Gibson [48]. This device is designed for water splitting in a way that prevents corrosion. The outer p-type layer is then contacted with the KOH electrolyte.

3.4 Multiple-Band PV Cells for Hydrogen Production

This method of hydrogen production differs from multi-junction thin film PV tandem cells because the PV cells, themselves, are developed upon one and other [49, 50]. In this sense, PV cells that are developed on a transparent conducting layer are attached in series. Figure 3.4 shows PEC arrangements in detail [51]. This illustration includes the use of PV cells, RuS_2 Photo anode (for oxygen production) and a platinum foil cathode for hydrogen production.

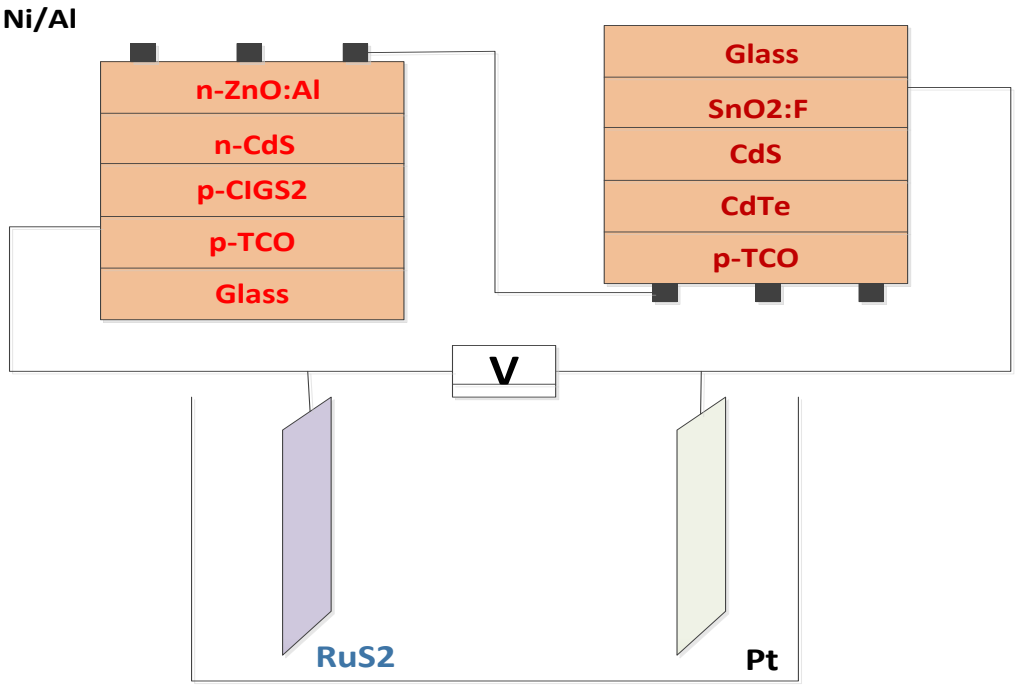

Figure 3.4: Schematic Diagram of Photo electrochemical setup including two PV cells, RuS2 photoanode for oxygen reaction, and Pt cathode for Hydrogen reaction (Modified from [1, 23].

3.5 Dye Sensitized Solar Cell for Solar Hydrogen Production

In this type of design, two cells are connected in series. The first cell absorbs the Ultraviolet light and blue light by utilizing thin Nano-crystalline metal oxide films for the production of electron-hole pairs. These electron-hole pairs are produced by utilizing the valance band holes that are used for oxidizing the water. The second cell absorbs light that is sent through the first cell. This process occurs in the green to red area of the solar spectrum. To generate hydrogen, electrons are

photo generated. These two cells work in the same manner analogous to the Z-scheme of photosynthesis, which can aid in water splitting. As a result of this system, solar to hydrogen conversion efficiency levels are observed to be 6% [52], which is shown in Figure 3.5.

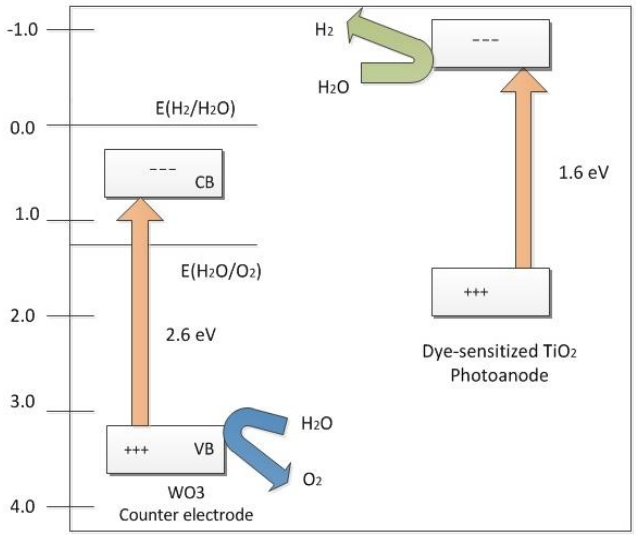

Figure 3.5: DSSC-based tandem cell for solar hydrogen production (Modified from [1, 23].

3.6 Photocatalytic Hydrogen Production

Past research has focused on the development of two half-cell reactions, separated by a membrane that uses a photo catalyst and sacrificial or non-sacrificial electron donor. A supramolecular complex results from utilizing small units in a photocatalytic hydrogen production scheme. The end result consists of high turnover rates and numerical Figures that ultimately create an area of interest [53]. Each unit in the supramolecule is responsible for a different function [54]. A supramolecular catalyst for solar hydrogen production, for example, usually consists of three different units [55]. These units include terminal ligands (also called light absorbing units), bridging ligands (also called electron relays) and electron collectors [56, 57]. The terminal ligand receives an electron from an electron donor material [58]. This received electron is then transferred to the electron collector using a bridging ligand [59]. Water is introduced at the electron collection center where it is reduced into the hydrogen gas and hydroxyl ions [60].

Ohta [61] has studied the photochemical production of hydrogen from water using solar radiation. In their studies, they considered the catalytic and energetic requirements of the photochemical and the electron transfer spectra of the catalyst ions to be of great importance [61]. Buehler et al. [62] have also photochemical hydrogen production with the use of cadmium sulfide suspensions. The study illustrates that by using platinum deposition on microcrystals of CdS powders, active photocatalysts for photochemical hydrogen production can be prepared [62]. Reber [63] has studied photochemical hydrogen production with the platinized suspensions of cadmium sulfide and cadmium zinc sulfide modified by silver sulfide. The studies show that the effective hydrogen production can be achieved by irradiating suspensions for platinized CdS in the solutions of the sulphur or sulfide ions [63]. Sakai et al. [64] have studied the homogeneous catalysis of the platinum (ll) complexes in photochemical hydrogen production from water. This research shows that the catalytic efficiency of the Pt catalyst is dependent upon a number of different factors, namely metal–metal interactions, coordination environments, steric factors, electron-acceptor capability, and photosensitizing abilities [64]. Sakai et al. [65] have studied the homogenous catalysis of the mixed-valent octa nuclear platinum complexes in photochemical hydrogen production from water. They have used an acetimidate-bridged mixed-valent octa nuclear platinum complex as a hydrogen producing catalyst in a photochemical model system containing EDTA as a sacrificial electron donor [65].

Akkerman et al. [66] have studied photo-biological hydrogen production (photochemical efficiency and bioreactor design). The study shows that biological production hydrogen can be achieved by means of photoautotrophic or photoheterotrophic organisms [66]. Darwent et al. [67] have studied photochemical hydrogen production using cadmium sulfide suspensions in aerated water. The results show that suspensions of CdS particles sensitize the photo-reduction of water by the cysteine and ethylenediamine-tetra-acetic acid with a quantum yield of 0.04 mol/ Einstein [67]. Striech et al. [68] have studied high-turnover photochemical hydrogen production system that is catalyzed by a model complex of the hydrogenase active site. The work shows that hydrogen has the potential to replace fossil fuels as the energy carrier of the future, particularly if it is produced in a renewable way (i.e., by means of photochemical water splitting).

Amao et al. [69] have studied a highly efficient photochemical hydrogen production system using zinc porphyrin and hydrogenase in the CTAB micellar system. The results of the study show that the effective photo-reduction of the mythylviologen and effective hydrogen production with hydrogenase were accomplished in the presence of a CTAB micellar system. The hydrogen production was also successful due to the optimization of the reaction condition [69]. Shamindri et al. [70] have studied photochemical hydrogen production from water using a new photo catalyst [$\{(bpy)_2Ru(dpp)\}_2RhBr_2](PF_6)_5\}$]. Research results show that the new photo catalyst goes through an excited state of intra-molecular electron transfer, allowing the photo-initiated electron collection on the reactive rhodium center to generate the Rh complex. This new complex leads to the photocatalytic production of hydrogen from water.

Zhou et al. [71] have studied artificial inorganic leaves in an attempt to discover efficient photochemical hydrogen production that is inspired by natural photosynthesis. The study demonstrates the use of artificial inorganic leaves composed of Pt/N-doped TiO_2 to achieve efficient water splitting under UV light. The visible light irradiation in the presence of sacrificial reagents uses natural leaves as the biotemplates. Li et al. [72] have studied photochemical hydrogen production that is catalyzed by the polypyridyl ruthenium-cobaloxime hetrobinuclear complexes with different bridges. They prepared hetero bi-nuclear complexes, in which the polypyridyl ruthenium photosensitizer and the cobaloxime catalyst are connected either by the conjugated or unconjugated bridges. Both of these complexes are used as the photo catalyst for hydrogen generation [72]. Reber et al. [73] have studied photochemical hydrogen production with the use of zinc sulfide suspensions. The study shows that good hydrogen production can be achieved by irradiating suspensions of the ZnS in the various electrolyte solutions (Sz-,SO:-, S20:-, H2P0) [73]. Xing et al. [74] have studied the band structure controlled solid solution of the Cd-ZnS photo catalyst for hydrogen production by water splitting. The work shows that the hydrogen production using Cd ZnS was achieved by splitting the water photocatalytically under the ultraviolet and visible light irradiation in an inner-irradiation reactor [74]. Amouyal [75] has studied photochemical hydrogen production and oxygen from water. Results show that hydrogen and oxygen are generated from the water by way of the visible region of the incident radiation [75].

Elvington et al. [76] have studied the photocatalytic hydrogen production from water employing a Ru, Rh, Ru molecular device for the photoinitiated electron collection. The study reflects the fact that the molecular devices for the photoinitiated electron collection (at a metal center), can photocatalytically produce hydrogen [76]. Hallenbeck et al. [77] have studied biological hydrogen production, namely the fundamentals and limiting processes. The work shows that the low-energy content of solar irradiation leads to a photosynthetic process that operates at high conversion efficiency levels and places restrictions on photo bioreactor economics. Also the dark fermentation of the biomass (or the waste), presents an alternative way to biologically produce hydrogen [27]. Kapdan et al. [78] have studied bio-hydrogen production from waste materials. Their research shows that various types of methods can be used to produce hydrogen because of its increasing demand. Some of these methods include: bio-photolysis of water by using algae, dark and photo-fermentation processes, waste (such as cellulose and starch that contain agricultural and food industry waste), and some food industry waste water which can be used for the production of hydrogen [78].

Brewer [79] has developed a new supramolecular catalyst for hydrogen production by using a photochemical process derived from water. Their catalyst contains Ru and Rh metals. They have used Ru in the terminal ligand, while Rh is bonded in the electron collector [80]. They have used various terminal ligands in their supramolecular catalyst, including 2,2-bipyridine (bpy), 1,10-phenanthroline(Phen) and 2,2',6',2''-terpyridine(tpy) [79].They also used two different bridging ligands, namely 2,3'-bis(2-pyridyl) pyrazine (dpp) and 2,2'-bipyrimidine (bpm) [80]. The chemical structure of the terminal and bridging ligands are shown in Figure 3.6. They have used the dimethylanyline (DMA) as a sacrificial electron-donor and dimethylformamide (DMF) and acetonitrile (CH_3CN) as the solvent [81]. Some of the catalysts prepared by Brewer et al. [79-80] are given in Table 3.2, while their chemical structures are shown in Figures 3.7 to 3.10.

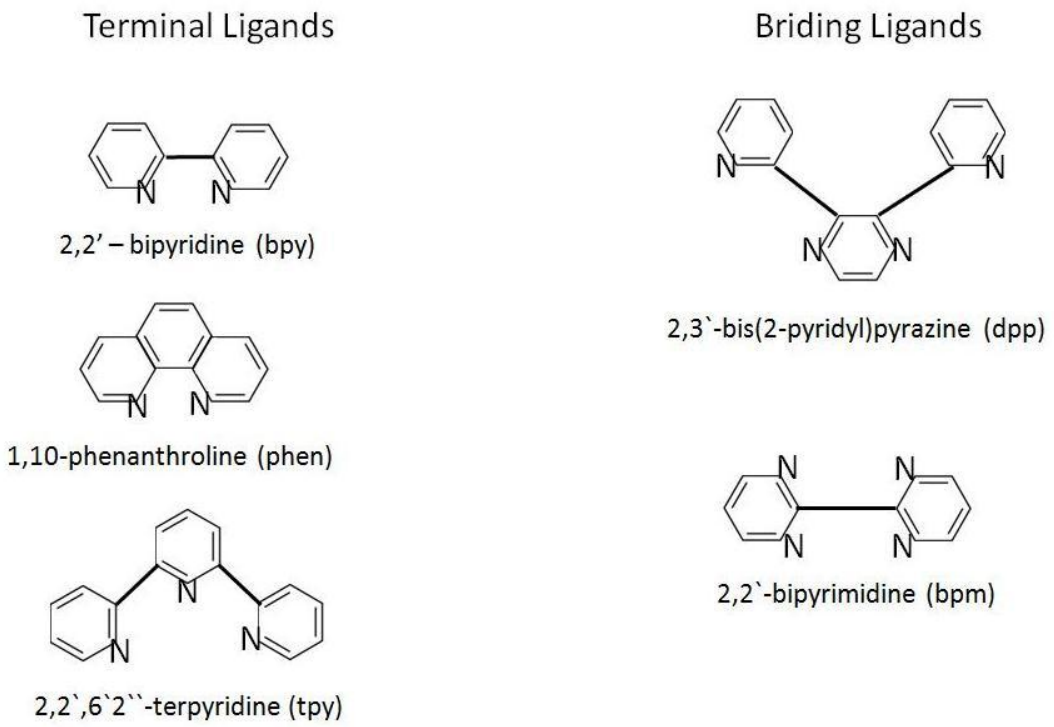

Figure 3.6: Chemical structure of terminal and bridging ligands by Brewer et al. [79-81].

Table 3.2: Photocatalytic hydrogen production from water using Ru, Rh, Ru photo-catalysts under various experimental parameters.

Complex [a]	[Complex] [μM]	[DMA] [M]	Solvent	H_2 [mL]	H_2 [μmol]	TON[b]	Max. Φ
$[\{(phen)_2Ru(dpp)\}_2RhBr_2]^{5+}$	65	1.5	CH_3CN	0.25±0.03	10±1	36±4	0.006
$[\{(Ph_2phen)_2Ru(dpp)\}_2RhCl_2]^{5+}$	65	1.5	CH_3CN	1.1±0.1	44±3	150±10	0.013
$[\{(Ph_2phen)_2Ru(dpp)\}_2RhBr_2]^{5+}$	65	1.5	CH_3CN	1.4±0.1	58±4	200±10	0.022
$[\{(bpy)_2Ru(dpp)\}_2RhBr_2]^{5+[c,d]}$	120	3.1	DMF	20	810	270	0.023
$[\{(phen)_2Ru(dpp)\}_2RhBr_2]^{5+[c]}$	120	3.1	DMF	4.5	180	62	0.008
$[\{(Ph_2phen)_2Ru(dpp)\}_2RhBr_2]^{5+[c]}$	120	3.1	DMF	44±6 (63)	1640±340 (2400)	610±90 (870)	0.073

In Table 3.1, [a] results correspond to the 20 h photolysis time using a 470 nm LED light source (light flux = $2.36*10^{19}$ photons/min; reaction solution volume = 4.5 mL; head space volume = 15.2 mL). The [b] values correspond to the turnovers per Rh catalytic center. The [c] experiment was performed using an increased reaction solution volume (24.8 mL), head space volume (25.0 mL), and light flux ($6.27*10^{19}$ photons/min). Values correspond to the 20 h photolysis time, unless otherwise stated. The values in parenthesis correspond to the 46 h photolysis time. (Note: [d] refers to reference [82]).

The increase in the efficiency level of the molecule, when changing the centered chlorine into bromine, is not well documented in the literature. As mentioned earlier, the terminal ligand (i.e., bpy, Phen and 2tpy) accepts an electron from a sacrificial electron donor (i.e. DMA) in a solvent (i.e. DMF, CH_3CN) when the photons of a particular wavelength (i.e. 470 nm of light) strikes it. This accepted electron is transferred into the Rh centered electron collector center where water is introduced. The water is reduced into hydrogen gas and hydroxyl ions. Over time, the concentration of the hydroxyl ions increases in the solution. These hydroxyl ions needed to be neutralized. Figure 3.11 illustrates the hydrogen production process that uses one of the Brewer catalysts.

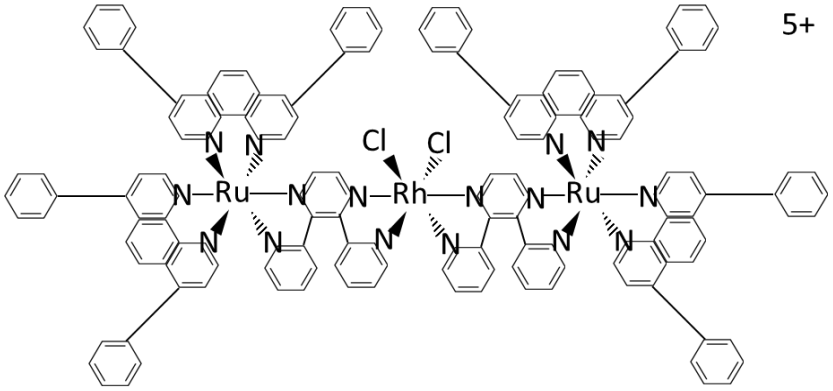

Figure 3.7: Chemical structure of a supramolecular structure $[\{(Ph_2phen)_2Ru(dpp)\}_2RhCl_2]^{+5}$ used in H_2 production [79-81].

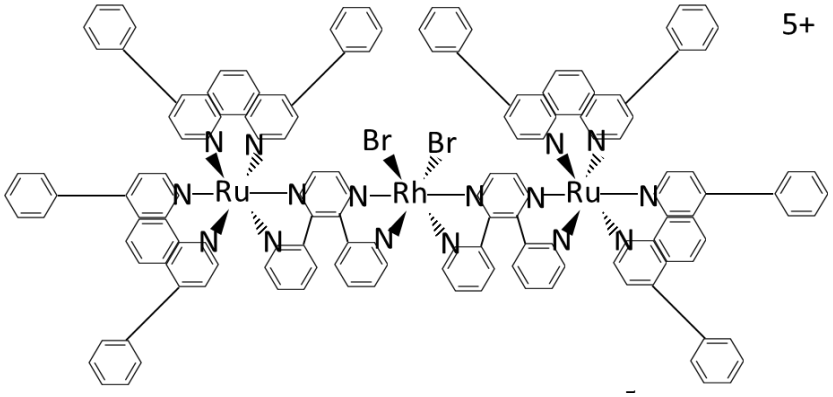

Figure 3.8: Chemical structure of a supramolecular structure $[\{(Ph_2phen)_2Ru(dpp)\}_2RhBr_2]^{+5}$ used in H_2 production [79-81].

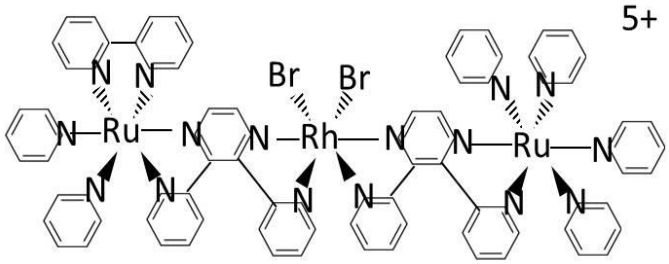

Figure 3.9: Chemical structure of a supramolecular structure $[\{(bpy)_2Ru(dpp)\}_2RhBr_2]^{+5}$ used in H_2 production [79-81].

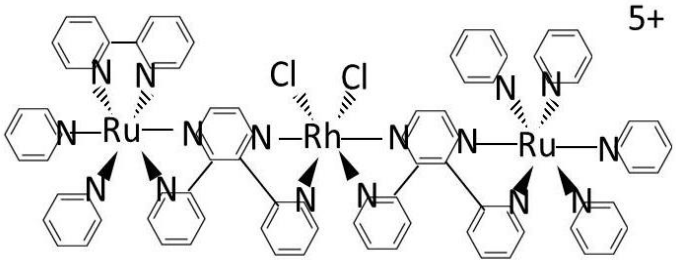

Figure 3.10: Chemical structure of a supramolecular structure $[\{(Ph_2phen)_2Ru(dpp)\}_2RhCl_2]^{+5}$ used in H_2 production [79-81].

3.7 Chloralkali Cells

The literature reviews for each of the three chloralkali cells are presented below.

3.7.1 Mercury Cell

Various researchers have worked on different areas of mercury cell chloralkali technology. Landis et al. [83] have studied the emission of inorganic divalent reactive gaseous mercury (RGM) from a mercury cell chloralkali plan (MCCAP). They also studied cell building and investigated the impact of near field (100 km) dry deposition. HY-SPLIT dispersion and deposition modeling found that the previous EPA emission scenario resulted in an overestimation of the near-field RGM deposition by more than an order of magnitude [83]. Grönlund et al. [84] have studied techniques of differential absorption lidar (DIAL) that have been utilized to measure the elemental gaseous mercury fluxes from the mercury cell chloralkali (MCCA). Large differences in the mercury emissions were observed in the summer and winter at different plants [84]. Kinsey et al. [85] have studied the fugitive (non-ducted) airborne mercury

emissions from the main production equipment of a mercury (Hg) cell during an extended period of operations in a chloralkali plant that is located in the south-eastern United States. The studies provided measurements of Hg fluxes from soil and the other exposed surfaces including waste contained mercury (Hg) [85].

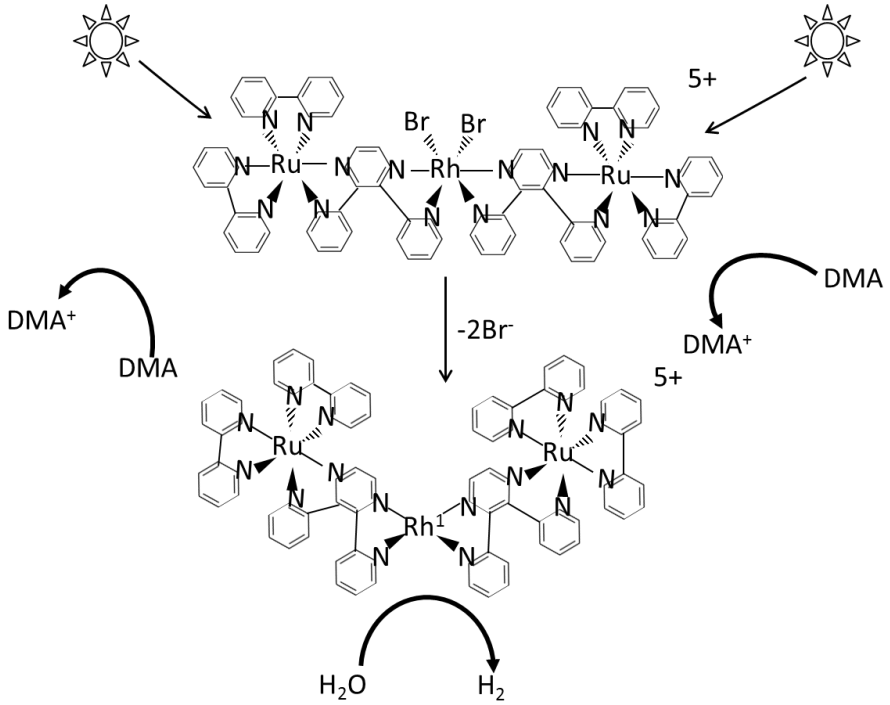

Figure 3.11: Photochemical chemical H_2 production from H_2O using $[\{(bpy)_2Ru(dpp)\}_2RhBr_2]^{+5}$ [79-81].

Kinsey et al. [86] have studied the mercury (Hg) mass flux from the cell building of the mercury cell under a range of the winter time meteorological conditions to perform an air flow balance for the building. They compared different mercury monitoring methods using different sampling conditions. They observed that the combined Hg, along with the long-path ultraviolet differential optical absorption spectrometer (UV-DOAS), were similar to measurements conducted by using a hand-held electrical resistance analyzer [86]. Busto et al. [87] have concluded that, if not properly secured, the mercury waste sludge from the chloralkaline industry poses a serious threat to the environment. The results showed that thermal retort ion can be used to remove the mercury from such waste. This treatment reduces the total mercury content [87].

Southworth et al. [88] have studied fugitive air emissions of the mercury at a chloralkali factory. They used a variety of mercury vapour analyzers to assess these fugitive air emissions of mercury. The work shows that fugitive air emissions vary in the different areas of the factory [88]. Reis et al. [88] have studied the mercury contamination in a mercury-cell chloralkali plant operated in the Estarraeja (North-western Portugal). The results show that the contamination affected the environment even after the chloralkali plant was shut down [89]. Barregard et al. [90] have found that the contamination of air with mercury around the chloralkali plants would increase the internal level of mercury in people living close to the plant [90]. Sensen et al. [91] have measured the concentration levels of the mercury coming out of a chloralkali factory in the vicinity of Dalhousie, New Brunswick, Canada. Research results show that the average lichen background mercury values were 0.008±0.005 Mg/g [91]. Raldúa et al. [92] have studied the mercury levels and the liver pathology in feral fish living in the vicinity of a mercury-cell chloralkali factory. Results show that the mercury concentration level in the muscle and the liver of the barbell located downstream of the factory plant were 10 to 30 times higher than those located upstream [92]. Gibicar et al. [93] have studied the impact of a mercury cell chloralkali complex in Rosignano Solvay (Tuscany, Italy). The study shows that the impact of emitted mercury is restricted to the close surroundings of the mercury-cell chloralkali plant [93].

3.7.2 Diaphragm Cell

Various areas of the diaphragm cell have been examined by numerous researchers. Rodrigues et al. [94] have studied the contamination of sodium hydroxide with chlorate, which creates a major problem for the chloralkali industry. The results indicate that the NaOH concentration is dependent on the migration of the hydroxyl ions to both the anodic side of the cell and the subsequent formation of chlorate [94].

Filho et al. [95] have reported the effects of different variables (e.g., weight, relationship between length of asbestos fibres, and the concentrations of NaCl, NaOH and SM2 polymer) that are involved in the performance of this diaphragm manufacturing process. The result is applicable for the industrial operational conditions of a chloralkali-based production plant that uses the diaphragm processes [95]. Vermeiren et al. [96] have examined the cast macro porous zirfon diaphragm and its use (including the use of space applications). The target of this

development was the casting of an electrode diaphragm electrode (EDE) as a single unit comprising: the anode, the diaphragm and cathode. The experiments showed that the best cathode performance was obtained with a cast Ni/Ir electrode composed of 90% by weight of Ni fibre and 10% by weight of PSU [96]. Lanz et al. [97] have studied titration with a diaphragm-free cell (cell design and applications). The results show that this optimisation involves both optimising the cell geometry and optimising the electro-chemical control of the titration (i.e., current generation at the iodine-generating anode and its cathode counter-electrode [97]). White et al. [98] have studied the system of producing flocs for the water treatment as part of the larger process of recycling the floc chemicals, (instead of dumping the waste at a treatment site). The research demonstrates the technical feasibility of producing flocs for the treatment of potable water by using an electric cell fitted with a porous inorganic membrane of the diaphragm [98]. Kiga [99] has studied a high electro-density diaphragm cell process. The study shows that the diaphragm cell consists of a layer mixture of asbestos fibres, and carbon fibres which are found in concentration levels ranging from 1% to 30%, by weight [99].

3.7.3 Membrane Cell

A number of researchers have addressed different aspects of membrane cell chloralkali technology. Madeni et al. [100] have studied the effect of impurities such as Mg^{2+},Ca^{2+},Fe^{2+}, and SO_4^{2-} in saturated brine within the chloralkali plant. The study reflects that the membranes (in combination with other treatment methods), may be used to decrease the impurities to a desirable level. They used seven polymeric membranes (FT30, PVD, DOW-PS, TFC-SR, BW30, 37100 and NF45) to treat the saturated brine [100]. Balster et al. [101] have studied the research and development of membrane reactors. They reviewed the electro-membrane technology (chloralkali electrolysis) and polymer-electrolyte fuel cells (FC) as an emerging technology. The study shows the way in which the membrane is catalytically effective, as well as how the membrane splits water into protons and hydroxyl ions with the help of the bipolar ion-exchange membrane technology [101].

Savari et al. [102] have examined composite cation exchange membranes, prepared from cross-linked styrene-divinylbenzene copolymers, for the electrolysis of the brine solution in order to produce the sodium hydroxide and chlorine by selective removal of sodium ions. They

prepared a composite membrane by first preparing a polymer syrup of styrene/DVB (using a dual initiator systemAIBN, BPO and DMA), and subsequently by coating it on a clay support [102]. Furuya et al. [103] have examined the electro-catalytic properties along with the lifetime of oxygen cathodes loaded with platinum and silver catalysts. They studied these properties under the practical conditions of chloralkali electrolysis as a function of the catalyst loading. The results mention that the catalytic activity of the cathode that is loaded with the platinum catalysts superior to catalyst loaded with silver [103].

Martel et al. [104] have investigated desalination in seawater and its importance in industries that affect the environment in Mediterranean countries and in Spain's Canary Islands. The work shows that the chloralkali industry activities have drawbacks and negative impacts on the environment and marine ecosystems. These negative impacts are a result of the generated brine being discharged into the sea. The research also shows that some economically viable and effective changes should be introduced, not only for the new plants that are set up, but also for the existing plants [104]. Kariduraganavar et al. [105] have studied the usage of ion-exchange membranes in different industrial processes, (i.e. edible salt production in the electrodialytic concentration of seawater, the desalination of saline water by electro-dialysis, the separation of the ionic materials from the non-ionic materials by the electro-dialysis, the recovery of acid and alkali from waste acid and alkali solution by diffusion dialysis and the dehydration of water-miscible organic solvent by pervaporation, etc.). Results show that the homogenous membranes (prepared by the condensation of the monomers), followed by formaldehyde cross linking, showed good chemical properties. The membranes, however also lacked mechanical strength. The heterogeneous membranes also showed good dimensional stability compared to the homogenous ion-exchange membranes [105].

Chikhi et al. [106] have examined the current distribution in a chloralkali membrane cell through experimental and modelling studies. Observations were made through a video camera. They used a 1-D model for the calculation of the current density distribution. The research showed that the model that was developed for a current density distribution of the FM01-LC (finite element method software), is in good agreement with experimental results [106]. Nagarale et al. [107] have studied the preparation of different types of ion-exchange membranes

characterization and their applications for different electro-membrane processes. The results show that these membranes can be used to solve different types of industrial problems, specifically in the chloralkali industry [107]. Seko et al. [108] have studied the ion-exchange membrane in chloralkali processes [108]. Bergner et al. [109] have investigated membrane cells for chloralkali electrolysis and discussed how this process was superior to mercury and diaphragm processes. The problem, however, of unstable ion exchange membranes in the presence of chlorine was not suitable for chloralkali electrolysis. The future membrane cell design will include thinner hydrophilic membranes with low over-voltage cathodes and a decreased gap between the anode and cathode [109].

McRae [110] has designed an improved integrated cyclic process and apparatus for the various processes that control the recycled waste fluid impurities in the membrane. The improved process and apparatus reduces energy costs and waste, while controlling impurities [110]. O' Brien [111] has studied a method of addition of the calcium ions to the salt-depleted sodium chloride before desaturation, where the concentration of the sulphate impurity is controlled. The process produces chlorine and a high purity alkali metal hydroxide solution [111]. Rutherford [112] has studied the methods of brine solution purification for electrolysis in chloralkali cells. Focus was placed specifically on reducing both the sulphate ion concentration from the membrane cells and the concentration of other undesirable ions (such as calcium and chlorate) [112]. Furuya et al. [113] have studied the fundamental properties and lifespan of the oxygen cathodes loaded with the platinum and silver catalyst while under chloralkali electrolysis. The research shows that a cathode loaded with a 2.63 mg/cm^2 silver catalyst has a three-year longer lifespan than under the practical chloralkali electrolysis conditions [113]. Ezzell et al. [114] have studied an electrolytic cell that is separated into an anode chamber and a cathode chamber using a fluorinated polymer membrane, in which the membrane comprises certain features. The study shows that these cells are specifically useful for the electrolysis of aqueous alkali metal halides [114].

McMichael et al. [115] have studied the membrane/electrode combination, which consists of an electrically conductive screen that has a first and second face. It also consists of an ion exchange membrane film containing a first and second face. The catalytically-active particles are

disposed of on the exposed portions of the first face of the membrane films. the particles are also in electrical and physical contact with the membrane and an electrically conductive screen [115]. Dempsey et al. [116] have studied the generation of the halogen (chlorine) by electrolysis of an aqueous solution of an alkali metal, sodium chloride, which is contained in a cell having the anolyte, and the catholyte chambers separated by a solid polymer electrolyte in the form of a cation-permeable ion exchange membrane. Once the brine solution comes into contact with the anode, it releases chlorine and sodium ions, which are transported through the ion exchange membrane and combined with the hydroxyl ions, in order to form sodium hydroxide [116].

Chapter 4

Experimental Design and Setup

4.1 Reactor Design

Photochemical reduction of water produces hydrogen and hydroxyl ions. In order to neutralize the OH^- ion from the photochemical hydrogen production cell, a new multi-membrane reactor is designed. It consists of three compartments, namely the hydrogen production compartment, chlorine production compartment, and sodium hydroxide collection chamber. Due to the relatively low energy input and high purity of production of sodium hydroxide, membrane technology is used in the newly developed reactor. As the hydrogen is also produced from a photochemical process, the reactor design is different than all of the current designs that are industrially practiced. The present reactor design consists of two membranes, whereas all other industrial membrane cells use a single membrane (i.e. cation exchange membrane). The reason for using two membranes is to avoid the mixing of NaOH with the solution of photocatalytic hydrogen production (Na_2S and ZnS). Using two membranes also helps to avoid the mixing of brine with NaOH in a continuous reactor. Initially, the experiments are performed using a power supply (electrolysis). The optimized results of electrolysis experiments are utilized in photo electrochemical experiments. Figure 4.1 shows a schematic of the new reactor for the electrolysis process. During the process, hydrogen gas is produced at the cathode leaving OH- in the catholyte compartment. Chlorine is produced at the anode leaving Na^+ in the anolyte compartment. Sodium ions pass through the cation exchange membrane, while hydroxyl ions

pass through the anion exchange membrane and form the sodium hydroxide in the middle compartment. In the case of electrolysis, the energy required for the reaction is provided by a power supply. In the case of the photo electrochemical process, however, the energy is provided by the sun.

4.2 Experimental Setup

The experimental setup is a control volume process in which the volume remains constant, yet the pressure changes with the production of gases. A pressure sensor is used to measure the pressure of the gas. The temperature sensor is used to record the temperature of the gas produced in the anolyte and the catholyte compartments. In order to measure the sodium hydroxide, a pH electrode, double-junction, epoxy body, sealed, polygel is used. In order to measure the concentration of sodium in the middle compartment of the reactor, a sodium ion selective electrode is also used in later experiments.

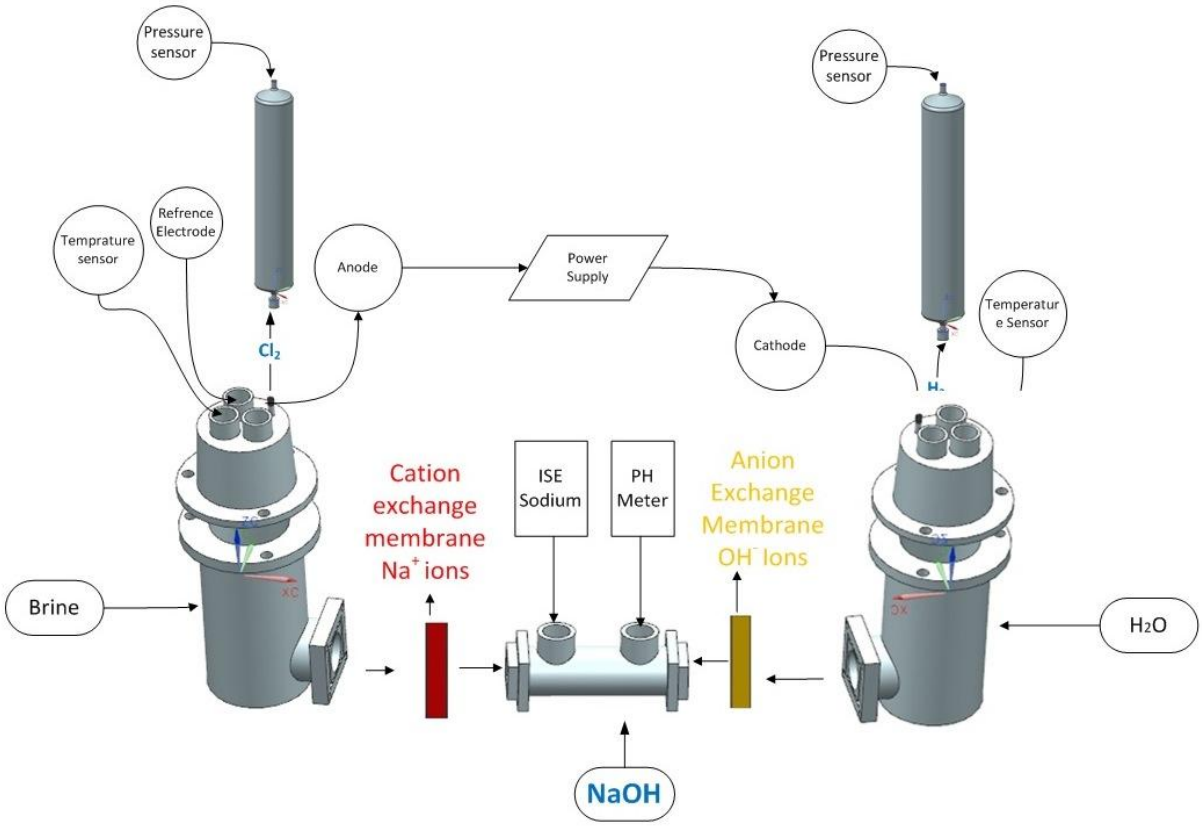

Figure 4.1: Schematic of new electrolysis based chloralkali process reactor.

In order to record the real-time experimental data, a data logger (known as "Pro-lite") from Vernier International is used. Table 4.1 shows some of the characteristics of the sensor. The anion and cation exchange membrane used in the case of electrolysis is developed by Membrane International. The cation exchange membrane has a functional group of sodium, while the anion exchange membrane has a functional group of chlorine. Due to a very low permeability level, a very small amount of water and electrolyte will pass through the membrane. Other technical details of the membrane are given in Table 4.2.

Table 4.1: Characteristics of the sensors.

	Range	Resolution	Response	Other Details
Pressure Sensor	0 to 210 kPa (0 to 2.1 atm or 0 to 1600 mm Hg)	0.05kPa (0.0005 atm or 0.40 mm Hg)	100µs	www.vernier.com /
Temperature Sensor	-20°C – 115°C	0.07°C	4s (to 90% of full reading in water)	www.vernier.com
pH Sensor	0 – 14	0.01	1s	www.vernier.com
Sodium ISE	0 - 19,999 ppm	0.01	1s	www.vernier.com

The electrolysis experiments are performed by using a power supply, PSU505, with 3 programmable outputs and 12-bit resolution. The total output power from all three channels is 120W: channels 1 and 2(30V/ 3A), provide 90 W each, while channel 3(10V/ 5A), provides 30W at a constant rate. The OVP (overvoltage protection) and OCP (over current protection) can be monitored on the front-panel LCD. The PSU505 is also highly efficient and remains stable. The PSU505 remains stable even when the voltage source and loads change. PSU505 has an average response time of 50 ms. Deionized water from "Turbo Water" is used for the experiments. Brine is prepared using sodium chloride salt supplied by Fisher Scientific. Sodium hydroxide is used as an electrolyte.

Table 4.2: Technical specifications of anion and cation exchange membrane in electrolysis chloralkali reactor.

Technical Specifications	CMI-7000 Cation Exchange	AMI-7001 Anion Exchange
Functionality	Strong Acid Cation Exchange	Strong Base Anion Exchange
Polymer Structure	Gel polystyrene cross linked	Gel polystyrene cross linked
Functional Group	Sulphonic Acid	Quaternary Ammonium
Ionic Form	Sodium	Chloride
Color	Brown	Light Yellow
Standard Size	US 48in x 120in	Standard Size
Standard Thickness (mm)	0.45±0.025	0.45±0.025
Electrical Resistance	<30	<40
Permselectivity (%) 0.1 mol	94	90
Total Exchange Capacity	1.6±0.1	1.6±0.1
Water Permeability	<3	<3
Mullen Burst Test strength	>80	>80
Thermal Stability (^{o}C)	90	90
Preconditioning Procedure	Membranes should be	Membranes should be
Other Details	http://www.membranesinternational.com/	

4.3 Experimental design

The experiments performed in the present investigation are divided into five categories as follows:

i. Electrolysis experiments
ii. Photo electrochemical experiments with deionized water
iii. Photo electrochemical experiments with salt water
iv. Photo electrochemical experiments without hole scavenger
v. Solarium experiment

4.4 Electrolysis Experiments

Initial experiments are performed by means of electrolysis. It is cheap and easy to perform electrolysis as compared to the photo-electrochemical process. The objective of the electrolysis

experiments is to assess the performance of the newly designed reactor and to optimize the different processing parameters before performing any photo-electrolysis experiments.

Based on the literature review, the following six different parameters are initially investigated for the newly designed reactor in the electrolysis experiments:

i. Concentration of electrolyte in the anolyte compartment
ii. Concentration of brine
iii. Cell voltage
iv. Brine temperature
v. Anode area in contact with electrolytic water
vi. Cathode material

The present electrolysis experiments are divided into three categories:

i. DOE for VBE
ii. DOE for VT
iii. DOE for VH

4.4.1 DOE for Voltage, Brine Concentration and Electrolyte Concentration (VBE)

Experiments are performed according to a statistical-based method called "design of experiments"(DOE). Factorial design was chosen for the DOE. Based on a literature search, three parameters are studied given as follows: concentration of electrolyte (i.e. sodium hydroxide) in the catholyte compartment, brine concentration, as well as cell voltage. The concentration of the brine in the anolyte compartment is varied in four different levels (i.e. from 150g/L to 225g/L). The concentration of the electrolyte is varied in three different levels (i.e. from 10g/L to 20g/L). The applied cell voltage is varied at five different levels (i.e. from 3V to 20V). The advantage to using more than two levels to conduct this experiment is that it gives the researchers a better indication of the production of hydrogen and chlorine than a two-level factorial approach would.

The Design-expert 8.1.6® is used for designing the experiments. All three process variables are used as numerical factors. The number of experiments in the factorial design can be calculated as

No. of experiments = (Levels of voltage) x (Levels of brine concentration) x (levels of electrolyte concentration) (4.1)

Table 4.3 shows the combinations of both the brine and electrolyte concentration levels, as well as the cell voltage with which the experiments have been performed. Each experimental run is performed for an hour.

Table 4.3: Factorial design of experiment (VBE).

No.	Salt Concentration(g/L)	Electrolyte Conc. (g/425mL)	Cell Voltage (V)
1	150	25	20
2	150	25	10
3	150	15	5
4	150	15	15
5	150	20	15
6	150	15	20
7	150	20	20
8	150	15	10
9	150	25	5
10	150	20	10
11	150	25	15
12	150	20	5
13	175	20	10
14	175	25	20
15	175	15	10
16	175	15	5
17	175	20	15
18	175	20	5
19	175	25	15
20	175	25	5
21	175	20	20
22	175	25	10
23	175	15	15
24	175	15	20
25	200	25	15
26	200	15	5
27	200	15	20

28	200	20	15
29	200	25	5
30	200	20	20
31	200	15	15
32	200	20	5
33	200	25	20
34	200	20	10
35	200	15	10
36	200	25	10
37	225	15	15
38	225	25	15
39	225	25	20
40	225	15	10
41	225	25	10
42	225	25	5
43	225	20	15
44	225	20	20
45	225	15	5
46	225	15	20
47	225	20	10
48	225	20	5
49	150	20	3
50	175	20	3
51	200	15	3
52	200	20	3
53	225	15	3
54	175	15	3
55	225	20	3
56	150	15	3
57	150	25	3
58	175	25	3
59	200	25	3
60	225	25	3

4.4.2 DOE for Voltage and Temperature (VT)

During the VBE experiments it is observed that the partial pressure of the chlorine gas is lower than that of the hydrogen. This is due to the higher solubility of chlorine. In order to explore this fact further, experiments are designed and performed using factorial design to find the effect of temperature and voltage on the rate of chloralkali products. The temperature is varied on three different levels (i.e. 30^{o}C, 50^{o}C and 70 ^{o}C), and the voltage is varied on five different levels (i.e.

3V, 5V, 10V, 15V, 20V). Optimized concentration levels of both the brine and electrolyte obtained from the VBE experiments are used (i.e. brine concentration = 225g/L, electrolyte concentration = 25g/425ml). Table 4.4 shows the combinations of temperatures and voltage levels in each experiment.

Table 4.4: Factorial design of experiment (VT)

No.	Voltage (V)	Temperature (^{o}C)
1	3	30
2	5	30
3	10	30
4	15	30
5	20	30
6	3	50
7	5	50
8	10	50
9	15	50
10	20	50
11	3	70
12	5	70
13	10	70
14	15	70
15	20	70

4.4.3 DOE for Voltage and Anode Area (VH)

Experiments are also performed with the same anode materials of two different heights in order to find the effect of the anode area (i.e. current density) based on the rate of hydrogen production and five different voltages (i.e. 3V, 5V, 10V, 15V, 20V). The concentration levels of the brine and electrolyte remain the same (i.e. brine concentration = 225g/L, Electrolyte concentration = 15g/425ml). Table 4.5 shows the combinations of temperature and anode height in each experiment.

Table 4.5: Factorial design of experiment (VH)

No.	Voltage (V)	Height (mm)
1	3	111.5
2	5	111.5
3	10	111.5
4	15	111.5
5	20	111.5
6	3	70
7	5	70
8	10	70
9	15	70
10	20	70

4.5 Electrode for Chlorine Evolution Reaction

Various different electrodes for the hydrogen evolution reaction have been discussed in the past literature. Chlorine is a reactive gas and reacts with almost all elements including hydrocarbons. Therefore it is important to use a proper electrode during this step. Keeping in view the availability, cost and machinability, five different corrosion resistant materials are tested to find the appropriate electrodes for the chlorine evolution reaction. These materials include corrosion-resistant alloys of copper, aluminum, steel, nickel, and graphite.

4.6 Experimental Procedure

Experiments are performed at the Clean Energy Research Laboratory (CERL) located at UOIT. The brine is prepared using 400mL of deionized water and sodium chloride for each run, in order to determine both the individual and mutual effects of brine concentration on other parameters (i.e. electrolyte concentration and voltage). Brine concentration levels are varied according to Table 4.3 in the anolyte compartment. The concentration level of the brine remains constant for both temperature and electrode-area experiments.

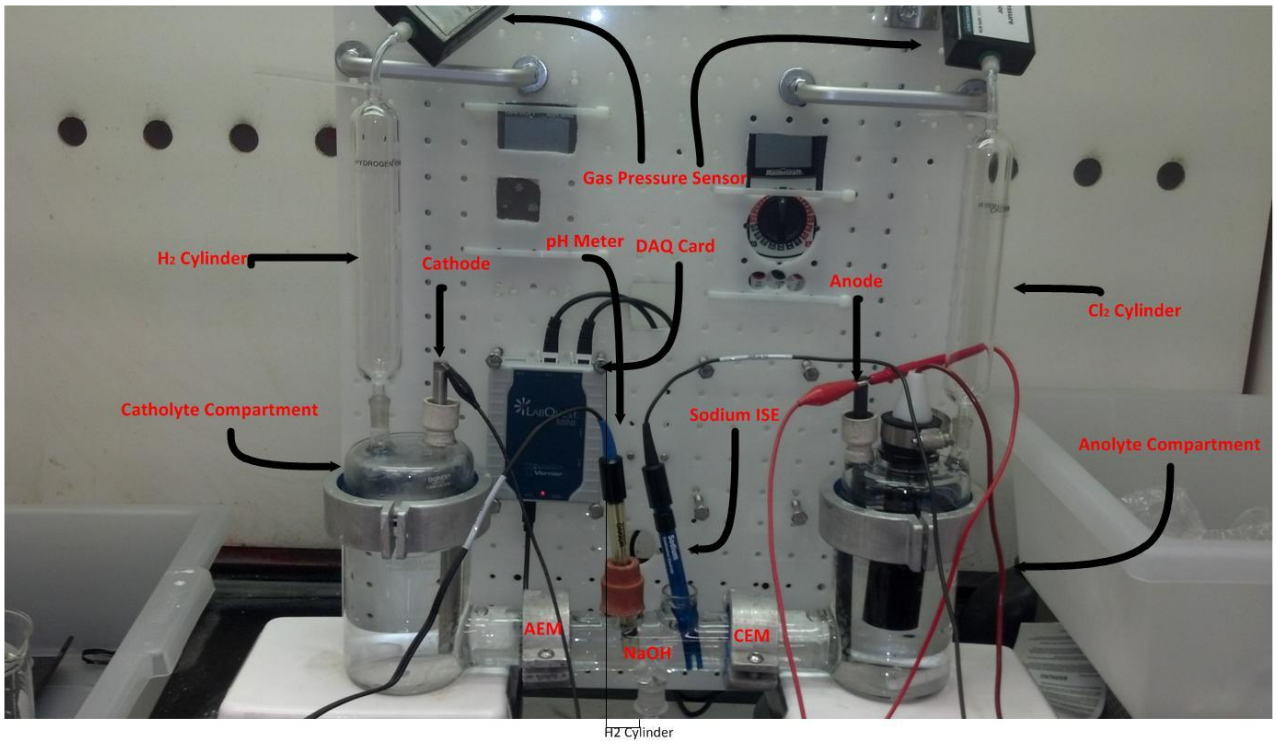

Figure 4.2: Multi membrane experimental reactor at CERL.

For the sodium hydroxide production compartment, 70mL of water combined with 2.5g sodium hydroxide is used. For the catholyte compartment, 400mL of the deionized water (with an electrolyte concentration from Table 4.3), is used. Electrodes with a diameter of 9.43mm are immersed in the anolyte and catholyte compartments. Corrosion-resistant nickel is used in the catholyte compartment, while different electrodes are tested in the anolyte compartment. Figure 4.2 shows the experimental setup for the experiments. The hydrogen and chlorine are collected in a gas collection chamber. The partial pressure of both hydrogen and chlorine increases over time. It is used to measure the rate of hydrogen, chlorine, and sodium hydroxide production.

4.7 Photo Electrochemical Experiments with Deionized Water

In photo-electrochemical experiments, zinc sulfide (ZnS) is used as a photo catalyst. Similarly, sodium sulfide is used as a hole scavenger. Because the ZnS works in an ultraviolet range, a mercury lamp is used as a light source.

The optimized levels of brine concentration, electrolyte concentration, and electrode materials (obtained from electrolysis experiments) are used. Initially 2.5g of sodium hydroxide is used in the sodium hydroxide chamber. The concentration levels of sodium sulfide remain constant in all photo experiments (i.e. 1M). Three parameters are studied which include:

i. Light intensity (W/m^2)
ii. Applied voltage (V)
iii. Catalyst concentration (g/425mL of solution)

Light intensity is varied in three different levels, ranging from 20 W/m^2 to 55 W/m^2. Applied voltage is varied in three different levels, ranging from 4V to 5V. Catalyst concentration levels are varied into four levels, ranging from 1g/425mL of solution to 4g/425mL of solution. Table 4.6 gives the experimental array that is present. The light intensity is measured by using a payranometer. Figure 4.3 shows the experimental setup for photo-electrochemical experiments.

Table 4.6: DOE for photo- electrochemical experiments with deionized water

Run No.	Light Intensity (W/m^2)	Applied Voltage (V)	Catalyst Concentration (g/425mL)
1	20	5	3
2	30	5	3
3	55	5	3
4	20	4.5	3
5	30	4.5	3
6	55	4.5	3
7	20	4	3
8	30	4	3
9	55	4	3
10	20	5	4
11	30	5	4
12	55	5	4
13	20	4.5	4
14	30	4.5	4
15	55	4.5	4
16	20	4	4

17	30	4	4
18	55	4	4
19	20	5	2
20	30	5	2
21	55	5	2
22	20	4.5	2
23	30	4.5	2
24	55	4.5	2
25	20	4	2
26	30	4	2
27	55	4	2
28	20	5	1
29	30	5	1
30	55	5	1
31	20	4.5	1
32	30	4.5	1
33	55	4.5	1
34	20	4	1
35	30	4	1
36	55	4	1

4.8 Photo Electrochemical with Salt Water

In process of photo-electrolysis with salt water, salt (i.e. NaCl) was added as an impurity to the hydrogen production unit to see its effect on the rate of hydrogen production. The optimized photo catalyst concentration level and other process parameters (obtained from electrolysis and Photo electrolysis with deionized water experiments) are implemented. The following three parameters are studied:

i. Salt concentration in the hydrogen production chamber (g/425mL)
ii. Light intensity (W/m^2)
iii. Applied voltage (V)

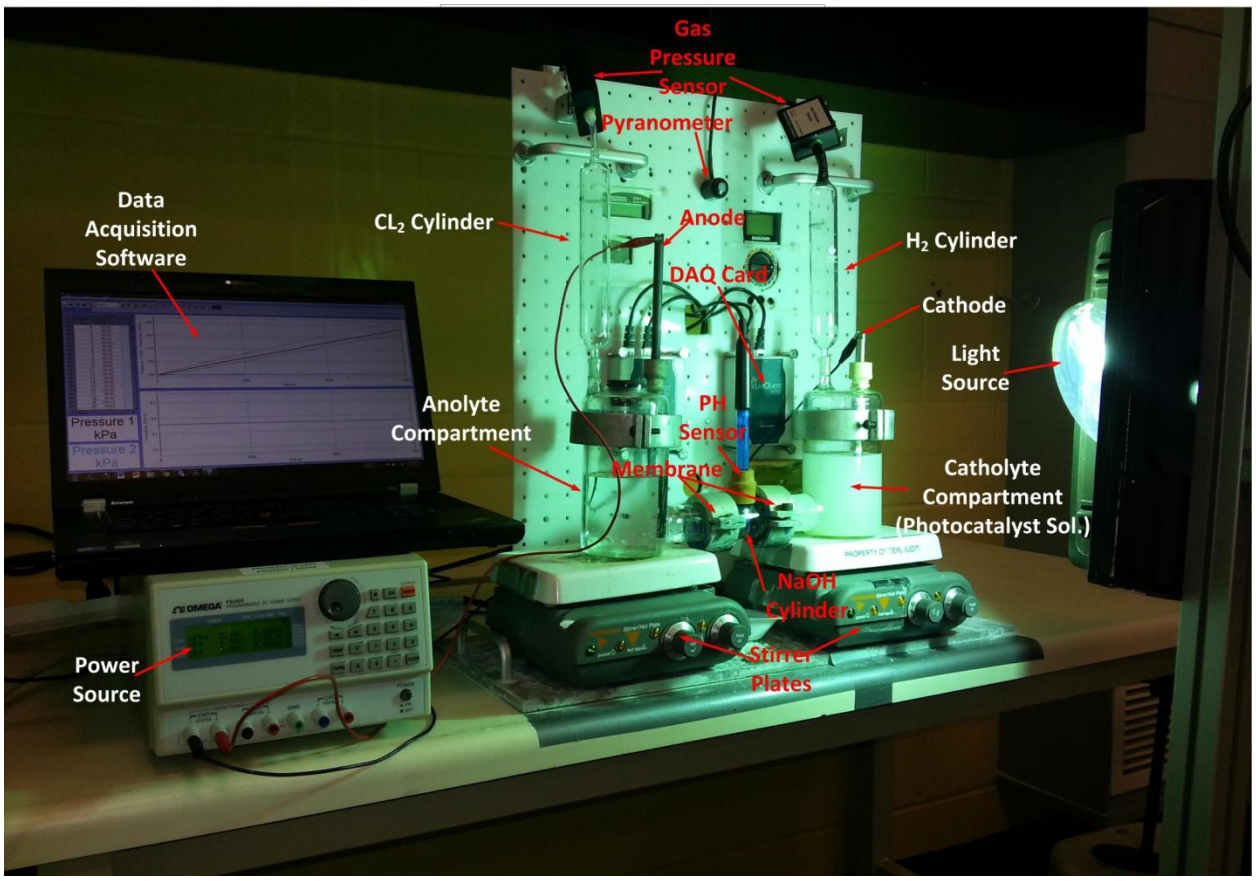

Figure 4.3: Experimental setup for photo-electrochemical experiments.

The respective light intensity is varied into three different levels, ranging from 20 W/m^2 to 55 W/m^2. Applied voltage is also varied into three different levels, ranging from 4V to 5V. The optimized value of catalyst concentration is also used. Salt concentration is varied into two different levels, ranging from 15g/425mL of solution to 30g/425mL of solution in the catholyte compartment. Table 4.7 shows the experimental array that is present.

4.9 Photo Electrochemical Experiments without Hole Scavenger

Sodium sulfide is a hole scavenger. Its main job is to donate electrons for photochemical hydrogen production. A single experiment is performed at a voltage level that is less than what is required for electrolysis (i.e. required voltage for electrolysis is 2.19V and the experiment is performed at 2V). The idea, here, is to supply the desired electrons for the photochemical hydrogen production with an electrical supply, instead of using the hole scavenger. By using this

approach, we can get rid of all of the consumables from our system, which ultimately leads to cost reduction and a high degree of purity of sodium hydroxide.

Table 4.7 DOE for photo electrochemical experiments with salt water

Run No.	Light Intensity (W/m^2)	Applied Voltage(V)	Salt concentration (g/425mL)
1	20	4	15
2	30	4	15
3	55	4	15
4	20	4.5	15
5	30	4.5	15
6	55	4.5	15
7	20	5	15
8	30	5	15
9	55	5	15
10	20	4	30
11	30	4	30
12	55	4	30
13	20	4.5	30
14	30	4.5	30
15	55	4.5	30
16	20	5	30
17	30	5	30
18	55	5	30

For these experiments, sodium sulfide is not added to the hydrogen production chamber. The optimized catalyst concentration level is once again implemented. Table 4.8 shows the experimental array that is present.

Table 4.8 DOE for photo electrochemical experiments without adding Na_2S.

Run No.	Light Intensity	Applied Voltage (V)
1	20.00	2
2	30.00	2
3	55.00	2

4.10 Solarium Experiment

After optimizing each of the parameters, a single experiment is performed under real sunlight. In this experiment, a method of harnessing the unused portion of the solar spectrum is simulated. Due to the high cost of the dielectric mirror required for this experiment, it is replaced with two light filters.

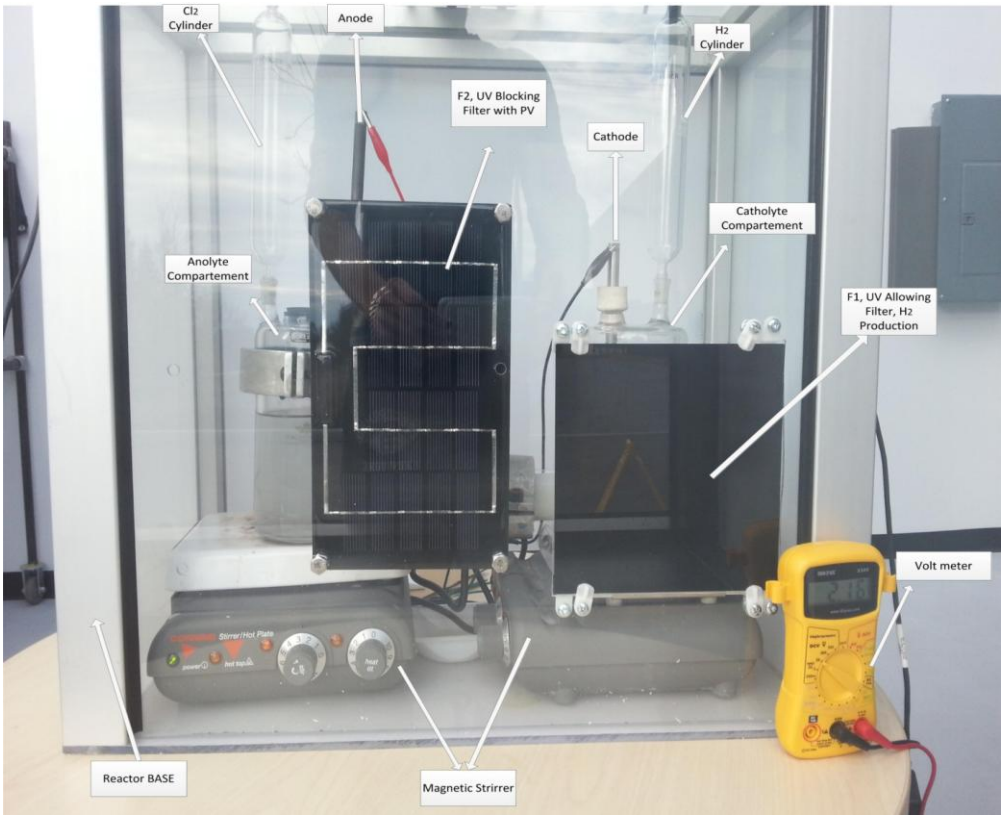

Figure 4.4: Experimental setup for solarium experiment.

The combination of these light filters simulates the same conditions as the dielectric mirror would provide. Figure 4.4 shows the experimental setup for the solarium experiments before and during the experiment. During this present study, ZnS is used as a photo catalyst, which works in the ultraviolet region of the solar spectrum (i.e. operating range of ZnS is between 313nm to 320nm). Filter F1 (which only allows the UV light to pass through), is used at this point (see I3 in Figure 2.4).

Figure 4.5 shows the transmittance spectrum for filter F1. Filter F2 is also used which blocks out UV radiations and allows all other wavelengths to pass through (see I2 in Figure 2.4). A PV array of 5"x3" is placed behind filter F2. The PV panel recovers the unused portion of the solar spectrum and produces electricity. This electricity is used to produce additional hydrogen by means of electrolysis. For the solarium experiment, the optimized catalyst concentration level obtained from the prior experiments is, once again, used.

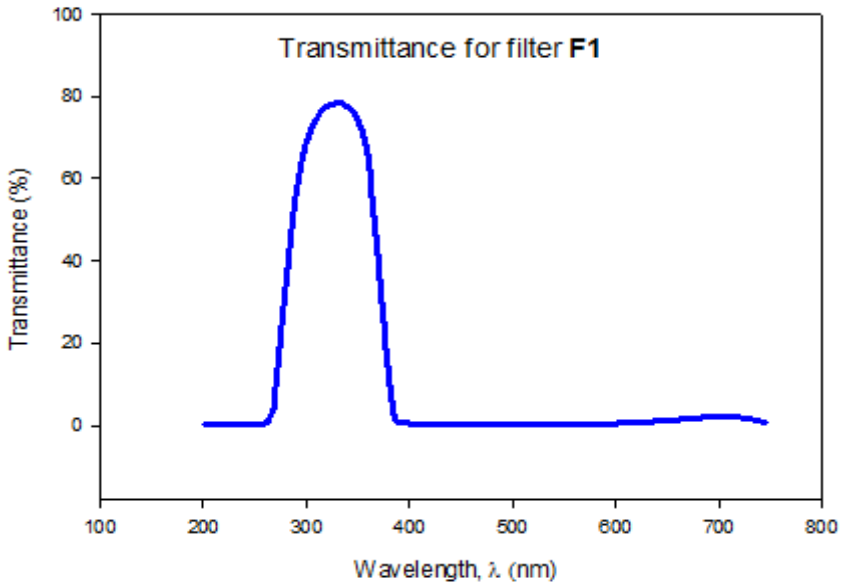

Figure 4.5: Transmittance spectrum for filter F1.

Chapter 5

Analysis and Modeling

5.1 Introduction

In this chapter, thermodynamic analysis, exergoeconomic analysis, electrochemical analysis and radiation modeling of the reactor are presented.

5.2 Energy and Exergy Analysis of a New Chloralkali Reactor

In order to assess the thermodynamic performance of the photo-electrochemical chloralkali process, an energy and exergy analysis is performed. It is important to find the theoretical energy requirement for this process. The total energy required can be determined by applying the following formula:

$$\Delta H = \Delta G + T\Delta S \tag{5.1}$$

where ΔG represents the net change in Gibbs free energy and it is equivalent to the required electrical energy for the process, TΔS represents the thermal portion of the required energy. The enthalpy and entropy values of H_2O, H_2, Cl_2 and NaOH are available in Engineering Equation Solver (EES), but for NaCl, correlations based on curve fitting of the data of Pitzer et al. [117] are used. These correlations are also presented. The minimum theoretical electrical potential for the anode and cathode is given in Table 5.1.

Table 5.1: Minimum required electrical potential.

Electrode	Reaction	Minimum required
Anode	$Cl^- \rightarrow Cl_2 + 2e^-$	1.35
Cathode	$2H_2O + 2e^- \rightarrow H_2 + 2OH^-$	0.83
Total	$2NaCl + 2H_2O \rightarrow H_2 + Cl_2 + 2NaOH$	2.18

5.2.1 Thermodynamic Analysis

The thermodynamic analysis (i.e. first and second law analysis) of the system for the continuous cycle is presented in this section. In the analysis, the following assumptions are made.

- A steady state operation to govern the process.
- The kinetic and potential energies and exergies are negligible for all system components.
- The ambient temperature and pressure are constant as T_0 =298K and P_0 =100kPa.
- The gases, hydrogen and chlorine, are treated as ideal gases.
- The heat losses occurring during the process are negligible.

5.2.1.1 Mass Balance

For a continuous photo-electrochemical reactor (Figure 5.1), the mass balance can be written as follows:

$$\dot{m}_1 + \dot{m}_7 = \dot{m}_2 + \dot{m}_3 + \dot{m}_5 + \dot{m}_6 + \dot{m}_4 \quad (5.2)$$

where $\dot{m}_1$ represents the mass flow rate of brine entering in the anolyte compartment (kg/s), $\dot{m}_2$ represents the mass flow rate of brine leaving from the anolyte compartment (kg/s), $\dot{m}_3$ represents the mass flow rate of chlorine gas leaving from the anolyte compartment (kg/s), $\dot{m}_4$ represents the flow rate of sodium ions traveling through cation exchange membrane (kg/s), $\dot{m}_5$ represents the flow rate of hydroxyl ions passing through the anion exchange membrane (kg/s), $\dot{m}_6$ represents the mass flow rate of hydrogen gas leaving from the catholyte compartment (kg/s) and $\dot{m}_7$ represents the difference between inlet and outlet water stream (kg/s).

$$\dot{m}_7 = \dot{m}_{WH,in} - \dot{m}_{WH,out} \quad (5.3)$$

where $\dot{m}_{WH,in}$ represents the mass flow rate of water inlet to the catholyte chamber and $\dot{m}_{WH,out}$ represents the mass flow rate of water outlet from the catholyte chamber.

where $\dot{m}_{w1}$ represents the mass flow rate of water in kg/s.

The difference in mass fraction of the inlet and outlet brine concentration level from the reactor can be represented by β and can be determined as

$$\dot{x}_{s1} - \dot{x}_{s2} = \frac{\beta}{100} \quad (5.4)$$

where $\dot{x}_{s2}$ represents the mass fraction of salt leaving the anolyte compartment. Because only sodium chloride will be utilized in the chlorine production chamber, the concentration of water will remain the same as expressed in the following formula:

$$\dot{m}_{w1} = \dot{m}_{w2} \quad (5.5)$$

where $\dot{m}_{w2}$ represents the mass flow rate of water leaving the anolyte compartment. The outlet mass flow rate in the chlorine production chamber can be given as

$$\dot{m}_2 = \dot{m}_{w2} + \dot{m}_{s2} \quad (5.6)$$

where $\dot{m}_{s2}$ represents the mass flow rate of NaCl leaving the anolyte compartment. The mass flow rate of sodium chloride leaving the reactor can be calculated as

$$\dot{m}_{s2} = \frac{\dot{x}_{s2}}{\dot{x}_{s1}} \dot{m}_{s1} \quad (5.7)$$

The sum of the mass fraction of sodium chloride and water in the brine is equal to 1 and can be written as

$$\dot{x}_{s1} + \dot{x}_{w1} = 1 \quad (5.8)$$

where $\dot{x}_{s1}$ represents the mass fraction of salt in brine and $\dot{x}_{w1}$ represents the mass fraction of water in brine.

The mass flow rate of sodium chloride entering the reactor can be written as

$$\dot{m}_{s1} = \dot{x}_{s1}\dot{m}_1 \tag{5.9}$$

where $\dot{m}_{s1}$ represents the mass flow rate of NaCl entering in anolyte compartment in kg/s.

The mass flow rate of water entering the reactor can be written as

$$\dot{m}_{w1} = \dot{x}_{w1}m_1 \tag{5.10}$$

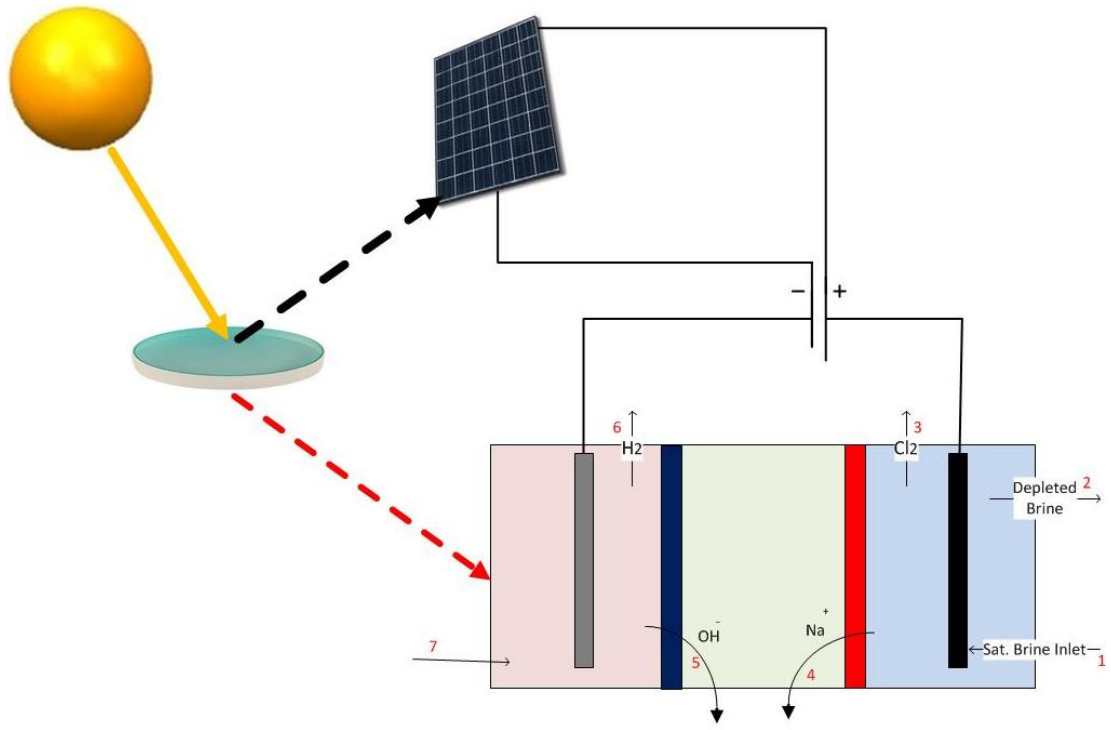

Figure 5.1: A continuous photo-electrochemical chloralkali process reactor.

The number of moles of sodium chloride consumed can be calculated as

$$n_{NaCl} = \frac{(\dot{m}_{s1} - \dot{m}_{s2})}{58.44} \text{ (Molar mass of NaCl is 58.44)} \tag{5.11}$$

where n_{NaCl} represents moles of sodium chloride consumed in anolyte compartment in kg/kmol. From a balance chemical equation, the number of moles of sodium chloride that are consumed in the process is equal to number of moles of water consumed in hydrogen production chamber.

$$n_{H_2O} = n_{NaCl} \tag{5.12}$$

where n_{H_2O} represents the moles of water consumed in catholyte compartment in kg/kmol. With this information, the amount of water consumed in H_2 production can be calculated as

$$n_{H_2O} = \frac{\dot{m}_7}{18} \quad \text{(Molar mass of } H_2O \text{ is 18)} \tag{5.13}$$

5.2.1.2 Energy Balance

For a continuous photo-electrochemical reactor (Figure 5.1), the rate equation representing the energy balance for a continuous reactor can be written as

$$\dot{m}_1 h_1 + \dot{m}_7 h_7 + \dot{Q} = \dot{m}_2 h_2 + \dot{m}_3 h_3 + \dot{m}_5 h_5 + \dot{m}_6 h_6 + \dot{m}_4 h_4 \tag{5.14}$$

The equation 5.14 counts no thermodynamics work involved in the system.

where h_1 represents the enthalpy of brine entering in the anolyte compartment (kJ/kg), h_2 represents the enthalpy of brine leaving from the anolyte compartment (kJ/kg), h_3 represents the enthalpy of chlorine gas leaving from the anolyte compartment (kJ/kg), h_4 represents the enthalpy of sodium ions traveling through cation exchange membrane (kJ/kg), h_5 represents the enthalpy of hydroxyl ions passing through the anion exchange membrane (kJ/kg), h_6 represents the enthalpy of hydrogen gas leaving from the catholyte compartment (kJ/kg), h_7 represents the difference between inlet and outlet water stream (kJ/kg) and $\dot{Q}$ represents the total solar input to the system.

The total solar input to the continuous photo-electrochemical reactor can be divided into two components a) photochemical b) electrochemical.

$$\dot{Q} = \eta_{pv} \cdot (1 - \varsigma) \cdot I \cdot A_{pv} + \varsigma \cdot I \cdot A_{reactor} \tag{5.15}$$

where η_{pv} represents the efficiency of the PV panels. I represents the intensity of light (W/m^2). represents the portion of the solar radiations which is used in photochemical hydrogen production. The value of can be found from Figure 2.5. For ZnS catalyst, $= 0.04$. A_{pv} represents the area of PV used to recover the unused portion (m^2). $A_{reactor}$ represents the area of the reactor exposed to solar radiations for photochemical hydrogen production (m^2).

5.2.1.3 Entropy Balance

For a continuous photo-electrochemical reactor (Figure 5.1), the rate equation representing the entropy balance for a continuous reactor can be written as

$$\dot{m}_1 s_1 + \dot{m}_7 s_7 + \dot{S}_{gen} + \frac{\dot{Q}}{T_s} = \dot{m}_2 s_2 + \dot{m}_3 s_3 + \dot{m}_5 s_5 + \dot{m}_6 s_6 + \dot{m}_4 s_4 \quad (5.16)$$

where s_1 represents the entropy of brine entering in the anolyte compartment (kJ/kg-K). s_2 represents the entropy of brine leaving from the anolyte compartment (kJ/kg-K). s_3 represents the entropy of chlorine gas leaving from the anolyte compartment (kJ/kg-K). s_4 represents the entropy of sodium ions traveling through cation exchange membrane (kJ/kg-K). s_5 represents the entropy of hydroxyl ions passing through the anion exchange membrane (kJ/kg-K). s_6 represents the entropy of hydrogen gas leaving from the catholyte compartment (kJ/kg-K). s_7 represents the entropy difference between inlet and outlet water stream (kJ/kg-K). $\dot{S}_{gen}$ represents the entropy generation in the system. T_s represents the temperature of sun and is equal to 100,000K.

5.2.1.4 Exergy Balance

For a continuous photo-electrochemical reactor (Figure 5.2), the rate equation representing the exergy balance for a continuous reactor can be written as

$$\dot{m}_1 ex_1 + \dot{m}_7 ex_7 + \dot{Q}\left(1 - \frac{T_o}{T_s}\right) = \dot{m}_2 ex_2 + \dot{m}_3 ex_3 + \dot{m}_5 ex_5 + \dot{m}_6 ex_6 + \dot{m}_4 ex_4 + \dot{E}x_{dest} \quad (5.17)$$

where ex_1 represents the exergy of brine entering in the anolyte compartment (kJ/kg). ex_2 represents the exergy of brine leaving from the anolyte compartment (kJ/kg). ex_3 represents the exergy of chlorine gas leaving from the anolyte compartment (kJ/kg). ex_4 represents the exergy of sodium ions traveling through cation exchange membrane (kJ/kg). ex_5 represents the exergy of hydroxyl ions passing through the anion exchange membrane (kJ/kg). ex_6 represents the exergy of hydrogen gas leaving from the catholyte compartment (kJ/kg). ex_7 represents the exergy difference between inlet and outlet water stream (kJ/kg).

The total exergy in a chemical reaction is a sum of flow exergy and chemical exergy. For any given state i, the total exergy can be as

$$ex_i = h_i - h_o - T_o(s_i - s_o) + ex_i^{ch} \quad (5.18)$$

where ex_i^{ch} represents the chemical exergy (kJ/kg), h_o represents the enthalpy of reference state (kJ/kg), h_i represents the enthalpy of i^{th} state (kJ/kg), T_o represents the reference temperature (K),), s_o represents the entropy of reference state (kJ/kg-K), s_i represents the entropy of i^{th} state (kJ/kg-K).

The exergy destruction can also be written as

$$\dot{E}x_{dest} = \dot{S}_{gen} T_o \quad (5.19)$$

where $\dot{E}x_{dest}$ represents the exergy destruction in kW.

5.2.1.4 Efficiency Analysis

Out of three chloralkali products, only hydrogen is a fuel; therefore, the energy efficiency for the electrolysis process can be written as

$$\eta_{en,H2} = \frac{\dot{m}_{H2} HHV_{H2}}{Vi} \quad (5.20a)$$

If the temperature is higher than the reference temperature, then the energy of chlorine and sodium hydroxide should be considered. The energy efficiency in that case can be written as.

$$\eta_{en,All} = \frac{\dot{m}_{H2} HHV_{H2} + \dot{m}_{Cl2} Cp_{Cl2}(T - T_o) + \dot{m}_{NaOH} Cp_{NaOH}(T - T_o)}{Vi} \quad (5.20b)$$

Similarly, the exergy efficiency can be determined as

$$\eta_{exe,H2} = \frac{\dot{m}_{H2} ex_{H2}^{ch}}{Vi} \quad (5.21)$$

If the chemical exergy of sodium hydroxide and chlorine is also included in the calculations, than exergy efficiency can be written as

$$\eta_{exe,All} = \frac{\dot{m}_{H2} ex_{H2}^{ch} + \dot{m}_{Cl2} ex_{Cl2}^{ch} + \dot{m}_{NaOH} ex_{NaOH}^{ch}}{Vi} \quad (5.22)$$

where ex_{H2}^{ch}. ex_{Cl2}^{ch}, ex_{NaOH}^{ch} represent the chemical exergy of hydrogen, chlorine and sodium hydroxide have respective values of 236.1 kJ/mol, 124 kJ/mol, 40 kJ/mol. V represents the applied voltage in volts and i represents the current in amperes.

For photo-electrochemical setup with electrical power input from an electrical power source, the energy efficiency can be written as

$$\eta_{en,photo} = \frac{\dot{m}_{H2} HHV_{H2} + \dot{m}_{Cl2} Cp_{Cl2}(T - T_o) + \dot{m}_{NaOH} Cp_{NaOH}(T - T_o)}{Vi + IA_{reactor}} \tag{5.23}$$

Similarly, the exergy efficiency for photo-electrochemical processes using an external power source can be written as

$$\eta_{exe,photo} = \frac{\dot{m}_{H2} ex_{H2}^{ch} + \dot{m}_{Cl2} ex_{Cl2}^{ch} + \dot{m}_{NaOH} ex_{NaOH}^{ch}}{VI + IA_{reactor}} \tag{5.24}$$

With respect to a continuous photo- electrochemical reactor, which harnesses the unused portion of the solar spectrum, the energy efficiency can be written as

$$\eta_{en,C} = \frac{\dot{m}_{H2} HHV_{H_2} + \dot{m}_{Cl2} Cp_{Cl2}(T - T_o) + \dot{m}_{NaOH} Cp_{NaOH}(T - T_o)}{\dot{m}_1 h_1 - \dot{m}_2 h_2 + \dot{m}_7 h_7 + (1-\varsigma)\cdot I \cdot A_{pv} + \varsigma \cdot I \cdot A_{reactor}} \tag{5.25a}$$

Similarly, the exergy efficiency can be written as

$$\eta_{exe,C} = \frac{\dot{m}_{H2} ex_{H2}^{ch} + \dot{m}_{Cl2} ex_{Cl2}^{ch} + \dot{m}_{NaOH} ex_{NaOH}^{ch}}{\dot{m}_1 ex_1 - \dot{m}_2 ex_2 + \dot{m}_7 ex_7 + (1-\varsigma)\cdot I \cdot A_{pv}\left(1 - \frac{T_o}{T_s}\right) + \varsigma \cdot I \cdot A_{reactor}\left(1 - \frac{T_o}{T_s}\right)} \tag{5.25b}$$

5.3 Thermodynamic Properties of Brine

The thermodynamic properties of water, chlorine, and hydrogen are available in a number of different software packages, (e.g. Engineering Equation Solver (EES), National Institute of Standards and Technology (NIST), etc.). The properties of brine, however, are not commonly available in past literature. Pitzer et al. [117] presented the properties of aqueous sodium chloride in tabular form. The reference temperature and pressure while evaluating the properties are taken

as To=25°C and Po=101.8 kPa. The results below show the correlations based on the Pitzer et al. [117] tables.

5.3.1 Solubility of NaCl in H_2O

The solubility of sodium chloride in water is dependent on temperature and can be estimated as [118]

$$X_{SAT} = 0.2628 + 62.75 * 10^{-6}T \quad (5.\ 26)$$

5.3.2 Vapor pressure of NaCl in H_2O

The vapour pressure of sodium chloride in water is a function of its concentration and temperature. It can be determined as [118]

$$P_{VAP} = A + BT + CT^2 + DT^3 + ET^4 \quad (5.27a)$$

$$0℃ \leq T \leq 150℃$$

$$A = (0.9083 - 0.569X + 0.1945X^2 - 3.736X^3 + 2.82X^4)10^{-3} \quad (5.27b)$$

$$B = (-0.0669 + 0.0582X - 0.1668X^2 + 0.6761X^3 - 2.091X^4)10^{-3} \quad (5.27c)$$

$$C = (7.541 - 5.143X + 6.482X^2 - 52.62X^3 + 115.7X^4)10^{-6} \quad (5.27d)$$

$$D = (-0.0922 + 0.0694X - 0.1313X^2 + 0.8024X^3 - 1.986X^4)10^{-6} \quad (5.27e)$$

$$E = (1.23 - 0.753X + 0.1448X^2 - 6.964X^3 + 15.61X^4)10^{-9} \quad (5.27f)$$

$$150℃ \leq T \leq 300℃$$

$$A - 3.248 + 7.081X - 49.93X^2 + 219.6X^3 - 308.5X^4 \quad (5.27g)$$

$$B = 0.0610 - 0.1185X + 0.7916X^2 - 3.474X^3 + 5.882X^4 \quad (5.27h)$$

$$C = (-0.4109 + 0.6789X - 5.155X^2 + 18.34X^3 - 25.89X^4)10^{-3} \quad (5.27i)$$

$$D = (1.13 - 1.432X + 7.169X^2 - 33.17X^3 + 47.45X^4)10^{-6} \quad (5.27j)$$

$$E = 0 \quad (5.27k)$$

5.3.3 Density of NaCl in H2O

The density of brine is dependent upon concentration of salt and temperature. It can be calculated as [118]

$$\rho = A + BT + CT^2 + DT^3 + ET^4 \quad (5.28a)$$

$$0℃ \leq T \leq 300℃$$

$$A = (1.001 + 0.7666X - 0.0149X^2 + 0.2663X^3 + 0.8845X^4)10^3 \quad (5.28b)$$

$$B = -0.0214 - 3.496X + 10.02X^2 - 6.56X^3 - 31.37X^4 \quad (5.28c)$$

$$C = (-5.263 + 39.87X - 176.2X^2 + 363.5X^3 - 7.784X^4)10^{-3} \quad (5.28d)$$

$$D = (15.42 - 167X + 980.7X^2 - 2573X^3 + 876.6X^4)10^{-6} \quad (5.28e)$$

$$E = (-0.0276 + 0.2978X - 2.017X^2 + 6.345X^3 - 3.914X^4)10^{-6} \quad (5.28f)$$

5.3.4 Enthalpy of NaCl in H_2O

The enthalpy of brine solution is a function of temperature and concentration. It can be estimated as [118]

$$h = A + BT + CT^2 + DT^3 + ET^4 \quad (5.29a)$$

$$0℃ \leq T \leq 300℃$$

$$A = (0.0005 + 0.0378X - 0.3682X^2 - 0.6529X^3 + 2.89X^4)10^3 \quad (5.28b)$$

$$B = 5.145 - 5.973X + 5.482X^2 + 18.31X^3 - 46.41X^4 \quad (5.29c)$$

$$C = 0.0007 - 0.0059X + 0.0854X^2 - 0.4951X^3 + 0.8255X^4 \quad (5.29d)$$

$$D = (-0.0048 + 0.0639X - 0.714X^2 + 3.273X^3 - 5.85X^4)10^{-3} \quad (5.29e)$$

$$E = (0.0220 - 0.2432X + 2.054X^2 - 8.211X^3 + 11.43X^4)10^{-6} \quad (5.29f)$$

5.3.5 Entropy of NaCl in H_2O

The entropy of brine solution is a function of temperature and concentration. It can be estimated as [118]

$$s = A + BT + CT^2 + DT^3 + ET^4 \quad (5.30a)$$

$$0℃ \leq T \leq 150℃$$

$$A = 0.0021 + 2.854X - 8.677X^2 + 23.77X^3 - 30.94X^4 \quad (5.30b)$$

$$B = 0.0154 - 0.0244X + 0.0686X^2 - 0.1232X^3 + 0.0616X^4 \quad (5.30c)$$

$$C = (-0.0295 + 0.1551X - 0.9586X^2 + 2.541X^3 - 2.078X^4)10^{-3} \quad (5.30d)$$

$$D = (0.0738 - 0.9527X + 6.969X^2 - 21.37X^3 + 20.94X^4)10^{-6} \quad (5.30e)$$

$$E = (-0.0982 + 2.104X - 16.89X^2 + 56.06X^3 - 58.71X^4)10^{-9} \quad (5.30f)$$

$$150℃ \leq T \leq 300℃$$

$$A = -0.0426 + 5.723X - 19.97X^2 + 39.79X^3 - 16.49X^4 \quad (5.30g)$$

$$B = 0.0157 - 0.0491X + 0.2286X^2 - 0.4118X^3 + 0.0236X^4 \quad (5.30h)$$

$$C = (-0.0258 + 0.1976X - 1.22X^2 + 2.77X^3 - 1.422X^4)10^{-3} \quad (5.30i)$$

$$D = (0.0339 - 0.3767X + 2.467X^2 - 6.613X^3 + 5.664X^4)10^{-6} \quad (5.30j)$$

$$E = 0 \quad (5.30k)$$

5.4 Exergoeconomic Analysis

Exergoeconomic analysis is an important tool to relate cost to thermodynamics, and to assess the performance of useful outputs. In this research, an exergoeconomic analysis is even more importance because all outputs are industrially useful. Not all of them, however, have high energy content. Energy and exergy efficiency only utilize hydrogen as a useful output. In order to assess the overall performance, a system of energy and exergy analysis is not sufficient. The

exergoeconomic covers all of the useful outputs, regardless of the energy content. The exergoeconomic equation for the chloralkali process can be written as

$$\dot{C}_{Brine} + \dot{Z}_a + \dot{C}_Q = \dot{C}_{H2} + \dot{C}_{Cl2} + \dot{C}_{NaOH} \quad (5.31a)$$

where $\dot{C} = c.ex$, $\dot{Z}_a$ represents the cost of equipment over the period of time of its utilization and $\dot{C}_Q$ represents the cost of energy input required for the reaction, all of these quantities are measured in \$/hr. In the photochemical process, the required energy is supplied by the sun, therefore, $\dot{C}_Q = 0$. Additionally, 90% of the total impurities present in sea water are sodium chloride; therefore $\dot{C}_{Brine}$ can also be neglected. The above exergoeconomic equation may be simplified as

$$\dot{Z}_Q = \dot{C}_{H2} + \dot{C}_{Cl2} + \dot{C}_{NaOH} \quad (5.31b)$$

Or it can also be written as

$$\dot{Z}_Q = c_{H2}ex_{H2} + c_{NaOH}ex_{NaOH} + c_{Cl2}ex_{Cl2} \quad (5.32)$$

where c_{H2}, c_{Cl2} and c_{NaOH} are unknown cost constants (measured in \$.kg/s), the hydrogen constant equation 5.32, can be written as

$$\frac{\dot{Z}_Q - c_{NaOH}ex_{NaOH} - c_{Cl2}ex_{Cl2}}{ex_{H2}} = c_{H2} \quad (5.33)$$

In the present analysis, there are three unknowns and one equation; therefore, there is no unique solution for the unknowns. Only one unknown can be determined by one equation. For this type of exergoeconomic problem, the mass flow rate is used instead of exergy. As a result, equation 5.30 can be re-written as

$$\dot{Z}_Q = c_{H2,m}\dot{m}_{H2} + c_{NaOH,m}\dot{m}_{NaOH} + c_{Cl2,m}\dot{m}_{Cl2} \quad (5.34)$$

where $c_{H2,m}, c_{Cl2,m}$ and $c_{NaOH,m}$ represents the cost flow constants, they are measured in \$/kg. Equation 5.34 can be rewritten in terms of the hydrogen flow constant as

$$\frac{\dot{Z}_Q - c_{NaOH,m}\dot{m}_{NaOH} - c_{Cl2,m}\dot{m}_{Cl2}}{\dot{m}_{H2}} = c_{H2,m} \quad (5.35)$$

If the unused portion is not enough to drive the anode reaction, then there will be an additional term added into equation 5.30.

$$c_{H2,m} = \frac{\dot{Z}_Q + \dot{C}_Q - c_{NaOH,m}\dot{m}_{NaOH} - c_{Cl2,m}\dot{m}_{Cl2}}{\dot{m}_{H2}} \quad (5.36a)$$

Here, $\dot{C}_Q$ is dependent upon the amount of energy recovered by the unused portion, along with the amount of energy required to drive the anode reaction. In equation 5.36, the market value should be used for the constants of chlorine and sodium hydroxide. It is important to mention that these constants are also time, location, and quantity dependent. Presently, in North America, the values of these constants for the bulk amounts are $c_{NaOH,m} = 1$ and $c_{Cl2,m} = 1.2$. The cost of equipment is divided into two components: namely, i) cost of heliostat and ii) cost of plant

The cost of the plant includes, tower, pump, chemicals, and other required components. The cost of the plant is scaled from a report [119] as

$$\dot{Z}_Q = \frac{(N_{Ho}A_{Ho}100) + C_{ref}\left(\frac{\dot{m}_6}{\dot{m}_{ref}}\right)^n}{T_C} \quad (5.36b)$$

where T_C represents the no. of operational seconds of the reactor in the life time of the reactor, N_{Ho} represents the number of heliostat. A_{Ho} represents the area of each heliostat(typical range is 4-6 m^2). $\dot{m}_{ref}$ represents the reference mass flow of hydrogen and C_{ref} represents the reference cost for producing $\dot{m}_{ref}$. In the present study, C_{ref} and $\dot{m}_{ref}$ are taken from a report submitted to the department of energy, which represents the cost of different hydrogen production technologies **[**119**]**. It should also be noted that 'n' represents the scaling; for solar technologies the typical value of n is 0.7.

5.5 Electrochemical Modeling

The OH^- ions are neutralized in an electrochemical process. It is important, therefore, to find the required potential for the reaction to happen. Electrochemical modeling is used to find the required potential by taking into account the decomposition voltage and ohmic losses across different components of the reactor. Chandrand and Chin [120] have discussed electrochemical modeling of a membrane based on a two-compartment chloralkali cell in an electrolysis process.

There will be, however, additional resistance due to the addition of an extra compartment in the reactor. Using Figure 5.1, the overall voltage balance across the reactor can be written as

$$V = E^o + V_A + V_{Sol,1} + V_{CEM} + V_{Sol,2} + V_{AEM} + V_{Sol,3} + V_C \quad (5.37)$$

where E^o represents the open circuit cell voltage (i.e. also known as decomposition voltage), V_A represents the voltage drop across the anode electrode, $V_{Sol,1}$ represents the voltage drop across solution 1 (i.e. voltage drop in brine solution), V_{CEM} represents the voltage drop across the cation exchange membrane, $V_{Sol,2}$ represents the voltage drop across solution 2 (i.e. voltage drop in the middle compartment), V_{AEM} represents voltage across the anion exchange membrane, $V_{Sol,3}$ represents the voltage drop across solution 1 (i.e. voltage drop in a mixture of water and electrolyte) and V_C represents the voltage drop across the cathode.

Here, each of the parameters mentioned above will be determined. At the location of the anode, the chlorine ion is oxidized into chlorine gas. The reaction is written as

$$2Cl^- \rightarrow Cl_2(g) + 2\bar{e} \quad (5.38)$$

The Nernst equation for equation 5.38 is written as

$$E_o^A = E^o_{Cl^-/Cl_2} + \frac{RT}{nF}\ln\left(\frac{P_{Cl_2}}{\gamma_{Cl^-}{}^2}\right) \quad (5.39)$$

where $E^o_{Cl^-/Cl_2}$ is the standard chlorine potential, it is available in a number of different published articles [121-126]. It is dependent upon temperature. Faita et al. [127] have presented the standard chlorine potential as a function of temperature from 25°C – 80°C.

$$E^o_{Cl^-/Cl_2} = 1.47252 + (5.82271 * 10^{-4})T - (2.90055 * 10^{-6})T^2 \quad (5.40a)$$

Mussini and Longhi [126] have also presented the chlorine electrode potential as a function of temperature and have determined it to be given as follows:

$$E^o_{Cl^-/Cl_2} = 1.48467 + (3.958492 * 10^{-4})T - (2.750639 * 10^{-6})T^2 \quad (5.40b)$$

The difference between these two correlations is 0.05V. R is the gas constant; it is equal to 8.3144621 $J\,K^{-1}\,mol^{-1}$. T represents the reactor temperature in K, whereas n represents the

electron in the reaction from equation 5.39 and n=2 for the chloralkali reaction. Also, F is representative of the Faraday constant, which is equal to 96 485.3415 s A / mol. P_{Cl_2} is the partial pressure of chlorine in the gas phase and γ_{Cl^-} and represents the activity coefficient.

At the location of the cathode, water is reduced into hydrogen gas and hydroxyl ions. The reaction is written as

$$2H_2O + 2\bar{e} \rightarrow H_2(g) + 2O\bar{H} \tag{5.41}$$

The Nernst equation for equation 5.86 at 1M water concentration can be written as

$$E_o = E^o_{H_2O/H_2+O\bar{H}} + 2.303\frac{RT}{2F}\log\left(\frac{P_{H_2}}{\gamma_{O\bar{H}}{}^{2.}}\right) \tag{5.42}$$

where $E^o_{H_2O/H_2}$represents the standard hydrogen potential, a typical value at 25°C is 0.83V can be determined. P_{H_2}represents the partial pressure of hydrogen. γ_{OH^-} is the activity coefficient of the hydroxyl ions. Equation 5.42 can be written as

$$E_o = E^o_{H_2O/H_2+O\bar{H}} + 2.303\frac{RT}{2F}\log(P_{H_2}) - 5.606\frac{RT}{2F}\log(\gamma_{O\bar{H}}) \tag{5.43}$$

The overall reaction taking place in the reactor can be calculated as

$$2NaCl + 2H_2O \rightarrow Cl_2(g) + H_2 + 2NaOH \tag{5.44}$$

The Nernst equation for the overall reaction can be written as [120]:

$$E_O = -2.18 + 0.0004272(T - 248) + \frac{8.314(T+546)\ln(\beta)}{96500} \tag{5.45}$$

Here, T is in Kelvin, β is dependent upon partial pressures of hydrogen and chlorine in the gas phase as well as the activity coefficients of sodium hydroxide and sodium chloride. β is written as

$$\beta = \frac{\gamma_{NaOH}(P_{Cl_2})^{\frac{1}{2}}(P_{H_2})^{\frac{1}{2}}}{\gamma_{NaCl}} \tag{5.46}$$

where γ_{NaOH} is dependent upon temperature and concentration levels and can be calculated as [120]

$$\log(\gamma_{NaOH}) = -\frac{U\sqrt{Mo_{NaOH}}}{1+\sqrt{2Mo_{NaOH}}} + BMo_{NaOH} + CMo_{NaOH}^2 + DMo_{NaOH}^3 + EMo_{NaOH}^4 \qquad (Mo_{NaOH} < 12) \tag{5.47}$$

where B, C, D, E and U are temperature dependent and can be estimated as

$$B = 0.0065 + 0.0016T - 1.8 * 10^{-5}T^2 \tag{5.48}$$

$$C = 0.014 - 0.0005T + 5.6 * 10^{-6}T^2 \tag{5.49}$$

$$D = 0.0006 + 5 * 10^{-5}T - 6.48 * 10^{-7}T^2 \tag{5.50}$$

$$E = 5.96 * 10^{-6} - 1.81 * 10^{-6}T + 2.4 * 10^{-8}T^2 \tag{5.51}$$

$$U = 0.00087T + 0.486 \qquad 25℃ \leq T \leq 40℃ \tag{5.52}$$

$$U = 0.00144T + 0.46 \qquad 40℃ \leq T \leq 100℃$$

For $Mo_{NaOH} \geq 12$, the activity coefficient can be estimated as

$$\log(\gamma_{NaOH}) = a + bMo_{NaOH} + cMo_{NaOH}^2 \qquad (Mo_{NaOH} \geq 12) \tag{5.53}$$

where a, b and c are temperature dependent variables, they can be evaluated as

$$a = -0.327 + 0.0031T - 3.29 * 10^{-5}T^2 \tag{5.54}$$

$$b = 0.0988 - 0.00059T \tag{5.55}$$

$$c = -2.14 * 10^{-6} - 3.93 * 10^{-7}T + 0.53 * 10^{-8}T^2 \tag{5.56}$$

The activity coefficient for sodium chloride is dependent upon concentration levels and can be evaluated as [120]

$$\gamma_{NaCl} = 0.63\exp^{0.028Mo_{NaCl}} \qquad 1.2 \leq Mo_{NaCl} < 2 \tag{5.57}$$

$$\gamma_{NaCl} = 0.575\exp^{0.07Mo_{NaCl}} \qquad 2 \leq Mo_{NaCl} < 3.5 \tag{5.58}$$

$$\gamma_{NaCl} = 0.5\exp^{0.112Mo_{NaCl}} \qquad 3.5 \leq Mo_{NaCl} < 6 \tag{5.59}$$

The voltage across brine can be determined as (i.e., $V_{Sol,\,1}$):

$$V_{Sol,1} = \left(\frac{il_1}{K_{Brine}}\right) 1000 \tag{5.60}$$

where i represents the current density, l_1 is the distance of the anode and cation exchange membrane, K_{Brine} represents the electrical conductivity of the brine. The electrical conductivity of the brine is a function of both its concentration and operating temperature and can be estimated as [120]

$$K_{Brine}(ohm^{-1}m^{-1}) = \left(1.1 - \left(0.33\sqrt{\Omega_{NaCl}}\right)\right)(\lambda_{NaCl}\Omega_{NaCl}) \tag{5.61}$$

where λ_{NaCl}, is the temperature dependent variable, it can be calculated as

$$\lambda_{NaCl} = 5.67 + 0.299T \tag{5.62}$$

Ω_{NaCl} is dependent upon the concentration and density levels of the brine and can be written as

$$\Omega_{NaCl} = \frac{Mo_{NaCl}d_{NaCl}}{1000+(58.5Mo_{NaCl})} \tag{5.63}$$

where d represents the density , it can be estimated from equation 5.27.

The voltage drops in the middle compartment (sodium hydroxide production chamber), can be calculated as ($V_{Sol,\,2}$):

$$V_{Sol,2} = \left(\frac{il_2}{K_{aq.NaOH}}\right) 1000 \tag{5.64}$$

where i represents the current density, l_2 is the distance of the anion and cation exchange membrane; $K_{aq.NaOH}$ represents the electrical conductivity of the aqueous sodium hydroxide. The electrical conductivity of the aqueous sodium hydroxide is a function of its concentration level and operating temperature; it can be calculated as [120]:

$$K_{aq.NaOH} = K_{aq.NaOH,100℃}\left(\frac{T}{373}\right)^s \exp\left(-\left(\frac{E^*}{R}\right)\left(\frac{1}{T}-\frac{1}{373}\right)\right) \tag{5.65}$$

where $K_{aq.NaOH,100^{o}C}$ represents the electrical conductivity of the aqueous sodium hydroxide at $100^{o}C$, it is dependent upon the concentration of the sodium hydroxide in the aqueous solution; it can be estimated as

$$K_{NaOH,100^{o}C}(ohm^{-1}m^{-1}) = 2.6 + 40.9\Omega_{NaOH} - 5.03\Omega_{NaOH}^{2} + 0.13\Omega_{NaOH}^{3} \quad (5.66)$$

$(2 \leq \Omega_{NaOH} < 7)$

$$K_{NaOH,100^{o}C}(ohm^{-1}m^{-1}) = 140.9 \qquad (7 \leq \Omega_{NaOH} < 9)$$

$$K_{NaOH,100^{o}C}(ohm^{-1}m^{-1}) = -1.5\Omega_{NaOH} + 156 \qquad (9 \leq \Omega_{NaOH} < 16)$$

Ω_{NaOH} is dependent upon density and concentration and it is evaluated as

$$\Omega_{NaOH} = \frac{Mo_{NaOH}d_{NaOH}}{1000+(40Mo_{NaOH})} \quad (5.67)$$

In equation 5.65, the coefficient $\frac{E^{*}}{R}$ is also dependent upon concentration and can be estimated as [120]

$$\frac{E^{*}}{R} = 4456.5 + \left((\Omega_{NaOH} - 2)(5109.5 - 4456.5)\right) \qquad (2 \leq \Omega_{NaOH} < 3) \quad (5.68)$$

$$\frac{E^{*}}{R} = 5409.6 + \left((\Omega_{NaOH} - 3)(4706.5 - 5109.8)\right) \qquad (3 \leq \Omega_{NaOH} < 4)$$

$$\frac{E^{*}}{R} = 535.2\Omega_{NaOH} + 2617.8 \qquad (4 \leq \Omega_{NaOH} < 7)$$

$$\frac{E^{*}}{R} = 967.5\Omega_{NaOH} + 548.2 \qquad (7 \leq \Omega_{NaOH} < 16)$$

$$s = -9.6 + \left((\Omega_{NaOH} - 2)(11.3 - 9.9)\right) \qquad (2 \leq \Omega_{NaOH} < 3) \quad (5.69)$$

$$s = -11.3 + \left((\Omega_{NaOH} - 3)(11.3 - 10)\right) \qquad (3 \leq \Omega_{NaOH} < 4)$$

$$s = -1.06\Omega_{NaOH} - 5.8 \qquad (4 \leq \Omega_{NaOH} < 7)$$

$$s = -2.44\Omega_{NaOH} + 5.3 \qquad (7 \leq \Omega_{NaOH} < 16)$$

The voltage drop across Sol 3 can be evaluated as

$$V_{Sol,3} = \left(\frac{il_3}{K_{aq.NaOH}}\right) 1000 \tag{5.70}$$

where l_3 represents the distance between the cathode and anion exchange membrane, the other parameters in equation 5.70 can be calculated using equations 5.65 to 5.69.

The voltage drop across the anion exchange membrane can be evaluated as

$$V_{AEM} = \left(\frac{i\sigma}{K_{AEM}}\right) 1000 \tag{5.71}$$

where i represents the current density, σ represents the membrane thickness and K_{AEM} represents the electrical conductivity of the membrane. It is dependent upon many factors, which include the chemical structure of the membrane, ionic form, operating temperature, pH of the fluids with which the membrane is in contact with, and the permeability of the membrane. It is usually estimated and provided by a membrane manufacturer after having performed the appropriate experiments.

The voltage drop across the anode can be calculated as

$$V_A = c_A \log\left(\frac{i}{i_o}\right) \tag{5.72}$$

where c_A is the constant determined experimentally, i_o represents the exchange current density. Both c_A and i_o are dependent upon the nature of the reaction (in the present study, this would be the chlorine evolution reaction, along with the operating conditions and electrode material),. For a dimensionally stable anode, the voltage drop for the chlorine evolution reaction can be calculated as

$$V_A = 0.0277 \log\left(\frac{i}{i_{o,A}}\right) \tag{5.73}$$

For graphite electrode, $i_{o,A} = 0.0125$ at 90^{o}C. The voltage drop across the anode can be determined as

$$V_C = c_c \log\left(\frac{i}{i_{o,C}}\right) \tag{5.74}$$

For the steel electrode, $c_c = 0.0656$. The exchange current density is dependent upon the amount of electrolyte concentration. When using sodium hydroxide as an electrolyte and a means for the hydrogen evaluation reaction for the steel electrode, it can be estimated as

$$\log(i_{o,C}) = -0.0045 Mo_{NaOH}^2 + 0.203 Mo_{NaOH} - 5.92 \tag{5.75}$$

The required dimensions (i.e. I_1, I_2, I_3) for the electrochemical modeling of the photo- electro chemical chloralkali reactor at CERL are shown in Figure 5.2.

For a photo-electrochemical system, the hydrogen production unit must consist of a photo catalyst, hole scavenger (or electron donor material), electrolyte, and water. In order to find the net conductivity of the hydrogen production unit, conductivities of the photo catalyst and hole scavenger (or electron donor material), is also required. In this present study, zinc sulfide is used as a photo catalyst, while sodium sulfide is used as a hole scavenger The conductivities were also measured in an aqueous solution using a conductivity probe by the Vernier instruments®. The conductivity (μS/cm) of zinc sulfide as a function of milliliters of water and grams of zinc sulfide can be determined with $\pm 1\%$ as

$$\frac{1}{(K_{ZnS})} = -0.2 + 4.34 * 10^{-3} V_{water} - 0.08 m_{ZnS} + 4.8 * 10^{-4} V_{water} m_{ZnS} - 2.5 * 10^5 V_{water}^2 + 0.04 * m_{ZnS}^2 - 1.0 * 10^{-6} V_{water}^2 m_{ZnS} - 1.5 * 10^{-4} V_{water} m_{ZnS}^2 + 6 * 10^8 V_{water}^3 - 1.9 * 10^{-3} m_{ZnS}^3 + 1.81 * 10^{-7} V_{water}^2 m_{ZnS}^2 + 8.3 * 10^{-10} V_{water}^3 m_{ZnS} - 5.4 * 10^{-6} V_{water} m_{ZnS}^3 - 4.9 * 10^{-11} V_{water}^4 - 2 * 10^{-3} m_{ZnS}^4 \tag{5.76}$$

Similarly, conductivity (μS/cm) of sodium sulfide as a function of milliliters of water and grams of sodium sulfide can be determined with $\pm 3\%$ as

$$\log_{10}(K_{Na_2S}) = 4.0 - 4.74 * 10^{-3} V_{water} + 0.6 m_{Na_2S} + 5.4 * 10^{-4} V_{water} m_{Na_2S} + 3.9 * 10^{-6} * V_{water}^2 - 0.13 m_{Na_2S}^2 + 2.9 * 10^{-4} V_{water} m_{Na_2S}^2 - 2.5 * 10^{-9} V_{water}^3 - 0.03 m_{Na_2S}^3 \tag{5.77}$$

In equations (5.76) and (5.77), V_{water} represents the volume of water (mL), m_{ZnS} represents the mass of photo catalyst (g), m_{Na_2S} represents the mass of hole scavenger (g).

This then completes the electrochemical modeling of the designed reactor.

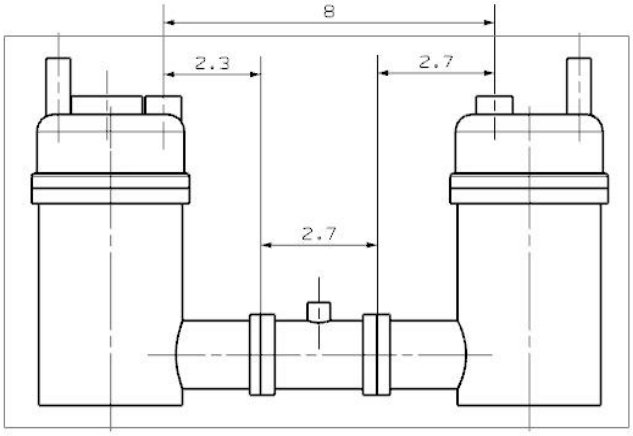

Figure 5.2: Dimensions of the photo-electrochemical process reactor required for electrochemical modeling (All dimensions are in inches).

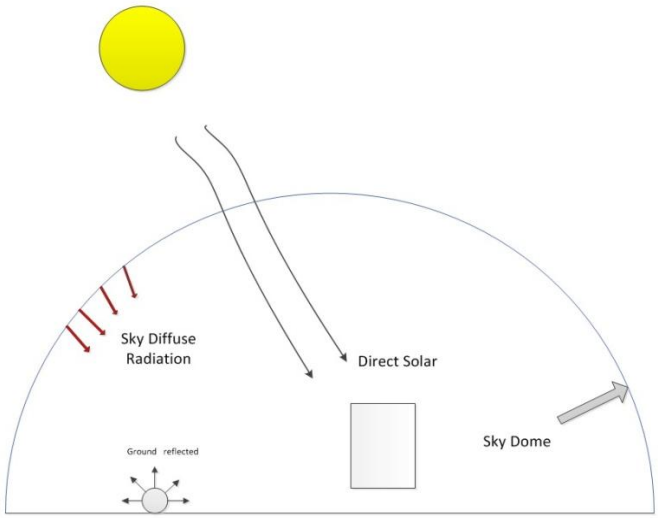

Figure 5.3: Total solar radiations on an object.

5.6 Radiation Model

The total radiation falling on a given surface is the sum of the normal, diffuse, and reflected component and can be expressed as

$$\dot{I}_t = \dot{I}_b + \dot{I}_d + \dot{I}_r \quad (5.78)$$

If the surface is tilted at an angle ∅, then the total solar radiation falling on a titled surface can be expressed as

$$\dot{I}_t = r_r \dot{I}_b + \frac{1+\cos\emptyset}{2}\dot{I}_d + \frac{1-\cos\emptyset}{2}(\dot{I}_b + \dot{I}_d)\chi \quad (5.79)$$

or it can be rewritten as

$$\dot{I}_t = r_r \dot{I}_b + \frac{1+\cos\emptyset}{2}\dot{I}_d + \frac{1-\cos\emptyset}{2}\dot{I}_t\chi \quad (5.80)$$

where $\dot{I}_b$, $\dot{I}_d$, $\dot{I}_r$ represents the beam, diffuse, and reflected components of the solar radiation on a horizontal surface, χ represents the reflectivity of the ground surface. Table 5.2 shows the reflectance values of different surfaces. The factor r_r can be determined as

$$r_r = \frac{\cos(\psi-\emptyset)\cos\delta\cos\omega+\sin(\psi-\emptyset)\sin\delta}{\cos(\psi)\cos\delta\cos\omega+\sin(\psi)\sin\delta} \quad (5.81)$$

where ψ represents the geographical latitude in degrees, ∅ represents the surface angle (also known as tilt angle) in degrees; ω represents the solar angle in radians and δ represents the declination angle.

The model develop by Iqbal [129] is adopted in order to find the normal, diffuse, and reflected component of the radiation. The normal direct radiation can be calculated as

$$\dot{I}_n = 0.9751 E_o \dot{I_{sc}} \tau_r \tau_o \tau_g \tau_w \tau_a \quad (5.82)$$

The eccentricity correction factor (E_o) can be calculated as

$$E_o = 1.00011 + 0.034221\cos\ + 0.00128\sin\ + 0.000719\cos 2\ + 0.000077\sin 2 \quad (5.83)$$

where is the day angle, it can be estimated in radians as

$$= 2\pi\left(\frac{N-1}{365}\right) \quad (5.84)$$

where N is the day number of the year,(i.e. for January 1 N=1 and for December 31, N=365),the dimensionless Rayleigh constant can be found as

$$_{r} \quad e^{-0.0903m_a^{0.84}(1\ \ m_a - m_a^{1.01})} \tag{5.85}$$

where m_a represents the air mass at actual pressure, m_r represents the mass at standard pressure (i.e. 101 kPa). m_a, however, can be correlated with m_r as

$$m_a = m_r\left(\frac{p}{1013.25}\right) \tag{5.86}$$

where p is the local pressure of air in millibars, the air mass at standard pressure can be estimated as

$$m_r = [\cos\theta_z + 0.15(93.885 - \theta_z)^{-1.253}]^{-1} \tag{5.87}$$

The dimensionless ozone constant can be calculated as

$$\tau_o = 1 - [0.1611U_3(1 + 139.48U_3)^{-0.3035} - 0.002715U_3(1 + 0.044U_3 + 0.0003U_3^2)^{-1}] \tag{5.88}$$

where U_3 is the ozone relative optical length, it can be calculated as

$$U_3 = l_{0z}m_r \tag{5.89}$$

Here, l_{0z} represents the vertical ozone layer thickness in centimeters. For this study it is determined to be 0.35cm [128].

The dimensionless gas constant can be determined as

$$\tau_g = e^{-0.0127m_a^{0.26}} \tag{5.90}$$

The dimensionless water constant can be calculated as

$$\tau_w = 1 - 2.4959U_1[(1 + 79.034U_1)^{0.6828} + 6.385U_1]^{-1} \tag{5.91}$$

where U_1 is the pressure corrected relative optical path length in centimeters.

$$U_1 = wm_r \tag{5.92}$$

where w represents the water vapour thickness at standard ambient conditions (i.e. P=101.325kPa and T=298K) in centimeters, the actual thicknesses w' can be estimated at other temperatures and pressures as

$$w = w' \left(\frac{p}{1013.25}\right)^{\frac{3}{4}} \left(\frac{273}{T}\right)^{\frac{1}{2}} \tag{5.93}$$

$$w' = 0.1e^{2.2572+0.05454T_{dew}} \tag{5.94}$$

where T_{dew} represents the dew point temperature

The dimensionless aerosols constant can be estimated as

$$\tau_a = e^{-l_{ao}^{0.873}(1+l_{0a}-l_{ao}^{0.7808})m_a^{0.9108}} \tag{5.95}$$

l_{0a} is the aerosol optical thickness and can be calculated as

$$l_{ao} = 0.2758l_{ao;\lambda|\lambda=0.38\mu m} + 0.35l_{ao;\lambda|\lambda=0.5\mu m} \tag{5.96}$$

An alternative correlation to calculate dimensionless aerosol constants (as a function of visibility), can be written as [129]

$$\tau_a = (0.97 - 1.265V_{is}^{-0.66})^{m_a^{0.9}} \tag{5.97}$$

where V_{is} is the visibility in kilometers, which can be calculated as

$$V_{is} = 147.994 - 1740.523[\beta_1\varphi - (\beta_1^2\varphi^2 - 0.17\beta_1\varphi + 0.011758)^{0.5}] \tag{5.98}$$

Here, φ can be calculated as

$$\varphi = 0.55^{-\beta_2} \tag{5.99}$$

where β_1 and β_2 are the Angstrom turbidity-parameters, the typical value for $\beta_2$is 1.3 [129]. The typical values for β_1 are given in Table 5.3

Table 5.2: Reflectance values for different surfaces [130-140].

Material/Category	**Reflectance**
Concrete	0.23
Cement board	0.25
Brick (clay brick)	0.3
Limestone	0.28
Steel	0.18
Shingles, asphalt	0.14
Granite	0.33
Sandstone	0.35
Wood, unpainted	0.4
Wood, painted	0.38
Iron	0.13
Site exposure	**Reflectance of snow-covered ground**
Typical city center	0.2
Typical urban site	0.4
Typical rural site	0.5
Isolated rural site	0.7
Soil and Vegetation	
Soil (Dark & Wet)	0.05~0.4
Soil (Light & dry)	0.15~0.45
Grass (Long to short)	0.16~0.26
Agricultural crops	0.18~0.25
Tundra	0.18~0.25
Forest (Delicious)	0.15~0.20
Forest (Coniferous)	0.05~0.15
Snow (old to fresh)	0.40~0.95

Table 5.3: Typical values of $\boldsymbol{\beta_1}$ [129]

Weather Condition	β_1
Clean	0
Clear	0.1
Turbid	0.2
Very turbid	0.4

The beam component of the total radiations can be found as

$$\dot{I}_b = \cos\theta_z \dot{I}_n \tag{5.100}$$

where θ_z is the zenith angle, the zenith angle can be calculated as

$$\cos\theta_z = \cos\delta\cos\psi\cos\omega + \sin\delta\sin\psi \tag{5.101}$$

where ψ is the geographical latitude, ω is the solar hour angle; δ is the solar declination angle and can be estimated as

$$\delta = 23.45 \sin\left(\frac{360(N+284)}{365}\right) \tag{5.102}$$

The hour angle ω is an angular measure of time. It is dependent upon local solar time (ST) and can be calculated as

$$\omega = 15(12 - ST) \tag{5.103}$$

The local solar time is a function of local standard time and is ultimately an equation of time. It can be determined as

$$ST = LT + \frac{ET}{60} - \frac{4}{60}(L_s - L_L) \tag{5.104}$$

where LT represents the local standard time, L_S is the standard meridian for the local time zone; L_L is the longitude of the location in degrees, whereas ET is the equation of time and can be calculated as

$$ET = 9.87\sin 2B - 7.53\cos B - 1.5\sin B \tag{5.105}$$

Here, B can be calculated as

$$B = \frac{360(N-81)}{365} \tag{5.106}$$

The diffuse component can be calculated as

$$\dot{I}_d = \dot{D}_r + \dot{D}_a + \dot{D}_m \tag{5.107}$$

where $\dot{D}_r$ represents the Rayleigh scattering after the first pass through the atmosphere, $\dot{D}_a$ represents the aerosols scattering after the first pass through the atmosphere. $\dot{D}_m$ represents the reflection processes between the ground and sky. All of which are measured in W/m^2

The Rayleigh scattering factor of the diffuse radiation can be calculated as

$$\dot{D}_r = \frac{0.79\dot{I}_{sc}\sin\alpha\tau_0\tau_g\tau_w\tau_{aa}0.5(1-\tau_r)}{1-m_a+m_a^{1.02}} \quad (5.108)$$

where $\dot{I}_{sc}$ represents the solar constant and its value of 1367 W/m^2, α represents the solar altitude and can be related with zenith angle as

$$\cos\theta_z = \sin\alpha \quad (5.109)$$

Here, τ_{aa} is the dimensionless constant and can be determined as

$$\tau_{aa} = 1 - (1-\omega_0)(1 - m_a + m_a^{1.06})(1-\tau_0) \quad (5.110)$$

where ω_0 is the single-scattering albedo fraction of the incident energy scattered to total attenuation by aerosols. Typical value of ω_0 is 0.9.

Note that the aerosols scattering after the first pass through the atmosphere of the total diffuse radiations and can be calculated as

$$\dot{D}_a = \frac{0.79\dot{I}_{sc}\sin\alpha\tau_0\tau_g\tau_w\tau_{aa}F_c(1-\tau_{as})}{1-m_a+m_a^{1.02}} \quad (5.111)$$

τ_{as} is dimensionless factor and can be related to τ_a and τ_{aa} as

$$\tau_{as} = \frac{\tau_a}{\tau_{aa}} \quad (5.112)$$

F_c is the ratio of forward scattering to total scattering. Typical value is $F_c = 0.84$.

The reflection processes between the ground and sky ($\dot{D}_m$) can be estimated as

$$\dot{D}_m = \frac{(\dot{I}_n\sin\alpha+\dot{D}_r+\dot{D}_a)\rho_g\rho_a}{1-\rho_g\rho_a} \quad (5.113)$$

Table 5.4: Typical values of $\boldsymbol{\rho_g}$ [129-131]

Material	ρ_g
Concrete	0.09
Uncolored concrete	0.35
White glazed surface	0.74
Grass	0.17.0.28
Wheat	0.16.0.26
Maize	0.18-0.22
Beets	0.18
Potato	0.19
Rain forest	0.12
Deciduous forest	0.10-0.20
Coniferous forest	0.05.0.15
Sub-artic	0.09-0.20
Savannah	0.16.0.21
Steppe	0.20
Fresh snow	0.75.0.95
Old snow	0.40-0.70
Wet dark soil	0.08
Dry dark soil	0.13
Dry sand	0.35
Boreal forest with snow	0.12.0.30
Dune sand	0.24
Sandy loam	0.10-0.19
Clay loam	0.10-0.14

where ρ_g is the dimensionless parameter represents the albedo of the ground and it is dependent upon weather conditions typical values are given in Table 5.4.

where ρ_a represents the albedo of the cloudless sky

$$\rho_a = 0.0685 + (1 - F_c)(1 - \tau_{as}) \tag{5.114}$$

This completes the radiation modeling. Combining the radiation model with the thermodynamic model can be used to predict the rate of hydrogen at a given time and location.

Chapter 6

Results and Discussion

6.1 Introduction

In this chapter, experimental results and analysis, parametric study of the electrochemical modeling, thermodynamic modeling, exergoeconomic analysis, and radiation modeling are presented in order to complete the photo-electrochemical chloralkali process.

6.2 Electrode for Chlorine Reaction

Chlorine is a corrosive gas that reacts with almost all elements. It even reacts with hydrocarbons; therefore, it is important to find a suitable material to act as the electrode when working in chlorine production media. Five different materials are tested.

6.2.1 Nickel

Nickel, when tested as an anode, reacts with chlorine and forms a jelly-like, greenish structure on its surface. This greenish structure is nickel chloride. The chemical reaction for the formation of nickel chloride occurs given as follows:

$$\mathrm{Ni} + \mathrm{Cl_2} \rightarrow \mathrm{NiCl_2} \tag{6.1a}$$

Corrosion-resistant nickel is not dimensionally stable in anolyte compartments; Therefore, it cannot be used in an anolyte compartment. Figure 6.1 shows the greenish structure that forms on the surface of the electrode.

Figure 6.1: Effect of chlorine on corrosion resistant nickel.

6.2.2 Multi-Purpose Copper

Due to its high level of electrical conducitivity, corrosion-resistant, multi-purpose copper is also tested. Chlorine also reacts with copper and forms copper chloride; the reaction occurs given as follows

$$Cu + Cl_2 \rightarrow CuCl_2 \qquad (6.1b)$$

Here, Figure 6.2 shows the formation of copper chloride on the surface of the electrode. This formation indicates that multi-purpose copper cannot be used as the anode because of its unstable nature in chlorine.

Figure 6.2: Effect of chlorine on multi-purpose copper.

6.2.3 Multi-Purpose Aluminum

Alumnium is a light-weight metal and has a high level of electrical condivity. Alumnium forms alumnium chloride when used as an anode in the chloralkali process. The reaction occurs given as follows:

$$2Al + 3Cl_3 \rightarrow 2AlCl_3 \qquad (6.1c)$$

Figure 6.3 shows the formation of alumnium chloride on the surface of the electrode. One can conclude that multi-purpose alumnium cannot be used as the anode because of its unstable nature in chlorine.

Figure 6.3: Effect of chlorine on corrosion-resistant aluminum.

6.2.4 Stainless Steel

Stainless steel is commonly used as an anode in many different chemical reactions because of its corrosion-resistant nature and good electrical conducitivity. It is not, however, stable in chlorine media. The iron in the steel reacts with chlorine to form iron chloride (i.e. a yellowish layer on the surface of electrode). The reaction occurs given as follows:

$$2\mathrm{Fe} + 3\mathrm{Cl}_2 \rightarrow 2\mathrm{FeCl}_3 \qquad (6.1\mathrm{d})$$

One can conclude that stainless steel cannot be used as the anode because of its unstable nature in chlorine.

6.2.5 Graphite

Graphite is the only stable electrode in chlorine. Due to its strong lattice bonding, it has a very stable structure. Graphite is a good electrical conductor due to an unbonded free electron in one direction .It also acts as an insulator in the other direction. The present electrode study concluded that between two different materials tested only graphite can be used as an anode for the production of chlorine.

6.3 Results of Electrolysis Experiments

6.3.1 Effect of Voltage, Brine and Electrolyte Concentration

6.3.1.1 Rate of Hydrogen Production

A linear model is used to find the effect of brine and electrolyte concentration levels as well as, voltage levels on the rate of hydrogen production. Table 6.1 shows ANOVA for the rate of hydrogen production. The Model F-value of 1244.81 implies the model is significant. There is

onlya 0.01% chance that a "Model F-Value" this large could occur due to noise. The values of "Prob > F" less than 0.0500 indicate that the model terms are significant. In this case C (Voltage) are significant model terms. The values greater than 0.1000 indicate that the model terms are not significant. To improve the accuray of the model, square root transformation along with backward elimination (i.e. the elimintation of all the terms from the model that do not have an effect on the response) is applied. Table 6.2 shows the removed terms that have a p-value greater than 0.1. "Adeq Precision" measures the signal to noise ratio. A ratio greater than 4 is desirable [23]. Adeq Precision for the hydrogen model is 67.533, which indicates an adequate signal. This model can then be used to navigate the design space. The regression for the rate of hydrogen production for the performed experiments can be written as

$$\sqrt{\dot{m}_{H2}} = 0.19 + 0.067V \quad (6.2)$$

where V represents the applied voltage in Volts. $R^2_{H2} = 0.96$ between the experimental data and statistical model prediction from equation 6.2.

Table 6.1: ANOVA for the rate of hydrogen production

Transform: Square root					
ANOVA for Response Surface Linear Model-H_2					
Source	Sum of Squares	df	Mean	F- Value	p-value
Model	10.58086	1	10.58086	1244.813	< 0.0001
C- Voltage (V)	10.58086	1	10.58086	1244.813	< 0.0001
Residual	0.492998	58	0.0085		
Cor Total	11.07386	59			

Table 6.2: Backward elimination for the rate of hydrogen production

Backward Elimination Regression with Alpha to Exit = 0.100			
Removed	Estimate	Coeff=0	Prob > |t|
B-Electrolyte	0.012752	0.580074	0.56419
A-Brine	-0.01644	-1.03036	0.30719

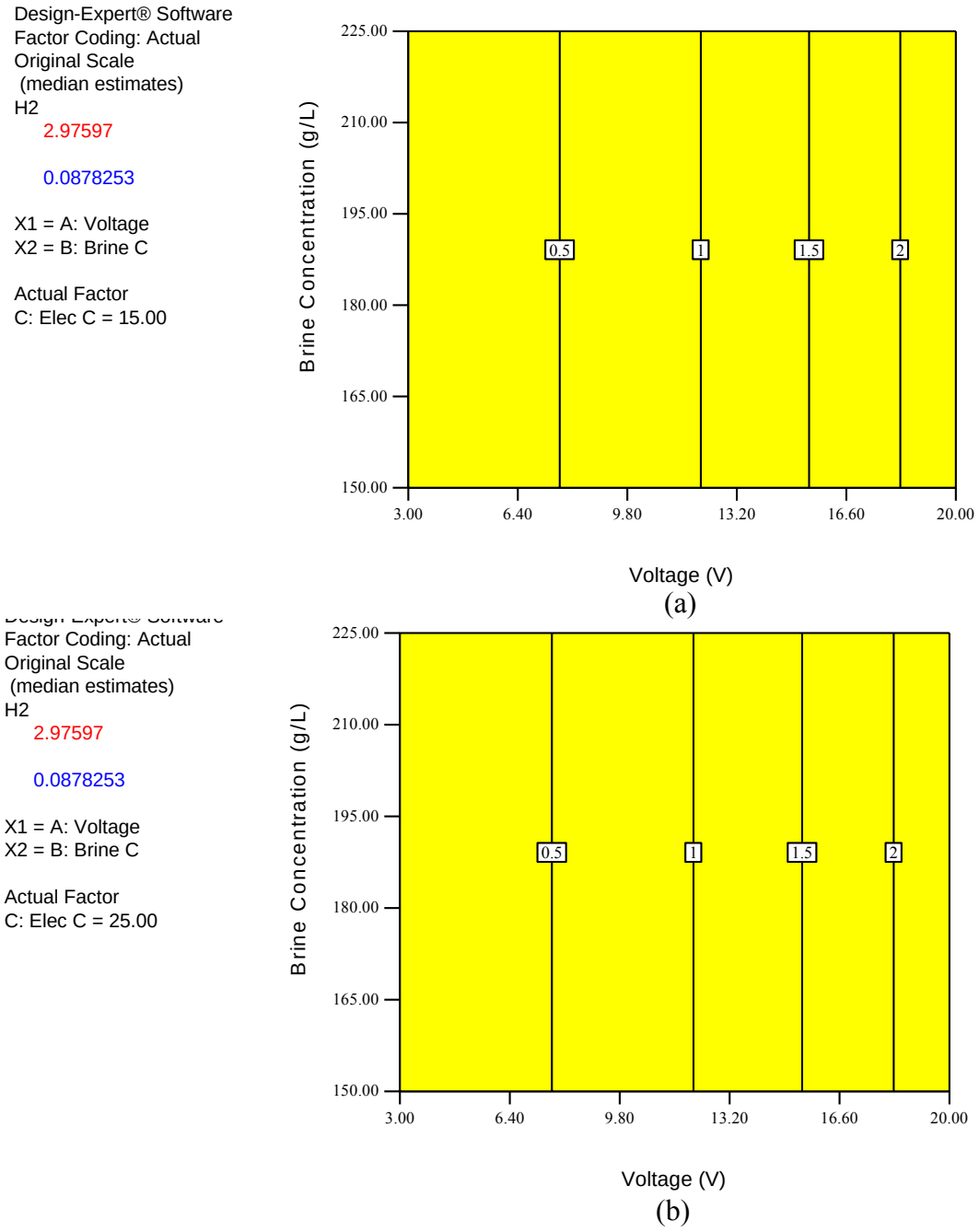

Figure 6.4: Effect of voltage (V) and brine concentration levels (g/425mL) on rate of hydrogen production (µg/s) at an electrolyte concentration of a) 15g/425mL b) 25g/425mL.

As suggested by the ANOVA model evidence, the only significant factor is the applied voltage. Increasing the applied voltage results in an increase to the rate of hydrogen production. Increasing or decreasing the concentration levels of the brine and electrolyte does not have a significant effect on the rate of hydrogen production. Figure 6.4 shows the interaction between

the applied voltage and the brine concentration level at a minimum and maximum electrolyte concentration and their mutual effect of these factors on the rate of hydrogen production. It should be noted that varying concentration levels are not significantly affecting the hydrogen production rate. This is because of the fact that changing the brine and electrolyte concentration changes the voltage drop across the solutions. This change in voltage drop is due to the change in electrical conductivity of the solution. However, changes in solution voltage drop are negligibly small. Due to which brine and electrolyte concentration do not have any significant effect on production rate. More details are given in Section 6.9.

6.3.1.2 Rate of Chlorine Production

A linear model is used to find the effect of the brine concentration levels, electrolyte concentration levels, and voltage on the rate of chlorine production. Table 6.3 shows ANOVA for the rate of chlorine production. The Model F-value of 1244.81 implies that the model is significant. There is only a 0.01% chance that a "Model F-Value" this large could occur due to noise. In this case, C (Voltage) are significant model terms. To improve the accuray of the model, square root transformation along with backward elimination. Table 6.4 shows the removed terms that have a p-value greater than 0.1. Adeq Precision (signal to noise ratio [23]) for the chlorine model is 67.5, which indicates an adequate signal.

Table 6.3: ANOVA for the rate of chlorine production

Transform: Square root						
ANOVA for Response Surface Linear Model-Cl_2						
Source	Sum of Squares	df	Mean Square	F- Value	p-value	
Model	370.3301	1	370.3301	1244.813	< 0.0001	Significant
C-Voltage	370.3301	1	370.3301	1244.813	< 0.0001	
Residual	17.25492	58	0.297499			
Cor Total	387.585	59				

Note that the regression for the rate of chlorine production for the performed experiments can be written as

$$\sqrt{\dot{m}_{Cl2}} = 1.15 + 0.38V \quad (6.3)$$

where V represents the applied voltage in Volts, $R^2_{Cl2} = 0.96$ between the experimental data and statistical model prediction from equation 6.3.

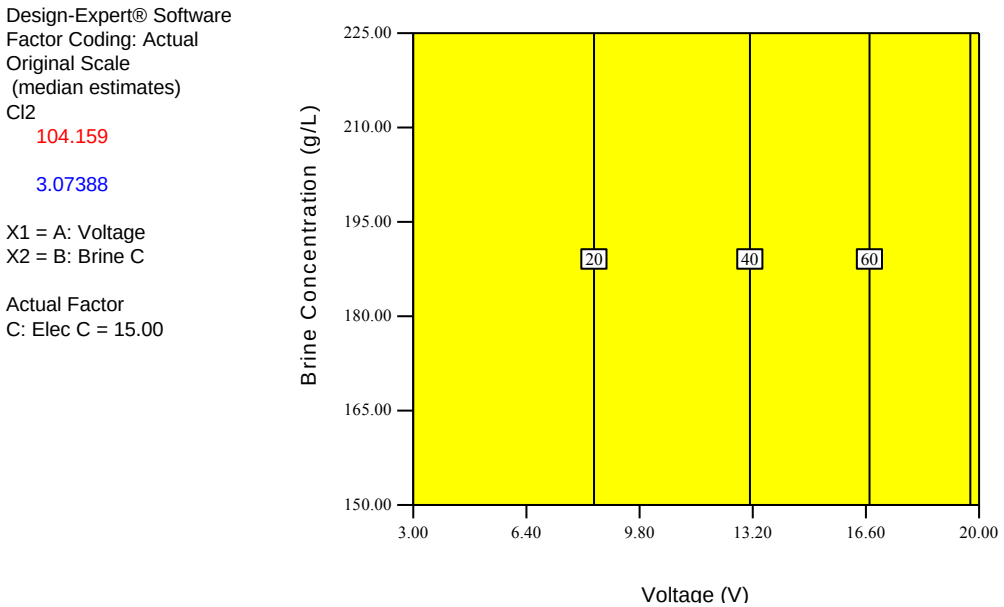

(a)

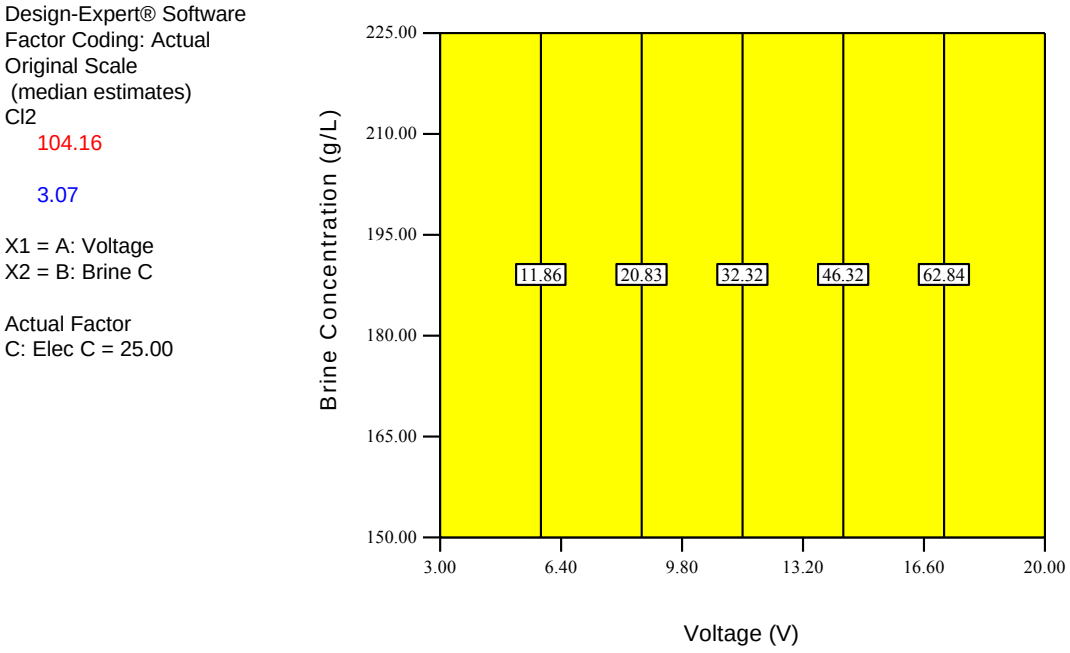

(b)

Figure 6.5: Effect of voltage (V) and brine concentration levels (M) on the rate of chlorine production (µg/s) at an electrolyte concentration level of a) 15g/425mL b) 25g/425mL.

Table 6.4: Backward elimination for the rate of chlorine production

Backward Elimination Regression with Alpha to Exit = 0.100			
Removed	Estimate	Coeff=0	Prob > |t|
B-Electrolyte	0.07544	0.580074	0.56419
A-Brine	-0.09729	-1.03036	0.30719

As suggested by the ANOVA model, applied voltage is the only significant factor. Increasing the applied voltage increases the rate of chlorine production because of high energy input in the system. Increasing or decreasing the concentration level of the brine and electrolyte levels does not have a significant effect on the rate of chlorine production (because of negliabile small voltage drop across anolyte solution). Figure 6.5 shows the interaction between applied voltage and brine concentration levels at a minimum and maximum electrolyte concentration and their mutual effect on the rate of chlorine production.

6.3.1.3 Rate of Sodium Hydroxide Production

A linear model is used to find the effect of brine and electorlyte concentration levels, along with the voltage levels on the rate of sodium hydroxide production. Table 6.5 shows ANOVA for the rate of hydrogen production. The Model F-value of 1244.81 implies that the model is significant. In this case, C (Voltage) are significant model terms. To improve the accuray of the model, square root transformation along with backward elimination is applied. Table 6.6 shows the removed terms that have a p-value that is greater than 0.1. Adeq Precision (signal to noise ratio [23]) for the sodium hydroxide model is 68, which indicates an adequate signal.

Table 6.5: ANOVA for the rate of sodium hydroxide production

Transform: Square root						
ANOVA for Response Surface Linear Model-NaOH						
Source	Sum of Squares	df	Mean Square	F- Value	p-value	
Model	423.2344	1	423.2344	1244.813	< 0.0001	significant
C-Applied	423.2344	1	423.2344	1244.813	< 0.0001	
Residual	19.71991	58	0.339998			
Cor Total	442.9543	59				

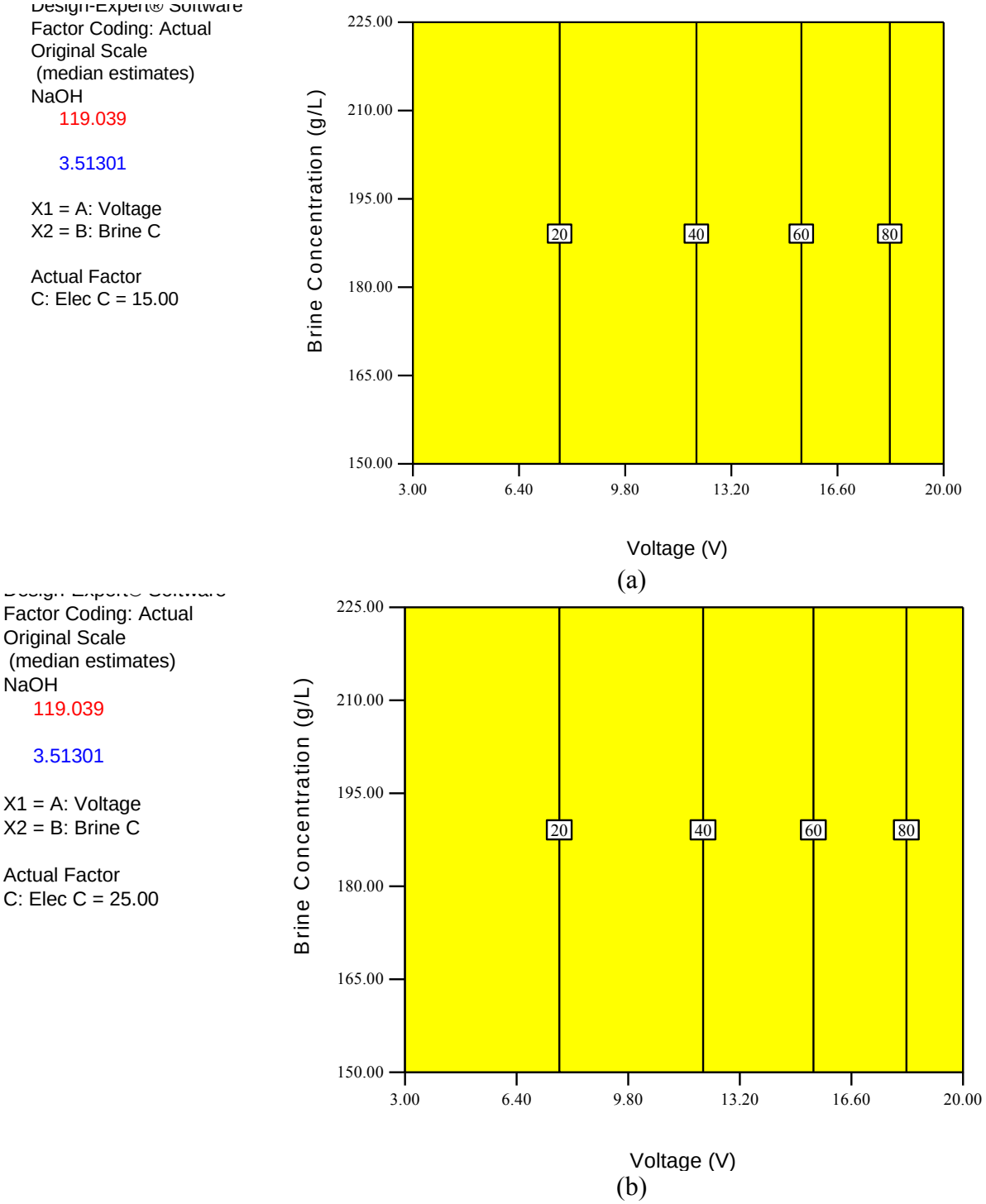

Figure 6.6: Effect of voltage (V) and brine concentration (g/L) on rate of sodium hydroxide (µg/s) at an electrolyte concentration of a) 15g/425mL b) 25g/425mL.

The regression for the rate of hydrogen production for the performed experiments can be written as

$$\sqrt{\dot{m}_{NaOH}} = 1.23 + 0.41V \quad (6.4)$$

where V represents the applied voltage in Volts, $R^2_{NaOH} = 0.95$ between the experimental data and statistical model prediction from Equation 6.4.

Table 6.6: ANOVA for the rate of sodium hydroxide production

Backward Elimination Regression with Alpha to Exit = 0.100			
Removed	Estimate	Coeff=0	Prob > |t|
B-Electrolyte	0.080648	0.580074	0.564191
A-Brine	-0.10401	-1.03036	0.307195

As suggested by the ANOVA model, applied voltage is the only significant factor. Increasing the applied voltage, increases the rate of sodium hydroxide production. This is because of higher production of Na^+ and OH- ions in anolyte and catholyte solution at high voltages. Increasing or decreasing the concentration levels of the brine and electrolyte does not have a significant effect on the rate of sodium hydroxide production (i.e. because of negiliable small voltage drop in the solution between anion and cation exchange membrane). Figure 6.6 shows the interaction between applied voltage and the brine concentration at a minimum and maximum electrolyte concentration, and their mutual effect on the rate of sodium hydroxide production.

6.3.1.4 Results of Efficiency for VBE

Using equations 5.20b and 5.22, energy and exergy efficiency rates are also calculated. As stated earlier, brine and electrolyte concentration levels do not affect the rate of chloralkali production. Increasing the voltage successfully increases the production rate of chloralkali products, but it also increases the energy input to the system. During the experiments, increasing the voltage also increases the current, which subsequently increases the energy input to the system (compared to the formation rate of chloralkali products). The energy and exergy efficiency levels decrease with an increase in voltage. This is because of the increase in energy input to the system. Also, chlorine and sodium hydroxide have a very low energy content (i.e. chlorine and sodium hydroxide are important industrial chemicals but they are not used as fuel) which results in lower efficiency.

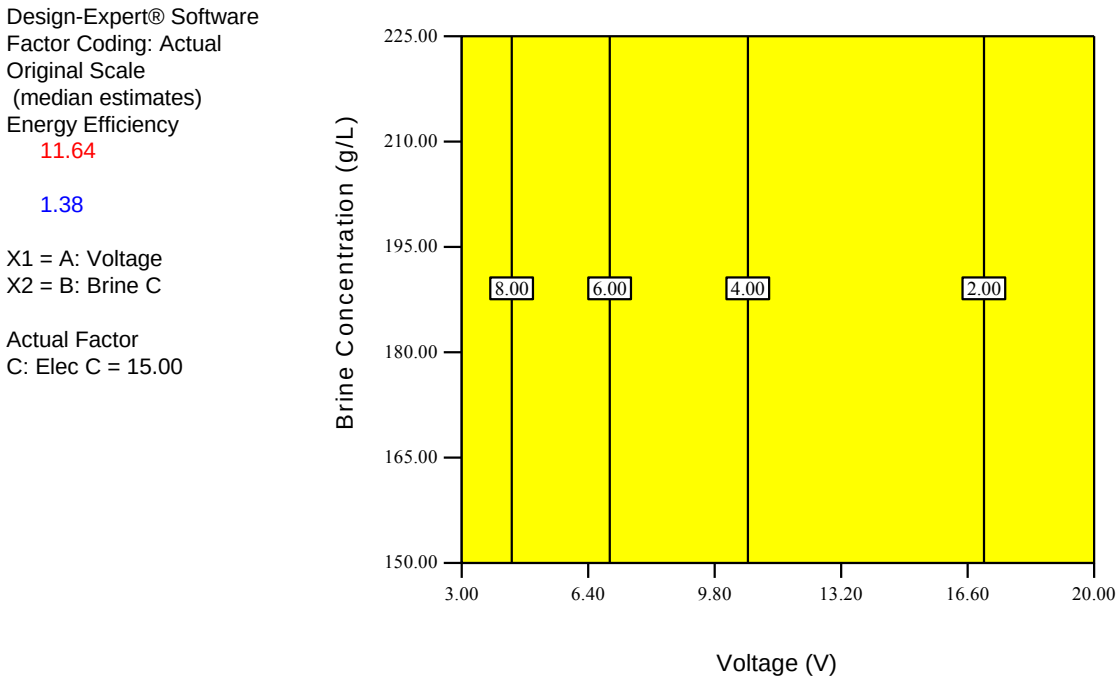

Figure 6.7: Effect of voltage (V) and brine concentration level (g/L) on energy efficiency at an electrolyte concentration level of 15g/425mL.

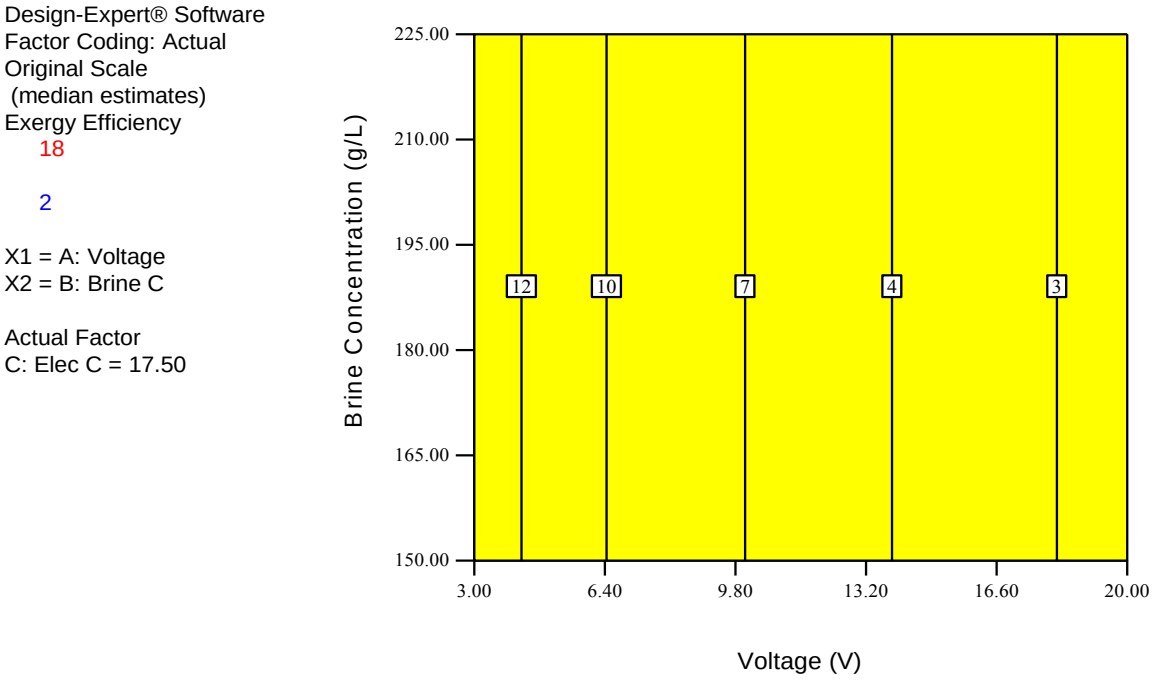

Figure 6.8: Effect of voltage (V) and brine concentration levels (g/L) on exergy efficiency values at an electrolyte concentration level of 17.5g/425mL.

Figures 6.7 and 6.8 show the interaction between applied voltage and brine concentration levels and their mutual effect on energy and exergy efficiency values of the system. The value of exergy efficiency is higher than energy efficiency. This is because of the addition of chemical exergies of chlorine and sodium hydroxide in the numerator term of exergy efficiency.

6.3.1.5 Optimization Results

The previous analysis shows that brine and electrolyte concentration have a small effect on the production rate of chloralkali products. It is still important, however, to find the optimal concentration levels that can maximize the energy and exergy efficiency values of the reactor for the next set of experiments. Stat-ease® 8.1.6 is used to find the optimal concentration levels at a given voltage. Stat-ease® defines a variable known as "desirability". Desirability characterizes how close the target is from the sample. Its value varies from 0 to 1; whereby 0 indicates highly non-desirable status, and 1 indicates a highly desirable status. Stat-ease® uses a method developed by Derringer and Suich. Table 6.7 shows the constraints present for optimization.

Table 6.7: Constraints for optimization of brine concentration, electrolyte concentration and applied voltage

Constraints						
Name	Goal	Lower Limit	Upper Limit	Lower Weight	Upper Weight	Importance
Brine Concentration (g/L)	Input Term	150	225	1	1	3
Electrolyte Concentration (g/425mL)	Input Term	15	25	1	1	3
Voltage (V)	Input Term	3	20	1	1	3
η_{en}(%)	Maximize	1.38	11.63	1	1	5
η_{exe}(%)	Maximize	2.13	17.89	1	1	5

Note that the objective desirability function for the constraints set in Table 6.7 can be written as

$$d_{exe} = \frac{\eta_{exe} - 2.13}{15.76} \tag{6.5}$$

$$d_{en} = \frac{\eta_{en} - 1.38}{10.25} \tag{6.6}$$

$$D = \sqrt{d_{exe} d_{en}} \tag{6.7}$$

where d_{exe} and d_{en} represents the individual desirabilites of energy and exergy efficiencies, and D represents the overall desirability. Figure 6.9 shows the interaction between the brine and electrolyte concentration levels and their mutual effect on the desirability factor at different voltages. It is evident that increasing the voltage causes a reduction to the desirability. Table 6.8 shows the optimal solutions obtained by using the Stat-ease®.

Table 6.8: The results of optimal solutions for VBE experiments.

No.	Voltage (V)	Brine Concentration (g/425mL)	Electrolyte Concentration (g/425mL)	η_{en} (%)	η_{exe} (%)	Desirability
1	3	225	25	10.17	15.6381	0.857171
2	3	150	15	10.17	15.6381	0.857171
3	5	200	25	7.52	11.5665	0.598818
4	5	150	20	7.52	11.5665	0.598818
5	10	150	20	4.08	6.26493	0.262422
6	10	200	20	4.08	6.26493	0.262422
7	15	225	15	2.07	3.18685	0.06711

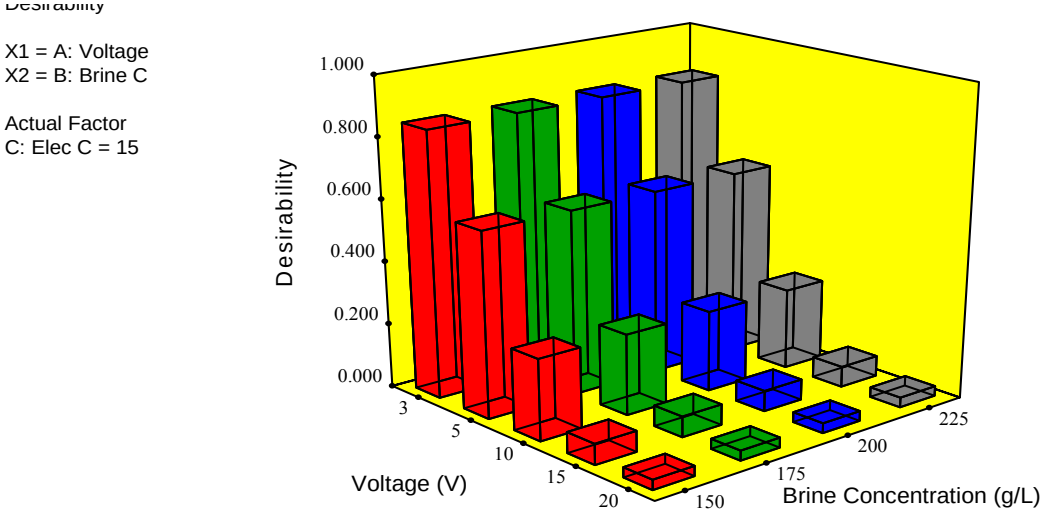

(a)

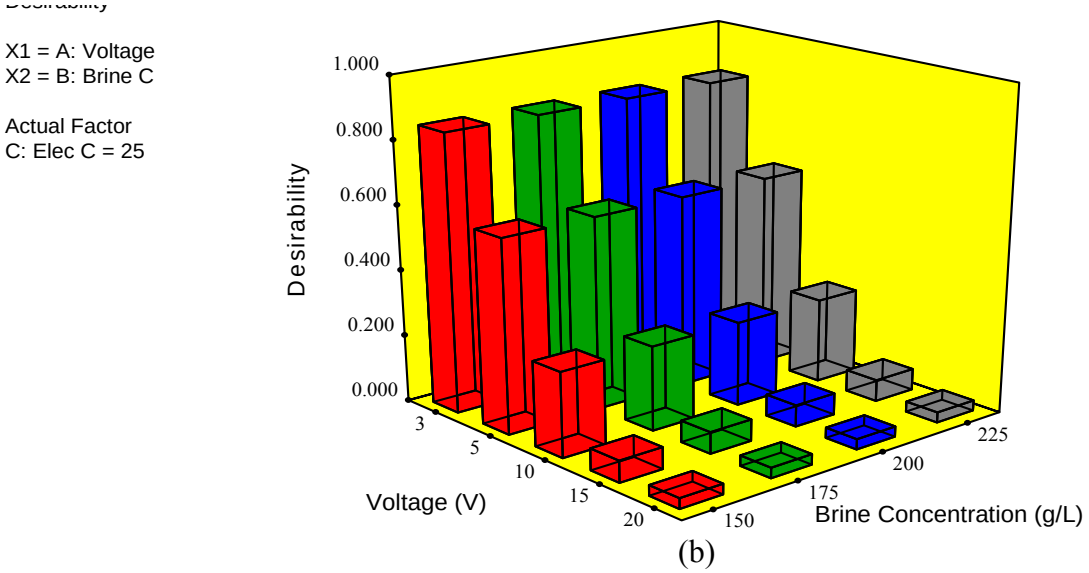

(b)

Figure 6.9: Effect of applied voltage (V) and brine concentration levels (g/425mL) on desirability factor at an electrolyte concentration level of a) 15g/425mL and b) 25g/425mL.

6.3.2 Effect of Temperature

During the VBE experiments, it is observed that the chlorine partial pressure is less than the level of hydrogen. Ideally, it should be equal to the hydrogen pressure level. For comparison purposes, Figure 6.10 shows the partial pressure level of hydrogen and chlorine for one of the tests from Table 3.1.

The reason for the lower partial pressure of chlorine is due to the fact that at a given temperature there is a higher solubility level of chlorine than there is of hydrogen in water. Solubility is strongly dependent upon temperature. Chlorine solubility decreases with an increase in temperature. Figure 6.11 shows the solubility of chlorine and hydrogen in water as a function of temperature. When increasing the temperature of the brine, one should also consider the stability of membranes. Usually, ion exchange membranes do not support very high temperatures.

Figures 6.12 and 6.13 show the partial pressure of the hydrogen and chlorine at different temperatures at 20V. Figure 6.12 shows that, with an increase in temperature, the solubility decreases which result in increased partial pressures of hydrogen and chlorine. Another reason for the increase to the production rate of gasses is due to the higher conductivity level of the electrolyte at higher temperatures. Higher conductivity results in lower over potential voltage

drop, which increases the production rate. The activity coefficients of the electrolyte source (NaOH in present study) decrease with an increase in temperature.

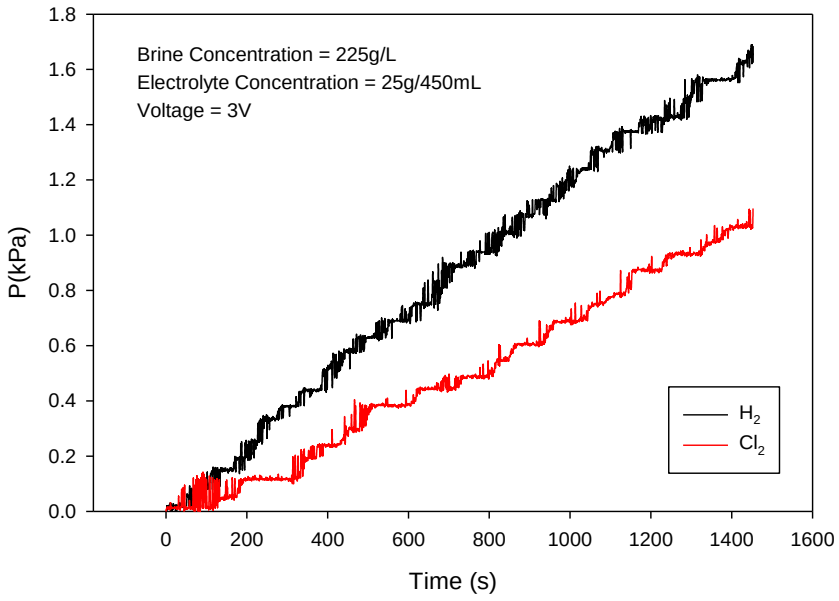

Figure 6.10: Partial pressure of hydrogen and chlorine.

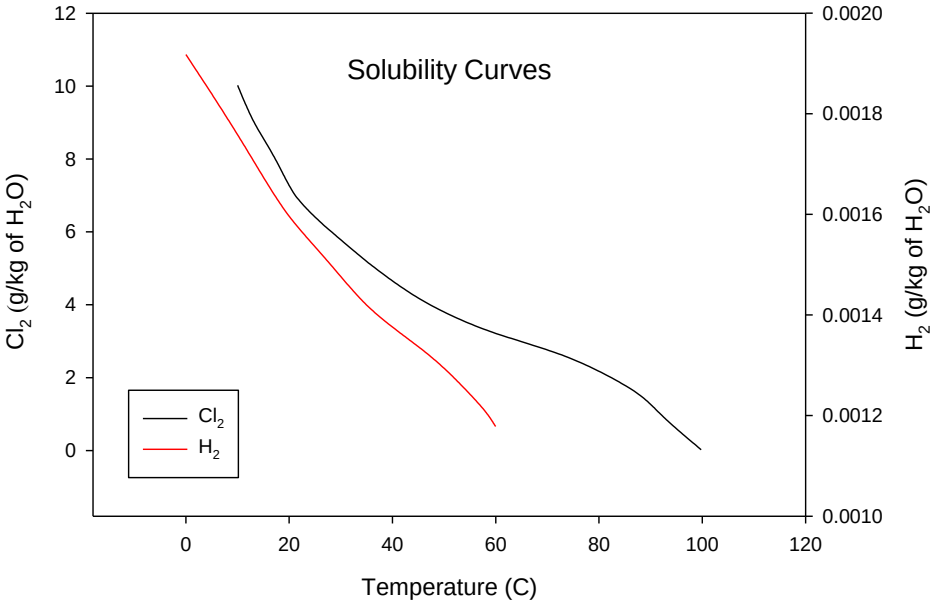

Figure 6.11: Solubility of chlorine and hydrogen in water at different temperatures.

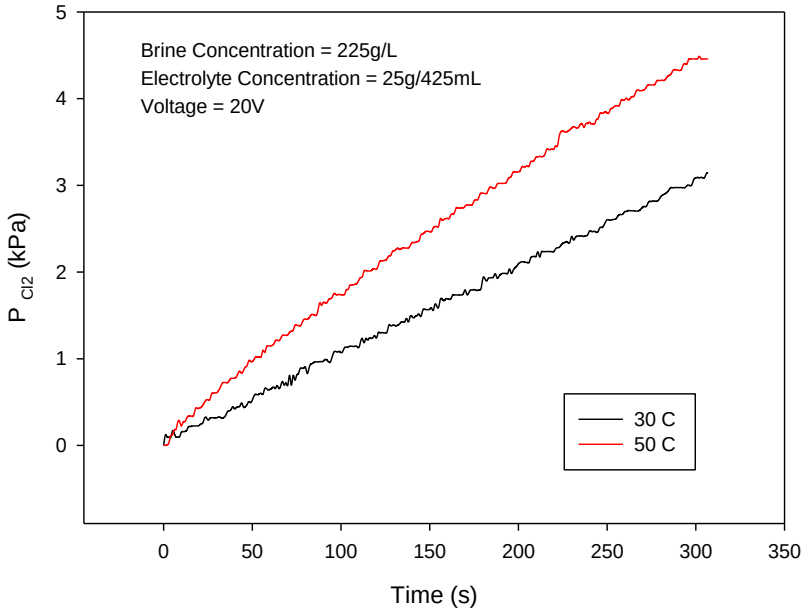

Figure 6.12: Partial pressure of chlorine at different temperatures at 20V.

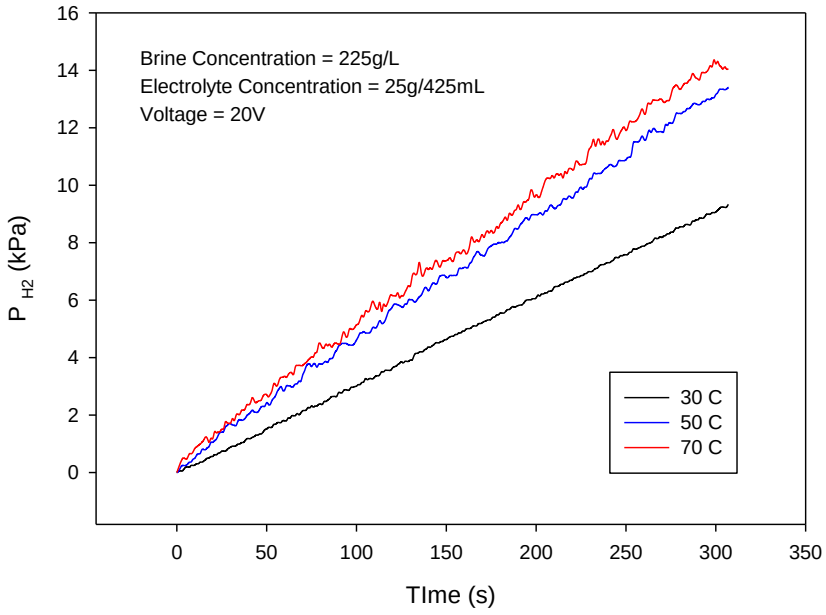

Figure 6.13: Partial pressure of hydrogen at different temperatures at 20V.

6.3.3 Effect of Electrode Surface Area

The electrode surface that is in contact with the working fluid (i.e., water and sodium hydroxide on the cathloyte and brine on the anolyte side), has a significant effect on the rate of hydrogen production. Changing the electrode height, changes the current density (due to the change in the electrode area in contact with fluid) which also changes the rate of production. Experiments are performed with two different electrodes of the same material at different heights (i.e. with nickel cathode). Increasing the electrode area (in contact with the water), increases the rate of hydrogen production and decreases the current density and vice versa. For a given voltage, decrease in current density results in lower voltage drop which results in higher production rate. Also increase in electrode area makes it easier for water to get electrons which results in higher production rate. Figure 6.14 shows the effect of voltage levels on the rate of hydrogen production at different heights even though the efficiency trend remains same. Increasing the voltage level causes a decrease in the efficiency rate due to high energy input to the system. Figure 6.15 shows the effect of voltage on energy and exergy efficiencies at different heights. More details about the effect of current density are discussed in Section 6.9.

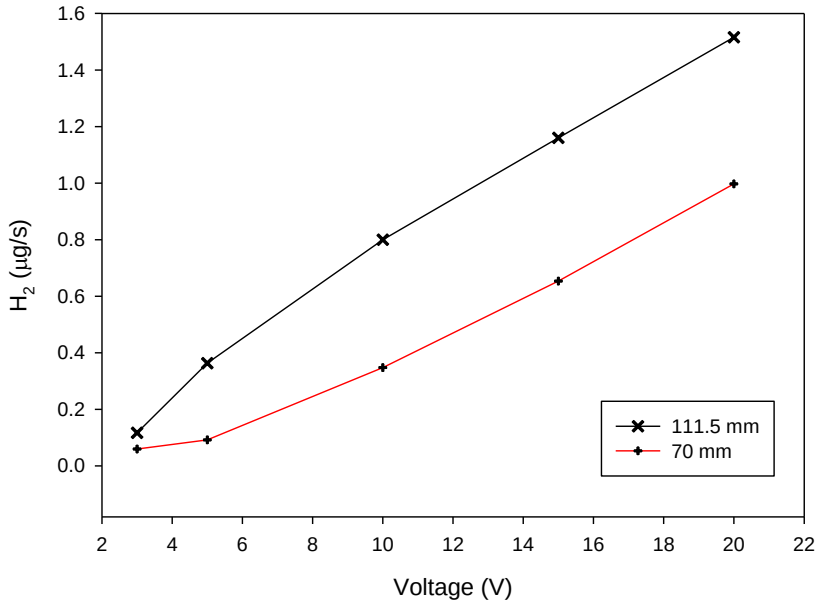

Figure 6.14: Effect of voltage on the rate of hydrogen production at different heights.

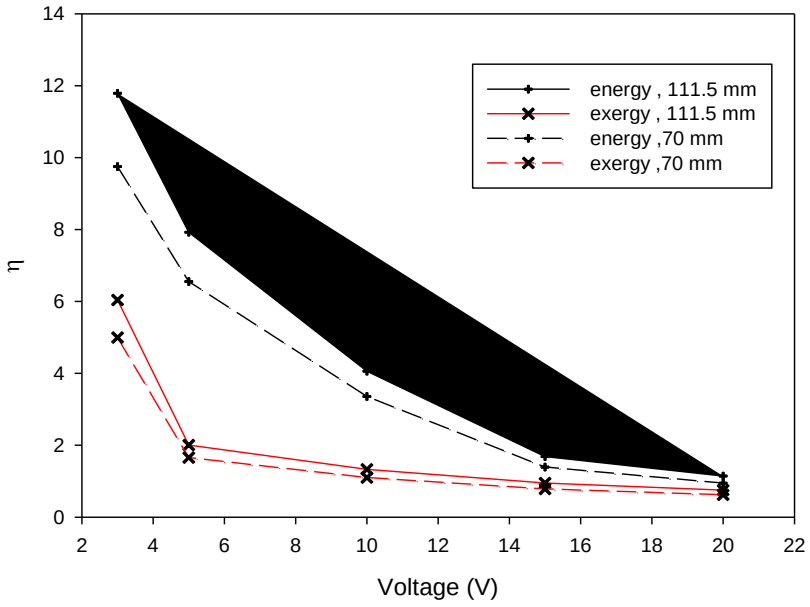

Figure 6.15: Effect of voltage on rate of energy and exergy efficiencies at different heights.

6.4 Results of Photo-Electrochemical Experiments

6.4.1 Photo Electrochemical H_2 Production

A sixth model is used to find the effect of applied voltage levels and amounts of catalyst and light intensity on the rate of hydrogen production. Table 6.9 shows ANOVA for the rate of photo-electrochemical hydrogen production. The Model F-value of 6812 implies that the model is significant. In this model, A, B, C, AB, AC, BC, A^2, B^2, C^2, A^2B, A^2C, AC^2, B^2C, BC^2, C^3, A^2B^2, A^2BC, ABC^2, B^2C^2, AC^3, BC^3, AB^2C^2, A^2C^3, ABC^3, B^2C^3, $A^2B^2C^2$, AB^2C^3 are significant model terms. Adeq Precision (Signal to noise ratio in the model) for the rate of the photo electrochemical hydrogen production model is 277.95, which indicates an adequate signal. The regression correlation for the rate of photo electrochemical hydrogen production as a function of intensity, applied voltage, and catalyst concentration is evaluated as

$$\dot{m}_{H2,PE}(\mu g/s) = -2.99 + 0.10A + 1.73B - 1.36C - 0.05\,AB + 0.13AC + 0.03BC - 2.17 * 10 - 3A^2 - 0.22B^2 + 0.95C^2 - 0.04ABC + 1.08 * 10^{-3}A^2B - 2.92 * 10^{-4}A^2\,C + 6.6 * 10^{-3}AB^2 - 0.07AC^2 + 0.05B^2C - 0.17BC^2 - 0.11C^3 - 1.2 * 10^{-4}A^2B^2 - 2.07 * 10^{-5}A^2BC +$$

$$1.35 * 10^{-4}A^2C^2 + 4.4 * 1010^{-3}AB^2C + 0.02ABC^2 - 5.9 * 10^{-4}B^2C^2 + 0.01AC^3 + 0.02BC^3 + 2.67 * 10^{-6}A^2B^2C - 2.65 * 10^{-3}AB^2C^2 - 1.82 * 10^{-5}A^2C^3 - 4.27 * 10^{-3}ABC^3 + 1.69 * 10^{-3}B^2C^3 + 3.39 * 10^{-7}A^2B^2C^2 + 4.67 * 10^{-4}AB^2C^3$$

(6.8)

Here, A represents the light intensity in W/m^2, B represents the applied Voltage in volts and C represents catalyst concentration in g/425mL. $R^2_{H2,PE} = 0.98$ between the experimental data and model equation (6.8).

Increasing the light intensity causes an increase to the rate of hydrogen production due to an increase in the photon rate. Figure 6.16 shows the effect of voltage levels on rates of photo electrochemical hydrogen production at different catalyst concentration levels and at different light intensities. As the hydrogen production is in dual manner (i.e. photochemical and electrochemical), the rate of hydrogen production also increases with increase in voltage. Increasing the catalyst concentration does not necessarily create a higher rate of hydrogen production.

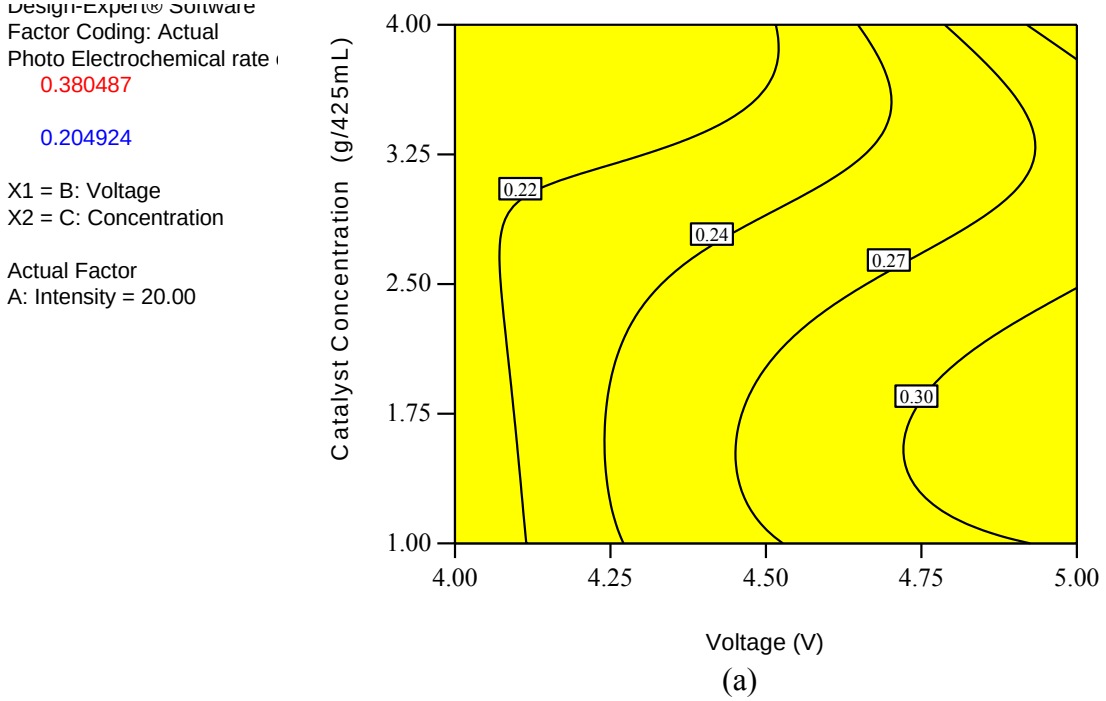

(a)

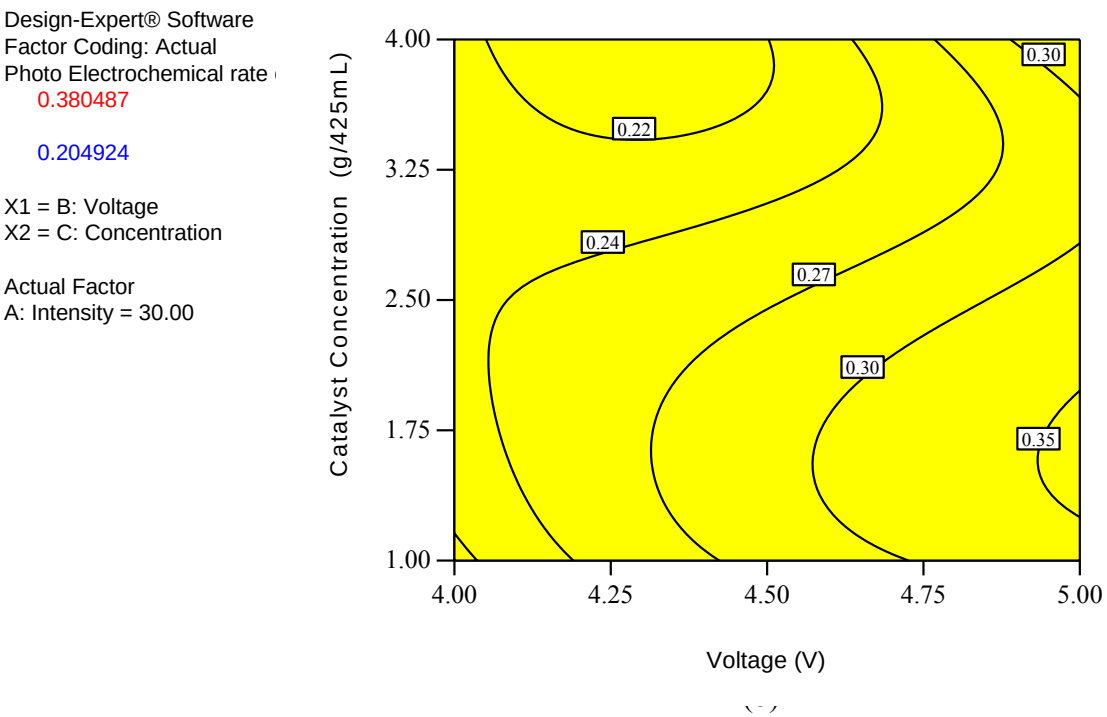

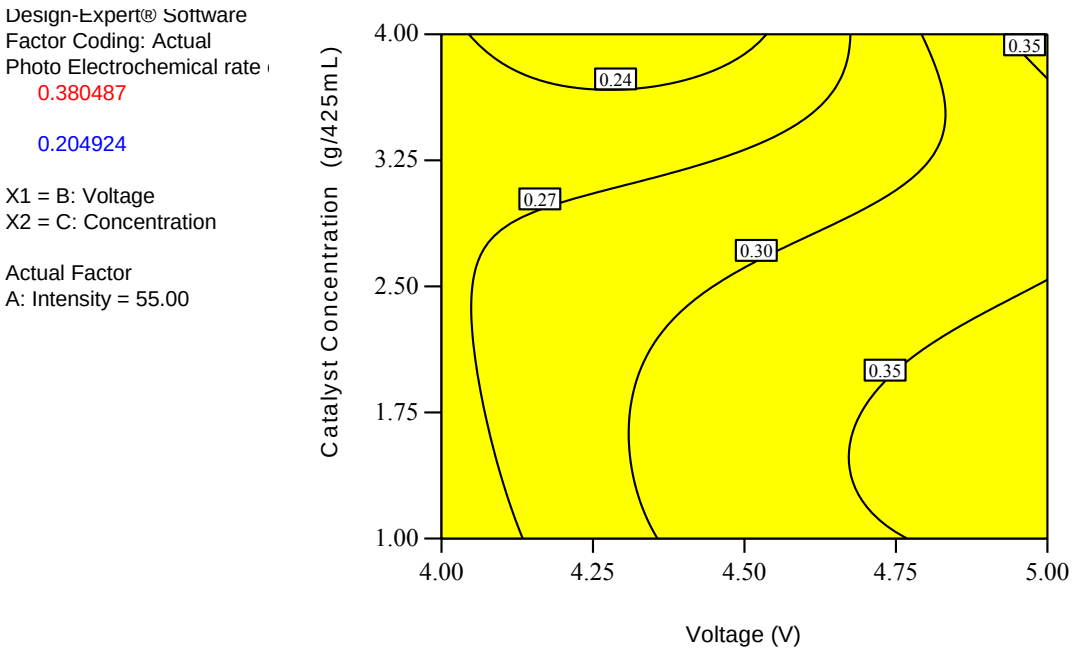

(c)

Figure 6.16: Effect of voltage levels on the of photo electrochemical hydrogen production at different catalyst concentration levels with a light intensity of a) 20W/m^2 b) 30 W/m^2 c) 55W/m^2.

Table 6.9: ANOVA for the rate of the photo electrochemical hydrogen production

Transform: None						
ANOVA for Response Surface Sixth Model- Photo Electrochemical H_2 production rate						
Source	Sum of	df	Mean Square	F- Value	p-value	
Model	0.094568	32	0.002955	6812.002	< 0.0001	significant
A:Intensity	0.002082	1	0.002082	4798.069	< 0.0001	
B:Voltage(V)	0.00629	1	0.00629	14499.8	< 0.0001	
C:Cat Conc. (g/425mL)	0.001085	1	0.001085	2500.43	< 0.0001	
AB	8.14E-06	1	8.14E-06	18.7605	0.0227	
AC	7.13E-06	1	7.13E-06	16.42356	0.0271	
BC	0.001769	1	0.001769	4077.601	< 0.0001	
A^2	9.4E-06	1	9.4E-06	21.66358	0.0187	
B^2	0.00014	1	0.00014	322.7644	0.0004	
C^2	0.000201	1	0.000201	463.2314	0.0002	
A^2B	8.33E-06	1	8.33E-06	19.20433	0.0220	
A^2C	6.16E-05	1	6.16E-05	141.8795	0.0013	
AC^2	0.000105	1	0.000105	241.6659	0.0006	
B^2C	0.000108	1	0.000108	250.0685	0.0005	
BC^2	0.001186	1	0.001186	2734.707	< 0.0001	
C^3	0.000333	1	0.000333	767.9026	0.0001	
A^2B^2	5.93E-05	1	5.93E-05	136.6795	0.0013	
A^2BC	3.35E-05	1	3.35E-05	77.25177	0.0031	
ABC^2	6.25E-05	1	6.25E-05	144.1379	0.0012	
B^2C^2	0.000104	1	0.000104	238.8082	0.0006	
AC^3	9.18E-06	1	9.18E-06	21.16544	0.0193	
BC^3	0.001946	1	0.001946	4486.446	< 0.0001	
AB^2C^2	6.8E-05	1	6.8E-05	156.6968	0.0011	
A^2C^3	7.01E-05	1	7.01E-05	161.5024	0.0011	
ABC^3	4.46E-06	1	4.46E-06	10.28122	0.0491	
B^2C^3	8.05E-05	1	8.05E-05	185.5685	0.0009	
$A^2B^2C^2$	6.15E-06	1	6.15E-06	14.16485	0.0328	
AB^2C^3	1.06E-05	1	1.06E-05	24.45972	0.0159	
Residual	1.3E-06	3	4.34E-07			
Cor Total	0.09457	35				

As the ANOVA model suggests, there is a very strong interaction between the input parameters and their effect on rate of hydrogen production. Increasing the catalyst concentration level for a given voltage, however, increases the rate of hydrogen production until it reaches an optimal value. After the optimal value of catalyst concentration, further increase in catalyst concentration results in the decrease to the rate of hydrogen production. It is also important to mention here that these results strictly apply to conditions whereby zinc sulfide is used as the photo catalyst. Because of similar nature, it can also be anticipated that cadmium sulfide (which is also a heterogeneous photo catalyst and works in the wavelength range of 520nm), will show similar behaviour. During the photo-electrochemical experiments, chlorine and sodium hydroxide are produced as by-products.

6.4.2 Electrochemical H_2 Production

A fifth model is also used to find the effect of the applied voltage, along with the amount of catalyst and light intensity on the rate of hydrogen production. Table 6.10 shows ANOVA for the rate of photo-electrochemical hydrogen production. The Model F-value of 63660000 implies that the model is significant. There is only a 0.01% chance that a "Model F-Value" this large could occur due to noise. In this case, B, C, BC, B^2, C^2, B^2C, BC^2, C^3, B^2C^2, BC^3 are significant model terms. To improve the accuray of the model, backward elimination is applied. Adeq Precision (Signal to noise ratio in the model) for the rate of electrochemical hydrogen production model is 65.320 which indicates an adequate signal.

The regression correlation for the rate of electrochemical hydrogen production as a function of intensity, applied voltage, and catalyst concentration, is evaluated as

$$\dot{m}_{H2,E}(\mu g/s) = +6.27 - 2.70A - 15.38B + 6.63AB + 0.30A^2 + 7.41B^2 - 0.71\,A^2B - 3.19\,A\,B^2 - 0.95B^3 + 0.34\,A^2B^2 + 0.41\,AB^3 - 0.04\,A^2B^3 \quad (6.9)$$

where A represents applied voltage in volts, and B represents catalyst Concentration in g/425mL. $R^2_{H2,E} = 0.99$ between the experimental data and model eqaution (6.9).

For electrochemical experiments, the power is supplied by an external power source. As a result, light intensity does not have an effect on the rate of hydrogen production. Figure 6.17 shows the effect that the voltage level can have on the rate of electrochemical hydrogen

production at different catalyst concentration levels (at different light intensities). Increasing the voltage causes an increase to the rate of hydrogen production.

Table 6.10: ANOVA for the rate of the electrochemical hydrogen production

Transform: None						
ANOVA for Response Surface Fifth Model- Electrolysis H_2 production rate						
Source	Sum of	df	Mean Square	F- Value	p-value	
Model	0.108114	10	0.010811	641.4546	< 0.0001	significant
B-Voltage	0.032736	1	0.032736	1942.245	< 0.0001	
C-Concentration	0.002107	1	0.002107	124.9866	< 0.0001	
BC	0.000918	1	0.000918	54.45041	< 0.0001	
B^2	5.99E-05	1	5.99E-05	3.556098	0.0710	
C^2	1.2E-07	1	1.2E-07	0.007101	0.9335	
B^2C	0.005697	1	0.005697	337.9941	< 0.0001	
BC^2	0.000383	1	0.000383	22.72189	< 0.0001	
C^3	5.11E-05	1	5.11E-05	3.029586	0.0941	
B^2C^2	0.000124	1	0.000124	7.385799	0.0118	
BC^3	0.000925	1	0.000925	54.87621	< 0.0001	
Residual	0.000421	25	1.69E-05			
Cor Total	0.108536	35				

It is important to note, however, that increasing the photo catalyst concentration level actually reduces the production rate. This can be explained in terms of electrical resistance caused by the Zinc sulfide particles. Zinc sulfide has a very low electrical conducitivity level,which results in an increase in resistance (thus decreasing the rate of hydrogen production). During the electrochemical experiments, chlorine and sodium hydroxide are produced as by-products.

6.4.3 Photochemical H_2 Production

A sixth model is used to find the effect of applied voltage and amount of catalyst and light intensity on the rate of hydrogen production. Table 6.11 shows ANOVA for the rate of photochemical hydrogen production. The Model F-value of 1854.8 implies that the model is significant. In this case, A, B, C, AB, AC, BC, A^2, B^2, C^2, A^2B, A^2C, AC^2, B^2C, BC^2, C^3, A^2B^2,

A^2BC, ABC^2, B^2C^2, AC^3, BC^3, AB^2C^2, A^2C^3, ABC^3, B^2C^3, $A^2B^2C^2$, AB^2C^3 are significant model terms. Adeq Precision (Signal to noise ratio in the model), for the rate of photochemical hydrogen production model is 277.95, which indicates an adequate signal. The regression correlation for the rate of photo-chemical hydrogen production as a function of intensity, applied voltage, and catalyst concentration is evaluated as

$$\dot{m}_{H2,P}(ug/s) = -9.26 + 0.10\,A + 4.42\,B + 14.02 - 0.05\,AB + 0.13AC - 6.60\,BC - 2.18*10^{-3}\,A^2 - 0.51\,B^2 - 6.47\,C^2 - 0.04\,ABC + 1.09*10^{-3}A^2B - 2.92*10^{-4}\,A^2C + 6.65*10^{-3}\,AB^2 - 0.07\,AC^2 + 0.75B^2C + 3.03BC^2 + 0.84\,C^3 - 1.23*10^{-4}A^2B^2 - 2.08*10^{-5}A^2BC + 1.36*10^{-4}\,A^2C^2 + 4.40*10^{-3}AB^2C + 0.02ABC^2 - 0.35B^2C^2 + 0.01AC^3 - 0.40BC^3 + 2.67*10^{-6}\,A^2B^2C - 2.66*10^{-3}\,AB^2C^2 - 1.82*10^{-5}\,A^2C^3 - 4.29*10^{-3}\,ABC^3 + 0.045\,B^2C^3 + 3.39*10^{-7}A^2B^2C^2 + 4.67*10^{-4}\,AB^2C^3 \quad (6.10)$$

Here, A represents the light A in W/m^2, B represents applied B in volts and C represents catalyst C in g/425mL. $R^2_{H2,P} = 0.95$ between the experimental data and model equation (6.10).

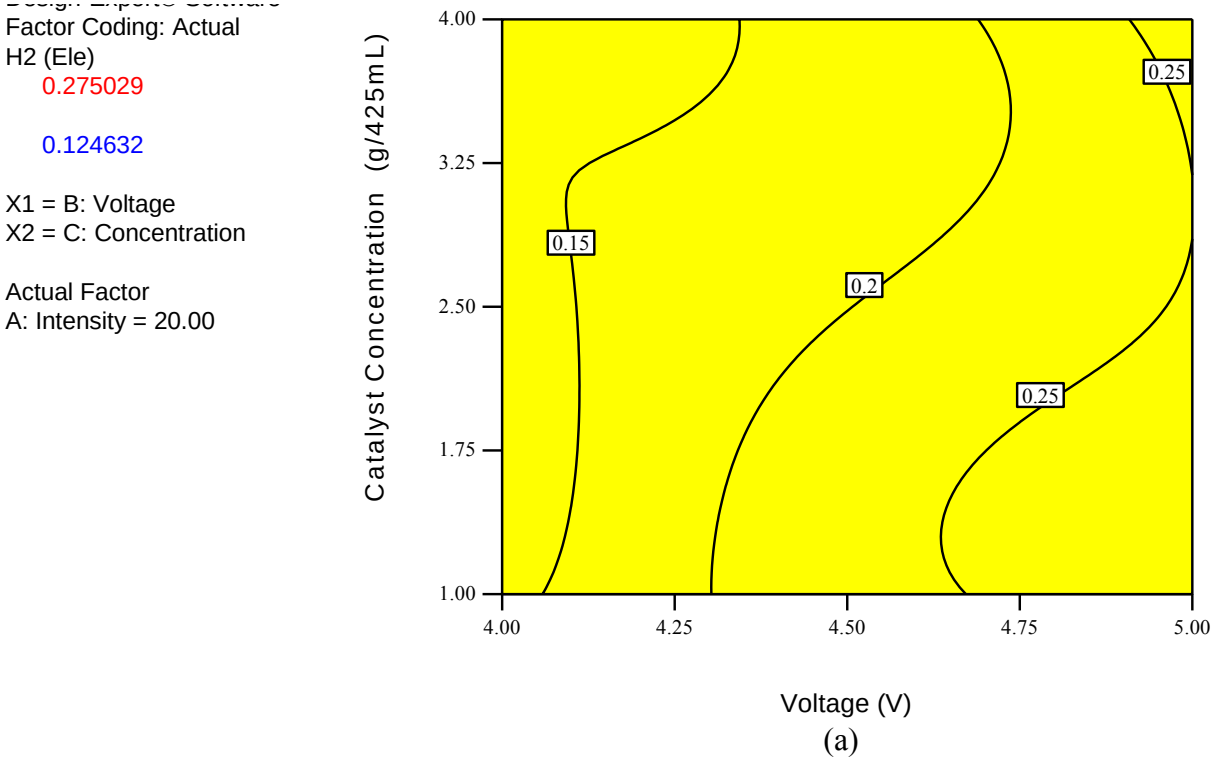

(a)

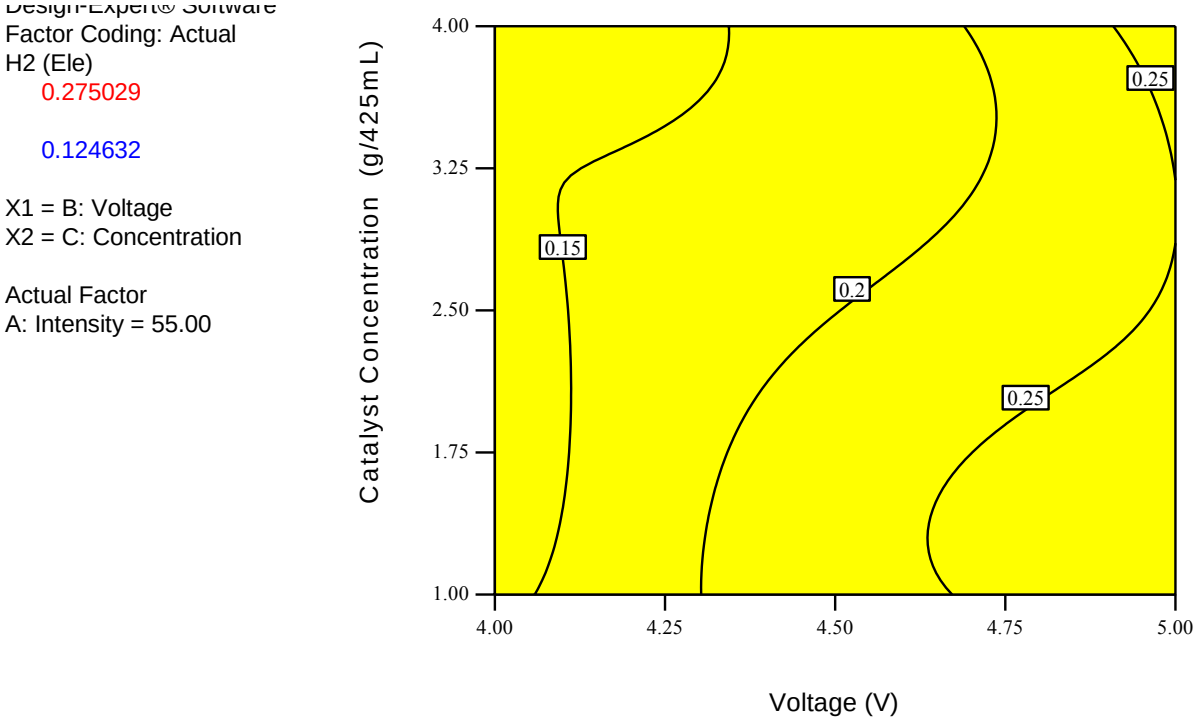

(b)

Figure 6.17: Effect of voltage levels on the rate of photochemical hydrogen production at different catalyst concentration levels at the light intensity of a) 20W/m^2 b) 55W/m^2.

Subtracting the electrochemical data from photo-electrochemical data gives us the rate of hydrogen production by photochemical means. Figure 6.18 shows the aeffect of voltage levels on the rate of photochemical hydrogen production at different catalyst concentration levels and at different light intensities. The trends are more or less similar to those of photo- electrochemical hydrogen production. Analysis of the electrolysis data shows no dependance of light intensity on the rate of hydrogen production (i.e. because electricity is supplied by power supply). However, it is interesting to note that photochemical hydrogen production is greatly affected by applied voltage. This is due to the supply of electrons from the power supply resulting in photochemical hydrogen production. This supply of electrons is provided by electricity instead of a hole scavenger (i.e Na_2S in present study). Another conclusion that can be drawn from Figure 6.16 is solid electrode can replace electron donor/hole scavenger material. Further details are disscussed below.

Table 6.11: ANOVA for the rate of the electrochemical hydrogen production

Transform: None						
ANOVA for Response Surface Sixth Model- Photochemical H_2 production rate						
Source	Sum of	df	Mean Square	F- Value	p-value	
Model	0.02575	32	0.000805	1854.824	< 0.0001	significant
A:Intensity (W/m^2)	0.002082	1	0.002082	4798.069	< 0.0001	
B:Voltage(V)	0.001118	1	0.001118	2576.904	< 0.0001	
C:Cat Conc. (g/425mL)	2.55E-05	1	2.55E-05	58.80835	0.0046	
AB	8.14E-06	1	8.14E-06	18.7605	0.0227	
AC	7.13E-06	1	7.13E-06	16.42356	0.0271	
BC	0.000253	1	0.000253	583.0162	0.0002	
A^2	9.4E-06	1	9.4E-06	21.66358	0.0187	
B^2	0.000234	1	0.000234	539.4837	0.0002	
C^2	0.000205	1	0.000205	473.4064	0.0002	
A^2B	8.33E-06	1	8.33E-06	19.20433	0.0220	
A^2C	6.16E-05	1	6.16E-05	141.8795	0.0013	
AC^2	0.000105	1	0.000105	241.6659	0.0006	
B^2C	0.00062	1	0.00062	1428.976	< 0.0001	
BC^2	0.00023	1	0.00023	529.1239	0.0002	
C^3	2.14E-05	1	2.14E-05	49.34058	0.0059	
A^2B^2	5.93E-05	1	5.93E-05	136.6795	0.0013	
A^2BC	3.35E-05	1	3.35E-05	77.25177	0.0031	
ABC^2	6.25E-05	1	6.25E-05	144.1379	0.0012	
B^2C^2	2.69E-05	1	2.69E-05	61.95696	0.0043	
AC^3	9.18E-06	1	9.18E-06	21.16544	0.0193	
BC^3	0.0002	1	0.0002	460.5151	0.0002	
AB^2C^2	6.8E-05	1	6.8E-05	156.6968	0.0011	
A^2C^3	7.01E-05	1	7.01E-05	161.5024	0.0011	
ABC^3	4.46E-06	1	4.46E-06	10.28122	0.0491	
B^2C^3	0.000853	1	0.000853	1966.694	< 0.0001	
$A^2B^2C^2$	6.15E-06	1	6.15E-06	14.16485	0.0328	
AB^2C^3	1.06E-05	1	1.06E-05	24.45972	0.0159	
Residual	1.3E-06	3	4.34E-07			
Cor Total	0.025751	35				

6.4.4 Photo-Electrochemical Cl_2 Production

A 3FI is used to find the effect of applied voltage and theamount of catalyst and light intensity on the rate of chlorine production. Table 6.12 shows ANOVA for the rate of chlorine production. The Model F-value of 38.68 implies that the model is significant. In this case, A (intensity), B (Voltage), C (catalyst concentration), AB (interaction between intensity and voltage), BC (interacction between voltage and catalyst concentration) are significant model terms. Values greater than 0.1000 indicate that the model terms are not significant. To improve the accuracy of the model, power transformation combined with backward elimination is applied with lambda=-1.75.

Table 6.13 tabulates the removed terms that have a p-value that is greater than 0.1. Adeq Precision (signal to noise ratio [23]) for the chlorine model is 19.717, which indicates an adequate signal. The regression for the rate of photo-electrochemical chlorine production as a function of intensity, applied voltage, and catalyst concentration has been evaluated.

$$\dot{m}_{Cl2,PE}^{-1.43}(\mu g/s) = 1.15 - 1.76 * 10^{-3}\,A - 0.45\,B - 0.48\,C + 1.90 * 10^{-4}AB + 0.21BC + 8.30 * 10^{-6}A^2 + 0.05B^2 + 1.41 * 10^{-3}C^2 - 0.02B^2C \quad (6.11)$$

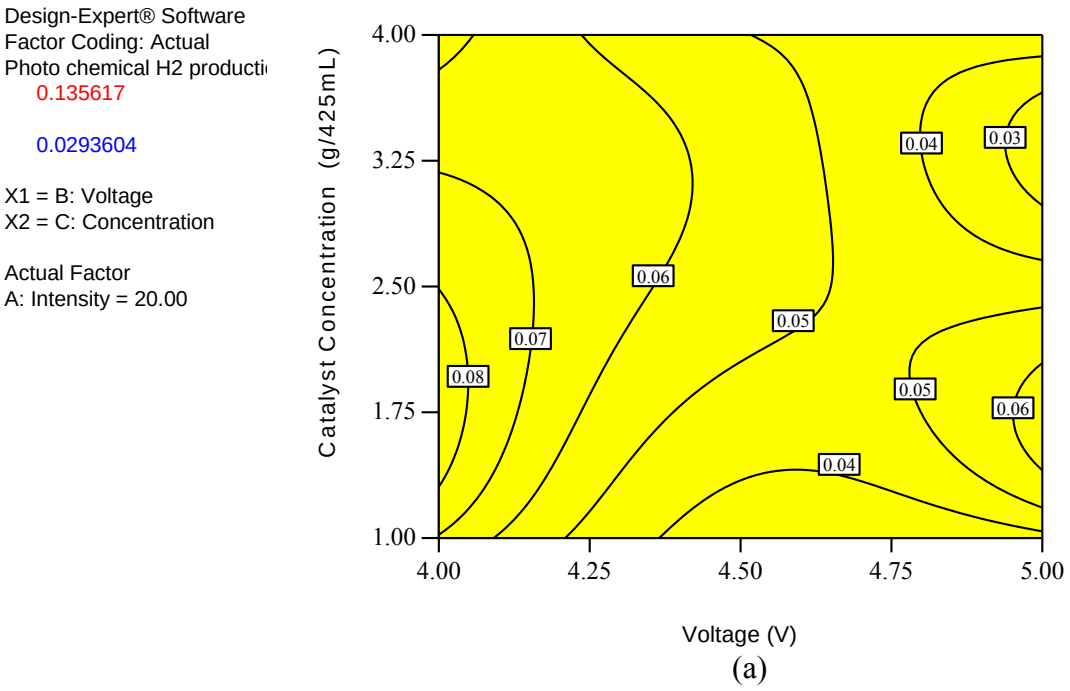

(a)

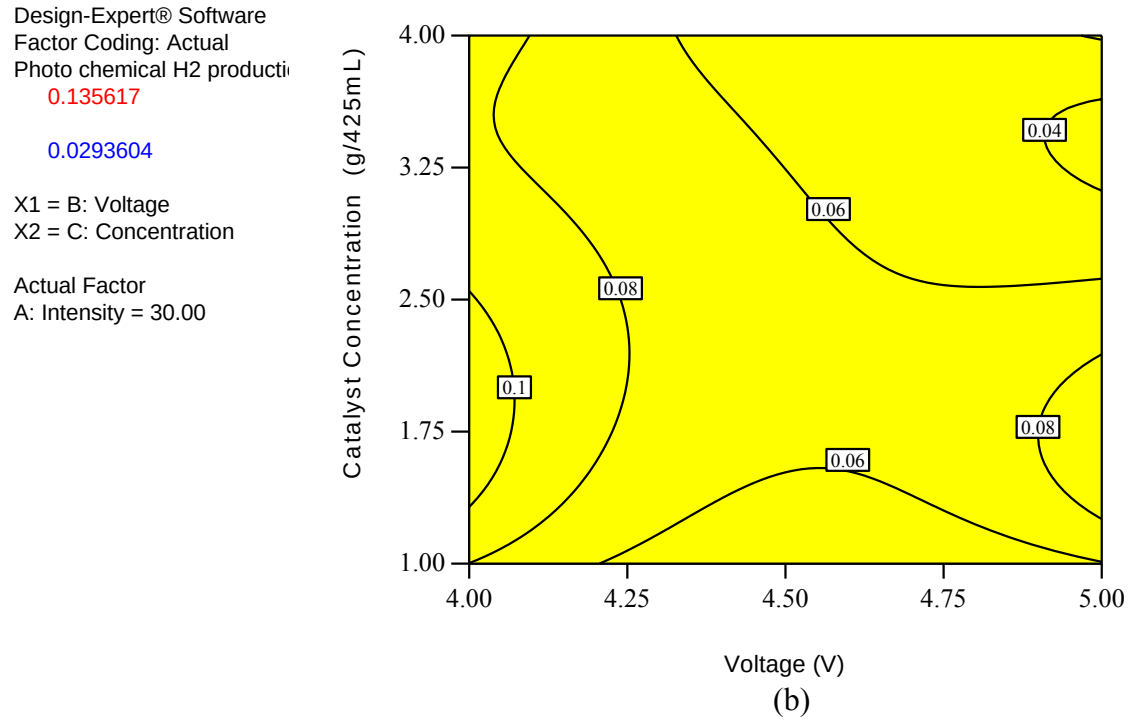

(b)

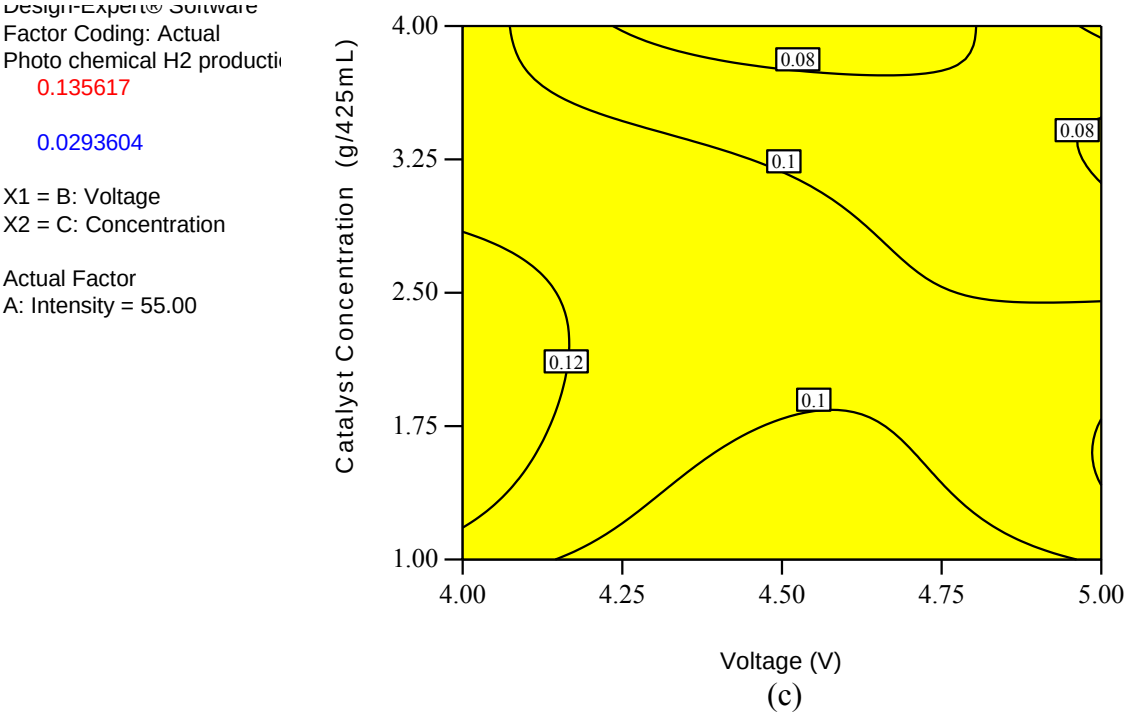

(c)

Figure 6.18: Effect of voltage levels on the rate of photochemical hydrogen production at different catalyst concentration levels with the light intensity of a) 20W/m^2 b) 30 W/m^2 c) 55W/m^2.

Here, A represents the light A in W/m^2, B represents applied B in volts and C represents catalyst C in g/425mL. $R^2_{Cl2,PE} = 0.95$ between the experimental data and model eqaution (6.11).

Table 6.12: ANOVA for the rate of chlorine production.

Transform: Power					Lambda = -1.43	
ANOVA for Response Surface 3FI- Cl_2 production rate						
Source	Sum of	df	Mean	F- Value	p-value	significant
Model	0.001458	17	8.58E-05	38.6755	< 0.0001	
A:Intensity (W/m^2)	0.000205	2	0.000103	46.31748	< 0.0001	
B:Voltage(V)	0.001018	2	0.000509	229.49	< 0.0001	
C:Cat Conc. (g/425mL)	6.27E-05	3	2.09E-05	9.429032	0.0006	
AB	3.24E-05	4	8.1E-06	3.65075	0.0240	
BC	0.00014	6	2.33E-05	10.49642	< 0.0001	
Residual	3.99E-05	18	2.22E-06			
Cor Total	0.001498	35				

Table 6.13: Backward elimination for the Cl_2 production rate.

Backward Elimination Regression with Alpha to Exit = 0.100			
Removed	F- Value	p-value	MSE
AC	0.723115	1	2.22E-06
ABC	1.382906	0.3605	2.22E-06

Here, chlorine is a by-product of the chloralkali process (assuming that hydrogen is the primary output of the process). Figure 6.19 shows the affect that voltage levels have on the rate of photo-electrochemical chlorine production at different catalyst concentration at different light intensities. The catalyst concentration and the light intensity have no direct effect on the rate of chlorine production. But, once photochemical hydrogen is produced, both the catalyst concentration and the light intensity do have an effect on the rate of chlorine production. This can be explained in terms of neutralization of hydroxyl ions. As previously mentioned, aside from hydrogen production, hydroxyl ions are also produced (including hydroxyl ions from photochemical and electrochemical processes). For continuous hydrogen production, hydroxyl

ions from both processes must be neutralized. In other words, the rate of hydroxyl ion production (by means of photochemical processes), allow the light intensity and catalyst concentration to have an effect on chlorine production.

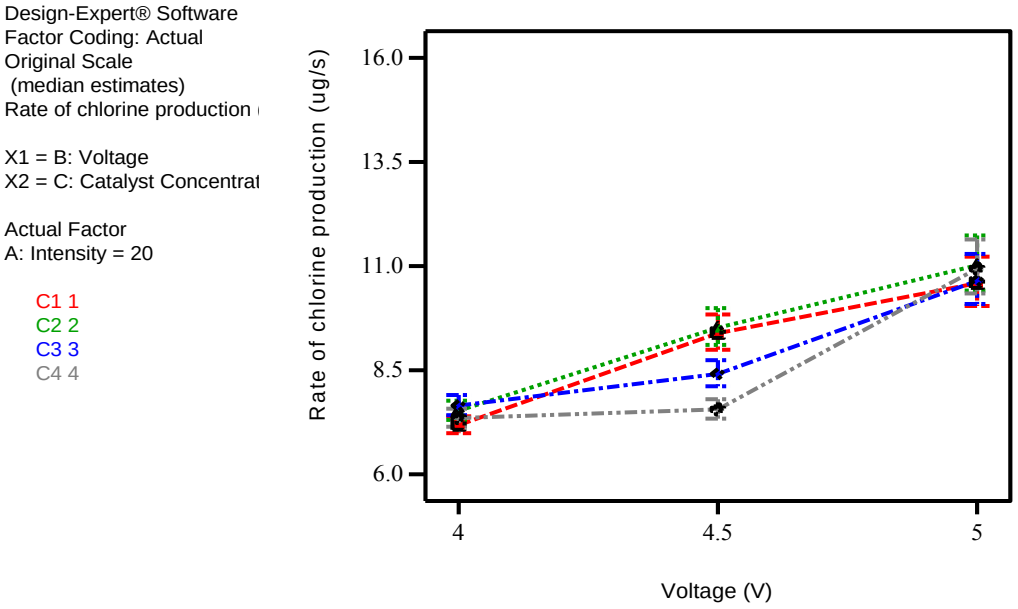

(a)

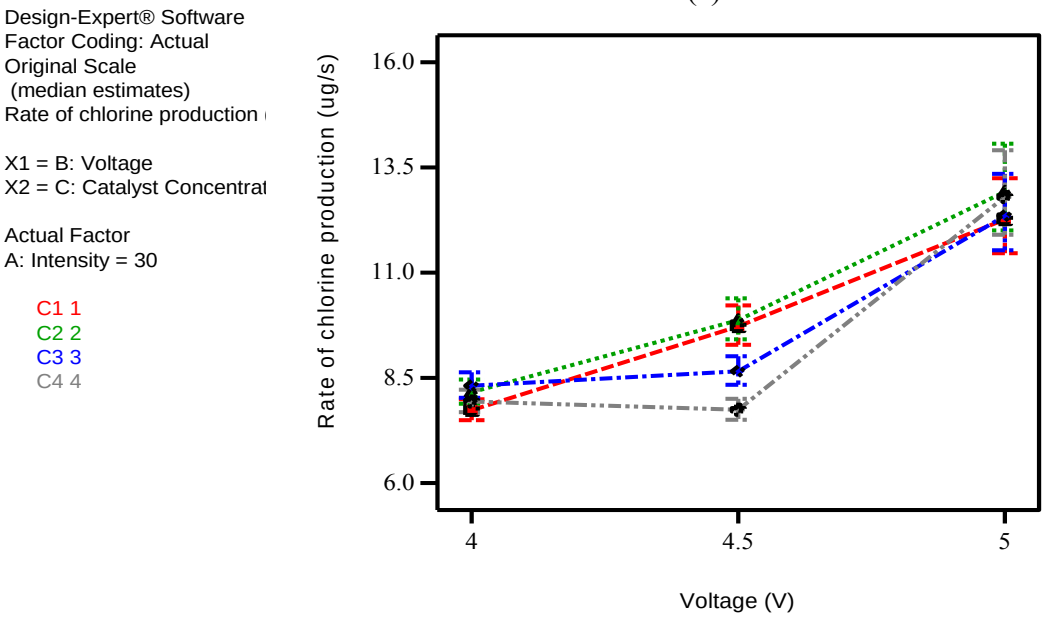

(b)

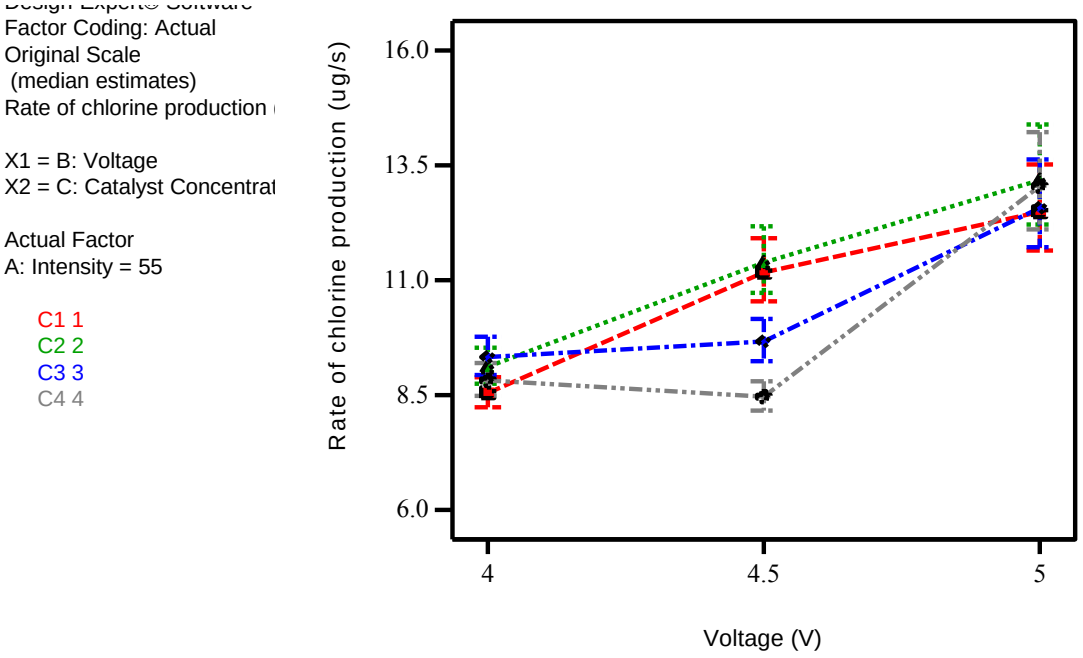

(c)

Figure 6.19: Effect of voltage levels on the rate of photo-electrochemical chlorine production at different catalyst concentration levels at the light intensity of a) 20W/m^2 b) 30 W/m^2 c) 55W/m^2.

Lower pressure levels of chlorine are observed during the experiments. As discussed previously (electrolysis experiments section), this drop in pressure is due to the higher solubility nature of chlorine in water as compared to hydrogen. The effect of absorbed chlorine is also visually evident. After the experiment, the color of the chlorine is also different. Figure 6.20 shows the effect of the absorbed chlorine in the brine solution.

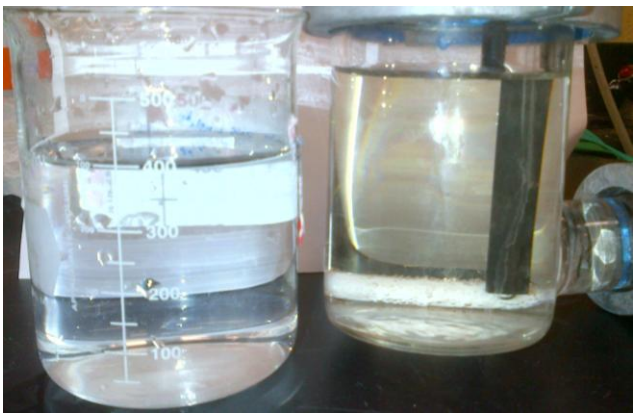

Figure 6.20: Stirred brine solution a) before experiment (left side) b) after experiment (right side).

6.4.5 Photo-Electrochemical NaOH Production

A 3FI is used to find the effect of the applied voltage levels, the amount of catalyst and light intensity levels on the rate of sodium hydroxide production. Table 6.14 shows ANOVA for the rate of hydrogen production. The Model F-value of 27.35 implies that the model is significant. There is only a 0.01% chance that a "Model F-Value" this large could occur due to noise. Values of "Prob > F" less than 0.0500 indicate that the model terms are significant. In this case, A (intensity), B (Voltage), C (Catalyst Concentration), AB (interaction between intensity and applied voltage), BC (interaction between voltage and catalyst concentration) are significant model terms.Values greater than 0.1000 indicate that the model terms are not significant. To improve the accuray of the model, inverse transformation along with backward elimination is applied. Table 6.15 gives the removed terms that have a p-value that is greater than 0.1. Adeq Precision for the sodium hydroxide model is 16.492, which indicates an adequate signal. This model can be used to navigate the design space. The regression correlation for the rate of photo-electrochemical sodium hydroxide production as a function of intensity, applied voltage, and catalyst concentration levels is evaluated as follows:

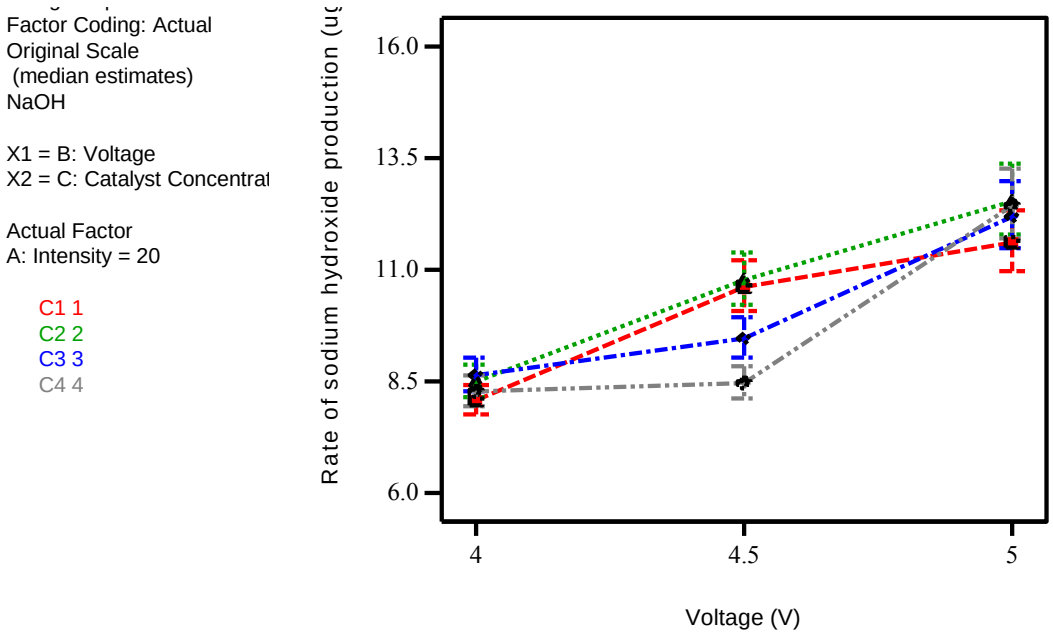

(a)

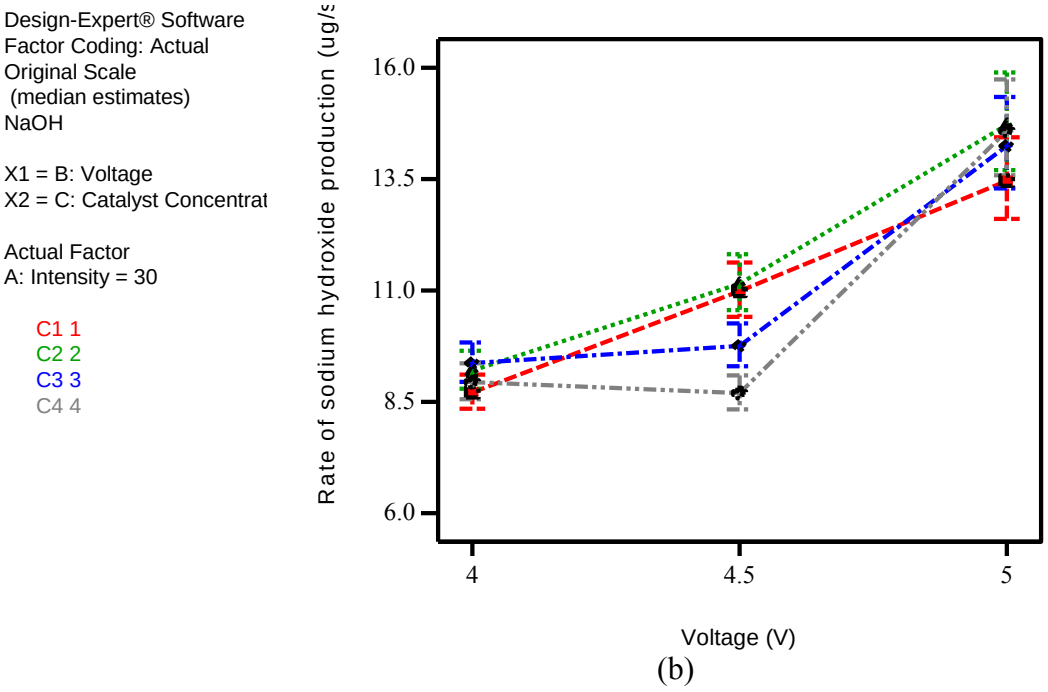

(b)

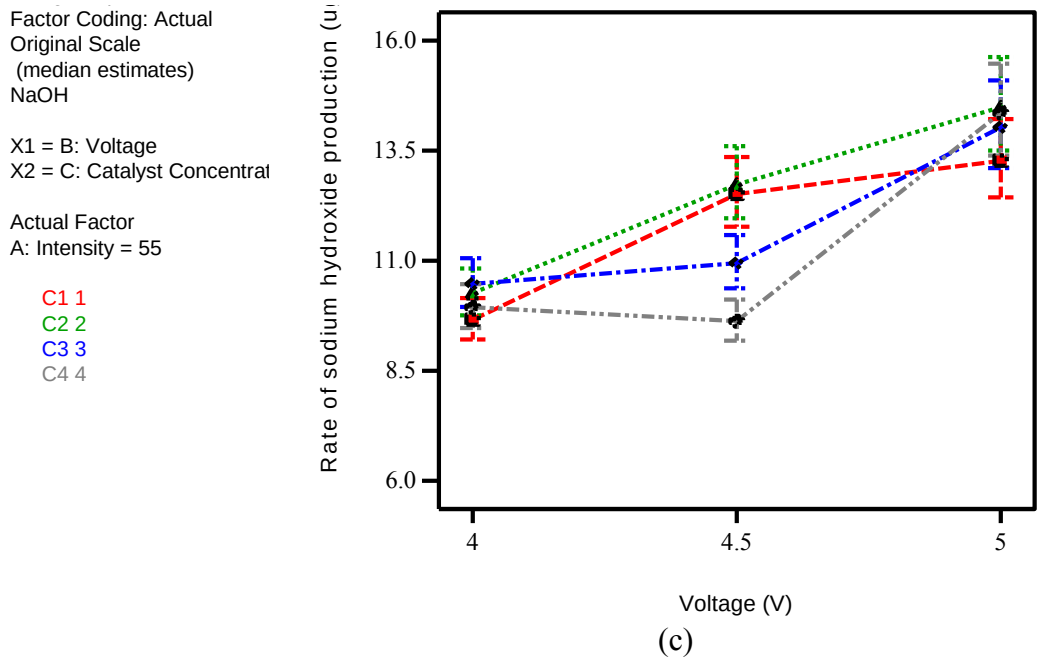

(c)

Figure 6.21: Effect of voltage (V) on the rate of photo-electrochemical sodium hydroxide production at different catalyst concentration levels (g/425mL) with levels of light intensity equal to a) 20W/m^2 b) 30 W/m^2 c) 55W/m^2.

$$\dot{m}_{NaOH,PE}^{-2.79} = 0.06 - 1.33 * 10^{-4}A - 0.02B - 4.80 * 10^{-3}C + 1.61 * 10^{-5}AB + 1.26 * 10^{-3}BC - 3.78 * 10^{-7}A^2 + 2.24 * 10^{-3}B^2 - 5.89 * 10^{-3}C^2 + 3.35 * 10^{-7}\ A^2B - 6.49 * 10^{-5}B^2C + 2.82 * 10^{-3}BC^2 - 2.83 * 10^{-8}A^2B^2 - 3.28 * 10^{-4}B^2C^2 \quad (6.12)$$

where A represents the light A in W/m^2, B represents applied B in volts, and C represents catalyst C in g/425mL. $R^2_{NaOH,PE} = 0.96$ between the experimental data and model equation (6.12).

Sodium hydroxide is both an important industrial base and a by-product in the chloralkali process (assuming that hydrogen is the primary output of the process). Figure 6.21 shows the effect that voltage levels have on the rate of photo-electrochemical chlorine production at different catalyst concentration levels at different light intensities. The same theory about the effect of light intensity and catalyst concentration (which is discussed in terms of chlorine production in section 6.3.4), applies for sodium hydroxide. The rate of hydroxyl ion production (by means of the photochemical process), allow for the light intensity and catalyst concentration levels to have an effect on sodium hydroxide production.

Table 6.14: ANOVA for the rate of chlorine production

Transform: Inverse					Lambda = -2.79	
ANOVA for Response Surface 3FI- NaOH production rate						
Source	Sum of	df	Mean	F- Value	p-value	significant
Model	0.010674	17	0.000628	27.34775	< 0.0001	
A:Intensity (W/m^2)	0.001373	2	0.000687	29.90517	< 0.0001	
B:Voltage(V)	0.007616	2	0.003808	165.8557	< 0.0001	
C:Cat Conc. (g/425mL)	0.000424	3	0.000141	6.154702	0.0046	
AB	0.000248	4	6.19E-05	2.698207	0.0638	
BC	0.001013	6	0.000169	7.355536	0.0004	
Residual	0.000413	18	2.3E-05			
Cor Total	0.011087	35				

Table 6.15: Backward elimination for the NaOH production rate

Backward Elimination Regression with Alpha to Exit = 0.100			
Removed	F- Value	p-value	MSE
AC	0.664235	1	2.3E-05
ABC	1.50549	0.3198	2.3E-05

6.4.6 Results of Efficiency

Energy efficiency of the chloralkali process is calculated by using equation 5.20b. Figure 6.22 shows the effect that voltage levels have on energy efficiency at different catalyst concentration levels with different light intensities. Results show that the catalyst concentration and applied voltage levels have very strong interaction with each other, and are both highly significant in terms of their effect on energy efficiency in the system. At 4V, the maximum efficiency value is observed at a catalyst concentration level of 3g/425mL, whereas a minimum efficiency is observed at 1g/425mL. Increasing the voltage level to 4.5V, increases the efficiency for the catalyst concentration levels of 1g/425mL and 2g/425mL (ultimately decreasing the efficiency of the catalyst concentration level of 3g/425mL and 4g/425mL). At 5V, the maximum efficiency value is observed at a catalyst concentration level of 2g/425mL; a minimum efficiency value is observed at 3g/425mL. The aforementioned results can be concluded because there is an optimal voltage level for a given catalyst concentration level in order to achieve maximum efficiency. Increasing the light intensity also increases the production rate (but only if the energy input to the system is increase).

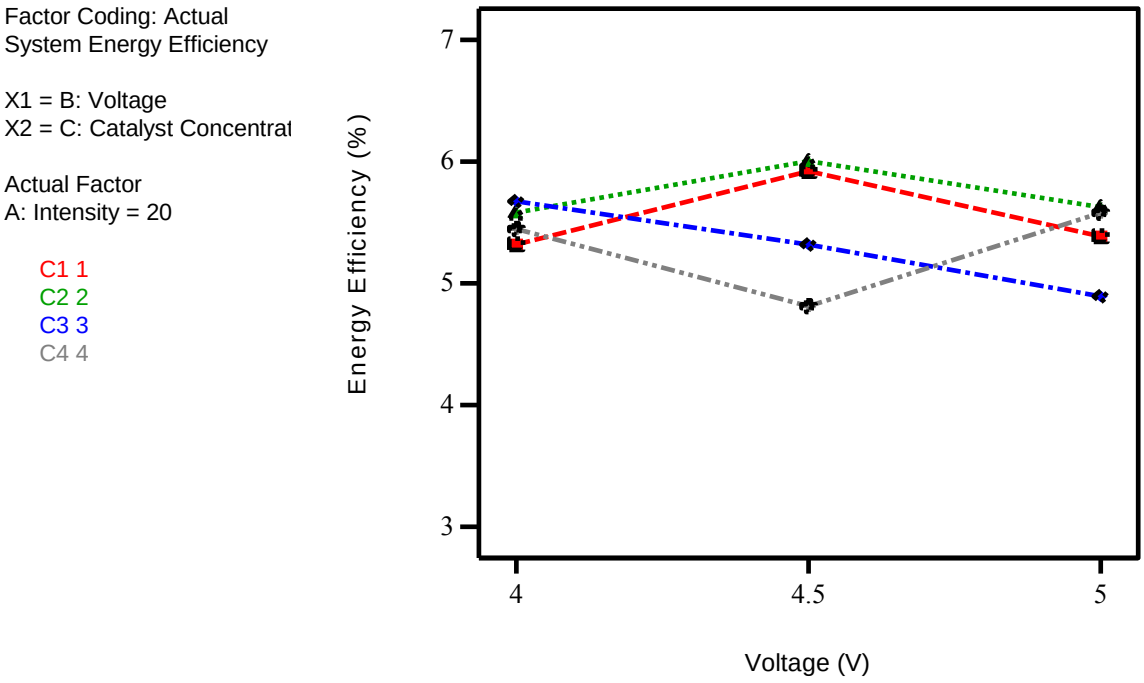

(a)

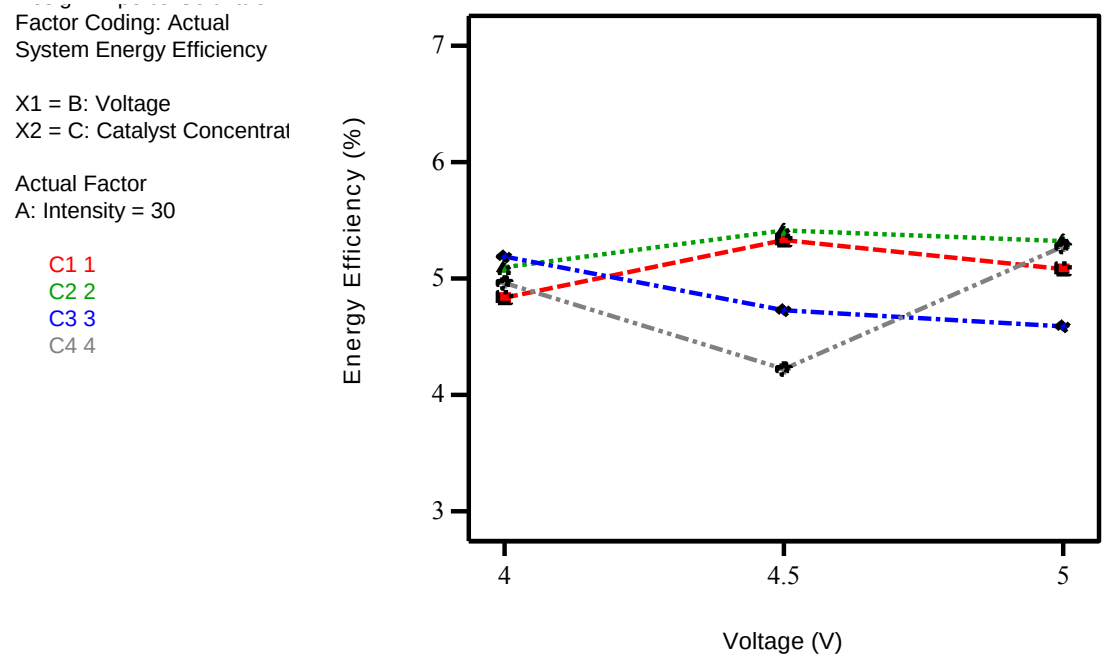

(b)

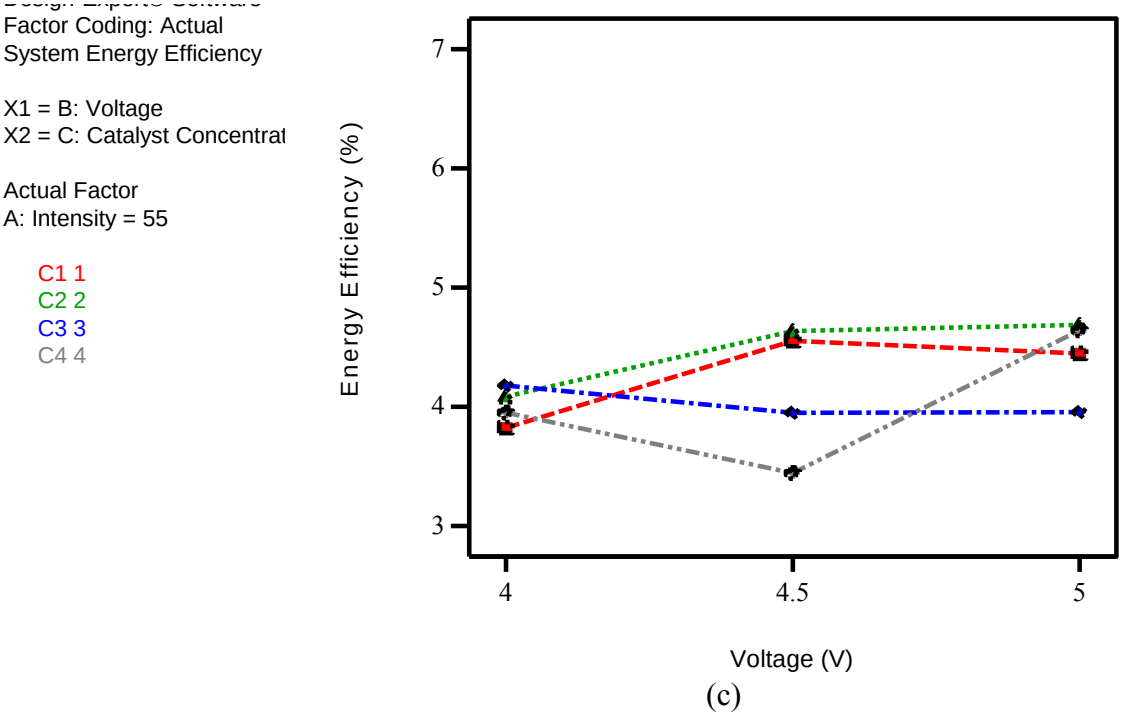

(c)

Figure 6.22: Effect of voltage (V) on energy efficiency at different catalyst concentrations (g/425mL) and at the light intensity of a) 20W/m^2 b) 30 W/m^2 c) 55W/m^2.

Factor Coding: Actual
System exergy - All

X1 = B: Voltage
X2 = C: Catalyst Concentrat

Actual Factor
A: Intensity = 20

C1 1
C2 2
C3 3
C4 4

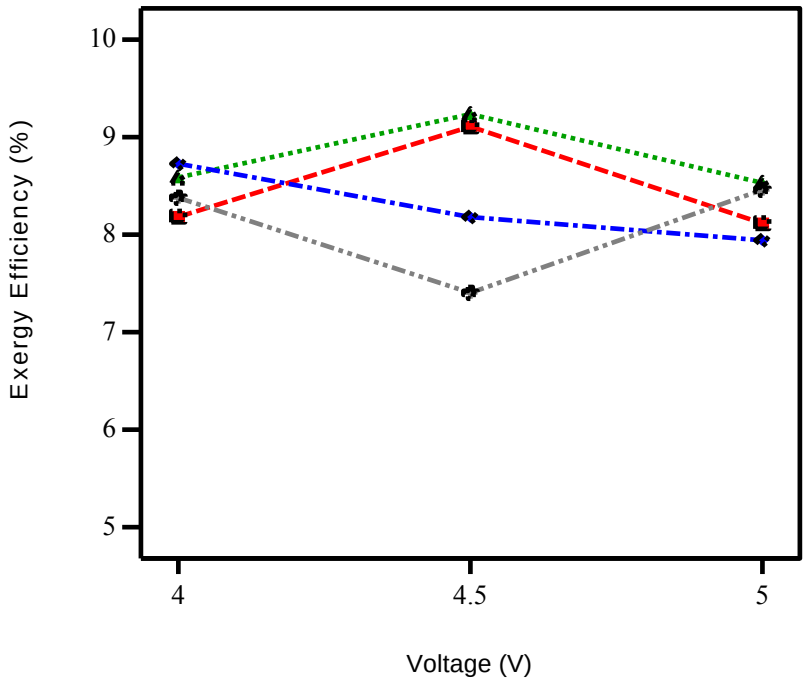

(a)

Factor Coding: Actual
System exergy - All

X1 = B: Voltage
X2 = C: Catalyst Concentrat

Actual Factor
A: Intensity = 30

C1 1
C2 2
C3 3
C4 4

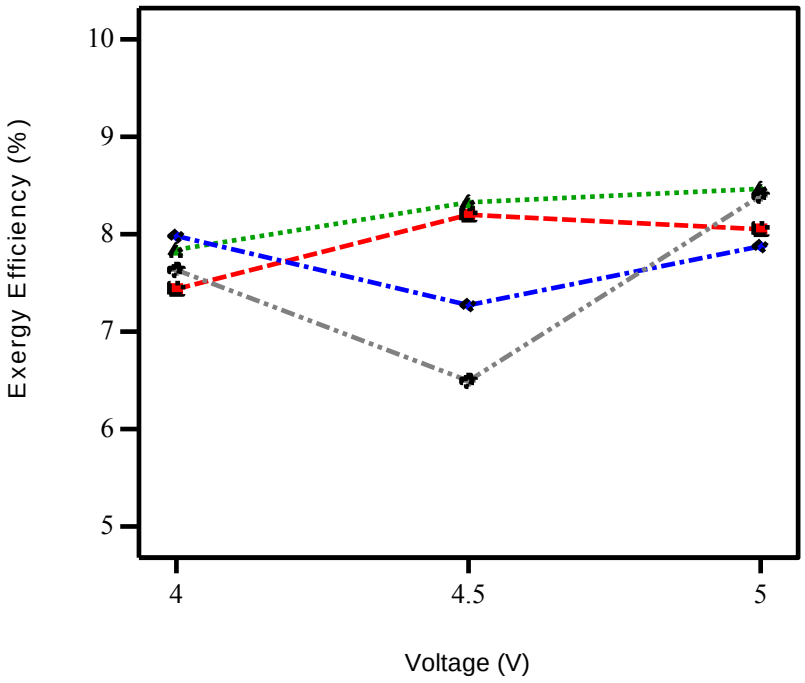

(b)

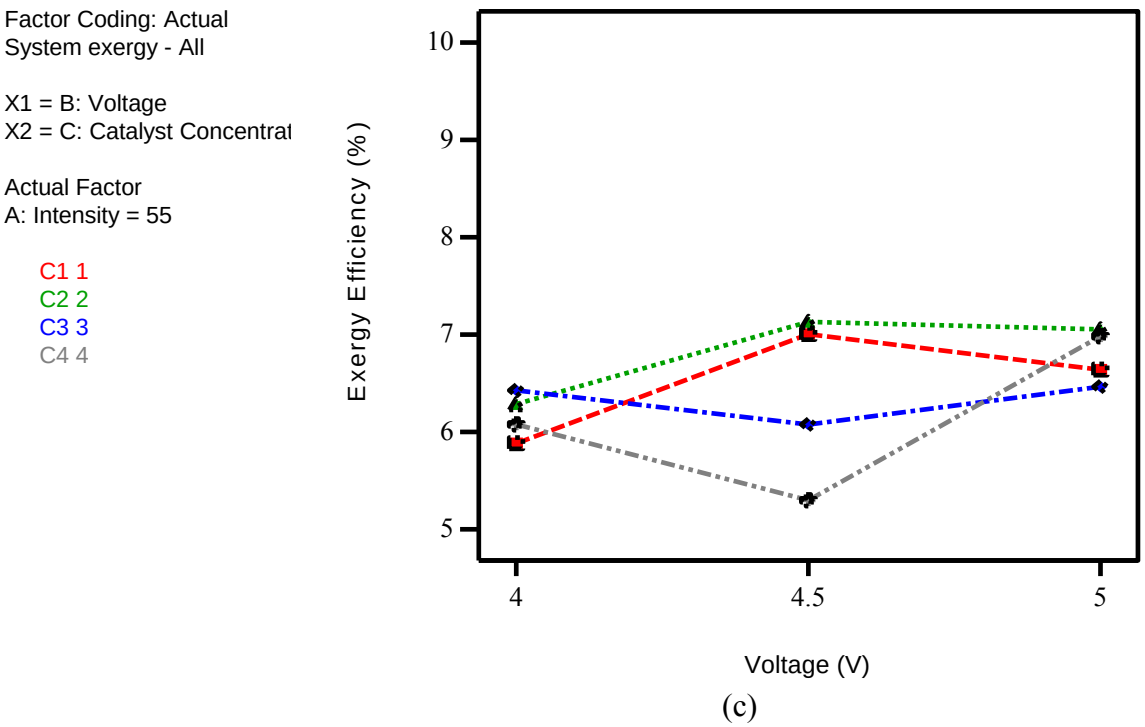

(c)

Figure 6.23: Effect of voltage (V) on energy efficiency values at different catalyst concentration levels (g/425mL) with a light intensity of a) 20W/m^2 b) 30 W/m^2 c) 55W/m^2.

It is noteworthy is the fact that the photo catalyst only uses a portion of the incident spectrum (i.e. ZnS works in UV region of the solar spectrum and uses only 4% of the total incident solar spectrum). This results in a decrease of efficiency with an increase in light intensity within the system. Exergy efficiency of the chloralkali process is calculated by using equation 5.22. Figure 6.23 shows the effect that voltage has on exergy efficiency at different catalyst concentration with different light intensities. Trends prove to be similar to energy efficiency values, however, they exist with higer values of exergy efficiency compared to energy efficiency. This condition is a result of the addition of chemical exergy of chlorine and sodium hydroxide in the numerator of the exergy efficiency formula. The highest efficiency rate is observed at 20W/m^2 , whereas thelowest efficiency rate is observed at 55 W/m^2.

6.4.7 Optimization Results

Optimization of the photo-electrochemical chloralkali process is performed by using Stat-ease® 8.1.6. Stat-ease® defines a variable known as desirability. This desirability factor characterizes

how close the target is from the sample. Its value varies from 0 to 1; where 0 indicates a highly non-desirable level,and 1 indicates a highly desirable level. Stat-ease® uses a method developed by Derringer and Suich for optimization. For the present analysis, optimization is performed separately for two different objectives individually: (i) hydrogen production optimization and (ii) efficiency optimization.

In hydrogen production optimization, the objective is to find the numerical values of the studied parameters (i.e. light intensity, applied voltage, catalyst concentration levels), which maximize the rate of photo-electrochemical hydrogen production. While focusing on efficiency optimization, the objective is to maximize the energy and exergy efficiency of the reactor. Table 6.16 shows the constriants for the optimization status of hydrogen production.

The objective desirability function for the constraints set in Table 6.16 can be written as

$$d_{H2} = \frac{\dot{m}_{H2} - 0.2}{0.18} \tag{6.13}$$

Because there is only one goal, the response desirability represents the overall desirability.

$$D = d_{H2} \tag{6.14}$$

where d_{H2} represents the individual desirability function of hydrogen production, D represents the overall desirability.

Table 6.16: Constraints for optimization of hydrogen production

Constraints						
Name	Goal	Lower	Upper	Lower	Upper	Importance
Intensity (W/m^2)	Input Term	20	55	1	1	3
Voltage (V)	Input Term	4	5	1	1	3
Cat Conc.	Input Term	1	4	1	1	3
$\dot{m}_{H2}$ (µg/s)	Maximize	0.20	0.38	1	1	3

The results show that the maximum amount of hydrogen is produced at a catalyst concentration level of 2g/425mL, light intensity of 55 W/m^2, and a voltage level of 5 V. Figure

6.24 shows the effect of voltage (V) and catalyst concentration levels (g/425mL) on the desirability factor at different light intensities.

X1 = B: Voltage
X2 = C: Concentration

Actual Factor
A: Intensity = 55

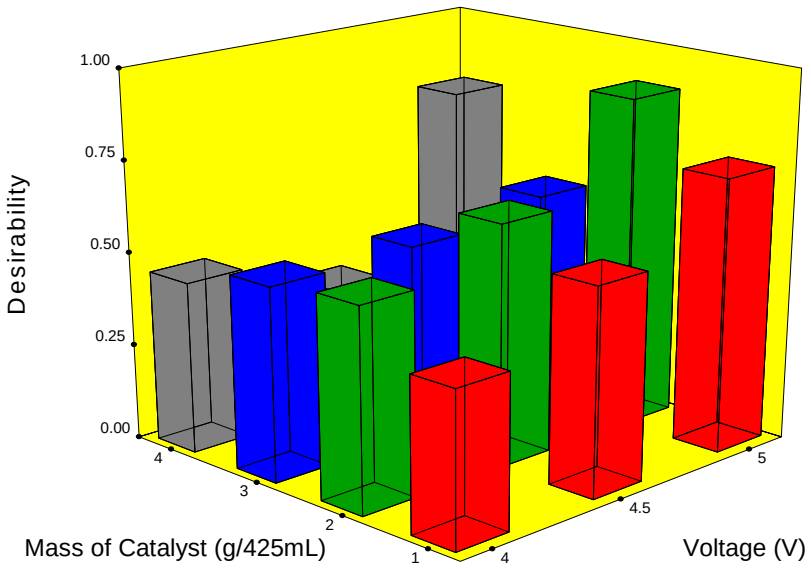

(a)

X1 = B: Voltage
X2 = C: Concentration

Actual Factor
A: Intensity = 30

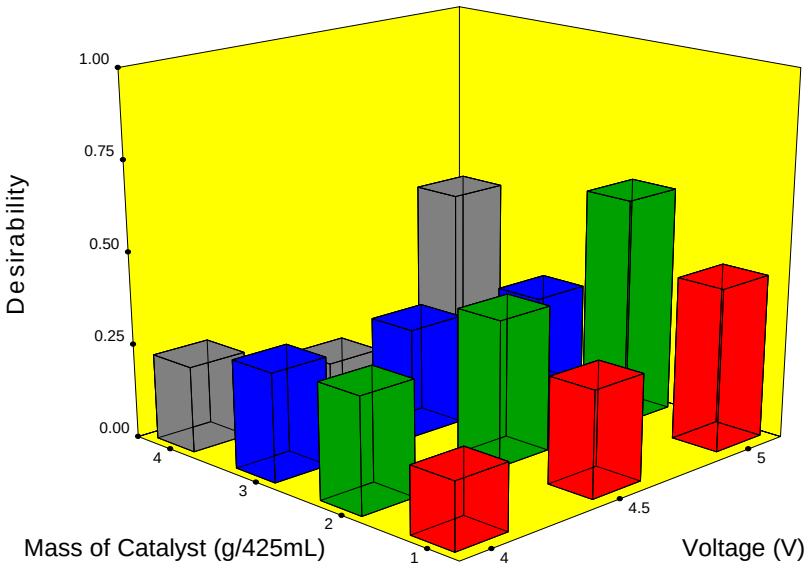

(b)

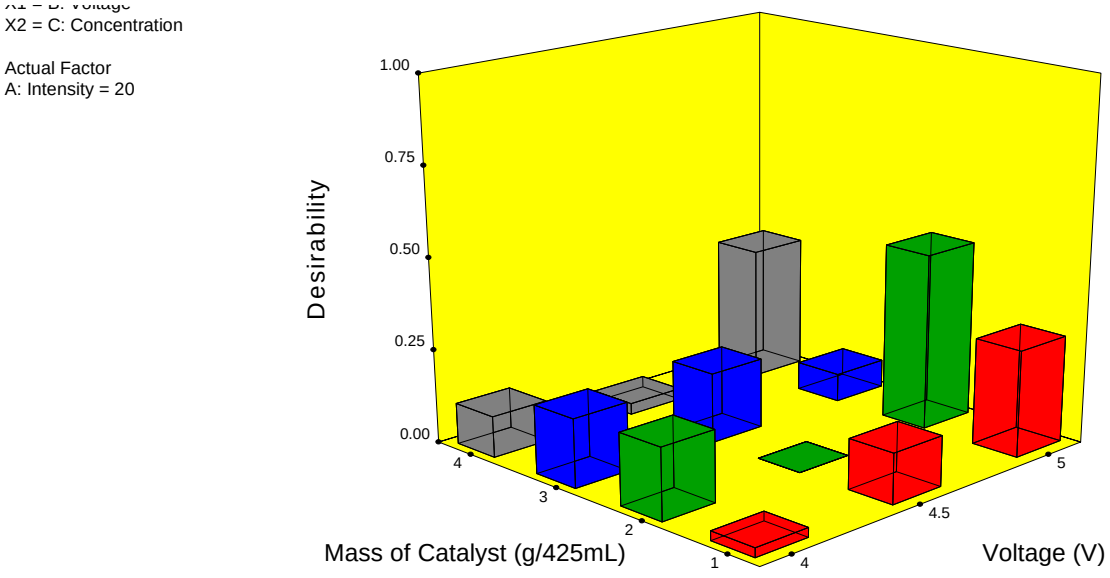

(c)

Figure 6.24: Effect of the amount of catalyst (g/425mL) and voltage levels on the desirability factor with a light intensity of a) 55 W/m^2 b) 30 W/m^2 c) 20 W/m^2.

The optimization results also confirm the fact that at a given voltage and catalyst concentration, increasing the light intensity increases the rate of hydrogen production. This increase is a result of an increase in photochemical hydrogen production. While at a specific intensity and amount of catalyst, increasing the voltage supply also increases the rate of hydrogen production; this increase is due to electrochemical hydrogen production. Table 6.17 shows the constriants for the optimization of energy and exergy efficiency.

The objective of the desirability function for the constraints set in Table 6.12 can be written as

$$d_{exe} = \frac{\eta_{exe} - 5.17}{4.02} \tag{6.15}$$

$$d_{en} = \frac{\eta_{en} - 3.36}{2.62} \tag{6.16}$$

$$D = \sqrt{d_{exe} d_{en}} \tag{6.17}$$

where d_{exe} and d_{en} represents the individual desirability functions of energy and exergy efficiencies, and D represents the overall desirability.

Table 6.17: Constraints for optimization of hydrogen production.

Constraints						
Name	Goal	Lower Limit	Upper Limit	Lower Weight	Upper Weight	Importance
Intensity (W/m^2)	Input Term	20	55	1	1	3
Voltage(V)	Input Term	4	5	1	1	3
Cat Conc.	Input Term	1	4	1	1	3
$\eta_{en}(\%)$	Maximize	3.36	5.98	1	1	3
$\eta_{exe}(\%)$	Maximize	5.17	9.19	1	1	3

The results show that energy and exergy efficiencies are at its maximum when the minimum voltage supply is applied with minimum light intensity. The optimal value of the catalyst concentration level (2g/425mL), however, remains same. Figure 6.25 shows the effect of voltage (V) and catalyst concentration levels (g/425mL) on the desirability factor at different light intensities.

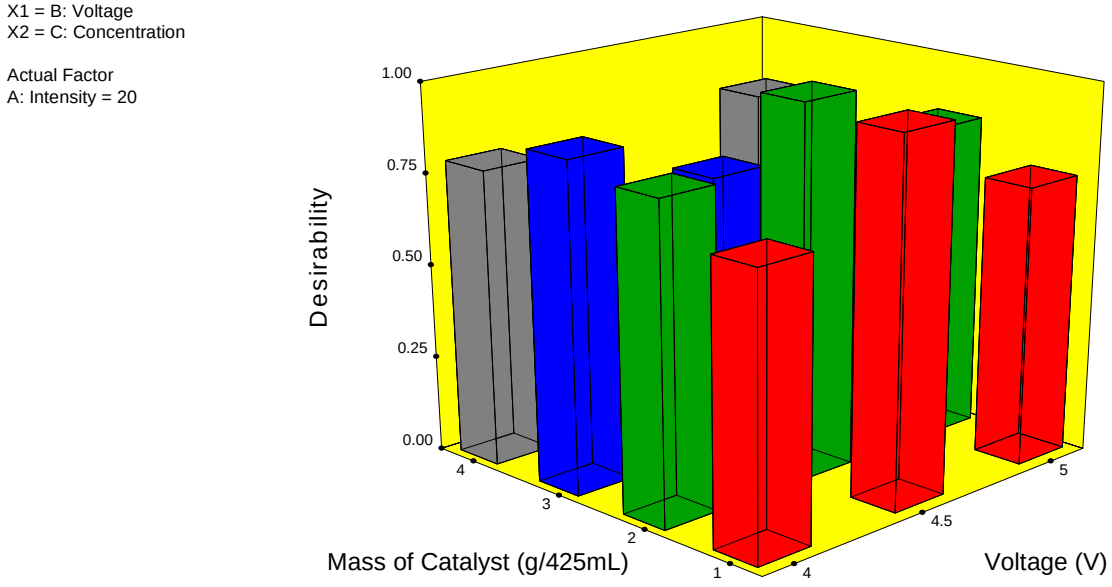

(a)

X1 = B: Voltage
X2 = C: Concentration

Actual Factor
A: Intensity = 30

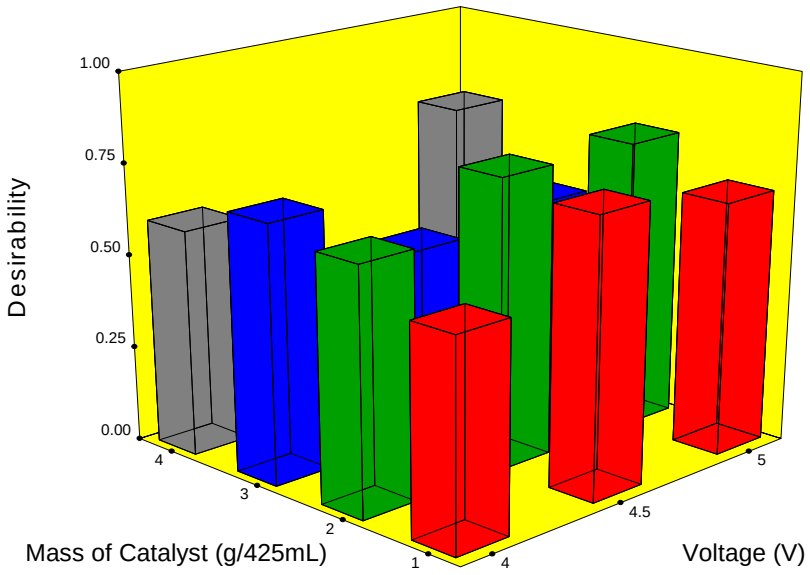

(b)

X1 = B: Voltage
X2 = C: Concentration

Actual Factor
A: Intensity = 55

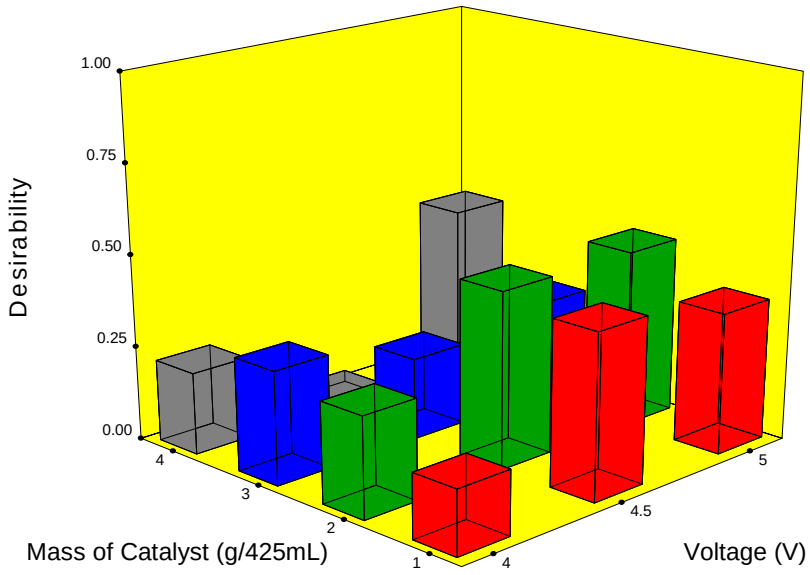

(c)

Figure 6.25: Effect of the amount of catalyst (g/425mL) and voltage on the desirability factor at the light intensity of a) 20W/m^2 b) 30W/m^2 c) 55 W/m^2.

6.5 Hydrogen Production in Salt Water

A sixth model is used to find the effect that applied voltage, amount of catalyst, and light intensity can have on the rate of hydrogen production. Table 6.18 shows ANOVA for the rate of photochemical hydrogen production. The Model F-value of 117756.4 implies that the model is significant. There is only a 0.01% chance that a "Model F-Value" this large could occur due to noise. Values of "Prob > F" less than 0.0500 indicate that the model terms are significant In this case, A, B, C, AB, AC, BC, A^2, B^2, ABC, A^2B, A^2C, AB^2, B^2C, A^2B^2, AB^2C are significant model terms. Those p-values greater than 0.1000 indicate that the model terms are not significant.

Table 6.18: ANOVA for the rate of the electrochemical hydrogen production.

Transform: None						
ANOVA for Response Surface Sixth Model- Photochemical H_2 production rate						
Source	Sum of	df	Mean Square	F- Value	p-value	
Model	0.051643	15	0.003443	117756.4	< 0.0001	significant
A: Intensity (W/m^2)	0.016391	1	0.016391	560619	< 0.0001	
B: Voltage(V)	0.005312	1	0.005312	181689.2	< 0.0001	
C: Cat Conc. (g/425mL)	5.78E-05	1	5.78E-05	1976.697	0.0005	
AB	0.001759	1	0.001759	60177.57	< 0.0001	
AC	0.001114	1	0.001114	38114.96	< 0.0001	
BC	0.00019	1	0.00019	6502.048	0.0002	
A^2	0.000248	1	0.000248	8485.933	0.0001	
B^2	0.000262	1	0.000262	8964.362	0.0001	
ABC	0.000354	1	0.000354	12116.17	< 0.0001	
A^2B	0.00018	1	0.00018	6140.926	0.0002	
A^2C	3.74E-05	1	3.74E-05	1277.679	0.0008	
AB^2	0.001545	1	0.001545	52831.7	< 0.0001	
B^2C	0.000781	1	0.000781	26696.38	< 0.0001	
A^2B^2	1.69E-06	1	1.69E-06	57.72741	0.0169	
AB^2C	0.000528	1	0.000528	18074.73	< 0.0001	
Residual	5.85E-08	2	2.92E-08			
Cor Total	0.051643	17				

Design-Expert® Software
Factor Coding: Actual
H2 (ug/s)
0.351526

0.178759

X1 = A: Intensity
X2 = C: Salt Concentration

Actual Factor
B: Voltage = 4.00

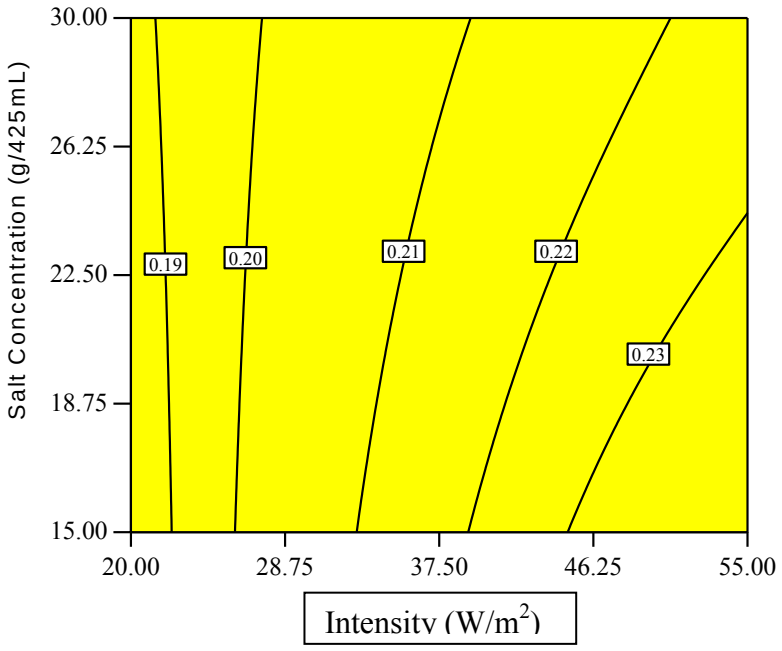

(a)

Design-Expert® Software
Factor Coding: Actual
H2 (ug/s)
0.351526

0.178759

X1 = A: Intensity
X2 = C: Salt Concentration

Actual Factor
B: Voltage = 4.50

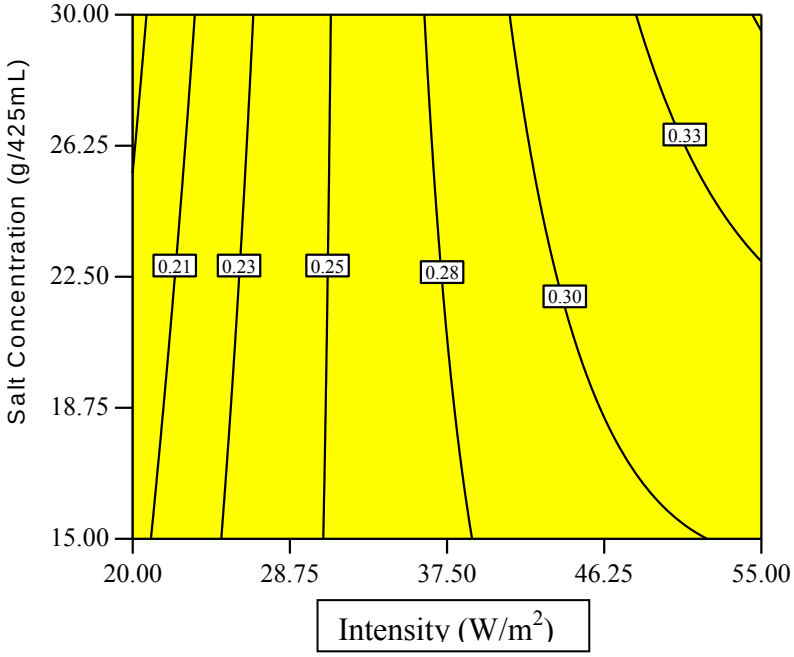

(b)

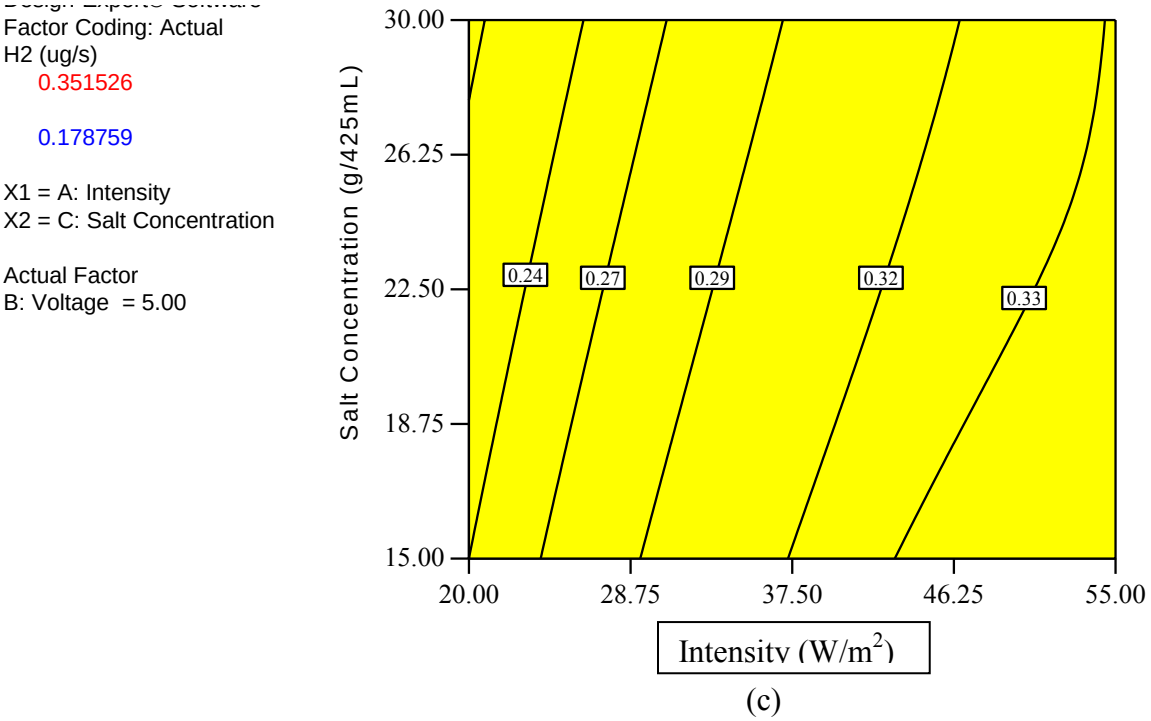

(c)

Figure 6.26: Effect of light intensity on the rate of photo-electrochemical hydrogen production at different salt concentration levels with a voltage level of a) 4V b) 4.5V c) 5V.

To improve the accuracy of the mode,l backward elimination (i.e. the elimination of all those terms from the model that do not have effect on the response), is applied. Adeq Precision (Signal to noise ratio in model) for the rate of the photochemical hydrogen production model is 1072.5, which indicates an adequate signal.

$$\dot{m}_{H2,SPE} = -1.70 + 0.10A + 0.76B + 0.18\,C - 0.05\,A\,B - 8.88 * 10^{-3} A\,C - 0.08BC - 2.50 * 10^{-4} A^2 - 0.08B^2 + 3.85 * 10^{-3} ABC + 1.37 * 10^{-4}\,A^2 B + 1.68 * 10^{-6} A^2 C + 5.58E - 003 * AB^2 + 8.06E - 003 * B^2 C - 2.27E - 005 * A^2 B^2 - 4.16E - 004 * AB^2 C \quad (6.18)$$

where A represents the light intensity in W/m^2, B represents applied voltage in volts, and C represents salt concentration in g/425mL. $R^2_{H2,SPe} = 0.96$ between the experimental data and model equation (6.18).

As discussed above, increasing the light intensity and voltage supply increases the rate of hydrogen production. Figure 6.26 shows the effect of light intensity on the rate of photo electrochemical hydrogen production at different catalyst concentration levels at different

voltages. At lower light intensity, salt concentration does not have any dominant effect on the rate of hydrogen production. Increasing the salt concentration at higher light intensities and voltages levels actually increases the rate of photo-electrochemical hydrogen production. This increase is caused by the higher electrical conductivity of the hydrogen production solution. This increase in conductivity results in a decrease in over potential, which ultimately results in increase to the rate of hydrogen production. Keeping in mind the wide availability of salt water around the globe today, this experimental result is certainly important and noteworthy.

6.6 Result of Hydrogen Production without Hole Scavenger

Figure 6.27 shows the effect that light intensity has on hydrogen production at a voltage level less than the level that is required for electrolysis in the chloralkali process (i.e. 2V) and at optimized catalyst concentration of 2g/425mL.

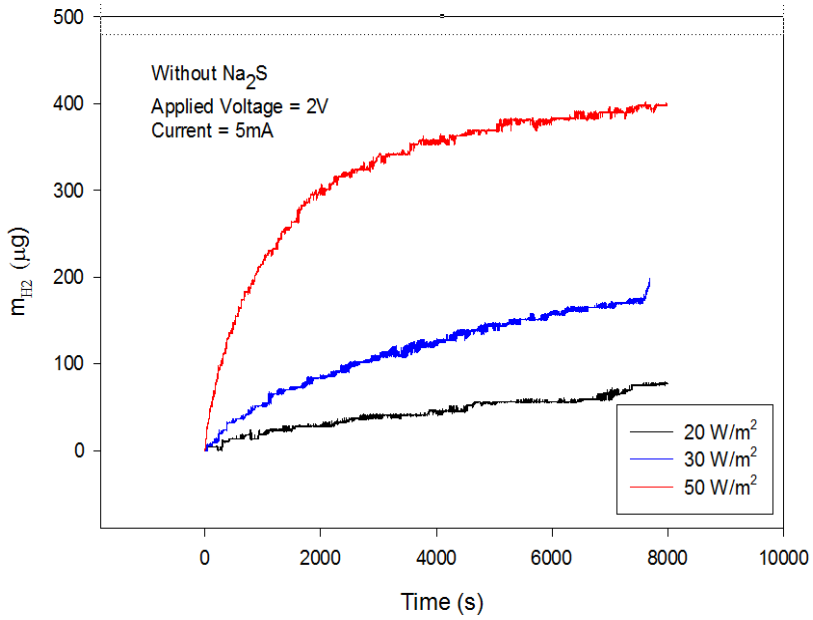

Figure 6.27: Effect of light intensity on hydrogen production at 2V without any hole scavenger material added in the hydrogen production unit of the reactor.

In these experiments, sodium sulfide (which is a hole scavenger material and the only consumable in the system), is not added to the catholyte solution. The supply of electrons is only provided by a cylindrical nickel electrode. At lower intensities, the amount of hydrogen produced is almost linear. After approximately twenty minutes at higher intensity levels,

however, the rate of hydrogen production is set to a steady state constant value. During these experiments neither chlorine nor sodium hydroxide was produced. The production of hydrogen, however, confirms that the hole scavenger can be replaced with an electrode in a photo electrochemical process. Eliminating the hole scavenger means that there are no consumables in the system except water which is available in enormous amounts. Using salt water, without any electron donor or hole scavenger material, results in significant cost reduction of the hydrogen production system.

6.7 Result of Solarium Experiments

Figure 6.28 shows the hydrogen and chlorine production in a photo-electrochemical chloralkali reactor under actual sunlight. Trends, therefore, are almost linear. Continuous hydrogen production is observed. At around 1000 seconds, the curve drops down slightly.

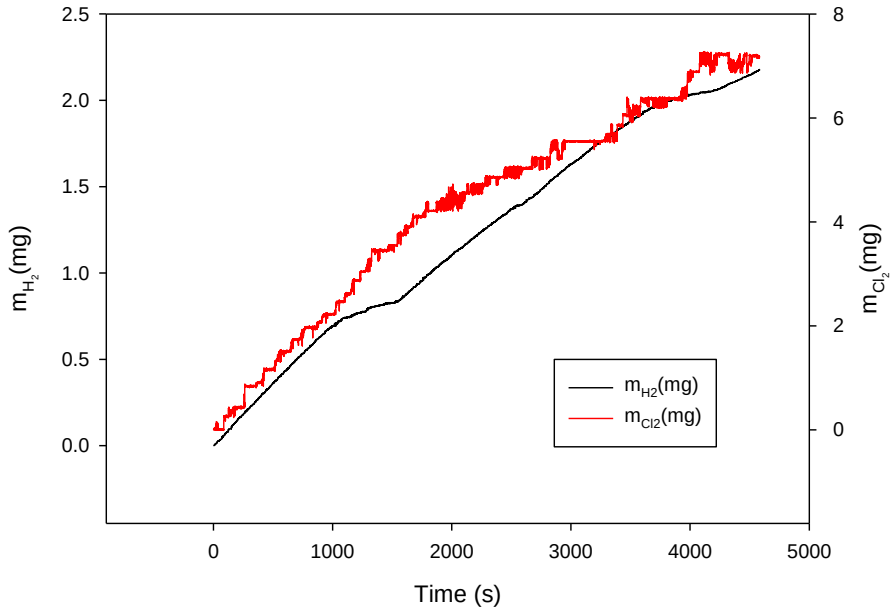

Figure 6.28: Hydrogen and Chlorine production in actual sunlight.

This is the result of a cloudy period. Once the cloudy period passes, the production is again increasing linearly over time. Due to the present safety concerns (related to the hydrogen

collection chamber made from glass), the experiment is stopped after 4600 sec. The increase to the partial pressure of the hydrogen is rapid and up to 30kPa was observed in 4600 sec. As concluded from the previous experimental results, the rate of hydrogen production by the sole means of the photochemical process alone is very small. Extracting the unused portion of the solar spectrum does improve the production rate, while simultaneously improving the efficiency of the process. Figure 6.29 shows the solar irradiance during the experiment. Because of the higher solubility of chlorine in water, lower chlorine pressure was observed. As shown in Figure 6.26 chlorine follows the same trends as hydrogen. The amount of chlorine produced, however, is higher due to its higher molecular mass.

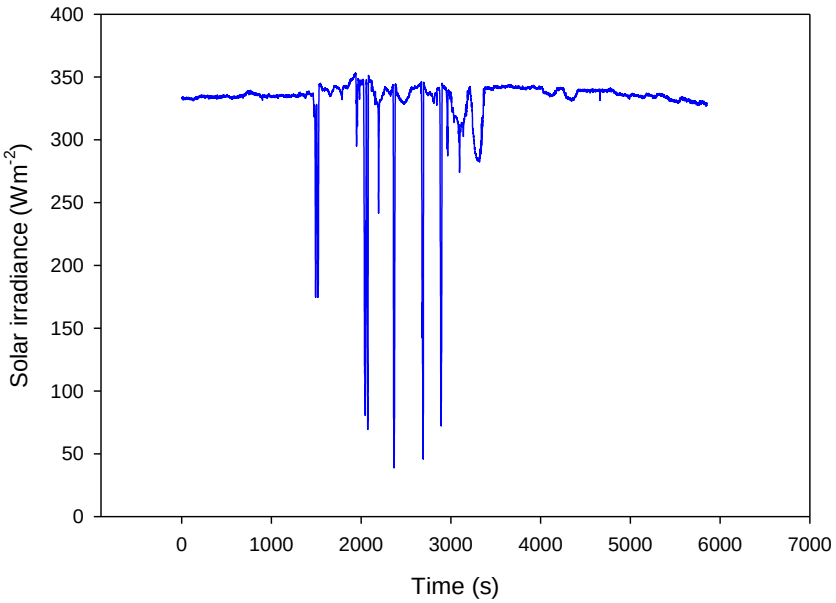

Figure 6.29: Solar irradiance for the solarium experiment.

6. 8 Results of Radiation and Thermodynamic Modeling

The thermodynamic and radiation modeling of the photo-electrochemical reactor is presented in section 5.5 and 5.6. In this section, a parametric study for a continuous plant is presented. Figure 6.30 shows the schematic of the proposed plant. Light is focused on the reactor by using heliostats. The, incoming light radiations are divided into two different light beams by using

dielectric mirror. One is used for photochemical hydrogen (i.e. direct reduction of water into hydrogen), while the other is used for electrochemical hydrogen production (by using unused portion of the solar spectrum by means of PV panel). The developed model is valid for any kind of photo catalyst. For parametric studying purpose, ZnS is used. ZnS works in the UV region, which is 4% of the total solar spectrum.

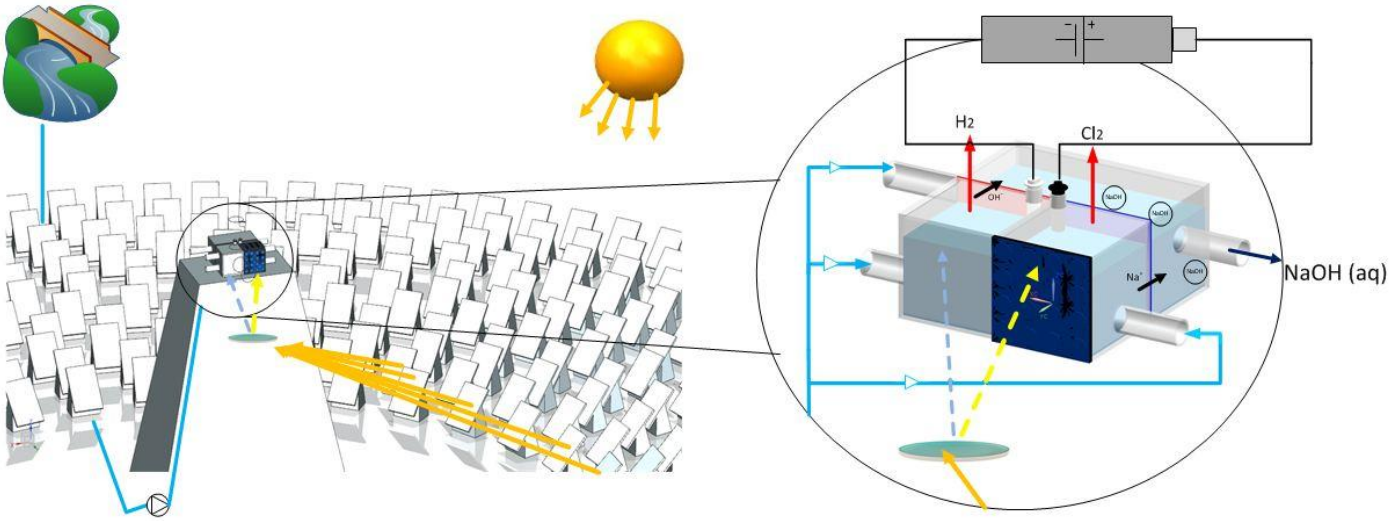

Figure 6.30: Schematic of a large scale plant.

6.8.1 Results of Light Intensity

Solar irradiance is the main driving force of the system. For this present study, the city of Toronto is selected for clear and turbid sky radiation modeling purposes. The model, however, can be applied to any location in the world with any present sky condition. Some of the parameters used in the radiation modeling are given in Table 6.19.

Figure 6.31 shows solar irradiance in W/m^2 at different surface angles (i.e. angle between the heliostat and the ground), for a clear sky condition for the city of Toronto. In this present model, solar irradiance is evaluated between 8 A.M to 4 P.M; the maximum intensity is usually present at noon hour. To reflect the incoming solar radiations from the heliostat to the solar tower, the surface angle must be between 0^o and 90^o. The optimum surface angle varies every day. For a clear sky model, reflected and diffused radiations also contribute significantly to the total radiations. The results also indicate that the maximum intensity occurs at a surface angle of 23^o during the summer season.

Table 6.19: Parameters for radiation modeling.

L_L	Longitude	79.404°
ψ	Latitude	43.64°
ΔT_{GMT}	Time difference for standard	5
L_{OZ}	Ozone Layer Thickness	0.35 cm
T_{dew}	Average dew point temperature	290K
ρ_g	Albedo of the ground	0.24
F_c	Ratio of forward scattering to	0.8
ω_0	single-scattering albedo fraction	0.9
$\dot{I}_{sc}$	Solar constant	1367 W/m^2
$\varkappa$	Number of heliostats	350

On a day with turbid sky conditions, the radiation reaching the earth decreases as a result of cloudy periods. Most of the high energy radiations being reached are absorbed. Figure 6.32 shows solar irradiance in W/m^2 at different surface angles for a turbid sky model for the city of Toronto (at different times). A maximum radiation reaches the earth during the summer season at approximately noon hour.

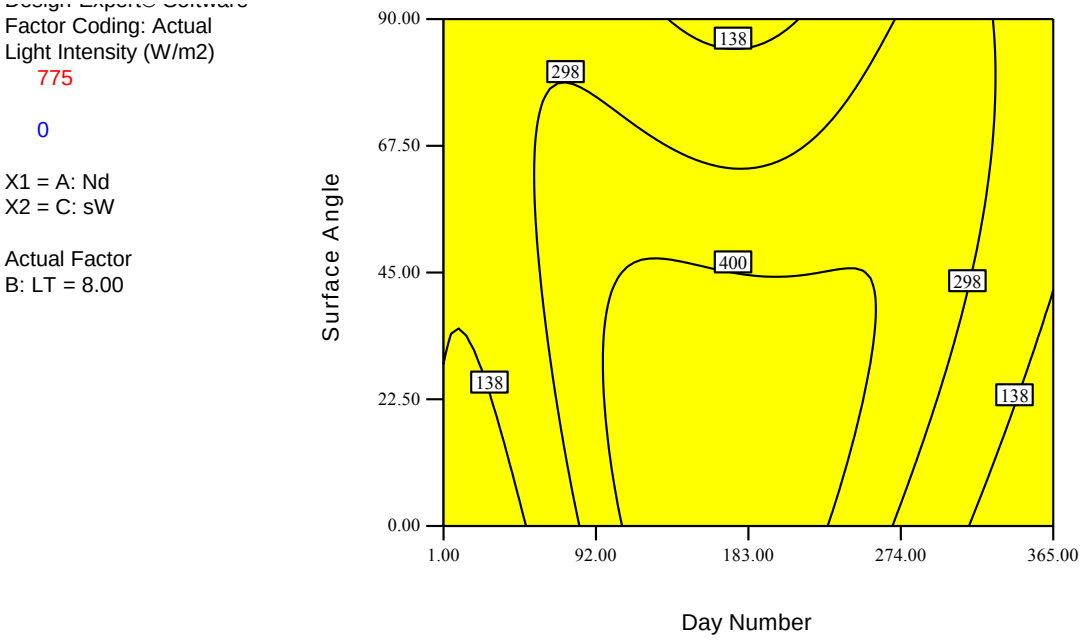

(a)

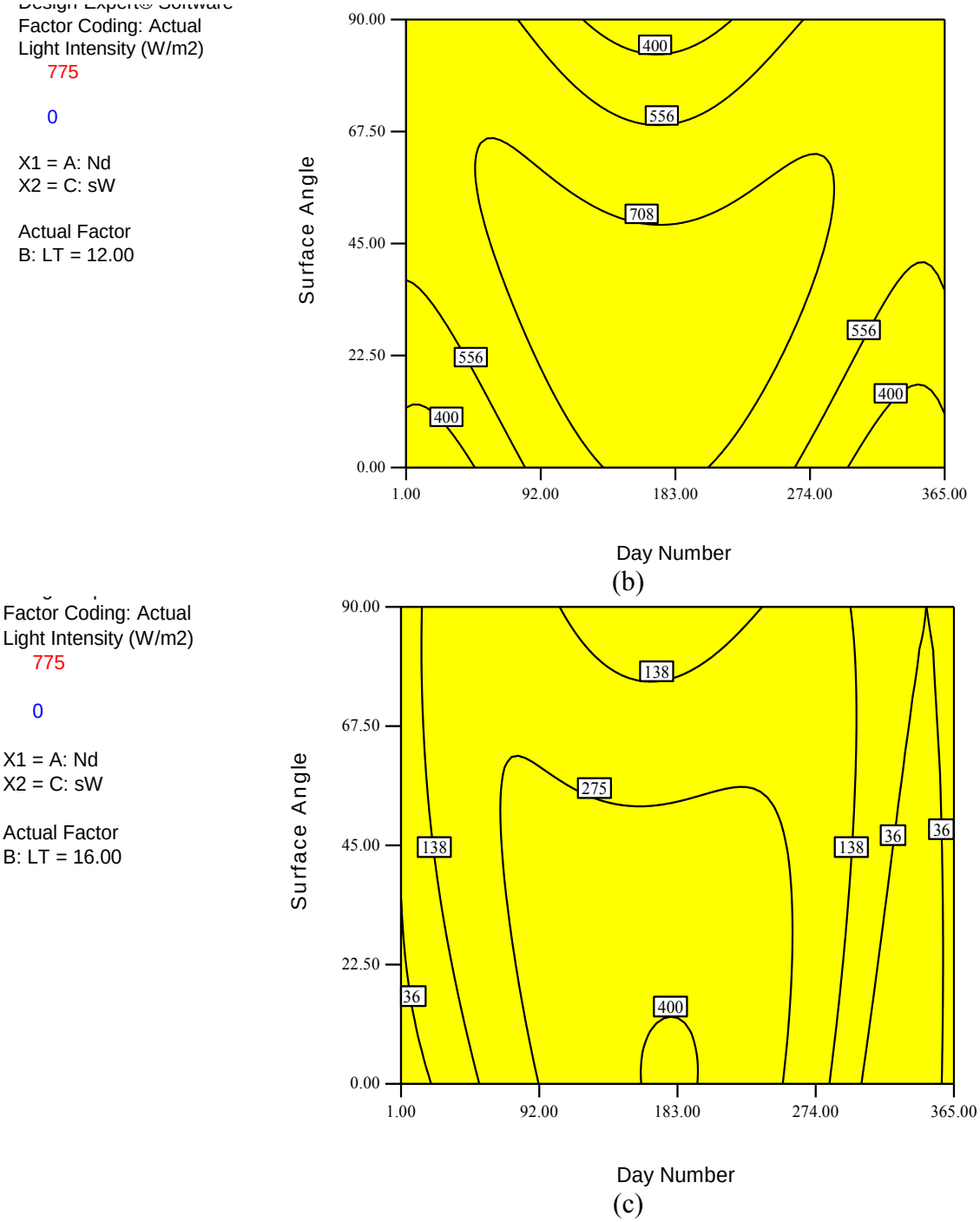

Figure 6.31: Solar radiation (W/m^2) at different surface angles on a) 8 A.M b) 12 P.M c) 4 PM for the city of Toronto for a clear sky condition.

Design-Expert® Software
Factor Coding: Actual
Light Intensity (W/m2)
581

0

X1 = A: Nd
X2 = C: Surface Angle

Actual Factor
B: LT = 8.00

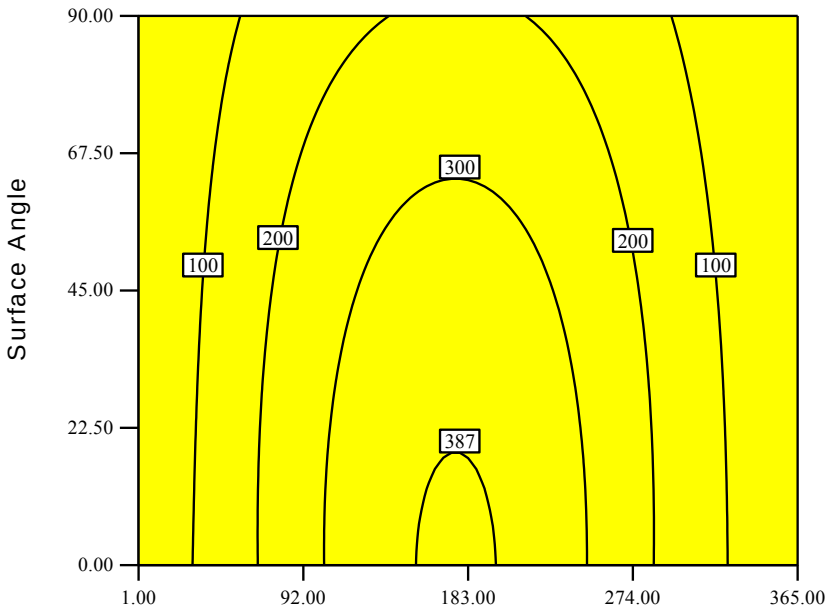

(a)

Factor Coding: Actual
Light Intensity (W/m2)
581

0

X1 = A: Nd
X2 = C: Surface Angle

Actual Factor
B: LT = 12.00

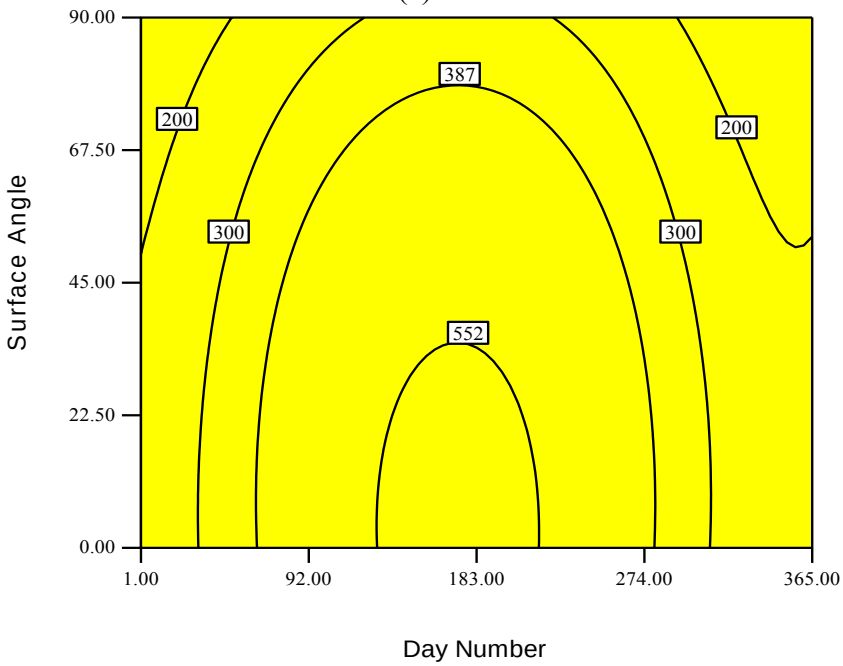

(b)

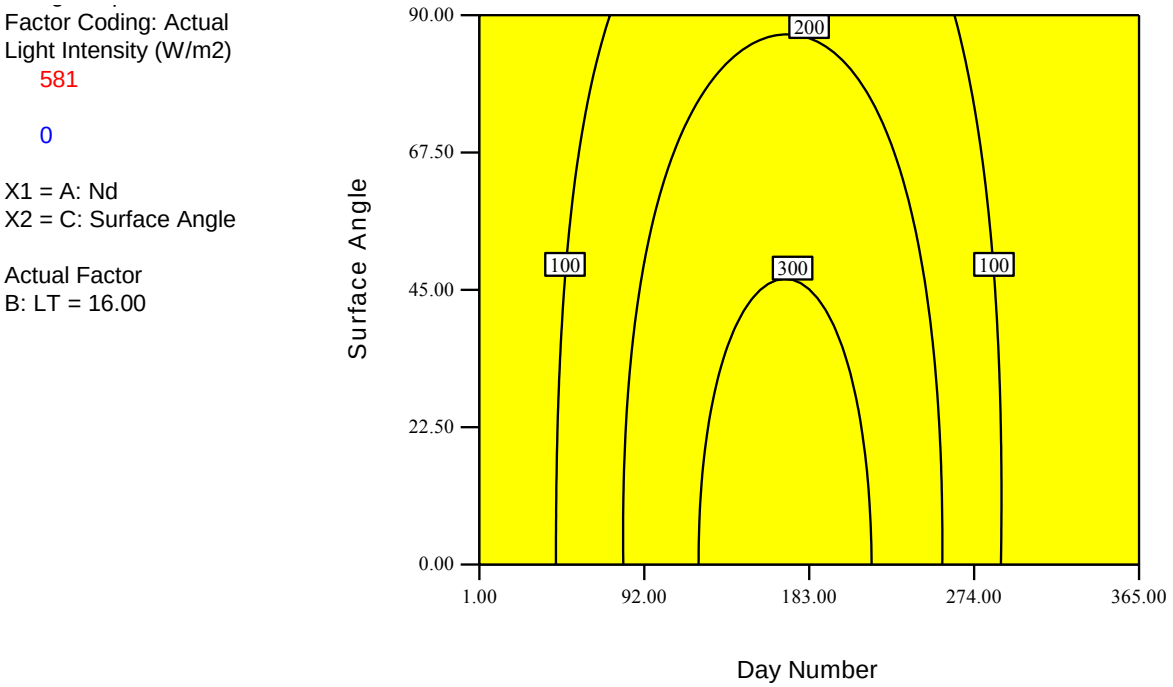

(c)

Figure 6.32: Solar radiation (W/m^2) at different surface angles on a) 8 A.M b) 12 P.M c) 4 P.M for the city of Toronto for a turbid sky.

Table 6.20: Parameters for radiation modeling.

	Fraction of total solar	0.04
β	Brine Concentration	15
T_o	Atmospheric temperature	300K
P_o	Atmospheric pressure	0.35 cm
$A_{reactor}$	Area of reactor exposed to the	10 m^2
η_{PV}	Efficiency of solar PV panels	13%
A_{PV}	Area of solar PV panels used	20 m^2
$\eta_{optical}$	Optical efficiency of dielectric	100%
DM	Transitivity of dielectric	100%

In turbid sky conditions, the reflected and diffused radiations do not contribute significantly. For this reason, the maximum intensity occurs at a surface angle of 0^o (i.e. horizontal surface). In order to reflect the radiations to the solar tower, however, the surface angle must be greater than zero. The optimum surface angle depends upon the path of the sun

and constantly changes. For this reason, a solar tracking heliostat would be preferred over a fixed one.

6.8.2 Results of Rate of Hydrogen Production

Using the thermodynamic model production rate for chloralkali products is determined. For a steady state steady flow reactor with a brine concentration difference of $(\beta) = 15$ rate of hydrogen production is evaluated. As a result, trends follow the similar path to the energy input (i.e. solar irradiance). Some of the parameters used for the thermodynamic modeling are given in Table 6.15.

Figure 6.33 shows the rate of hydrogen production (kg/s) at different surface angles. The maximum production is observed during noon hour in the summer season. Chlorine and sodium hydroxide show similar trends as hydrogen, but with a higher rate of production than hydrogen. This can be explained by referring to a balance chemical equation (Table 5.1).

For each mole of hydrogen, one mole of chlorine and two moles of sodium hydroxide is produced. Due to the greater molecular weight of chlorine (i.e. 70 kg/kmol) to hydrogen (i.e. 2.01 kg/kmol), one mole of chlorine is 35 times heavier than hydrogen. Similarly, one mole of sodium hydroxide (with a molecular mass of 40 kg/kmol), is 20 times heavier than hydrogen. So from this balanced chemical equation perspective, for each kg of hydrogen, 35 kg of chlorine and 80 kg of sodium hydroxide is produced. In a large scale heliostat-based plant, the solubility of chlorine in water is lessened due to the concentrated light that will heat up the solution.

The rate of chloralkali product creation also decreases in a turbid sky setting. The trends used to explain these results are similar to the intensity model. Figure 6.34 shows the rate of hydrogen production (kg/s) at different surface angles for a turbid sky setting. Maximum production is observed during noon hour in the summer season. As a result of the higher intensity of a horizontal surface in a turbid sky setting, the model predicts the maximum rate of production at 0^o. As previously mentioned, the surface should be greater than 0 and less than 90^o (the typical angle range is between 25^o - 45^o). In conclusion, in order to obtain the maximum production rate, the surface angle must be set to an optimum value.

Factor Coding: Actual
Rate of Hydrogen Productio
1.5

0.0

X1 = A: Nd
X2 = C: sW

Actual Factor
B: LT = 8.00

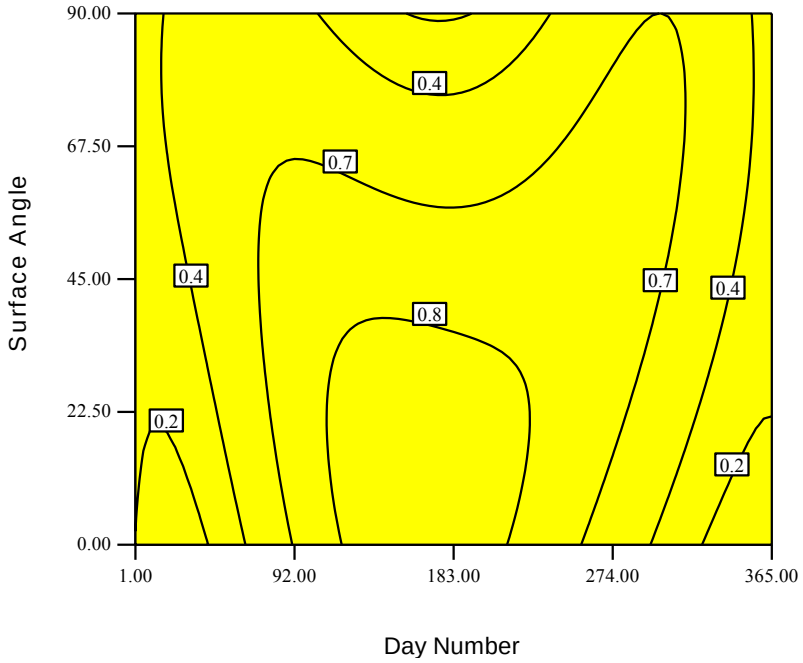

(a)

Factor Coding: Actual
Rate of Hydrogen Productio
1.5

0.0

X1 = A: Nd
X2 = C: sW

Actual Factor
B: LT = 12.00

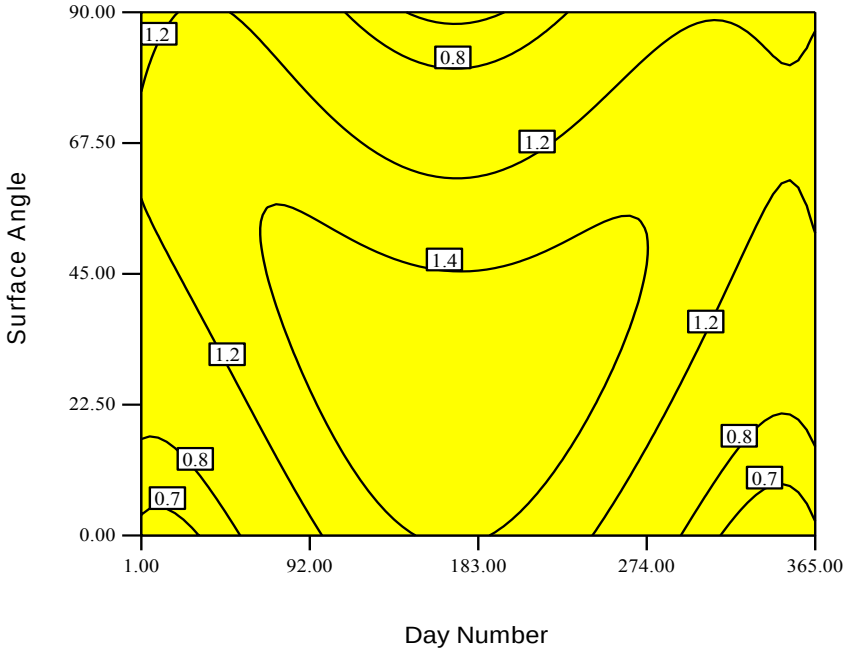

(b)

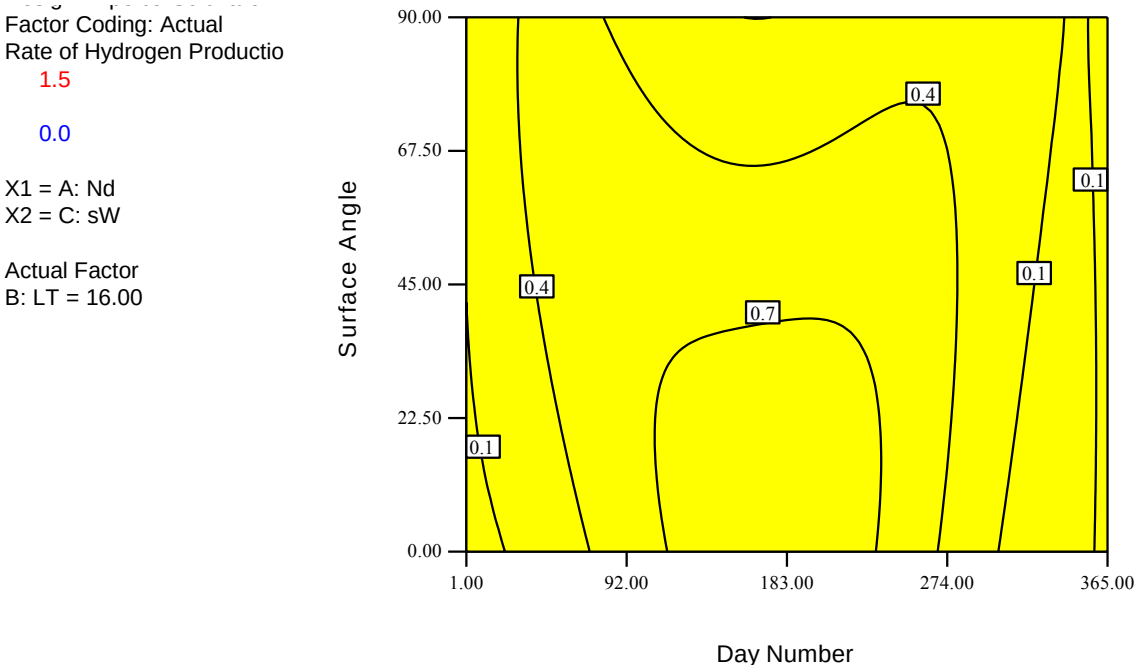

(c)

Figure 6.33: Rate of hydrogen production (kg/s) at different surface angles on a) 8 A.M. b) 12 P.M. c) 4 P.M. for the city of Toronto, with a clear sky setting.

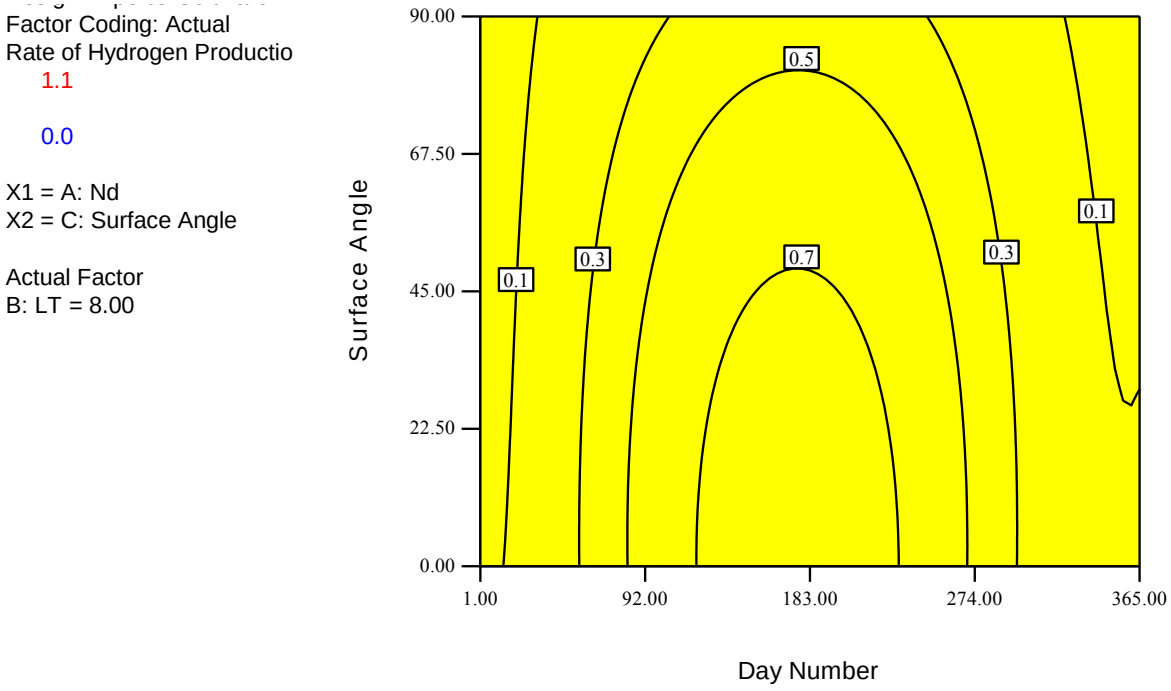

(a)

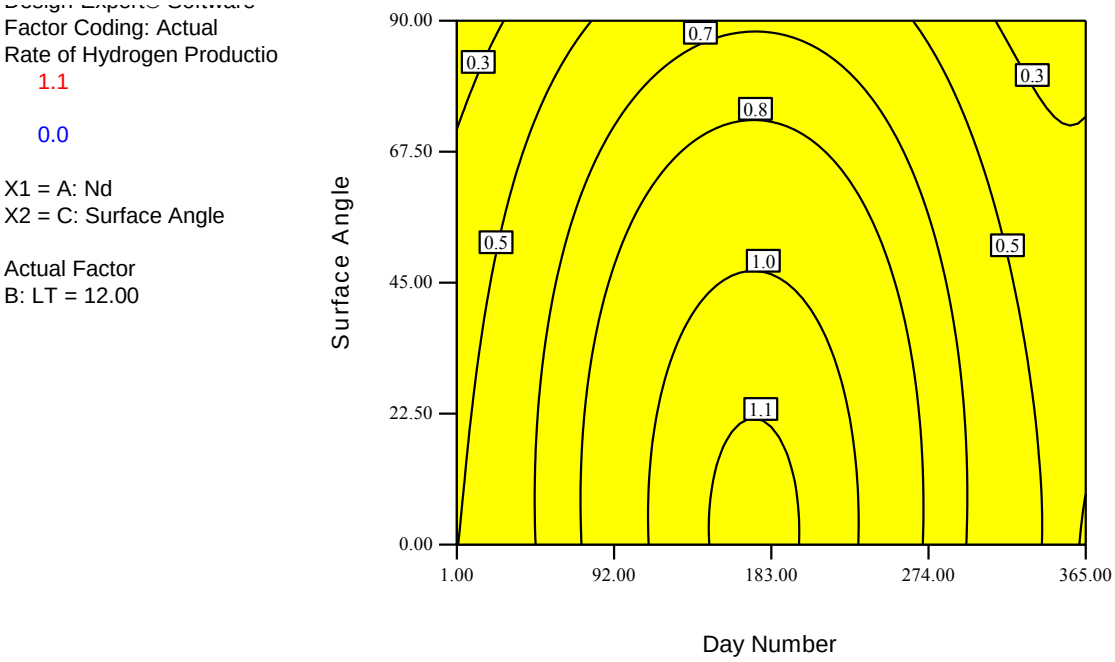

(b)

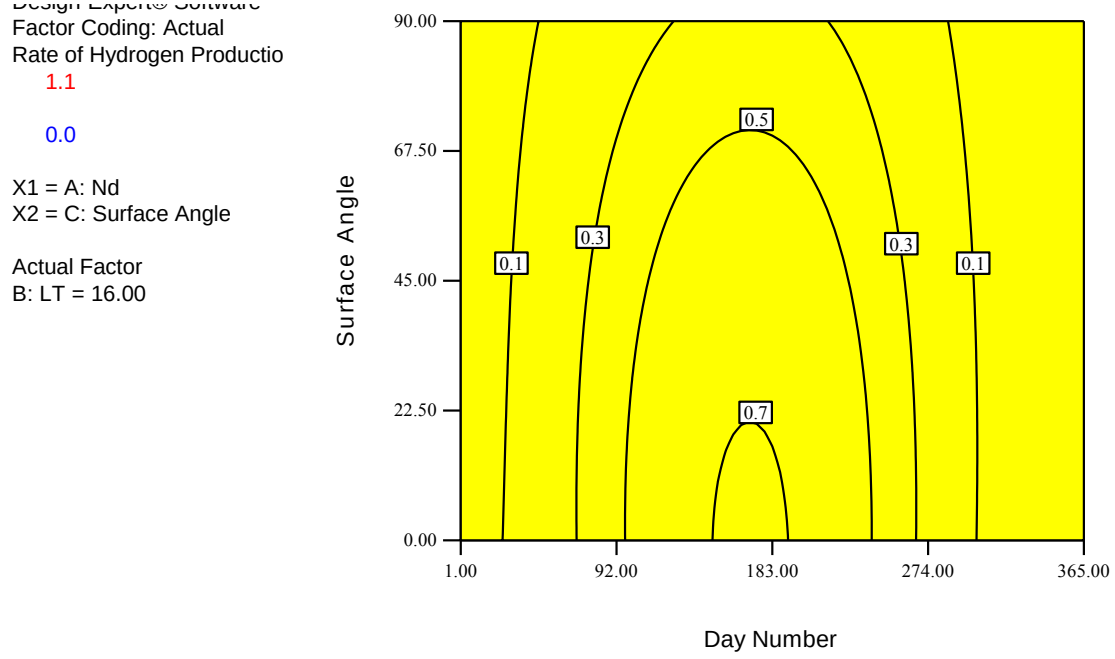

(c)

Figure 6.34: Rate of hydrogen production (kg/s) at different surface angles on a) 8 A.M b) 12 P.M c) 4 P.M for the city of Toronto in a turbid sky setting.

6.8.3 Cost of Hydrogen

The cost of hydrogen is a very dynamic parameter. It depends upon many different factors, which include: the efficiency of the hydrogen production system, market value of by-products, and the amount of by-products produced. Other important factors include the capacity of the hydrogen production plant, location of the plant, annual weather conditions, value of scaling factor, life time of the plant, etc. For the purposes of this present analysis, the cost of hydrogen is evaluated using equation (5.36). The scaling factor used for the present study is 0.7. The reference cost ($\mathbf{C_{ref}}$) and reference production scale ($\mathbf{\dot{m}_{ref}}$) are taken from a report submitted to department of energy (which represents the cost of different hydrogen production technologies using heliostat based plant) for the purposes of this study [119].

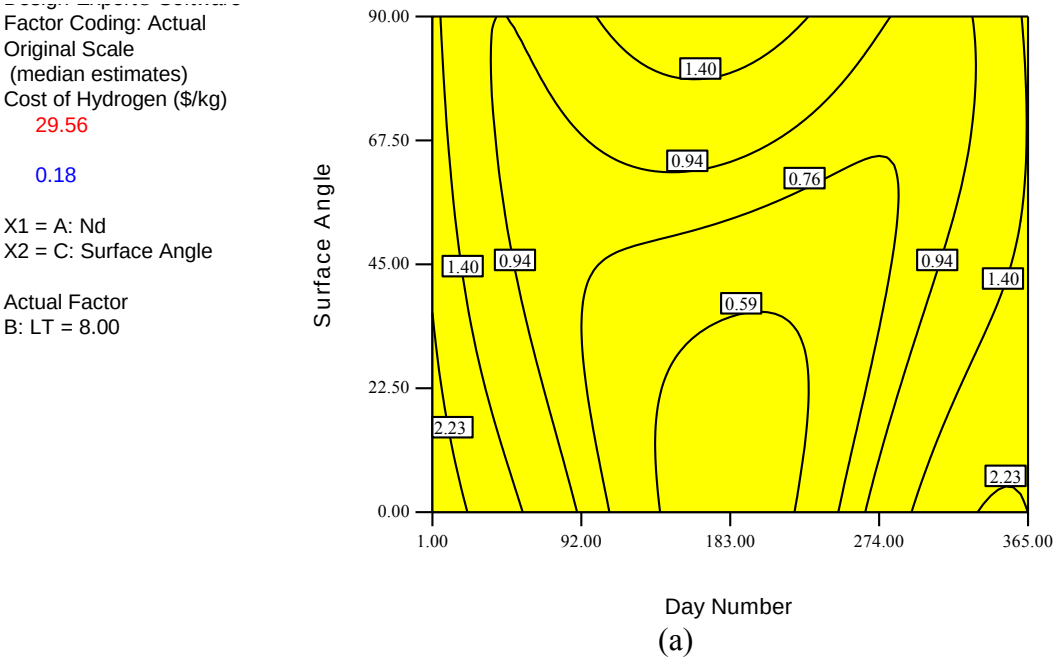

(a)

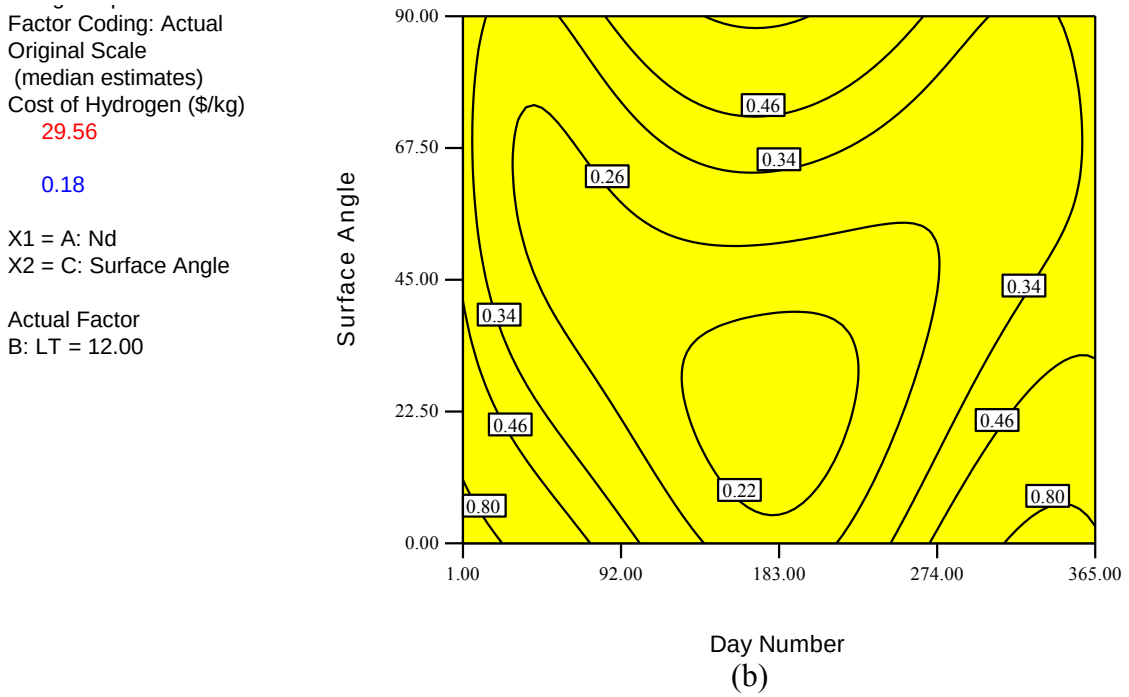

(b)

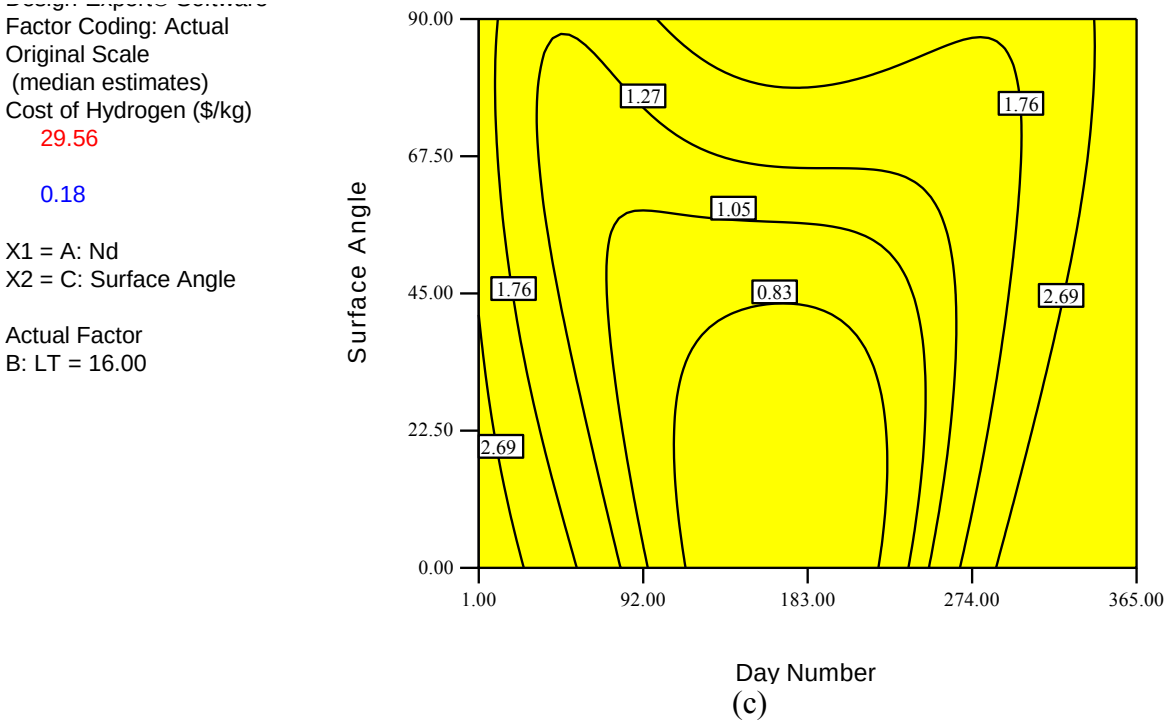

(c)

Figure 6.35: Cost of hydrogen ($/kg) at different surface angles on a) 8 A.M b) 12 P.M c) 4 P.M for the city of Toronto in a clear sky setting.

Figure 6.35 shows the cost of hydrogen at different surface angles and at different times during the day in a clear sky setting. For the purposes of this study, the cost of chlorine and

sodium hydroxide is assumed to be 0.05$/kg each. The trends for the cost of these factors are opposite to the solar irradiance and rate of hydrogen production. The cost is lowest during noon hour and at its highest during the start or end of the day. The negative values of these costs proves that the cost of chlorine and sodium hydroxide (which is 0.05$/kg in present study), surpasses the input costs.

The annual average cost is calculated to be 0.7$/kg with an average light intensity of 447W/m^2. The annual average hydrogen production rate for present study is calculated to be 0.86kg/s, with a chlorine production rate of 30 kg/s and a sodium hydroxide rate of 35kg/s. Increasing the cost of the by-products (i.e. chlorine and sodium hydroxide), will drastically reduce the price of hydrogen.

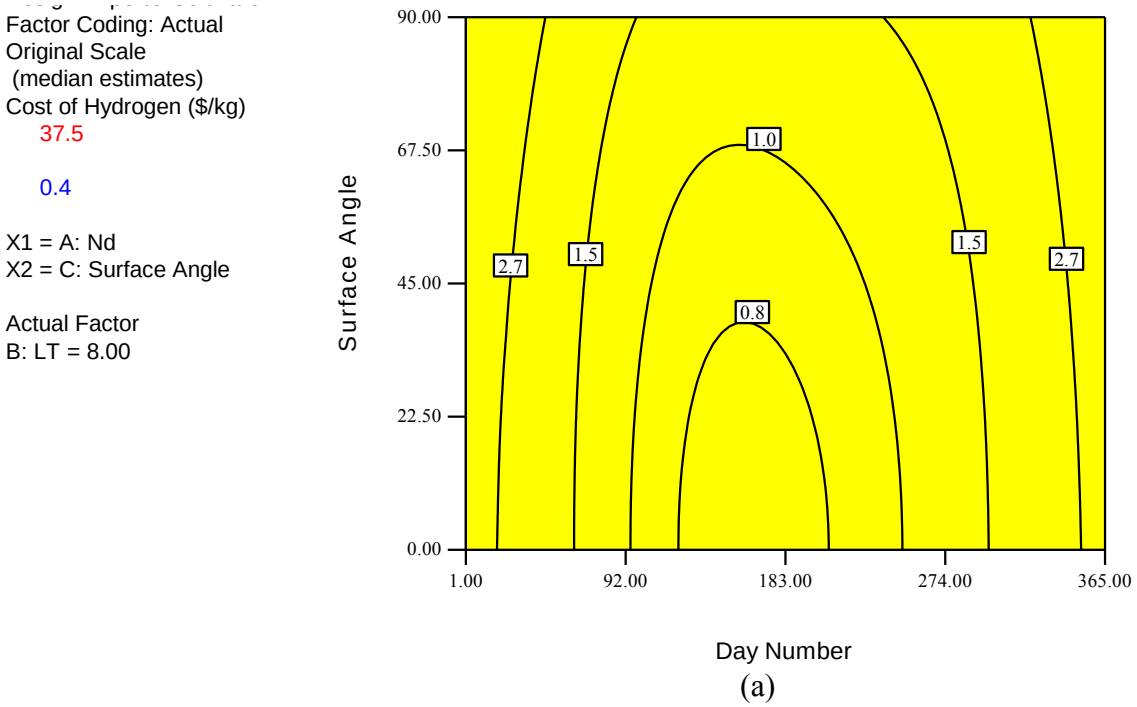

(a)

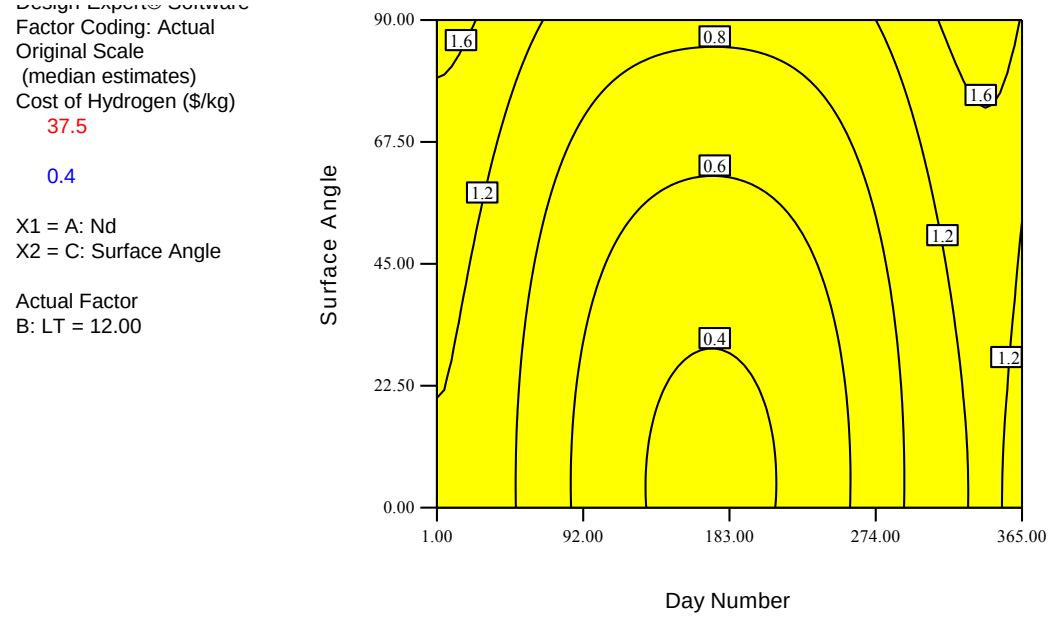

(b)

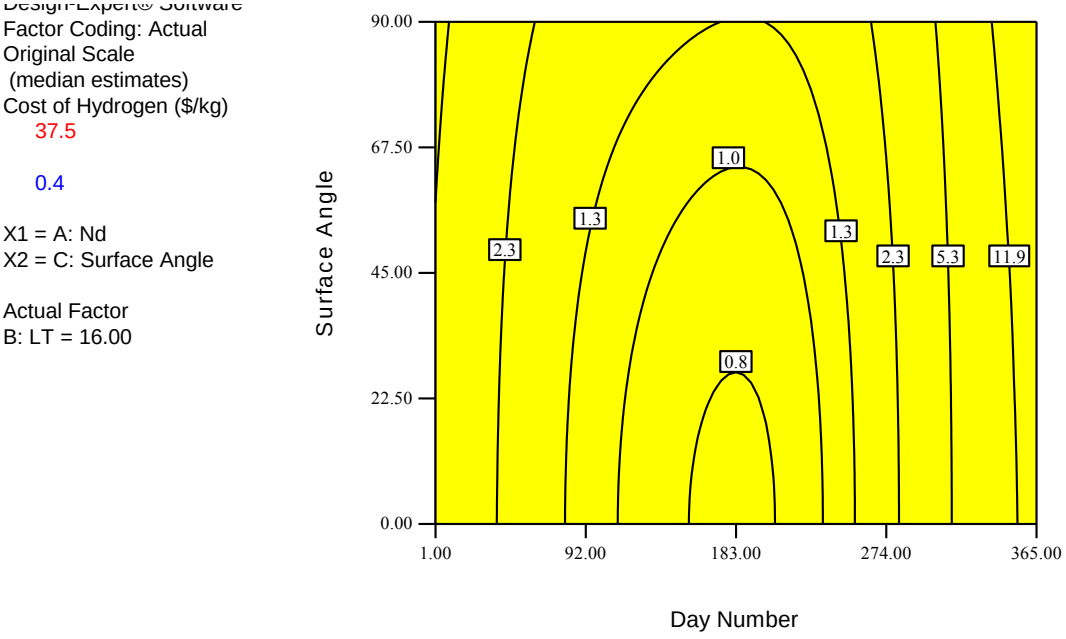

(c)

Figure 6.36: Cost of hydrogen ($/kg) at different surface angles at a) 8 A.M b) 12 P.M c) 4 P.M for the city of Toronto in a turbid sky setting.

Figure 6.36 shows the cost of hydrogen at different surface angles and at different times during the day for a turbid sky setting. The average hydrogen production rate is estimated to be 0.5kg/s, with a chlorine production rate of 18kg/s and rate of sodium hydroxide production of 20kg/s (with the average light intensity of 270W/m^2). The annual average cost of hydrogen is

estimated to be 1.4$/kg in a turbid sky setting (the cost of chlorine and sodium hydroxide was set to be 0.05$/kg during this simulation). It is important to mention that the market value of chlorine and sodium hydroxide in this north American region is much higher than what has been used in this present analysis ($C_{NaOH} = 1\$/kg$ and $C_{Cl2} = 1.2\ \$/kg$). Increasing the cost of chlorine and sodium hydroxide will drastically reduce the price of hydrogen.

6.8.4 Efficiency Analysis

The energy and exergy efficiencies of the photo-electrochemical system are calculated using the equations 5.25a and 5.25b. Simulation results show that efficiencies remain constant for varying intensities. The energy efficiency of the system is calculated to be 3.9%, while the exergy efficiency is calculated to be 7.1%. The higher value of the exergy efficiency level as opposed to the energy efficiency level is a result of the addition of chemical exergy (namely chlorine and sodium hydroxide), in the numerator term. The constant values of these efficiencies are a result of the fact that at a given reactor temperature increasing the light intensity increases the production rate, while decreasing the intensity leads to a decrease in the production rate. The ratio of production rate over light intensity, however, remains constant.

If the unused portion of the solar spectrum is not recovered, an external power supply is required to neutralize the OH^- ions. This would greatly reduce the efficiency level of the system. The efficiency values in this regard would be calculated by using equations 5.65 and 5.66.

6.9 Results of Electrochemical Modeling

Electrochemical analysis is used to find the overall potential in the chloralkali cell. All of the electrochemical modeling for the newly designed reactor is discussed in Section 5.5. The effects of five different parameters on the cell voltage are determined. The parameters include current density (W/m^2), distance between electrodes (mm), cell temperature (^oC), brine concentration levels (g/425mL), and electrolyte concentration (g/60mL) in the sodium hydroxide chamber. For the purpose of parametric study, $l_1 = l_2 = l_3 = \text{Distance}$ is used in this simulation.

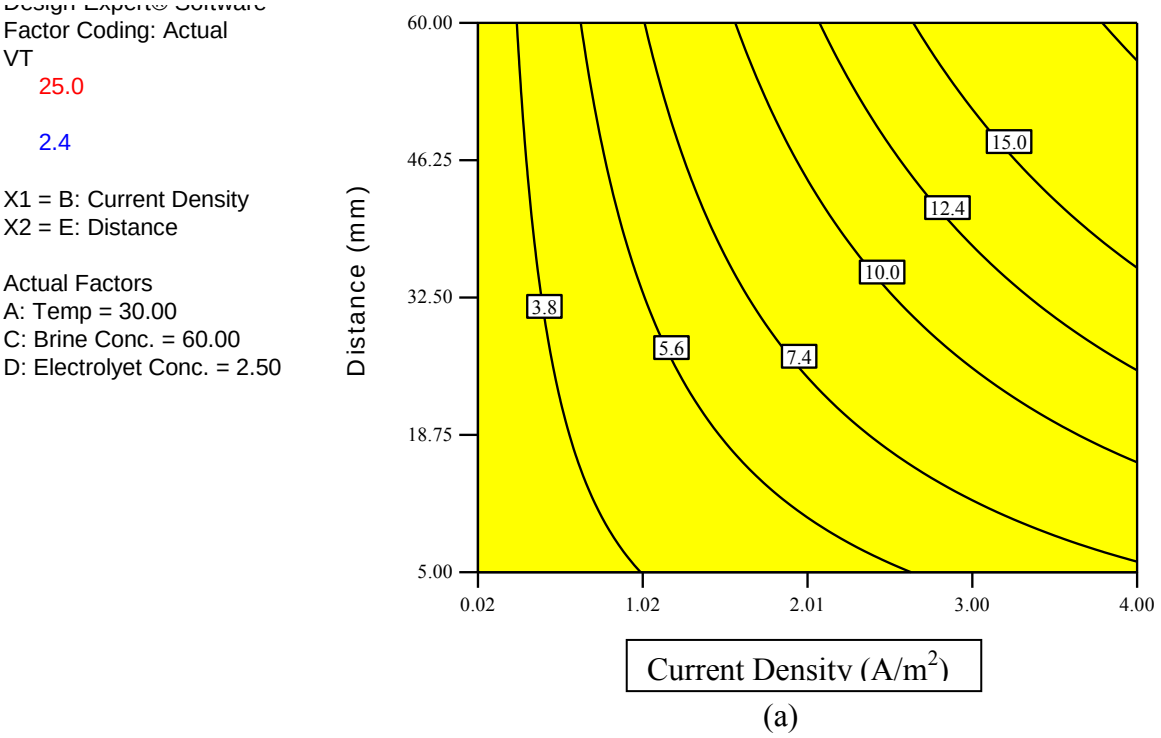

(a)

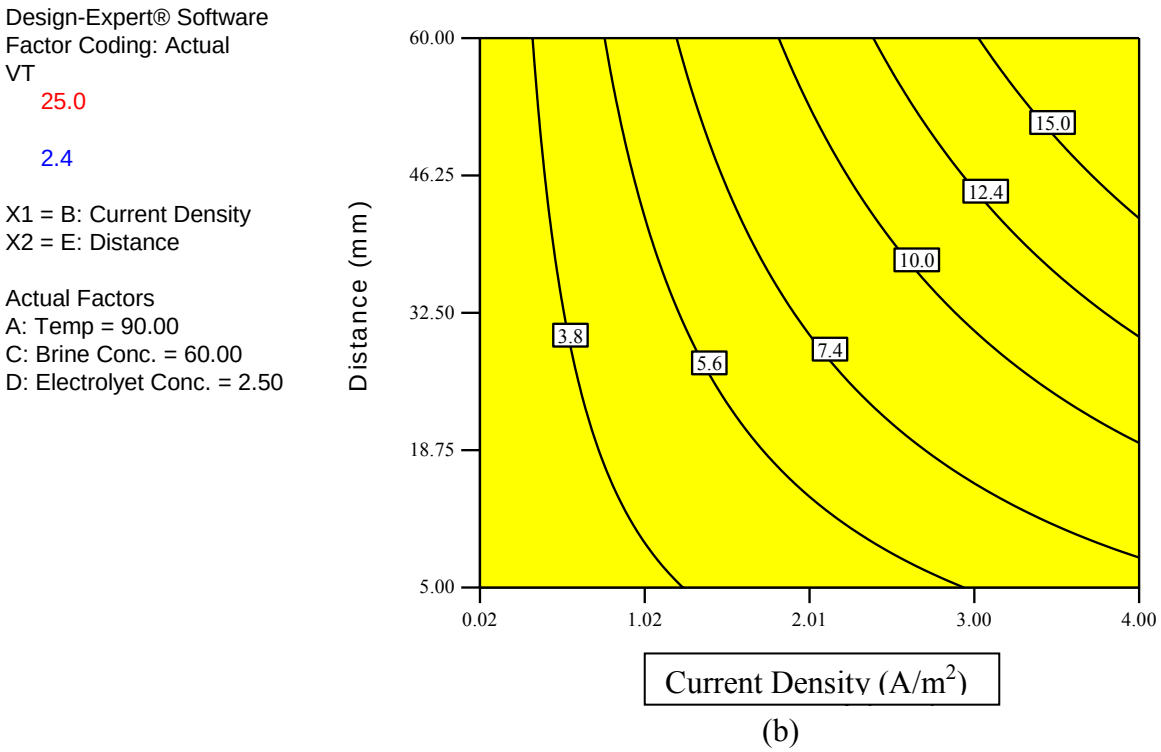

(b)

Figure 6.37: Effect of current density (W/m^2) and distance between electrodes (mm) on cell voltage (V) at a) T =30°C b) T = 90°C.

Figure 6.37 shows the effect of the current density level (W/m^2) and distance on the cell voltage (V) at different temperatures. Results show that all three factors have significant effects on the cell voltage.

Increasing the current density, for example, increases the cell voltage level due to increase in overall voltage. Increasing the current density results in an increase to the overall potential of the cell voltage, including solutions, membranes, and electrodes. Increasing the distance between the electrode and the membrane increases the voltage drop across the solutions. This results in an increase in voltage requirements of the cell. Electrical conductivity of the solution is a function of concentration and temperature. Increasing the temperature results in an increase to the conductivity of the solution (which results in a lower potential drop across the solutions). Another important factor is the dependence of open circuit voltage (decomposition voltage of the brine concentration, electrolyte concentration, temperature of the cell, and partial pressures of the chlorine and hydrogen). Increasing the temperature ultimately reduces the activity coefficient of sodium hydroxide, but does not affect the activity coefficient of the sodium chloride.

The activity coefficient of sodium chloride is a function of brine concentration levels. Figure 6.38 shows the activity coefficient of the sodium chloride as a function of brine concentration levels. Keeping these factors in mind, increasing the temperature reduces the open circuit voltage. Figure 6.39 shows the effect of brine concentration levels and temperatures on decomposition voltage. The voltage drop across the membrane is one of the highest among other components of the reactor. Usually the membrane thickness is very small; however, due to the very low electrical conductivity of the membrane material, the voltage drop is very high. The nature of these voltage level drops across the membrane is a strong function of current density. Figure 6.40 shows the voltage across membrane.

Note that changing the brine concentration levels does not have a significant effect on the cell voltage. The cell voltage slightly decreases with an increase to the brine concentration level. This is a result of an increase in conductivity of the solution. Figure 6.41 shows the effect of

brine concentration level adjustments on the cell voltage for different distances between the electrodes.

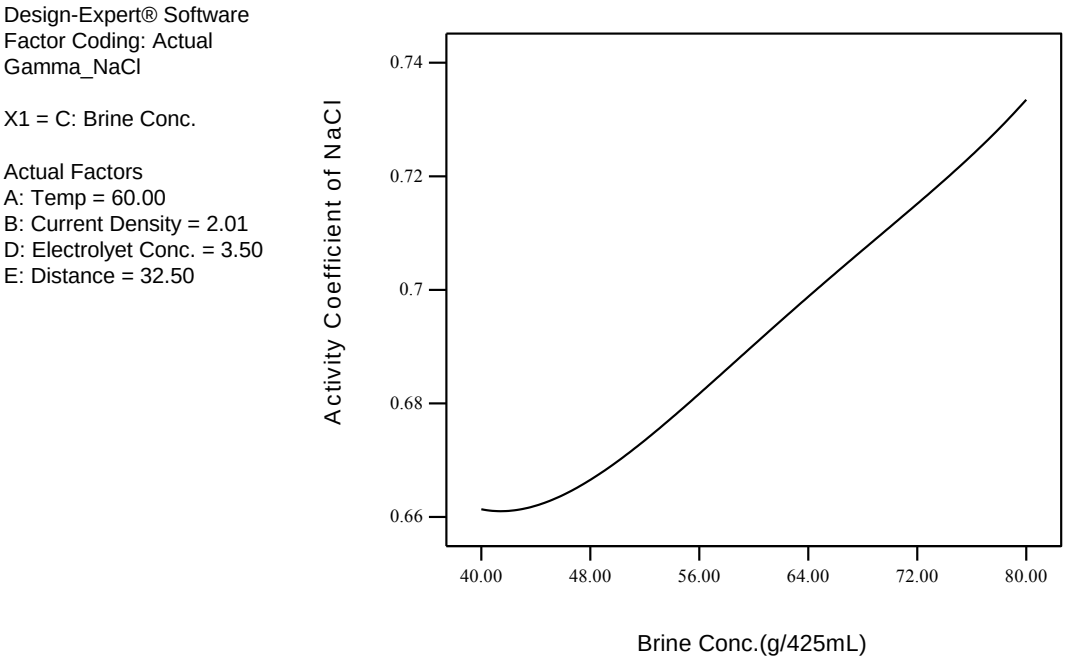

Figure 6.38: Effect of brine concentration levels (g/425mL) on activity coefficients of the sodium chloride.

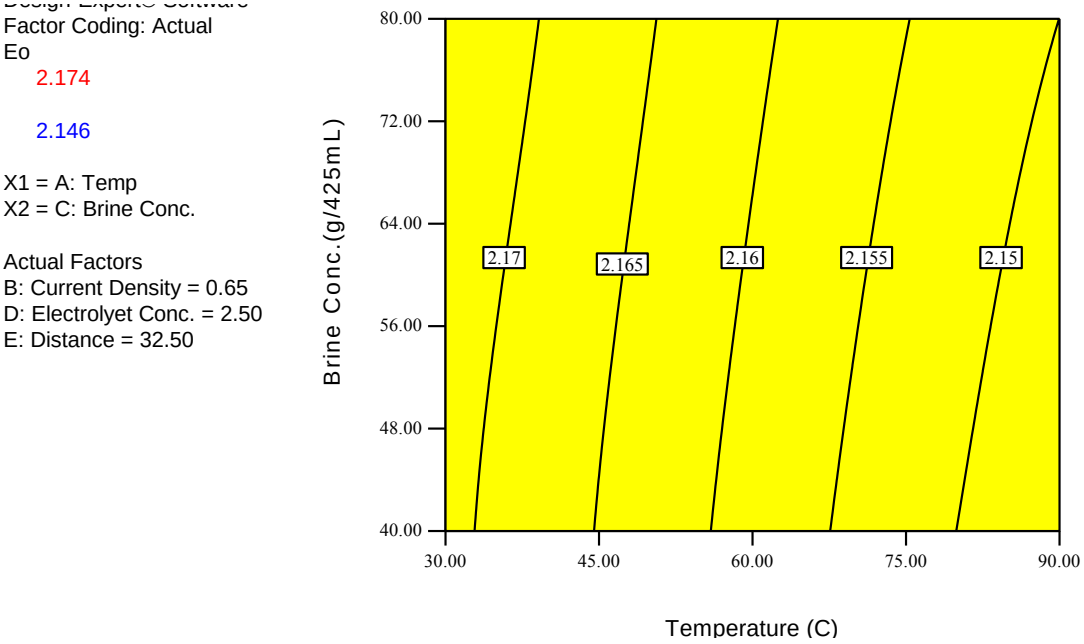

Figure 6.39: Effect of temperature (°C) and brine concentration levels (g/425mL) on the decomposition voltage (V).

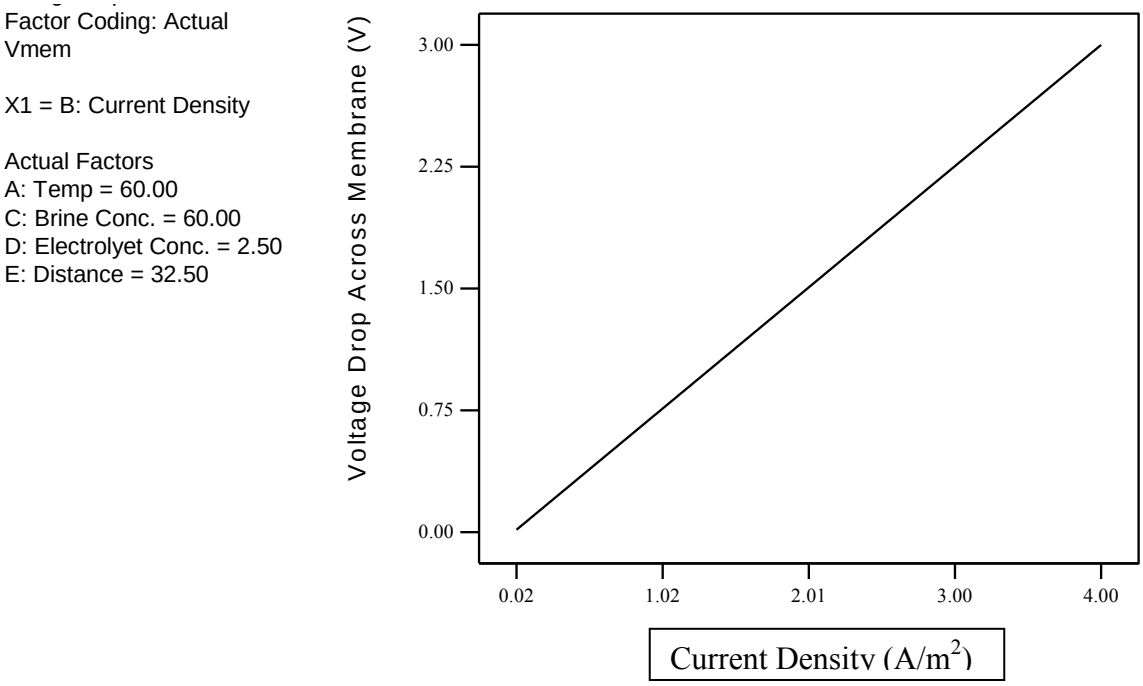

Figure 6.40: Effect of current density (A/m^2) on voltage drop (V) across membrane.

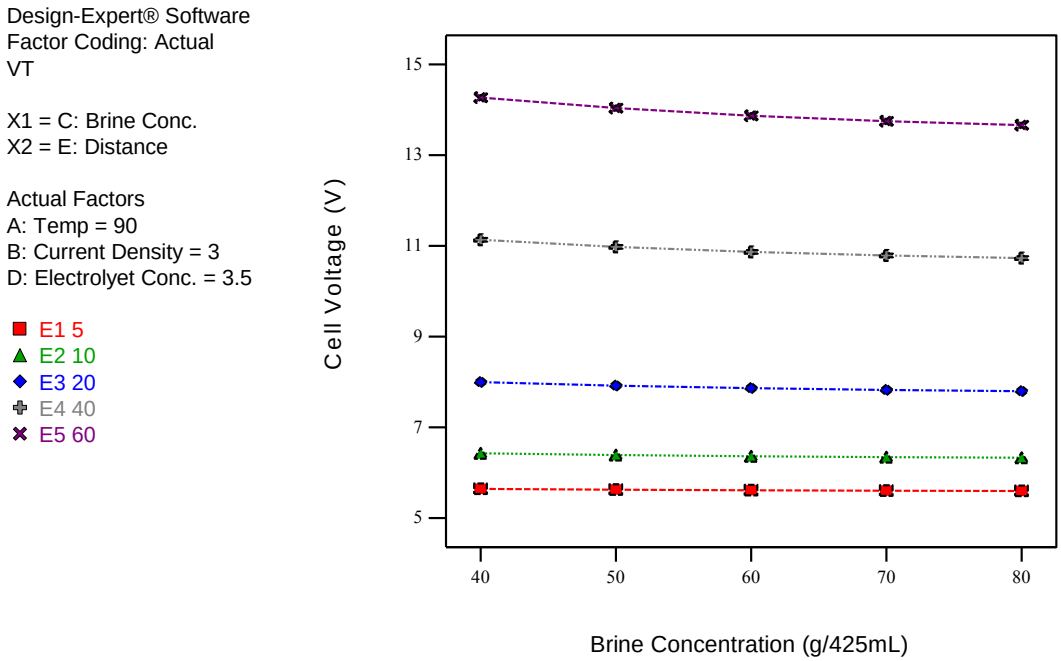

Figure 6.41: Effect of current density (W/m^2) and brine concentration (g/425mL) to the cell voltage (V).

Electrolyte concentration in sodium hydroxide does not have a significant effect on cell voltage. Increasing the electrolyte concentration (i.e. NaOH which is used as an electrolyte this

present study), increases the pH of the solution. As a result of which, there is a slight decrease in the cell voltage level while there is an increase in electrolyte concentration levels. Figure 6.42 shows the effect of the electrolyte concentration levels on cell voltage at different distances between electrodes.

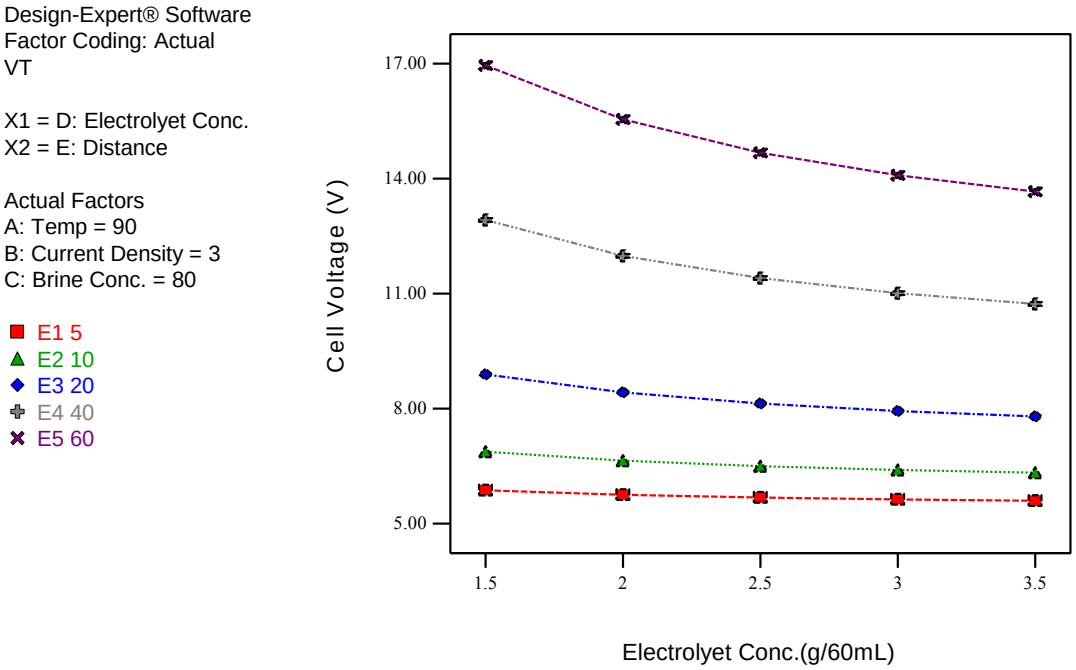

Figure 6.42: Effect of electrolyte concentration (g/60mL) and distance between electrodes (mm) on cell voltage (V).

6.9.2 Optimization Results

An optimization study is performed in order to find the optimal parameters that will minimize the cell voltage. Table 6.21 shows the constraints for optimization of the electrochemical modeling.

The objective desirability function for the constraints set in Table 6.16 can be written as

$$d_{VT} = \frac{V_T - 2.355}{22.635} \tag{6.19}$$

$$D = d_{VT} \tag{6.20}$$

where d_{VT} represents the individual desirability functions of cell voltage, and D represents the overall desirability.

Table 6.21: Constraints for optimization of the electrochemical modeling.

Constraints						
Name		Lower	Upper	Lower	Upper	Importance
Temperature (^{o}C)	Input Term	30	90	1	1	3
Current Density (A/m^2)	Input Term	0.02	4	1	1	3
Brine Conc.(g/425mL)	Input Term	40	80	1	1	3
Electrolyte Conc.(g/60mL)	Input Term	1.5	3.5	1	1	3
Distance (mm)	Input Term	5	60	1	1	3
Cell Voltage(V)	Minimize	2.355	24.99	1	1	5

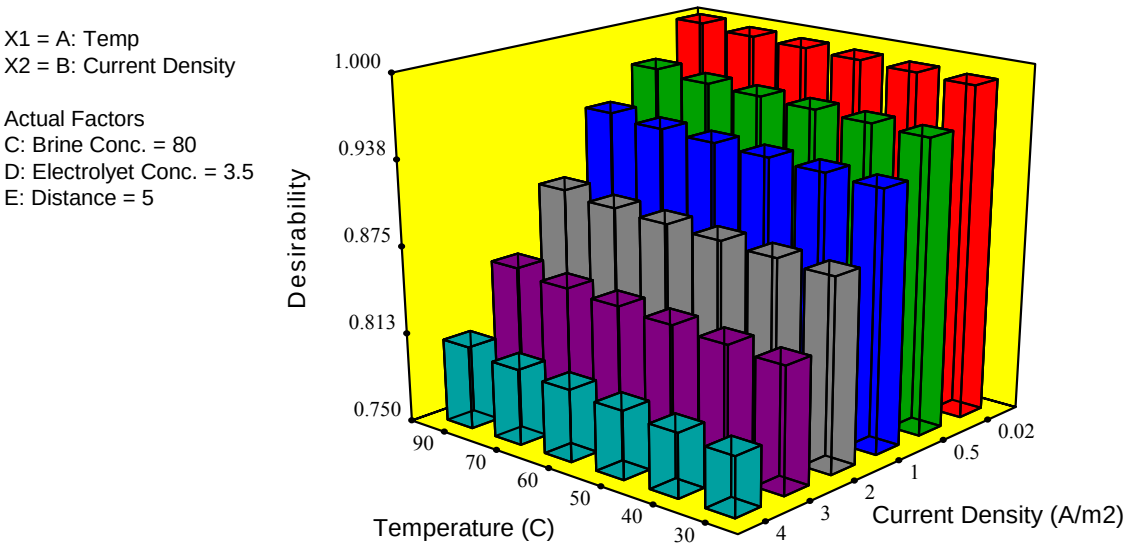

Figure 6.43: Effect of amount of temperature (°C) and current density (A/m^2) on the desirability factor.

The results of the completed optimization process shows that a minimum cell voltage level can be achieved at the highest temperature setting (i.e. 90^{o}C in the present study). The other factors that contributed to the optimization process include a minimum current density (0.02 A/m^2 in present study), at a minimum distance between electrodes (15mm in this present study). Also,

contributing to this process is the maximum electrolyte concentration level (3.5g/60mL in this present study), and a maximum brine concentration level (80g/425mL in present study). Figure 6.43 shows the effect of temperature and current density on the desirability factor. Maximum desirability is achieved under the aforementioned conditions.

6.10 Chloralkali and Water Treatment Processes

Here, water treatment is one of the potential applications that will use Cl_2 and NaOH to refresh exhausted resins. Water contains both anionic and cationic impurities. Mineralized water enters into the cation exchange bed, where impurities such as Ca^{+2}, Mg^{+2} and Na^{+} will be replaced with H^{+} from the cation exchange resin, causing the water to become acidic. At this point, the acidic water passes from the anion exchange bed where impurities like $SO_4^{-2}, NO_3^{-1}, CO_3^{-2}, HCO_3^{-1}$ and Cl^{-} will be replaced with OH^{-} of the anion exchange resin.

Cation Exchange Bed

$$-RSO_3^-H^+ + K^+ \rightarrow -RSO_3^-K^+ + H^+ \quad (6.21)$$

$$2(-RSO_3^-H^+) + Ca^{+2} \rightarrow (-RSO_3^-)_2Ca^{+2} + 2H^+ \quad (6.22)$$

$$2(-RSO_3^-H^+) + Mg^{+2} \rightarrow (-RSO_3^-)_2Mg^{+2} + 2H^+ \text{ [6]} \quad (6.23)$$

$$3(-RSO_3^-H^+) + Fe^{+3} \rightarrow (-RSO_3^-)_3Fe^{+3} + 3H^+ \text{ [7]} \quad (6.24)$$

Anion Exchange Bed

$$-R_4N^+OH^- + Cl^- \rightarrow -R_4N^+Cl^- + OH^- \quad (6.25)$$

$$-R_4N^+OH^- + HCO_3^- \rightarrow -R_4N^+HCO_3^- + OH^- \quad (6.26)$$

$$-R_4N^+OH^- + NO_3^{-1} \rightarrow -R_4N^+NO_3^- + OH^- \quad (6.27)$$

$$-R_4N^+OH^- + SO_4^{-2} \rightarrow -(R_4N^+)_2SO_4^{-2} + 2OH^- \quad (6.28)$$

$$-R_4N^+OH^- + CO_3^{-2} \rightarrow -(R_4N^+)_2CO_3^{-2} + 2OH^- \quad (6.29)$$

As a result, H^+ from the cation exchange bed and OH^- from anion exchange bed will form water. This is called neutralization. Since the dissociation constant for water is very small, the neutralization reaction happens very quickly and occurs only in the forward reaction.

$$H^+ + OH^- \rightarrow H_2O \quad (6.30)$$

When all the resin is utilized and does not have additional sites for replacement, this phenomenon is called resin exhaust. As a result, one needs to either replace the resin or regenerate the exhausted resin. In general, the practice to replace resin is not economically viable, therefore resins are mostly refreshed. Sodium hydroxide and chlorine produced in the chloralkali processes can be used in resin refreshment. So, in this sense, one can successfully couple a water treatment plant with a hydrogen production unit. Sodium hydroxide is also used to refresh the anion resin. Chlorine reacts with hydrogen to form hydrochloric acid, which can be used to refresh the cation exchange resin. Upon refreshing the resin, the exhausted cation exchanger will react with acid and the Ca^{+2}, Mg^{+2} and Na^+ sites in the resin, which will not only be replaced with H^+ , but will also form salt. The exhausted anion exchanger resin will react with the base and will not only replace all $SO_4^{-2}, NO_3^{-1}, CO_3^{-2}, HCO_3^{-1}$ and $Cl^-$with OH^- , but will also form salt.

Refreshing Resin - Cation Exchange Bed

$$-RSO_3^-K^+ + HCl \rightarrow -RSO_3^-H^+ + KCl \quad (6.31)$$

$$(-RSO_3^-)_2Ca^{+2} + 2HCl \rightarrow 2(-RSO_3^-H^+) + CaCl_2 \quad (6.32)$$

$$(-RSO_3^-)_2Mg^{+2} + 2HCl \rightarrow 2(-RSO_3^-H^+) + MgCl_2 \quad (6.33)$$

$$(-RSO_3^-)_2Fe^{+3} + 3HCl \rightarrow 3(-RSO_3^-H^+) + FeCl_3 \quad (6.34)$$

Refreshing Resin - Anion Exchange Bed

$$-R_4N^+Cl^- + NaOH \rightarrow -R_4N^+OH^- + NaCl \quad (6.35)$$

$$-R_4N^+HCO_3^- + NaOH \rightarrow -R_4N^+OH^- + NaHCO_3 \quad (6.36)$$

$$-R_4N^+NO_3^- + NaOH \rightarrow -R_4N^+OH^- + NaNO_3 \quad (6.37)$$

$$-(R_4N^+)_2SO_4^{-2} + 2NaOH \rightarrow 2(-R_4N^+OH^-) + Na_2SO_4 \quad (6.38)$$

$$-(R_4N^+)_2CO_3^{-2} + 2NaOH \rightarrow 2(-R_4N^+OH^-) + Na_2CO_3 \quad (6.39)$$

where R represents the resin in the above equation. Some common resins are shown in Figure 6.44.

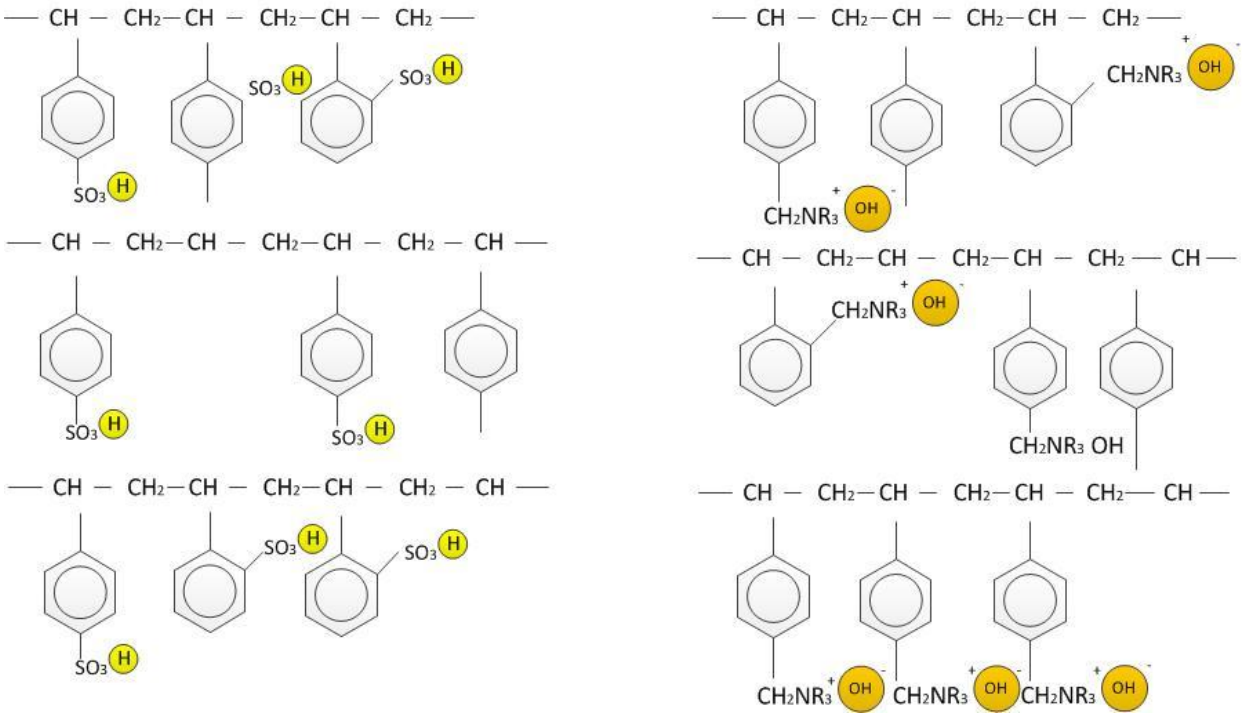

Figure 6.44: Common resins used in water treatment a) Cation (left) b) Anion (right).

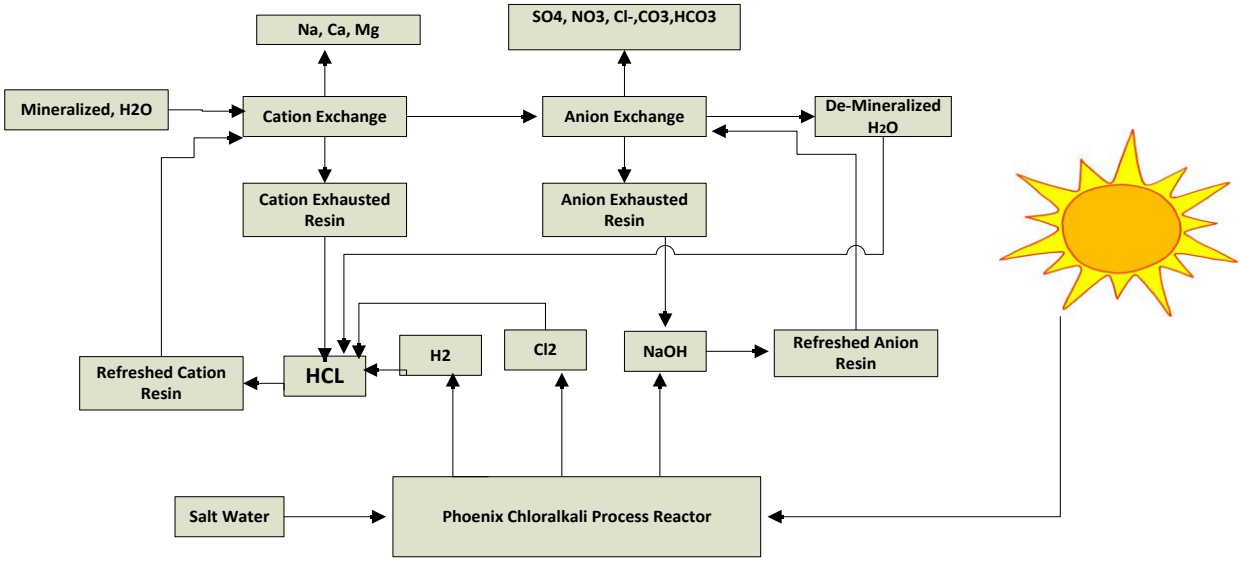

Figure 6.45: Integration of a water treatment plant with the chloralkali reactor

Chapter 7

Conclusions and Recommendations

7.1 Conclusions

This study provides detailed information about design, analysis, and optimization of a newly designed photo-electrochemical chloralkali process. This study is the first one of its kind to address the photo-electrochemical chloralkali process. Thermodynamic, thermo economic, electrochemical, radiation, and statistical modeling have been performed. The conclusions drawn from the present study are summarized as follows:

- A new photo-electrochemical chloralkali reactor, which is the first of its kind, is designed. It is a multi-membrane hybrid reactor that integrates photochemical hydrogen with the electrochemical chloralkali process.
- The OH^- ions (which are the by-products of water reduction during the photochemical hydrogen production process), are neutralized during the formation of sodium hydroxide.
- Five different electrode materials (namely corrosion-resistant aluminum, corrosion-resistant nickel, corrosion-resistant steel, multi-purpose copper and graphite), are tested for chlorine evolution reaction. Only graphite is stable in chlorine. All the other electrode materials react with chlorine and form chlorides.
- VBE experiments show that brine and electrolyte concentration levels in the catholyte compartment of the cell do not have any significant effect on the rate of hydrogen, chlorine, and sodium hydroxide production. The only effective parameter is the adjustment of applied

voltage. Increasing the voltage leads to an increase in the production rate of chloralkali products, but decreases the efficiency of the process due to the increase in energy input to the system. The optimal brine concentration level is 225g/L, while the optimal electrolyte concentration level is 25g/450ml.

- During the experiments, it is observed that the partial pressure of chlorine is less than that of hydrogen due to the higher solubility of chlorine over hydrogen.
- VT experiments show that both temperature and applied voltage have significant effects on the overall production rate. Increasing the temperature reduces the solubility of both the chlorine and hydrogen in the water. Increasing the temperature reduces the overall efficiency rate due to an increase in energy input to the system. It is also not recommended to heat the water because the output is very small compared to the energy input to the system (i.e. only 8g of Cl_2 and 0.01g of H_2 if the temperature of water is increased from 30^oC to 90^oC).
- VH experiments show that increasing the height of the electrode in contact with the water increases the surface area, which results in a decrease in the current density, yet increases the production rate of the chloralkali products.
- The effect of light intensity, applied voltage, and catalyst concentration is studied in photo-electrochemical experiments. All three factors have significant effects on the rate of hydrogen production. Increasing the light intensity and applied voltage levels also increases the production rate. Increasing the catalyst concentration level, however, does not necessarily achieve a higher production rate. The optimal catalyst concentration level was found to be 2.45g/425mL.
- Salt (sodium chloride), was introduced as an impurity in the catholyte compartment to see its effect on the production rate. It was observed that salt concentration does not have any significant effect on the rate of hydrogen production. This is a very important finding considering the vast availability of salt water around the globe, combined with the economic pressures of cleaning water. ZnS was used as a photo catalyst; therefore this result strictly applies to ZnS only.
- During the initial experiments, sodium sulfide was used as a hole scavenger material. Later experiments demonstrated that solid electrodes can replace sodium sulfide and can ultimately supply electrons by using electric supply. This adjustment eliminates all of the consumables

in the system. It is recommended to use an electrode with a large surface area so that electrons can easily be transferred to the system.

- The photo catalyst uses only a portion of the solar spectrum. This results in a decrease in the efficiency of the system. Use of dielectric mirror is suggested to harness the energy from unused portions of the solar spectrum. The unused portions can be used to produce electricity via PV panels. This electricity can produce additional hydrogen by means of electrolysis by neutralizing OH^- ions and replacing the external voltage being supplied to the system. This results in improvement in efficiency of the system.
- Because solar intensity is the driving force in this process, radiation modeling is performed. The city of Toronto is assumed to be the location where the plant will be built. Maximum intensity is observed to occur at noon hour in a clear sky setting, at a surface angle of 23^o.
- The thermodynamic model is developed for a continuous heliostat-based photo-electrochemical chloralkali plant. The model is coupled with the radiation model. The model results suggest that increasing the radiation intensity also increases the energy input to the system (ultimately increasing the rate of chloralkali product creation). It also increases the entropy generation in the system. For a large scale plant, using the high efficiency PV panels can greatly improve the efficiency of the process.
- The cost of hydrogen in a chloralkali process is a function of capital cost (cost of by-products and intensity of light). In this present study, for a clear sky model, the cost of hydrogen is calculated to be 0.7$/kg, whereas a turbid sky model has a determined cost of hydrogen to be calculated as 1.3$/kg (note that the cost of by-products is assumed to be 0.04$/kg). This is well below the DOE target.
- In order to find the required voltage for the chloralkali reactor, an electrochemical model is developed. A parametric study is performed to determine the effect of the different parameters on the required voltage of the reactor. Results indicate that brine and electrolyte concentration levels do not have any significant effect on reactor voltage. Increasing the temperature, results in a decrease of the cell voltage. Increasing the distance between electrodes, results in an increase of the over potential of the reactor. Increasing the current density increase the over potential and required cell voltage. The results match quite well with the two chamber reactor model presented in the literature.

7.2 Recommendations

The results obtained from this present study suggest several routes for future studies, as summarized below:

- To analyze the performance of the reactor with other photo catalysts that work on higher wavelengths. A suggestion includes the , which works at a wavelength of 520nm.
- To build up a continuous system to see the effect that mass flow rate has on the chloralkali production rate.
- Due to the limited funds provided for this current study, conditions of harnessing the unused portion of light had to be implemented by using alternative light mirrors. It is, therefore, important to build up a system with the proper dielectric mirror to see how effectively the unused portion of the spectrum can be recovered.
- To use an electrode with a large surface area in the hydrogen production chamber to see how effectively the electrode can replace the hole scavenger material in a continuous cycle.
- Study the performance of the reactor using a homogenous catalyst such as a brewer catalyst.

References

[1] C. A. Grimes , O. K. Varghese , S. Ranjan , Light, Water, Hydrogen: The Solar Generation of Hydrogen by Water Photoelectrolysis, 2007.

[2] S. Pachauri, D. Spreng, Measuring and monitoring energy poverty, Energy Policy, Volume 39, December 2011, Pages 7497-7504.

[3] C. J. Campbell, The Coming Oil Crisis. Multi-Science Publishing Company & Petro-consultants S.A., Essex, United Kingdom, 1997.

[4] D. Rahm, US public policy and emerging technologies: The case of solar energy, Energy Policy, Volume 21, 1993, Pages 374-384.

[5] S. Arrhenius, On the influence of carbonic acid in the air upon the temperature of the ground. Philosophical Magazine Volume 41, 1986, Pages 237-276.

[6] M. I. Hoffert, K. Caldeira, G. Benford, D. R. Criswell, C .Green, H. Herzog, A. K. Jain, H. S. Kheshgi, K. S. Lackner, J. S. Lewis, H. D. Lightfoot, W. Manheimer, J. C. Mankins, M. E. Mauel, L. J. Perkins, M. E. Schlesinger, V. T, T.M. L Wigley , Advanced technology paths to global climate stability: Energy for a greenhouse planet. Science 298:981.987, 2002.

[7] M. Jefferson, Sustainable energy development: performance and prospects. Renewable energy 31:571.582, 2006.

[8] M. Bailey, A. Ö. Arnas, R. Potter, J. W. Samples, The 20 year evolution of an energy conversion course at the United States Military Academy, Energy Conversion and Management, Volume 45, 2004, Pages 495-509.

[9] F. McGowan, The single energy market and energy policy: conflicting agendas? Energy Policy, Volume 17, 1989, Pages 547-553.

[10] M. Lazzarini, P. Reddy Marpu, H. Ghedira, Temperature-land cover interactions: The inversion of urban heat island phenomenon in desert city areas, Remote Sensing of Environment, Volume 130, 2013, Pages 136-152.

[11] J. A. Turner, A Realizable Renewable Energy Future, Vol. 285 No. 5428, July 1999, Pages. 687-689.

[12] M. Ni, M. K. H. Leung, K. Sumathy, D. Y. C. Leung, International Journal of Hydrogen Energy, Volume 31, 2006, Pages 1401–1412.

[13] J. Turner, G. Sverdrup, M. K. Mann, P. C. Maness, B. Kroposki, M. Ghirardi, R. J. Evans, D. Blake, Renewable hydrogen production, International Journal of Energy Research, Volume 32, 2008, Pages 379–407.

[14] J. F. Reber, M. Kurt, Photochemical Production of Hydrogen with Zinc Sulfide Suspensions, The Journal of Physical Chemistry, 1984, Pages 5903-5913.

[15] G. Naterer, I. Dincer, M. Rabbani, Photo electrochemical hydrogen production in a chloralkali process. Opic - Pop Research Proposal, 2012.

[16] H. V. D. Dolder, Process analyzers in the chloralkali industry, O Analytica Chimica Acta, Volume 190, 1986, Pages 25-31.

[17] Ullmann's Encyclopaedia of Industrial Chemistry, VCH publishers, New York, 1989.

[18] The Chlorine Institute, Inc., Washington, DC, January 1991.

[19] Chloralkali electrolysis without mercury, Membrane Technology, Volume 1993, Issue 43, November 1993, Page 6.

[20] D. C. Montgomery, Design and Analysis of Experiments, 5th Edition, John Wiley & Sons, 2000.

[21] D. C. Montgomery, Statistical process control, John Wiley & Sons, 2003.

[22] I. Lind, Regressor and Structure Selection: Uses of ANOVA in System Identification, 2006.

[23] Design Expert, State Ease, Version 8.1.6, 2021 E. Hennepin Avenue, Suite 480, Minneapolis, MN 55413-2726.

[24] R. K. Burdick, C. M. Borror, D. C. Montgomery, Design and Analysis of Gauge R&R Studies: Making Decisions with Confidence Intervals in Random and Mixed Anova Models, Society for Industrial Applied Mathematics, 2005.

[25] C. P. Doncaster, A. J. H. Davey, Analysis of Variance and Covariance: How to Choose and Construct Models for the Life Sciences, Cambridge University Press, 2007.

[26] G. P. Quinn, M. J. Keough, Experimental Design and Data Analysis for Biologists, Cambridge University Press, 2002.

[27] D. C. Montgomery, R. H. Myers, Response Surface Methodology: Process and Product Optimization Using Designed Experiments.

[28] A. I. Khuri, Response Surface Methodology And Related Topics, World Scientific Publishing Company, 2006.

[29] A. I. Khuri, Linear Model Methodology, Chapman & Hall/CRC, 2009.

[30] E. Bilgen, Solar hydrogen from photovoltaic electrolyzer systems. Energy Conversion and Management, Volume 42, 2001, Pages 1047-1057.

[31] A. Siegel, T. Schott, Optimization of photovoltaic hydrogen production. International Journal of Hydrogen Energy, Volume 13, 1988, Pages 659-675.

[32] R. Muhida, M. Park, M. Dakkak, K. Matsuura, A. Tsuyoshi, M. Michira , A maximum power point tracking for photovoltaic-SPE system using a maximum current controller. Sol Energy Mater Sol Cells Volume 75, 2003, Pages 697-706.

[33] A. Brinner, H. Bussmann, W. Hug, W. Seeger , Test results of the HYSOLAR 10 kW International Journal of Hydrogen Energy, Volume 17, 1992, Pages 187-197.

[34] A. Brinner, http://www.hysolar.com; for more details about 350 KW PV-electrolysis plant.

[35] C. A. Schug, Operational characteristics of high pressure, high-efficiency water-hydrogen-electrolysis, International Journal of Hydrogen Energy Volume 23, 1998, Pages 1113-1120.

[36] T. Ohmori, H. Go, N. Yamaguchi, A. Nakayama, H. Mametsuka, E. Suzuki , Photovoltaic water electrolysis using the sputter-deposited a-Si/c-Si solar cells, International Journal of Hydrogen Energy Volume 26, 2001, Pages 661-664.

[37] A. Currao, V. R. Reddy, M. K. V. Veen, R. E. I. Schropp, G. Calzaferri , Water splitting with silver chloride photoanode and amorphous silicon solar cell, Photochemical & Photobiological Sciences, Volume 3, 2004, Pages 1017-1025.

[38]. S. S. Kocha, D. Montgomery, M. W. Peterson, J. A. Turner , Photoelectrochemical decomposition of water utilizing monolithic tandem cells, Sol Energy Mater Sol Cells, Volume 52, 1998, Pages 389-397.

[39] X. Gao, S. Kocha, A. J. Frank, J. A. Turner , Photoelectrochemical decomposition of water using modified monolithic tandem cells, International Journal of Hydrogen Energy, Volume 24, 1999, Pages 319-325.

[40] O. Khaselev, A. Bansal, J. A. Turner, High-efficiency integrated multijunction photovoltaic/electrolysis systems for hydrogen production. International Journal of Hydrogen Energy 26:127-132, 2001.

[41] S. Licht, B. Wang, S. Mukerji, T. Soga, M. Umeno, H. Tributsch , Efficient solar water splitting, exemplified by RuO_2 catalyzed AlGaAs/Si photoelectrolysis, The Journal of Physical Chemistry Volume 104, 2000, Pages 8920-8924.

[42] M. F. Weber, M. J. Dignam, Splitting water with semiconducting photoelectrodes--Efficiency considerations. International Journal of Hydrogen Energy Volume 11, 1986, Pages 225-232.

[43] J. R. Bolton, S. J. Strickler, J. S. Connolly , Limiting and realizable efficiencies of solar photolysis of water, Nature, Volume 316, 1985, Pages 495-500.

[44] S. Licht, B. Wang, S. Mukerji, T. Soga, M. Umeno, H. Tributsch , Over 18% solar energy conversion to generation of hydrogen fuel; theory and experiment for efficient solar water splitting, International Journal of Hydrogen Energy, Volume 26, 2001, Pages 653-659.

[45] S. Litcht , Multiple band gap semiconductor/electrolyte conversion. The Journal of Physical Chemistry, Volume 105, 2001, Page 6281-6294.

[46] S. Licht, L. Halperin, M. Kalina, M. Zidman, N. Halperin , Electrochemical potential tuned solar water splitting. Chem Commun, 2003, Pages 3006-3007.

[47] Y. Yamada, N. Matsuki, T. Ohmori, H. Mametsuka, M. Kondo, A. Matsuda, E. Suzuki , One chip photovoltaic water electrolysis device. International Journal of Hydrogen Energy, Volume 28, 2003, Pages 1167-1169.

[48] N. A. Kelly, T. L. Gibson , Design and Characterization of a robust photoelectrochemical device to generate hydrogen using solar water splitting. International Journal of Hydrogen Energy, Volume 31, 2006, Pages 1658-1673.

[49] N. G. Dhere, A. H. Jahagirdar, Photoelectrochemical water splitting for hydrogen production using combination of CIGS2 solar cell and RuO_2 photocatalyst, Thin Solid Films, Volumes 480–481, 2005, Pages 462-465.

[50]. U. S. Avachat, A. H. Jahagirdar, N. G. Dheere , Multiple band gap combination of thin film photovoltaic cell and a photoanode for efficient hydrogen and oxygen generation by water splitting. Solar Energy Materials and Solar Cells, Volume 90, 2006, Pages 2464-2470.

[51] U. S. Avachat, N. G. Dheere , Preparation and characterization of transparent conducting ZnTe:Cu back contact interface layer for CdS/CdTe solar cell for photo electrochemical application, Journal of Vacuum Science & Technology, Volume 24, 2006, Pages 1664-1667.

[52] M. Gratzel, Mesoscopic solar cells for electricity and hydrogen production from sunlight, Chem Letters, Volume 34, 2005, Pages 8-13.

[53] E. S. Andreiadis, M. Chavarot-Kerlidou, M. Fontecave, Artificial Photosynthesis: From Molecular Catalysts for Light-driven Water Splitting to Photo electrochemical Cells, Photochemistry and Photobiology, Volume, 87 (5), 2011, Pages 946-964.

[54] M. Elvington, J. Brown, S. M. Arachchige, K. J. Brewer, Photocatalytic Hydrogen Production from Water Employing A Ru, Rh, Ru Molecular Device for Photoinitiated Electron Collection, Journal of the American Chemical Society, Volume 129 (35), 2007, Pages 10644-10645.

[55] S. M. Arachchige, J. Brown, K. J. Brewer, Photochemical hydrogen production from water using the new photo catalyst $[\{(bpy)_2Ru(dpp)\}_2RhBr_2](PF6)^5$, Journal of Photochemistry and Photobiology, Volume 197, 2008, Pages 13-17.

[56] A. J. Prussin II, D. F. Zigler, A. Jain, J. R. Brown, B. S. J. Winkel, K. J. Brewer, Photochemical methods to assay DNA photocleavage using supercoiled pUC18 DNA and LED or xenon arc lamp excitation, Journal of Inorganic Biochemistry, Volume 102, 2008, Pages 731-739

[57] T. A. White, K. Rangan, K. J. Brewer, Synthesis, characterization, and study of the photophysics and photocatalytic properties of the photoinitiated electron collector $[\{(phen)_2Ru(dpp)\}_2RhBr_2](PF6)^5$, Journal of Photochemistry and Photobiology A: Chemistry, Volume 209, 2010, Pages 203-209.

[58] M. Elvington, J. R. Brown, D. F. Zigler, K. J. Brewer, Supramolecular Complexes as Photo initiated Electron Collectors: Applications in Solar Hydrogen Production, Department of Chemistry, Virginia Polytechnic Institute and State University, Blacksburg VA USA 24061-0212.

[59] K. Rangan, S. M. Arachchige, J. R. Brown, K. J. Brewer, Solar energy conversion using photochemical molecular devices: photocatalytic hydrogen production from water using mixed-metal supramolecular complexes , Energy & Environmental Science, Volume 2, 2009, Pages 410-419.

[60] S. M. Arachchige, J. R. Brown, Eric Chang, A. Jain, D. F. Zigler, K. Rangan, K. J. Brewer, Design Considerations for a System for Photocatalytic Hydrogen Production from Water Employing Mixed-Metal Photochemical Molecular Devices for Photoinitiated Electron Collection, Inorganic Chemistry, Volume 48 (5), 2009, Pages 1989-2000.

[61] T. Ohta, Solar-hydrogen energy systems, Oxford and New York, Pergamon Press, 1979, Pages 115.135.

[62] N. Buehler, K. Meier, J. F. Reber, Photochemical hydrogen production with cadmium sulfide suspensions, The Journal of Physical Chemistry, 1984, Pages 3261-3268.

[63] J. F. Reber, M. Rusek, Photochemical hydrogen production with platinized suspensions of cadmium sulfide and cadmium zinc sulfide modified by silver sulfide, The Journal of Physical Chemistry, 1986, Pages 824–834.

[64] K. Sakai, H. Ozawa, Homogeneous catalysis of platinum(II) complexes in photochemical hydrogen production from water, Coordination Chemistry Reviews, Volume 251, 2007, Pages 2753-2766.

[65] K. Sakai, Y. Kizaki, T. Tsubomura, K. Matsumoto, Homogeneous catalyses of mixed-valent octanuclear platinum complexes in photochemical hydrogen production from water, Journal of Molecular Catalysis, Volume 79, 1993, Pages 141-152.

[66] I. Akkerman, M. Janssen, J. Rocha, H. René. Wijffels, Photobiological hydrogen production: photochemical efficiency and bioreactor design, International Journal of Hydrogen Energy, Volume 27, November–December 2002, Pages 1195-1208.

[67] J. R. Darwent, G. Porter, Photochemical Hydrogen Production using Cadmium Sulfide Suspensions in Aerated Water, Journal of the Chemical Society, Chemical Communications, 1981, Pages 145-146.

[68] D. Streich, Y. Astuti, M. Orlandi, L. Schwartz, R. Lomoth, L. Hammarstrçm, S. Ott, High-Turnover Photochemical Hydrogen Production Catalyzed by a Model Complex of the [FeFe]-Hydrogenase Active Site, Chemistry - A European Journal, Volume 16, 2010, pages 60–63.

[69] Y. Amao, Y. Tomonou, I. Okura, Highly efficient photochemical hydrogen production system using zinc porphyrin and hydrogenase in CTAB micellar system, Solar Energy Materials and Solar Cells, Volume 79, 2003, Pages 103-111.

[70] M. S. Arachchige, J. Brown, K. J. Brewer, Photochemical hydrogen production from water using the new photocatalyst $[\{(bpy)_2Ru(dpp)\}_2RhBr_2](PF_6)^5$, Journal of Photochemistry and Photobiology A: Chemistry, Volume 197, 2008, Pages 13-17.

[71] H. Zhou, X. f. Li, T. Fan, F. E. Osterloh, J. Ding, E. M. Sabio, D. Zhang, and Q. Guo, Artificial Inorganic Leafs for Efficient Photochemical Hydrogen Production Inspired by Natural Photosynthesis, Advanced Materials, Volume 22, 2010, Pages 951–956.

[72] C. Li, M. Wang, J. Pan, P. Zhang, R. Zhang, L. Sun, Organometallics for Energy Conversion, Journal of Organometallic Chemistry, Volume 694, 2009, Pages 2814-2819.

[73] J. F. Reber , M. Rusek, Photochemical hydrogen production with platinized suspensions of cadmium sulfide and cadmium zinc sulfide modified by silver sulfide, The Journal of Physical Chemistry, Volume 90 (5), 1986, Pages 824-834.

[74] C. Xing, Y. Zhang, W. Yan, L. Guo, Band structure-controlled solid solution of Cd-ZnS photo catalyst for hydrogen production by water splitting , International Journal of Hydrogen Energy, Volume 31, 2006, Pages 2018-2024.

[75] E. Amouyal, Photochemical production of hydrogen and oxygen from water: A review and state of the art, Solar Energy Materials and Solar Cells, Volume 38, 1995, Pages 249–276

[76] M. Elvington, J. Brown, M. S. Arachchige, and K. J. Brewer, Photocatalytic Hydrogen Production from Water Employing A Ru, Rh, Ru Molecular Device for Photoinitiated Electron Collection, Journal of the American Chemical Society, Volume 129 (35), 2007, Pages 10644-10645.

[77] P. C. Hallenbeck , J. R. Benemann, Biological hydrogen production; fundamentals and limiting processes, International Journal of Hydrogen Energy, Volume 27, December 2002, Pages 1185-1193.

[78] I. K. Kapdan, F. Kargi, Bio-hydrogen production from waste materials, Enzyme and Microbial Technology, Volume 38, 2006, Pages 569-582.

[79] K. J. Brewer, Supramolecular complexes as photocatalysts for the production of hydrogen from water, Patent number: 7582584, 2009.

[80] M. M. Richter, K. J. Brewer, Spectroscopic, electrochemical, and spectroelectrochemical investigations of mixed-metal osmium(II)/ruthenium(II) bimetallic complexes incorporating polypyridyl bridging ligands, Inorganic Chemistry, Volume 31 (9), 1992, Pages 1594–1598.

[81] M. Elvington and K. J. Brewer*, Department of Chemistry, Virginia Polytechnic Institute and State University, Blacksburg, Virginia 24060-0212, Inorganic Chemistry, Volume 45 (14), 2006, Pages 5242-5244.

[82] S. A. Arachchige, R. Shaw, T. A. White, V. Shenoy, H.-M.Tsui, K. J. Brewer, High Turnover in a Photocatalytic System for Water Reduction to Produce Hydrogen Using a Ru, Rh, Ru Photoinitiated Electron Collector, ChemSusChem, Volume 4, 2011, Pages 514-518.

[83] M. S. Landis, G. J. Keeler, K. I. Al-Wali, R. K. Stevens. Divalent inorganic reactive gaseous mercury emissions from a mercury cell chloralkali plant and its impact on near-field atmospheric dry deposition. Atmospheric Environment, Volume 38, 2004, Pages 613-622.

[84] R. Grönlund, M. Sjöholm, P.Weibring, H. Edner, S. Svanberg. Elemental mercury emissions from chloralkali plants measured by lidar techniques, Atmospheric Environment, Volume 39, 2005, Pages 7474-7480.

[85] J. S Kinsey, F.R Anscombe, S. E Lindberg, G. R. Southworth, Characterization of the fugitive mercury emissions at a chloralkali plant: overall study design, Atmospheric Environment, Volume 38, 2004, Pages 633-641.

[86] J. S. Kinsey, J. Swift, J. Bursey, Characterization of fugitive mercury emissions from the cell building at a US chloralkali plant, Atmospheric Environment, Volume 38, 2004, Pages 623-631.

[87] Y. Busto, X. Cabrera, F.M.G. Tack, M.G. Verloo, Potential of thermal treatment for decontamination of mercury containing wastes from chloralkali industry, Journal of Hazardous Materials, Volume 186, 2011, Pages 114-118.

[88] G.R. Southworth, S.E. Lindberg, H. Zhang, F.R. Anscombe, Fugitive mercury emissions from a chloralkali factory: sources and fluxes to the atmosphere, Atmospheric Environment, Volume 38, 2004, Pages 597-611.

[89] A. T. Reis, S. M. Rodrigues, C. Araújo, J. P. Coelho, E. Pereira, A. C. Duarte,Mercury contamination in the vicinity of a chloralkali plant and potential risks to local population, Science of The Total Environment, Volume 407, 2009, Pages 2689-2700.

[90] L. Barregard, M. Horvat, B. Mazzolai, G. Sällsten, D. Gibicar, VesnaFajon, S. diBona, J. Munthe, I. W. berg, M. H. Eugensson, Urinary mercury in people living near point sources of mercury emissions, Science of The Total Environment, Volume 368, 2006, Pages 326-334.

[91] M. Sensen, D. H.S Richardson, Mercury levels in lichens from different host trees around a chloralkali plant in New Brunswick, Canada Science of The Total Environment, Volume 293, 2002, Pages 31-45.

[92] D. Raldúa, S. Díez, J. M. Bayona, D. Barceló, Mercury levels and liver pathology in feral fish living in the vicinity of a mercury cell chloralkali factory, Chemosphere, Volume 66, 2007, Pages 1217-1225.

[93] D. Gibicar, M. Horvat, M. Logar, V. Fajon, I. Falnoga, R. Ferrara, E. Lanzillotta, C. Ceccarini, B. Mazzolai, B. Denby, J. Pacyna, Human exposure to mercury in the vicinity of chloralkali plant, Environmental Research, Volume 109, 2009, Pages 355-367.

[94] P. R. Lima, A. Mirapalheta, M. H. d. S. Andrade, E. O. Vilar, C. L. d. P. E. S. Zanta, J. Tonholo, Energy loss in electrochemical diaphragm process of chlorine and alkali industry – A collateral effect of the undesirable generation of chlorate, Energy, Volume 35, 2010, Pages 2174-2178.

[95] E.M. A. Filho, E.O. Vilar, A.C.O. Feitoza,Physical–chemical characterization and statistical modeling applied in a chloralkali diaphragm-cell process, Chemical Engineering Research and Design, Volume 89, 2011, Pages 491-498.

[96] P. Vermeiren, J.P. Moreels, A. Claes, H. Beckers,Electrode diaphragm electrode assembly for alkaline water electrolysers, International Journal of Hydrogen Energy, Volume 34, 2009, Pages 9305-9315.

[97] M. Lanz, C.A. De Caro, K. Rüegg, A. De Agostini, Coulometric Karl Fischer titration with a diaphragm-free cell: Cell design and applications, Food Chemistry, Volume 96, 2006, Pages 431-435.

[98] D.A. White, J. Helbig,The production of flocs for water treatment by electrodialysis in a diaphragm cell, Journal of Membrane Science, Volume 113, 1996, Pages 331-336.

[99] S. Kiga, Diaphragm process electrolytic cell, Patent number: 3989615,Filing date: 20 Aug 1973, 1976

[100] S.S. Madaeni, V. Kazemi, Treatment of saturated brine in chloralkali process using membranes, Separation and Purification Technology, Volume 61, 2008, Pages 68-74.

[101] J. Balster, D. F. Stamatialis, M. Wessling, Electro-catalytic membrane reactors and the development of bipolar membrane technology. Chemical Engineering and Processing: Process Intensification, Volume 43, Issue 9, September 2004, Pages 1115-1127

[102] S. Savari, S. Sachdeva, A. Kumar, Electrolysis of sodium chloride using composite poly(styrene-co-divinylbenzene) cation exchange membranes, Journal of Membrane Science, Volume 310, 2008, Pages 246.261.

[103] N. Furuya, H. Aikawa, Comparative study of oxygen cathodes loaded with Silver and Platinum catalysts in chloralkali membrane cells, ElectrochimicaActa, Volume 45, 2000, Pages 4251-4256.

[104] N. Melián-Martel, J.J. Sadhwani, S. Ovidio Pérez Báez, Saline waste disposal reuse for desalination plants for the chloralkali industry: The particular case of pozoizquierdo SWRO desalination plant, Desalination, Volume 281, 2011, Pages 35-41.

[105] M.Y. Kariduraganavar, R.K. Nagarale, A.A. Kittur, S.S. Kulkarni Ion-exchange membranes: preparative methods for electrodialysis and fuel cell applications, Desalination, Volume 197, 2006, Pages 225-246.

[106] M. Chikhi, M. Rakib, P. Viers, S. Laborie, A. Hita, G. Durand,Current distribution in a chloralkali membrane cell: experimental study and modeling, Desalination, Volume 149, 2002, Pages 375-381.

[107] R.K. Nagarale, G.S. Gohil, Vinod K. Shahi, Recent developments on ion-exchange membranes and electro-membrane processes, Advances in Colloid and Interface Science, Volume 119, 2006, Pages 97-130.

[108] M. Seko, The Ion-Exchange Membrane, Chloralkali Process, Ind. Eng. Chem. Prod. Res. Dev., 1976, Volume 15 (4), 1976, Pages 286-292.

[109] D. Bergner, Membrane cells for chloralkali electrolysis, Applied Electrochemistry, Volume 12, 1982, Pages 631-644,

[110] W. A. McRae, Process and Apparatus for Controlling Impurities and Pollution from Membrane Chloralkali Cells, Patent number: 4242185, 1979.

[111] T. F. O'Brien, Control of sulphates in membrane cell chloralkali process, Patent number: 4586993, 1986.

[112] J. Rutherford, Purification of chloralkali membrane cell brine, Patent number: 5126019, 1992.

[113] N. Furuya, H. Aikawa, Comparative study of oxygen cathodes loaded with Silver and Platinum catalysts in chloralkali membrane cells, Electrochimica Acta, Volume 45, Issues 25–26, 31 August 2000, Pages 4251-4256.

[114] B. R. Ezzell, W. P. Carl, W. A. Mod, Electrolytic cell having an improved ion exchange membrane and process for Operating, Patent number: 4470889, 1984.

[115] J. W. McMichael, R. D. Door, Supported membrane/electrode structure combination wherein catalytically active particles are coated onto the membrane, Patent number: 4752370, 1988.

[116] R. M. Dempsey, T. G. Coker, A. B. LaConti, A. R. Fragala, Production of halogens by electrolysis of alkali metal halides in an electrolysis cell having catalytic electrodes bonded to the surface of a solid polymer electrolyte membrane. Patent number: 4224121, 1980.

[117] K. S. Pitzer1, J. C. Peiper1, R. H. Busey, Thermodynamic Properties of Aqueous-Sodium Chloride Solutions, Journal of Physical and Chemical Reference Data, Volume 13, 1984. Pages 102.

[118] B. S. Sparrow, Empirical equations for the thermodynamic properties of aqueous sodium chloride, Desalination, Volume 159, 2003, Pages 161-170.

[119] M. Kromer, K. Roth, R. Takata, P. Chin, Support for Cost Analyses on Solar-Driven High Temperature Thermochemical Water-Splitting Cycles, Final Report to: Department of Energy, Order DE-DT0000951, Report prepared by TIAX LLC, Reference D0535, February 22, 2011.

[120] R. R. Chandrand, D.T. Chin, Reactor analysis of chloralkali membrane cell, Electrochimica Acta, Volume 31 (1),1986, Pages 39-50.

[121] M. Pourbaix, Atlas of Electrochemical Equilibria in Aqueous Solutions, Pergamon Press, Oxford, 1966.

[122] A. J. Downs and C.J. Adams. Chlorine, Bromine, Iodine, and Astatine. In A.F.T. Dickerson (ed.). Comprehensive, Inorganic Chemistry, Volume 2, 1970, Page 107.

[123] W. M. Latimer, The Oxidation Potentials of the Elements and Their Potentials in Aqueous Solutions, Prentice-Hall, Englewood Cliffs, 1961.

[124] A. J. deBethune and N.A.S. Loud, Standard Aqueous Electrode Potentials and Temperature Coefficients at 25°C, Clifford A. Hampel, Skokie, 1964.

[125] T. Mussini and G. Faita, Chlorine. In A.J. Bard (ed.), Encyclopedia of Electrochemistry of the Elements, Vol. 1, 1973, Page 1.

[126] T. Mussini and P. Longhi, Chlorine. In, A. J. Bard, R. Parsons, and J. Jordan (eds). Standard Potentials in Aqueous Solutions, Marcel Decker, 1985, Page 70

[127] G. Faita, P Longhi, and T. Mussini, Journal of The Electrochemical Society, Volume 114, 1967, Page 340.

[128] M. Iqbal , An introduction to solar radiation. Toronto: Academic press, 1983.

[129] L.T. Wong, W.K. Chow, Solar radiation model , Applied Energy, Volume 69, 2001, Pages 191-224.

[130] C. D. Ahrens, Meteorology Today. An Introduction to Weather, Climate, and the Environment. Eighth Edition. Thompson, Brooks/Cole. United States, 2006.

[131] H. Akbari, A. Desjarlais,Cooling down the house: residential roofing products soon will boast "cool" surfaces, Journal Professional Roofing, 2005, Pages 32-38.

[132] P. Berdahl, S.E. Bretz. 1997. Preliminary Survey of the Solar Reflectance of Cool Roofing Materials. Energy and Buildings 25: 149-158.

[133] J. A. Clarke, Energy Simulation in Building Design, 2nd ed. Butterworth Heinemann: Oxford, 2001.

[134] T. l. Jackson, J. J. Feddema, K. W. Oleson, G. B. Bonan, and J. T. Bauer, Parameterization of urban characteristics for global climate modeling. Annals of the Association of American Geographers Special Issue on Climate Change, 2010.

[135] R. Levinson and A. Hashem. Effects of Composition and Exposure on the Solar Reflectance of Portland Cement Concrete. Lawrence Berkeley National, 2001.

[136] T. Muneer, Solar Radiation and Daylight Models for the Energy Efficient. Second edition. Elsevier Press, 2004.

[137] T. R. Oke, Boudary Layer Climates, 2nd edition. Methuen: New York, 2001.

[138] B. E. Psiloglou and H. D. Kambezidis, "Estimation of the ground albedo for the Athens area, Greece." Journal of Atmospheric and Solar-Terrestrial Physics Volume 71(8-9), 2009, Pages 943.954.

[139] D. Thevenard, and K. Haddad, Ground reflectivity in the context of building energy simulation, Energy and Buildings, Volume 38(8), 2006, Pages 972-980.

[140] UCSB library. Material Emissivity. Institute for Computational Earth System Science, University of California, Santa Barbara.